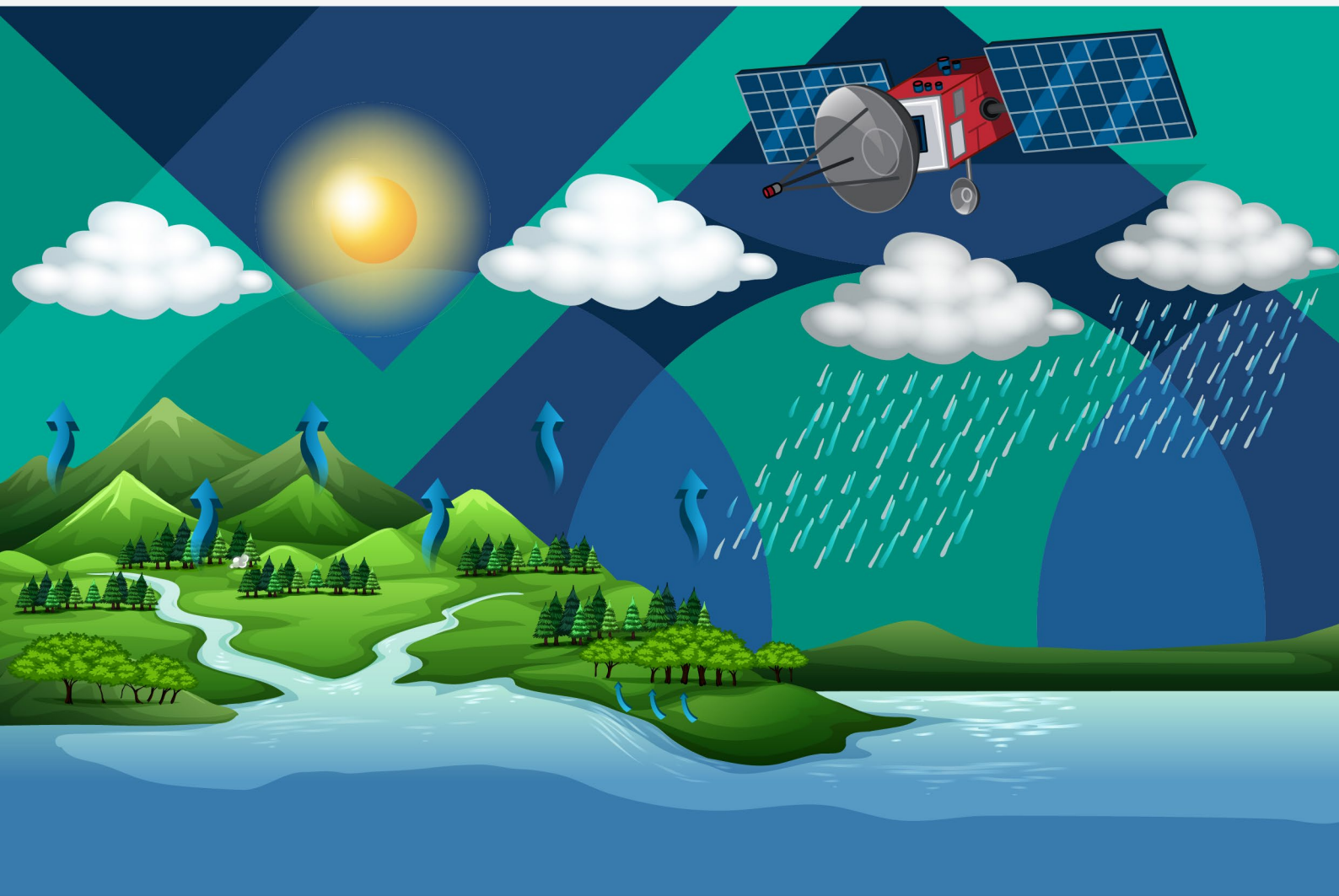




Food and Agriculture
Organization of the
United Nations

REMOTE SENSING DETERMINATION OF **EVAPOTRANSPIRATION**

*Algorithms, strengths and weaknesses, uncertainty
and best fit-for-purpose*



REMOTE SENSING DETERMINATION OF EVAPOTRANSPIRATION

*Algorithms, strengths and weaknesses, uncertainty
and best fit-for-purpose*

Required citation:

FAO. 2023. *Remote sensing determination of evapotranspiration – Algorithms, strengths, weaknesses, uncertainty and best fit-for-purpose*. Cairo. <https://doi.org/10.4060/cc8150en>

The designations employed and the presentation of material in this information product do not imply the expression of any opinion whatsoever on the part of the Food and Agriculture Organization of the United Nations (FAO) concerning the legal or development status of any country, territory, city or area or of its authorities, or concerning the delimitation of its frontiers or boundaries. The mention of specific companies or products of manufacturers, whether or not these have been patented, does not imply that these have been endorsed or recommended by FAO in preference to others of a similar nature that are not mentioned.

ISBN 978-92-5-138242-4

©FAO, 2023, last updated 18/04/2024



Some rights reserved. This work is made available under the Creative Commons Attribution-NonCommercial-ShareAlike 3.0 IGO licence (CC BY-NC-SA 3.0 IGO; <https://creativecommons.org/licenses/by-nc-sa/3.0/igo>).

Some rights reserved. This work is made available under the Creative Commons Attribution-NonCommercial-ShareAlike 3.0 IGO licence (CC BY-NC-SA 3.0 IGO; <https://creativecommons.org/licenses/by-nc-sa/3.0/igo/legalcode>).

Under the terms of this licence, this work may be copied, redistributed and adapted for non-commercial purposes, provided that the work is appropriately cited. In any use of this work, there should be no suggestion that FAO endorses any specific organization, products or services. The use of the FAO logo is not permitted. If the work is adapted, then it must be licensed under the same or equivalent Creative Commons licence. If a translation of this work is created, it must include the following disclaimer along with the required citation: "This translation was not created by the Food and Agriculture Organization of the United Nations (FAO). FAO is not responsible for the content or accuracy of this translation. The original [Language] edition shall be the authoritative edition."

Disputes arising under the licence that cannot be settled amicably will be resolved by mediation and arbitration as described in Article 8 of the licence except as otherwise provided herein. The applicable mediation rules will be the mediation rules of the World Intellectual Property Organization <http://www.wipo.int/amc/en/mediation/rules> and any arbitration will be conducted in accordance with the Arbitration Rules of the United Nations Commission on International Trade Law (UNCITRAL).

Third-party materials. Users wishing to reuse material from this work that is attributed to a third party, such as tables, figures or images, are responsible for determining whether permission is needed for that reuse and for obtaining permission from the copyright holder. The risk of claims resulting from infringement of any third-party-owned component in the work rests solely with the user.

Sales, rights and licensing. FAO information products are available on the FAO website (www.fao.org/publications) and can be purchased through publications-sales@fao.org. Requests for commercial use should be submitted via: www.fao.org/contact-us/licence-request. Queries regarding rights and licensing should be submitted to: copyright@fao.org.

Cover design: ©FAO/Angham Abdelmageed

CONTENTS

Acknowledgements	vii
Foreword	ix
Abbreviations	x
Symbols	xvi
Executive summary	xxi
1. Introduction	1
2. Background on the selected RS ET models	5
2.1 The Surface Energy Balance (SEB)	5
2.2 The Penman-Monteith (PM) model	11
2.3 The Satellite Psychrometric Approach (SPA)	12
2.4 Specific peculiarities of the selected models	13
2.4.1 SEBAL	13
2.4.2 METRIC	15
2.4.3 ALEXI - DisALEXI	17
2.4.4 SSEBop	21
2.4.5 PT-JPL	22
2.4.6 ETLook	24
2.4.7 ETMonitor	28
2.4.8 ETWatch	30
3. Comparative analysis of the selected RS ET models	37
4. Background on the selected RS ET databases/portals	47
4.1 USGS FEWS NET	47
4.2 WaPOR	48
4.3 GloDET	49
4.4 EEFlux	49
4.5 OpenET	50
5. Comparative analyses of the selected RS ET databases/portals	53

6. Some field applications	57
6.1 Experience from the NENA Region	57
6.2 SIMS (Satellite Irrigation Management Support)	59
6.3 IrriWatch	61
7. Uncertainty review on RS ET determinations	65
7.1 Background on methods for addressing and applying uncertainty analysis	65
7.2 Overview of the selected RS ET models' uncertainty	76
7.2.1 Some highlights on model inter-comparisons	84
7.3 On the acceptable limits of uncertainty towards best fit-for-purpose	88
8. Prospects for the near future	93
8.1 ECOSTRESS	93
8.2 Copernicus	94
8.3 WaPOR Phase II	95
8.4 Hydrosat	96
9. Concluding remarks	99
10. References	104
ANNEXES	
Annex I – List of speakers of the remote sensing determination of evapotranspiration webinar series	118
Annex II – Example of semi-empirical decomposition of RS ET uncertainty with METRIC	123

BOXES

1	Some terms, notations and definitions in uncertainty analysis	67
---	---	----

FIGURES

1	Schematic diagram representing the two-source land-surface scheme (left) and the time-integrated ABL closure component (right) of the ALEXI mode	18
2	Schematic diagram representing the ALEXI (a) and DisALEXI (b) modeling scheme	20
3	Graphical conceptualization of ETLook	24
4	A sketch of the trapezoidal vegetation coverage/land surface temperature (Fc/LST) space	26
5	Flowchart of the ETMonitor model	28
6	Schematic representation of the relevant resistances and latent heat fluxes of the soil-vegetation canopy system considered in ETMonitor	29
7	Typical ETWatch processes flowchart	31
8	Relationships between uncertainty and complexity in modeling	66
9	Linear regression between modeled values (e.g. RS ET) and reference values (e.g. Field ET)	73
10	Examples of r^2 values that can be encountered in regression analysis	74
11	Total growing season weighted mean ET (n = 15 sites with 40 total growing seasons) for six satellite-driven ET models, the ensemble mean ET, and ET calculated from the closed and unclosed energy balances at each flux tower site	85
12	Comparison of ETa obtained from various models and ETIa-WPR (represented by the orange dashed line) used as reference to compare the other model performances	85
13	Scatterplot between the <i>in situ</i> decadal ET (observed ET) and estimated decadal ET by TSEB-PT (left graph) and ETLook (right graph). Subscripts 'w' and 'c' refer to WaPOR-like and Copernicus input data source, respectively	86
14	Scatterplot between the <i>in situ</i> decadal ET and estimated decadal ET by TSEB-PT (left graph) and ETLook and WaPOR (right graph). Subscripts 'w' and 'c' refer to WaPOR-like and Copernicus input data sources, respectively. The WaPOR ET product was downloaded from the FAO Portal	87
15	Cumulative ET of pomegranate orchards cultivated in the Newland area of Egypt, as determined by ETLook (WaPOR), SSEBop, METRIC (EEFlux), ALEXI (GloDET) and <i>in-situ</i>	87

TABLES

1 Primary ALEXI input data sources	20
2 Distinctive features of the selected models	42
3 Comparison of key features among the RS ET databases and portals	54
4 Qualitative rating of model performance	76
5 Draft categorization of application type, order of magnitude of water amount per application, approximated acceptable limits of uncertainty per application, and likely classes of RS ET model and satellite to be used	89
6 Tentative ranking of model relative complexity	100
A2.1 Estimated error in ET produced by METRIC (plus or minus, where the values represent two standard deviations of error from the true value). Parameters in Eq. x1 are listed in A2.2	123
A2.2 Values for $ET_{r_{\text{representation error}}}$, $ET_{r_{\text{image_systematic_error}}}$ and $ET_{r_{\text{image_random_error}}}$ used to produce ET_{rF} error estimates in Table 1. Values for ET_{rF} are dimensionless	124

ACKNOWLEDGEMENTS

The authors are deeply indebted to the FAO-RNE management and the team of Regional Initiative on Water Scarcity for the Near East and North Africa (WSI), in particular, whose support has been fundamental for the accomplishment of the RS ET webinar series and of this publication.

Special thanks go to Mohamed AlHamdi (Delivery manager of the WSI), Domitille Vallee (Chief Technical Advisor of the Water Efficiency, Productivity and Sustainability project), and the support team composed of Simon Tanios, Jiro Ariyama, Mohamed Abdallah, Hichem Charieg, Wided Khechimi, and Heba Fahmy.

Likewise, a determinant role has been played by Mariam Elghamrawy and other members of the communication team for taking close care of the communication and dissemination of the webinar series through the various media.

We are also deeply grateful to Angham Abdelmageed who cured the graphic design and editing of the RS ET webinar series and of this publication.

Finally, the WSI team and the authors would like to express profound gratitude to the Swedish International Development Cooperation Agency (Sida) for its financial and partnership support to both the webinar series and this publication.

Lead Authors

Pasquale Steduto

Former FAO Chief of Water Service and Delivery
Manager of Regional Initiative on Water Scarcity for the
Near East and North Africa

Rick G. Allen

University of Idaho, Kimberly, Idaho, United States of
America

Ayse Kilic

University of Nebraska-Lincoln, Lincoln, Nebraska,
United States of America

Contributing Authors

Martha C. Anderson

USDA Agricultural Research Service - Hydrology and
Remote Sensing Laboratory, Beltsville, Maryland, United
States of America

Wim Bastiaanssen

IrriWatch Maurik, of the Kingdom of the Netherlands

Chandrashekhar Biradar

ICARDA, Cairo, Egypt

Arnaud Caiserman

University of Central Asia Khorog-Dushanbe, Tajikistan

Richard Crago

Bucknell University, Lewisburg, Pennsylvania, United
States of America

Mohamed Abdalla El-Sheikh

FAO-SD (Food and Agriculture Organization of the
United Nations—Country Office of Sudan)
Khartoum, Sudan

Joshua B. Fisher

Former Science Lead at Jet Propulsion Laboratory
(NASA) Pasadena, California, United States of America
Presently, Professor at Chapman University, Orange
County, California

Ajit Govind

ICARDA, Cairo, Egypt

Radoslaw Guzinski

DHI GRAS Hørsholm, Denmark

Christopher Hain

NASA's Marshall Space Flight Center Huntsville,
Alabama, United States of America

Jippe Hoogeveen

FAO, Rome, Italy

Li Jia

Chinese Academy of Science, Beijing, China

Ihab Jnad

ACSAD, Damascus, Syrian Arab Republic (the)

Annemarie Klaasse

eLEAF, Wageningen, the Kingdom of the Netherlands

Benjamin Koetz

European Space Agency (ESA-ESRIN), Frascati, Italy

Forrest Melton

NASA Ames Research Center & California State University, Monterey Bay, Moffett Field, California, United States of America

Michel Massart

Earth Observation Unit Directorate General for Defence Industry and Space European Commission Brussels, Belgium

Marloes Mul

IHE-Delft, Delft, the Kingdom of the Netherlands

Christopher Neale

Robert B. Daugherty Water for Food Global Institute at the University of Nebraska Lincoln, Nebraska, United States of America

Hector Nieto

University of Copenhagen, Copenhagen, Denmark

Osama Owaneh

National Agricultural Research Center of Jordan, Amman, Jordan

Livia Peiser

FAO, Rome, Italy

Henk Pelgrum

eLEAF, Wageningen, the Kingdom of the Netherlands

Lisa-Maria Rebelo

IWMI (International Water Management Institute), Colombo District, Western, Sri Lanka

Gabriel Senay

USGS Earth Resources Observation & Science Center Colorado State University, Fort Collins, Colorado, United States of America

Nabil Sghaier

AOAD, Khartoum, Sudan

Ayman Suleiman

University of Jordan, Amman, Jordan

Masahiro Tasumi

University of Miyazaki, Miyazaki, Japan

Bingfang Wu

Chinese Academy of Science, Beijing, China

FOREWORD

The Near East and North Africa (NENA) Region has always suffered from chronic water scarcity due to natural causes. However, in recent decades, several drivers related to demography, food security policies, and overall socio-economic development have intensified the scarcity of water. Additionally, the impacts of climate change and the food insecurity consequent to the war in Ukraine have rapidly and considerably amplified the pressure on the scarce water resources of the region.

Countries of the region are continuously searching for optimal ways for allocating these scarce water resources, promoting sound water accounting, monitoring water resources use from strategic hydrological systems, and enhancing water productivity and efficiency towards an improved saving of water to be reallocated.

One important variable to determine for these various actions is the consumption of water, or evapotranspiration, particularly from irrigated agriculture that consumes more than 85 percent of renewable fresh water resources, while continues to be essential to the sustainability of the food sector and farming systems.

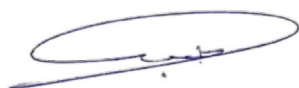
The spatial scales involved are substantial and, with the rapid advances of space science and remote sensing technology, it was natural to call upon the satellites' developments for the determination of evapotranspiration.

The FAO Regional Initiative on Water Scarcity for the Near East and North Africa (WSI), which is providing support to the countries' efforts in addressing the sustainability of water resources management, has thus undertaken the enterprise to pull together major world-class experts in the determination of evapotranspiration through satellite remote sensing, to provide guidance to the different water actors of the NENA Region. Furthermore, the scope of the enterprise expanded to the other FAO regions around the world, through the inter-Regional Technical Platform on Water Scarcity (IRTP-WS).

First, a series of 25 webinars was thus organized to open the dialogue between experts and water actors. Second, the present publication was developed to report the outcome of the webinars series, along with further explorations, analysis, and insights on the subject of satellite remote sensing determination of evapotranspiration.

The present publication intends thus to provide: knowledge update and capacity development of water professionals; more awareness on the strengths, limitations, and fits-for-purpose for the range of remote sensing of evapotranspiration models and databases available; more clarity on issues related to operational aspects, including proper spatial and temporal resolutions for given applications and accuracy of the determinations provided by the various models and databases.

Overall, the publication is expected to serve as a useful reference for several water actors and professionals working for the sustainability of water resources management.



Abdulhakim Elwaer

Assistant Director-General and Regional Representative for the Near East and North Africa

ABBREVIATIONS

ABL	atmospheric boundary layer
ACSAD	Arab Center for the Studies of Arid Zones and Dry Lands
AE	absolute error
AGRI	Advanced Geostationary Radiation Imager on board geostationary satellite Fengyun-4
AgriMet	Columbia-Pacific Northwest Region meteorological network
AIRS	Atmospheric Infrared Sounder
ALARM	Analytical land atmosphere radiometer model
ALEXI	Atmosphere-Land Exchange Inverse algorithm
AMSR-E	Advanced Microwave Scanning Radiometer-Earth Observing System
API	Application Programming Interface
ASCE-EWRI	American Society of Civil Engineers - Environmental & Water Resources Institute
ASE	Association for Science Education
AWR	the Australian Water Resources
AZMET	Arizona Meteorological Network
BEAREX	Bushland Evapotranspiration and Agricultural Remote sensing Experiment
BESS	Breathing Earth System Simulator
C3S	Copernicus Climate Change Service
CAMS	Copernicus Atmosphere Monitoring Service
CEMS	Copernicus Emergency Management Service
CEOS	Committee on Earth Observation Satellites
CERES	Clouds and Earth's Radiation Energy Systems
CFSR	Climate Forecast System Reanalysis
CHIRPS	Climate Hazards group InfraRed Precipitation with Station data
CIMEC	calibration through inverse modeling at extreme conditions
CIMIS	Spatial California Irrigation Management System
CLMS	Copernicus Land Monitoring Service
CMEMS	Copernicus Marine Environment Monitoring Service

CNN	convolutional neural network
CPRL	Conservation and Production Research Laboratory
CSV	comma separated value data
DAISY	Danish Soil-Plant-Atmosphere System model
DAYMET	Daily Surface Weather and Climatological Summaries
DEM	digital elevation model
DHI	Remote Sensing Company in Denmark
DisALEXI	Atmosphere Land Exchange Inverse Disaggregation algorithm
DWFI	Daugherty Water for Food Global Institute
ECMWF	European Centre for Medium-Range Weather Forecasts
ECOSTRESS	ECOsysteM Spaceborne Thermal Radiometer Experiment on Space Station
EEFlux	Earth Engine Evapotranspiration Flux
EORS	USGS Earth Resources Observation System
ERA5	The 5th generation ECMWF Reanalysis for the Global Climate and Weather data
ESA	European Space Agency
ESI	evaporative stress index
ESSIC	Earth System Science Interdisciplinary Center
ESVEP	End-member-based Soil and Vegetation Energy Partitioning
ET	evapotranspiration
ETIa	actual evapotranspiration and interception
ETLook	A remote sensing-based model to compute evapotranspiration of large areas
ETMonitor	A remote sensing-based model to compute evapotranspiration of large areas combining optical and microwave remote sensing observations
ETO	grass reference evapotranspiration
ETRS	evapotranspiration obtained by remote sensing
ETWatch	A remote sensing-based model to compute evapotranspiration of large areas
ETWB	ET derived through the water balance
EUMETSAT	European Organization for the Exploitation of Meteorological Satellites
FAO	Food and Agriculture Organization of the United Nations
FEWS NET	Famine Early Warning Systems Network
FLUXNET	A Global Network of Micrometeorological Tower Sites

GDAS	Global Data Assimilation System
GESEBAL	Google Earth Engine-SEBAL
GEF	Global Environment Facility
GEOS	Goddard Earth Observing System
GIS	Geographic Information Systems
GloDET	Global Daily Evapotranspiration Portal
GOES	Geostationary Operational Environmental Satellite
GPP	Gross Primary Production
GRACE	Gravity Recovery and Climate Experiment
GRAPEX	Grape Remote-Sensing Atmospheric Profile and Evapotranspiration eXperiment
GRD	Sentinel-1 Ground Range Detected
GRIDMET	A Dataset of Daily High-Spatial Resolution Surface Meteorological data
HIRAS-II	Hyperspectral Infrared Atmospheric Sounder-II on board polar satellite Fengyun-3
HLS	Harmonized Landsat-Sentinel
HYDRUS	Finite element model for simulating the one-dimensional movement of water, heat, and multiple solutes in variably saturated media
I	water Interception
IAHS	International Association of Hydrological Sciences
ICARDA	International Center For Agricultural Research In The Dry Areas
ICT	Information and Communications Technology
IHE-Delft	Institute for Water Education
IWMI	International Water Management Institute
JSON	JavaScript Object Notation
LAI	leaf area index
LAS	large aperture scintillometers
LCC	Land Cover Classification
LDAS	Land Data Assimilation System
LEDAPS	Landsat Ecosystem Disturbance Adaptive Processing System
LEO	low Earth orbit
L8SR	Landsat 8 Surface Reflectance
LST	Land Surface Temperature

LSTM	Land Surface Temperature Monitoring
LULC	land use and land cover
LWIR	Long Wavelength Infrared
MAD	mean absolute difference
MAE	mean absolute error
MAPE	Mean Absolute Percentage Error
MBE	mean bias error
MENA	Middle East and North Africa
MERSI-LL	Medium Resolution Spectral Imager-LL on board polar satellite Fengyun-3
METEOSAT	Geostationary Meteorological Satellites Operated by EUMETSAT
METRIC	Mapping Evapotranspiration at high Resolution with Internalized Calibration model
MODIS	Moderate Resolution Imaging Spectroradiometer
MPI	Max Planck Institute
MRD	mean relative difference
MRE	mean relative error
MSC	Multi-spectral camera on board Resources satellite three of China
MSG	Meteosat Second Generation
MSI	MultiSpectral Instrument (MSI) on board Sentinel-2
NASA	National Aeronautics and Space Administration
NCDC	National Climatic Data Center
NDVI	Normalized Difference Vegetation Index
NENA	Near East and North Africa
NGO	Non-governmental Organization
NIR	near infrared
NLCD	National Land Cover Database
NLDAS	North American Land Data Assimilation System
NOAA	National Oceanic and Atmospheric Administration
NPP	Net Primary Production
NRMSE	Normalized Root Mean Square Error
NSE	Nash-Sutcliffe Efficiency coefficient

NSIDC	National Snow and Ice Data Center
P	precipitation
PAR	photosynthetically active radiation
PHyTIR	Prototype HypsIRI Thermal Infrared Radiometer
PRISM	Parameter-elevation Regressions on Independent Slopes Model
PT-JPL	Priestley-Taylor Jet Propulsion Laboratory
PYSEBAL	Python version of SEBAL
RA	transport resistances
RE	relative error
RET	Reference Evapotranspiration
RF	Random Forest Algorithm
RH	relative humidity at air temperature
RMSD	Root Mean Square Deviation or Difference
RMSE	root mean square error
RS	remote sensing
RVI	radar vegetation index
RX	bulk leaf boundary layer
SAR	Synthetic Aperture Radar
SAVI	soil adjusted vegetation index
SBG	Surface Biology and Geology
SE	standard error
SEB	surface energy balance
SEBAL	Surface Energy Balance Algorithm for Land
SEVIRI	The Spinning Enhanced Visible and InfraRed Imager (SEVIRI) on board MSG
SIMS	Satellite Irrigation Management Support
SLSTR	Sea and Land Surface Temperature Radiometer
SMACEX	Soil Moisture Atmosphere Coupling Experiment
SMAP	Soil Moisture Active Passive Satellite
SMOS	Soil Moisture Ocean Salinity Satellite
SPA	Satellite Psychrometric Approach

SPC	surface psychrometric constant
SR	solar radiation
SRTM	Shuttle Radar Topography Mission
SSEBop	Simplified Surface Energy Balance model
SW	Shuttleworth-Wallace
TBP	Total Biomass Production
THEMIS	Thermal Emission Imaging Spectrometer
TIR	thermal infrared
TM	Thematic Mapper
TOA	top-of-atmosphere
TOC	top-of-canopy
TRISHNA	Thermal infraRed Imaging Satellite for High-resolution Natural resource Assessment
TSEB	Two Source Energy Balance
UCSB	University of California, Santa Barbara
ULB	Urmia Lake Basin
USDA-ARS	United States Department of Agriculture-Agricultural Research Service
USGS	United States Geological Survey
VIIRS	Visible Infrared Imaging Radiometer Suite
VISSR-II	Stretched Visible and Infrared Spin Scan Radiometer-II on board geostationary satellite Fengyun-2
VNIR	Visible and Near-Infrared
VPD	vapor pressure deficit
VSWIR	Visible to Shortwave Infrared
WAPOR	FAO Water Productivity Open-access Portal
WFV	Chinese GF-1 Wide Field View
WP	Water Productivity
WRF	Weather Research and Forecasting model
WSI	Regional Initiative on Water Scarcity for the Near East and North Africa
WUE	water use efficiency

SYMBOLS

a and b	Empirically determined constants for a given satellite image and thermal conditions
c₁ and c₂	Empirically determined coefficients
C_p	Specific heat of air at constant pressure (J kg ⁻¹ K ⁻¹)
c_p	Specific heat capacity of air at constant pressure
d	The surface's zero-plane displacement height
dT	Near-surface temperature difference between the surface and a near-surface height or between two near-surface heights
dT/dx	Temperature gradient (K m ⁻¹)
E	Soil evaporation
e_a	Actual vapor pressure (kPa)
e_s	Saturation water vapor pressure at the air temperature (kPa)
e_s - e_a RH	The vapor pressure deficit
ET_{24h}	Daily actual ET for the day of the satellite image
ET_f	Dryness of the surface' expressed as ET fraction (ratio between actual and maximum ET)
ET_{inst}	Computed instantaneous ET for each pixel
ET_O	The grass reference Evapotranspiration
ET_{ref}	Standardized reference ET
ET_{ref,24h}	Daily reference ET for the day of the satellite image
ET_{ref}F	Reference ET fraction
ET_rF	The actual ET expressed as a fraction of reference ET
ET_{WB}	The ET derived through the water balance
F	Leaf area index
F_{c,eff}	The effective fraction of ground covered or shaded by vegetation near solar noon
fg	Green canopy fraction
f_M	The plant moisture constraint
f_M	The plant moisture constraint
fPAR_A	The fraction of the photosynthetic active radiation (PAR) absorbed by the green vegetation cover

f_{PAR_i}	The fraction of the PAR intercepted by the total vegetation cover
f_{SM}	The soil moisture constraint
f_T	The plant temperature constraint
f_{wet}	Relative surface wetness
g	Gravitational acceleration (= 9.807 m s^{-2})
G	The seasonal cycle of soil temperature changes.
G	Soil heat flux.
H	The sensible heat flux
h	The mean height of the vegetation in m
H_c	Sensible heat flux from the crop (W m^{-2})
H_s	Sensible heat flux from the soil (W m^{-2})
I	The precipitation interception by the canop
K	Von Karman's constant (0.41).
k_0	The weighting factor of the isotropic scattering component
k_2	The weighting factor based on surface scattering and the shadow casting theory
$K_{c,min}$	The minimum K_{cb} for bare soil
$K_{cb,full}$	The estimated K_{cb} during nearly full ground cover (or LAI >3)
K_e	Soil evaporation coefficient
L	Monin-Obukhov length
LAI_{daily}	Daily Leaf Area Index (LAI) values
LA_{leff}	Effective leaf area index (adimensional)
m	Momentum
M_L	A multiplier on $F_{c,eff}$ describing the effect of canopy density on shading and on maximum relative ET per fraction of ground shaded
$net R_L$	The net long wave radiation
p	Air pressure.
P	Precipitation
Q	Total heat energy stored in the unit surface layer (J m^{-2})
Q_h	Heat flux density (W m^{-2})
R	Universal gas constant
r^2	Coefficient of determination

$r_{a,a}$	Aerodynamic resistance between the canopy source height and the reference height above the canopy ($s \cdot m^{-1}$)
r_{a-c}	Aerodynamic resistance - vegetation (or canopy)
r_{ah}	Aerodynamic resistance to heat transfer from surface to height of T_a ($s \cdot m^{-1}$).
r_{a-s}	Aerodynamic resistance - Soil
$r_{c,min}$	The minimum canopy resistance
r_{canopy}	Canopy resistance
RH	Relative humidity at air temperature (%)
$R_L \uparrow$	Outgoing long-wave radiation ($W \cdot m^{-2}$)
$R_L \downarrow$	Incoming long-wave radiation ($W \cdot m^{-2}$)
RMSE	Actual measure of the ET model uncertainty
Rn	Net surface irradiance (commonly referred to as the net radiation)
$R_{n,i}$	The instantaneous net radiation
Rn_{24h}	The 24-h integrated value of Rn
Rn_c	Canopy net radiation ($W \cdot m^{-2}$)
R_n	The net radiation at the top of canopy
Rn_s	Soil net radiation ($W \cdot m^{-2}$)
r_s	Surface resistance ($s \cdot m^{-1}$)
r_s	Surface resistance
Rs	Solar radiation
$r_{s,clear}$	The bulk stomatal resistance of the well-illuminated leaf on the clear-day
$R_s \downarrow$	Incoming short-wave radiation, both direct and diffused ($W \cdot m^{-2}$)
r_{s-c}	Vegetation (or canopy) surface resistance
r_{soil}	Surface resistance
r_{s-s}	Soil surface resistance
$r_{s,canopy,min}$	Minimum stomatal resistance (in $s \cdot m^{-1}$)
RVI	The radar vegetation index
S_m	The soil moisture stress originating from a lack of soil moisture in the root zone.
S_r	The radiation stress induced by the lack of incoming shortwave radiation
S_t	The temperature stress
S_v	The vapor pressure stress induced due to persistent vapor pressure deficit

SM_{clear}	The soil moisture content retrieved from the microwave radar information
SM_{daily}	The daily soil moisture content
s_{oz}	The solar zenith angle
t	Time (s)
T	Crop transpiration
T_a	Near surface air temperature where T_a is used as a surrogate temperature for the total integrated effective atmospheric emitting temperature (K)
T_{aero}	The 'aerodynamic' temperature
T_c	Canopy surface aerodynamic temperature (K)
T_c	The cold/wet limit surface temperature (also expressed in K).
T_d	Air temperature measured by the dry-bulb thermometer (K)
T_{max}	Daily maximum air temperature
T_s	Land surface temperature (K)
Ts_{cold}	Satellite-based T_s at the cold pixel where NDVI > 0.8
T_{s_datum}	Radiometric surface temperature adjusted to a common elevation for each image pixel
$T_{s_datum_cold}$	Delapsed surface temperature at the cold pixel
$T_{s_datum_hot}$	Delapsed surface temperature at the hot pixel
T_w	Air temperature measured by the wet-bulb thermometer (K);
U	Wind speed
$u.$	Friction velocity
$u.$	Friction velocity ($m\ s^{-1}$)
u_z	Wind speed ($m\ s^{-1}$) at height z (m)
z_2	Height above the surface where T_a is measured
z_{om}	Momentum roughness length (m).
z_{om} and z_{oh}	The surface's roughness length for momentum and heat transfer
z_1 and z_2	Heights above ' $d+z_{oh}$ ' of the vegetation
$(1-\epsilon_o) R_L\downarrow$	The reflected portion of the incoming long-wave radiation ($R_L\downarrow$).
α	Surface albedo (dimensionless)
α	Priestley-Taylor constant (=1.26)
$\alpha R_S\downarrow$	The reflected portion of the incoming short-wave radiation ($R_S\downarrow$),
αc	PT coefficient

γ	Psychrometric constant (kPa °C ⁻¹)
γ^s	Surface psychrometric constant (SPC), expressed in K ⁻¹
Δ	Slope of the relationship between saturation vapor pressure and temperature (kPa °C ⁻¹)
ΔS	The change in water storage of the system
$\Delta\theta$	The fraction between actual and saturated soil moisture
ϵ_o	Broad-band surface thermal emissivity (dimensionless)
ϵ_a	Apparent atmospheric emissivity (dimensionless)
θ_m	Mixed layer potential temperature
$\theta_s(z)$	An early morning ABL potential temperature
κ	Thermal conductivity (W m ⁻¹ K ⁻¹)
λ	Latent heat of evaporation
λE	The <i>latent heat flux</i>
λE_c	Latent heat flux from the crop (W m ⁻²)
λE_s	Latent heat flux from the soil (W m ⁻²)
ρ_a	Air density (kg m ⁻³)
σ	Stefan–Boltzmann constant (5.670374 × 10 ⁻⁸ W m ⁻² K ⁻⁴)
ψ	Boundary layer stability
ψ_{sm} and ψ_{sh}	Integrated stability functions between the surface and z ₂ height
$\Omega(\theta)$	Vegetation clumping factor apparent at view angle
$\alpha c f g \left(\frac{\Delta}{\Delta + \gamma} \right) R n c$	A modified Priestley-Taylor (PT) equation for transpiration (λE_c)
γ	Psychrometric constant (kPa °C ⁻¹)
τ	Transmissivity

EXECUTIVE SUMMARY

In agricultural and other vegetated lands, Evapotranspiration (ET) nearly always represents the largest share of water outflow from the system, identified as the 'consumptive' fraction of water use.

Quantifying ET in space and time, thus, is extremely relevant for water resources management applications, including: monitoring water consumption by various land use systems; water allocation, transfer and regulations; management of irrigation at the scheme and on-farm levels; determination of crop water productivity; prediction of yield through models; assessment of agricultural drought indexes; performing water balance and water accounting within hydrologic systems at a wide range of scales; development of effective strategies of adaptation to climate changes.

At local or field scale several methods and instrumentations for ET determination have been developed over time (e.g. soil-moisture measurements for water depletion monitoring; weighing lysimeters; the Penman-Monteith equation; the Bowen-ratio/energy balance; the Eddy covariance; the Large Aperture Scintillometer). However, these methods are generally complex, expensive, often focused on limited spatial scales, and mostly confined to academic and research environments. Scaling them up to larger areas is still prohibitive due to cost. For large scales, such as irrigation schemes, watershed, sub-national, national and basin scales, the only feasible and affordable methods, so far, for ET determination are through satellite remote sensing (RS).

The literature provides ample and diversified offers of RS ET models and platforms, and users are concerned with operational issues such as: proper spatial and temporal resolution for given applications; accuracy of the ET determinations provided by the various models and databases; methods to conduct qualitative and quantitative error analyses of RS-ET determinations; modalities to test the RS ET with field ET measurements; and criteria to know which ET data sources best fit one's purpose.

The FAO Regional Initiative on Water Scarcity for the Near East and North Africa (WSI) of the Near East and North Africa (NENA) region has then taken the initiative of addressing these concerns in consultations with various countries' stakeholders in the region, partners and major experts in the RS ET domain, and with the support of the Swedish International Development Cooperation Agency (Sida). Two major enterprises were carried out: (i) a plan of a webinars series¹, (ii) the present publication reporting on the major outcomes of the webinars series, adding further insights, and providing an enriched literature review.

The selected RS ET models, considered as most operational and presented to the webinars series and discussed in this publication, are: SEBAL (Surface Energy Balance Algorithm for Land);² METRIC (Mapping Evapotranspiration at high Resolution with Internalized Calibration);³ ALEXI/DisALEXI (Atmosphere-Land Exchange Inverse);⁴ SSEBop

¹ <https://dgroups.org/fao/wateraccounting/library/sqff8vmt?o=lc>

² Bastiaanssen W.G.M., Menenti M., Feddes R.A. and Holtslag A.A.M. (1998a). A remote sensing surface energy balance algorithm for Land (SEBAL), Part 1: Formulation. *J. Hydrol.*, 212-213: 198–212.
Bastiaanssen W.G.M., Pelgrum H., Wang J., Ma Y., Moreno J.F., Roerink G.J. and van der Wal T. (1998b). A remote sensing surface energy balance algorithm for land (SEBAL)—Part 2. Validation. *J. Hydrol.*, 212-213: 213–229
[https://doi.org/10.1016/S0022-1694\(98\)00254-6](https://doi.org/10.1016/S0022-1694(98)00254-6)

³ Allen R.G., Tasumi M. and Trezza R. (2007a). Satellite-based energy balance for mapping evapotranspiration with internalized calibration (METRIC) - model. *J. Irrig. Drain. Eng. ASCE*, 133: 380–394.
Allen R.G., Tasumi M., Morse A., Trezza R., Wright J.L., Bastiaanssen W., Kramber W., Lorite I. and Robison C.W. (2007b). Satellite-based energy balance for Mapping evapotranspiration with Internalized Calibration (METRIC) - Applications. *J. Irrig. Drain. Eng.*, 133(4): 395–406. [https://doi.org/10.1061/\(ASCE\)0733-9437\(2007\)133:4\(395\)](https://doi.org/10.1061/(ASCE)0733-9437(2007)133:4(395)).

⁴ Anderson M.C., Norman J.M., Diak G.R., Kustas W.P. and Mecikalski J.R. (1997). A two-source time-integrated model for estimating surface fluxes using thermal infrared remote sensing. *Remote sensing Environ.*, 60: 195-216.
Anderson M.C., Norman J.M., Mecikalski J.R., Torn R.D., Kustas W.P. and Basara J.B. (2004). A multi-scale remote sensing model for disaggregating regional fluxes to micrometeorological scales. *J. Hydrometeorol.*, 5: 343-363.
Anderson M.C., Kustas W.P., Norman J.M., Hain C.R., Mecikalski J.R., Schultz L., González-Dugo M.P., Cammalleri C., d'Urso G., Pimstein A. and Gao F. (2011). Mapping daily evapotranspiration at field to continental scales using geostationary and polar orbiting satellite imagery. *Hydrol. Earth Syst. Sci.*, 15: 223-239.

(Simplified Surface Energy Balance – Operational;⁵ PT-JPL (Priestley-Taylor from Jet Propulsion Lab);⁶ ETLook;⁷ ETMonitor;⁸ ETWatch.⁹

The selected RS ET models can be grouped into different categories, depending on the core algorithms used (e.g. surface energy balance, Penman-Monteith, psychrometry), the way the 'surface' is characterized (e.g. single layer or two-layer, also referred to as single-source or two-source), the spatial resolution and coverage (e.g. coarse or fine resolution, with global or local coverage), and a few other distinguishing factors. However, the various RS ET models may not fall rigidly into only one category, and often, adopt a mix of approaches.

The key categories and related RS ET models are the following.

The Surface Energy Balance (SEB). The exchange of energy between the land surface and the overlying atmosphere, and the underlying ground, involves four important energy terms: the net radiation (Rn), representing the net between gain and losses of radiation energy by the surface; the sensible heat flux (H), representing the loss (or gain) of energy by the surface as heat transfer to the atmosphere; the ground heat flux (G), representing the loss (or gain) of energy by heat conduction through the lower boundary of the surface layer; the latent heat flux (λE), representing a loss (or gain) of energy from the surface due to evaporation.

All terms have the unit of $W\ m^{-2}$ and they are in balance through the following equation:

$$\lambda E = Rn - G - H$$

λE is the residual of the surface energy balance, as derived by the RS models that are based on SEB. To derive the amount of water evapotranspired, E, (expressed in kg), λE is divided by λ , the latent heat of vaporization (expressed in $J\ kg^{-1}$).

Major RS ET models based on SEB are: SEBAL; METRIC; ALEXI-DisALEXI; and ETWatch (though, in combination with others). All of them are one-source models, except ALEXI-DisALEXI, which is a two-source model, and they all can achieve a fine spatial resolution (e.g. 30 m).

While the SEB is a reliable approach that is based on sound physics, cloud cover is considered a serious interference to RS ET applications in various parts of the world (e.g. Asia and other regions of Africa and Europe). In fact, cloud cover reduces the number of clear images to be processed and thereby extends time periods between clear images.

The Penman-Monteith (PM) model. To circumvent the problem of cloud-cover interference indicated for the SEB approach, the Penman-Monteith (P-M) model can be adopted, i.e. using the PM equation below:

$$\lambda E = \frac{\Delta (Rn - G) + \frac{\rho_a C_p (e_s - e_s RH)}{r_a}}{\Delta + \gamma \left(1 + \frac{r_s}{r_a} \right)}$$

⁵ Senay G.B., Buddle M., Verdin J. and Melesse A. (2007). A coupled remote sensing and simplified surface energy balance approach to estimate actual evapotranspiration from irrigated fields. *Sensors*, 7(6): 979. <https://doi.org/10.3390/s7060979>.

Senay G.B., Bohms S., Singh R.K., Gowda P.H., Velpuri N.M., Alemu H. and Verdin J.P. (2013). Operational evapotranspiration mapping using remote sensing and weather datasets: A new parameterization for the SSEB approach. *JAWRA*, 49(3): 577-591. <https://doi.org/10.1111/jawr.12057>.

Senay G.B. (2018a). Satellite psychrometric formulation of the Operational Simplified Surface Energy Balance (SSEBOP) model for quantifying and mapping evapotranspiration. *Amer. Soc. Agric. Biol. Eng.*, 34(3): 555-566. EST FIT-FOR-PURPOSE

Senay G.B. (2018b). Landsat-based illustrative implementation of Satellite Psychrometry for ET Mapping. U.S. Geological Survey data release. doi.org/10.5066/F7ZS2VR6.

Senay G.B., Kagone S. and Velpuri N.M. (2020). Operational global actual evapotranspiration: development, evaluation, and dissemination. *Sensors*, 20: 1915 [doi:10.3390/s20071915].

⁶ Fisher J.B., Tu K.P. and Baldocchi D.D. (2008). Global estimates of the land-atmosphere water flux based on monthly AVHRR and ISLSCP-II data, validated at 16 FLUXNET sites. *Remote sensing Environ.*, 112: 901-919.

⁷ Bastiaanssen W.G.M., Cheema M.J.M., Immerzeel W.W., Miltenburg I.J. and Pelgrum H. (2012). Surface energy balance and actual evapotranspiration of the transboundary Indus Basin estimated from satellite measurements and the ETLook model. *Water Resour. Res.*, Vol. 48, W11512, doi: 10.1029/2011WR010482.

⁸ Hu G. and Jia L. (2015). Monitoring of evapotranspiration in a semi-arid inland river basin by combining microwave and optical remote sensing observations. *Remote sensing*, 7: 3056-3087 doi:10.3390/rs70303056.

⁹ Wu B.F., Xiong J. and Yan N.N. (2008). ETWatch for monitor regional evapotranspiration with remote sensing. *Advances Water Sci.*, 19(5): 671-678.

Wu B.F., Xiong J. and Yan N.N. (2011). ETWatch: models and methods. *J. Remote sensing*, 15(2): 224-239.

Wu B., Zhu W., Yan N., Xing Q., Xu J., Ma Z. and Wang L. (2020). Regional Actual evapotranspiration estimation with land and meteorological variables derived from multi-source satellite data. *Remote sensing*, 12, 332; doi:10.3390/rs12020332.

where: Δ is the slope of the relationship between saturation vapor pressure and temperature ($\text{kPa } ^\circ\text{C}^{-1}$); e_s is the saturation water vapor pressure at the air temperature (kPa); RH is the relative humidity at air temperature (%); γ is the psychrometric constant ($\text{kPa } ^\circ\text{C}^{-1}$); ρ_a is the air density (kg m^{-3}); C_p is the specific heat of air at constant pressure ($\text{J kg}^{-1} \text{K}^{-1}$); r_s is the surface resistance (s m^{-1}); r_a is the aerodynamic resistance (s m^{-1}), and Rn and H already defined.

While Rn and G terms are computed as for the SEB, the PM equation requires the determination of the vapor pressure deficit, the aerodynamic resistance (r_a) and the surface resistance (r_s).

The vapor pressure deficit is derived by using meteorological data (T_a and RH), usually taken by other RS sources. The aerodynamic resistance (r_a) is derived through numerical iteration and r_s depends on the type of vegetation cover and minimum stomatal resistance, largely influenced by soil moisture content. Passive microwave radiometer (AMSR-E) imagery can be used to derive continuous surface soil moisture as it is little influenced by cloud cover. The root-zone soil moisture can then be derived through additional modeling (water balance, etc.) and thus providing the adjustment for the r_s .

There are two approaches to having the model address the two-source of λE (soil and vegetation separately). One considers the aerodynamic resistance of the soil (r_{a-s}) separated from the one of the vegetation, or canopy, (r_{a-c}). Similarly, the surface resistance (r_s) is disaggregated into the soil surface resistance (r_{s-s}) and the vegetation (or canopy) surface resistance (r_{s-c}). The other considers the Shuttleworth–Wallace (SW) equation, based on the PM equation, to solve for the two latent heat fluxes.

A reduced version of the PM model is represented by the Priestley-Taylor (PT) equation for the determination of the potential evapotranspiration (ETp) of an extensive areas of well-watered vegetation, and it is obtained by the product of equilibrium evaporation (e) and the Priestley-Taylor constant (-1.26).

Major RS ET models based on PM (or its SW and PT versions) are: ETLook (using the original PM equation, as dual-source); ETMonitor (using the SW equation, as dual-source); ETWatch (using a combination of the PM equation and the SEB approach); PT-JPL (using the PT equation).

The Satellite Psychrometric Approach (SPA). The Satellite Psychrometric Approach (SPA) follows an analogy with the principles of psychrometry for the determination of the water vapor content of the air.

The instrument used in psychrometry (the psychrometer) consists of two thermometers with one thermometer-bulb kept continuously wet (wet-bulb) while the other thermometer-bulb is measuring the ambient air temperature (dry-bulb). The wet-bulb thermometer registers a lower temperature than the dry-bulb thermometer as a result of the cooling effect of evaporation, under equilibrium heat exchange condition. The actual water vapor pressure of the air (e_a , in kPa) is then determined through the difference between the dry- and wet-bulb readings along with a psychrometric constant (γ , in kPa K^{-1}), i.e.

$$e_a = e_s - \gamma(T_d - T_w)$$

where e_s is the saturation vapor pressure at the temperature of the wet bulb (kPa), and T_w and T_d are the air temperature measured by the wet-bulb and dry-bulb thermometers (K), respectively.

The relative humidity (RH), obtained by the ratio e_a/e_s , is thus a measure of the 'dryness' of the air, and it is obtained as

$$RH = \frac{e_a}{e_s} = \frac{e_s}{e_s} - \frac{\gamma}{e_s}(T_d - T_w) = 1 - \frac{\gamma}{e_s}(T_d - T_w)$$

The RS modeling of ET based on SPA adopts an analogy between the 'dryness of the air' (RH) and the 'dryness of the surface' expressed as ET fraction (ETf), i.e.

$$ETf = 1 - \gamma^s(T_s - T_c)$$

where ETf represents the ratio between actual and maximum ET, nominally varying between 0 and 1; γ^s is denoted as a "surface psychrometric constant" (SPC) based on the aerodynamic properties of a dry-bare surface (K^{-1}); T_s is the satellite-derived land surface temperature (LST, in K); and T_c is the cold/wet limit surface temperature (K).

The only RS ET model based on the SPA approach is the SSEBop.

A summary of the different features of the selected models (including conceptual approach, input variables, sources of inputs data, output spatial and temporal scales, and major application) is reported in the following table.

Model	Conceptual approach	Input variable	Sources ^(*)	Output spatial scale	Output temporal scale ^(**)	Major application
SEBAL	Residual Surface Energy Balance 1-source ($\lambda E = R_n - H - G$)	LST	VIIRS, Landsat, ECOSTRESS,	30 m (Landsat)	1 day (VIIRS, MODIS)	District Water Balance
		Albedo, NDVI	Sentinel, Landsat	375 m (VIIRS)	8 days (Landsat)	Irrigation
		Land surface elevation	SRTM, Copernicus	1 Km (MODIS)		Crop yield
		Cloud cover (LandSAF)	MSG			Carbon sequestration
		Ta, RH, wind	CFSR, GEOS			
METRIC	Residual Surface Energy Balance 1-source ($\lambda E = R_n - H - G$)	LST	Landsat or VIIRS	30 m (Landsat)	8 days (Landsat)	ET from parcels > 5ha
		Albedo	Landsat, Sentinel 2	30 m (VIIRS)		District Water Balance
		Land surface elevation	SRTM - DEM	LST sharpened using Sentinel 2)		Irrigation
		Land Cover Type	NLCD or ESA WorldCover			Basin Water Balance
		NDVI or LAI	Landsat, Sentinel 2			
	E _{Tr} , Wind speed	Weather Stations or NLDAS or CFSV2 or GridMET				
ALEXI-DisALEXI	Residual Surface Energy Balance 2-source ($\lambda E = R_n - H - G = \lambda E_c + \lambda E_g$)	LST	GOES (for ALEXI)	5-10 km (ALEXI)	1 day (ALEXI)	Continental ET Monitoring;
			LANDSAT (for DisALEXI)	30 m (DisALEXI)	8 days (DisALEXI)	Drought Indexing (ALEXI)
		Albedo	MODIS (for ALEXI)			
			Landsat (for DisALEXI)			Local ET Monitoring;
		NDVI or LAI	MODIS (for ALEXI)			District Water Balance;
			Landsat (for DisALEXI)			Irrigation (DisALEXI)
	Land Cover	NLCD				
	Ta profile & other meteorological inputs	CFSR				

Model	Conceptual approach	Input variable	Sources ^(*)	Output spatial scale	Output temporal scale ^(**)	Major application
SSEBop	Psychrometric Approach 1-source	LST	MODIS or Landsat	30 m (Landsat)	1 day (MODIS)	Continental Drought Indexing, ET monitoring Crop Water Use Assessment
		Ta	PRISM or Chelsa/ WorldClim	1 Km (MODIS)	8 days (Landsat)	
		Albedo	MODIS or Landsat			
		Land surface elevation	SRTM - DEM			
		NDVI	MODIS or Landsat			
		ETr	GRIDMET/GDAS			
PT-JPL	Priestley-Taylor 3-source including interception evaporation	LST	ECOSTRESS, MODIS, VIIRS or Landsat	3 m (Planet) 30 m (Landsat)	1 day (MODIS) 2-5 days (ECOSTRESS)	Local to Global scale ET monitoring
		Albedo	MODIS or Landsat	70 m (ECOSTRESS)	8 days (Landsat)	
		NDVI or LAI	Landsat, MODIS, VIIRS, Planet, Sentinel-2	1 Km (MODIS)		
		meteorological inputs	GEOS-FP, MODIS, CFSR for Ta, RH			
ETLook	Penman-Monteith 2-source	LST	MODIS, VIIRS, Sentinel-3 or Landsat	10m (Sentinel-2) 30 m (Landsat)	1 day (inputs are interpolated/extrapolated between observations)	Field-scale to continental ET monitoring Agricultural water management
		Albedo	MODIS/VIIRS/Sentinel-3 or Landsat/Sentinel-2	375m (VIIRS) 1 Km (MODIS, Sentinel-3)		
		NDVI	MODIS, VIIRS, ProbaV, Sentinel2 and 3, Landsat			
		Land surface elevation	Copernicus DEM or SRTM DEM			
		meteorological inputs	GEOS-5, ERA5 ³ , Gridded Meteostations			

Model	Conceptual approach	Input variable	Sources ^(*)	Output spatial scale	Output temporal scale ^(**)	Major application
ETMonitor	Shuttleworth–Wallace (modified PM) 2-source	Surface/Top Soil Moisture	AMSR-E	1 Km (MODIS)	1 day (MODIS)	Regional & National ET monitoring
		Albedo	GLASS or MODIS			Basin Water Balance
		NDVI	MODIS			
		Land Cover	Variable sources			
		Land surface elevation	Variable DEMs			
		Soil physical properties	Variable maps			
		meteorological inputs	Gridded or Weather Stations			
ETWatch	Residual Surface Energy Balance & Penman-Monteith & Water balance 1-source	LST	MODIS & MERSI-LL ² & Landsat TM/ETM/TIRS	5m (MSC) 10m (MCI)	1 day (MODIS & MERSI-LL)	Basin Water resource impact assessment of projects on water conservancy and ecological protection Water accounting of irrigation district Regional & National ET monitoring
		Albedo	MODIS & MERSI-LL & TM/ETM/OLI	16m (WV) 30m (TM/OLI)	4-10 day (MCI & GRD)	
	Surface/Top Soil Moisture	AMSR-E, SMOS ³ , SMAP ⁴	250m-1 Km (MODIS/ MERSI-LL)	4-16 days (WV/ TM)		
	Land surface elevation	Variable DEMs				
	NDVI	MODIS & MERSI-LL				
	Sunshine Duration	TM/ETM/OLI & WV ⁵ & MSI ⁶				
		MSC ⁷ VISSR-II ⁸ / AGR ⁹				
	Surface roughness	SEVIRI ¹⁰				
	Boundary layer height & parameters	MODIS & MERSI-LL GRD ¹¹ AIRS & MODIS & HIRAS-II ¹²				
	meteorological inputs	Gridded or Weather Stations				

(*) These sources are continuously evolving as more satellite missions are launched and more databases are made available. Furthermore, the geographic selection may provide alternative and more appropriate sources.

(**) This temporal scale refers to the minimum interval between key satellites overpasses

Notes: 1. The 5th generation ECMWF Reanalysis for the Global Climate and Weather data.

2. Medium Resolution Spectral Imager-LL on board polar satellite Fengyun-3.

3. Soil Moisture Ocean Salinity Satellite.

4. Soil Moisture Active Passive Satellite.

5. Chinese GF-1 Wide Field View.
6. MultiSpectral Instrument (MSI) on board Sentinel-2.
7. Multi-spectral camera on board Resources satellite three of China.
8. Stretched Visible and Infrared Spin Scan Radiometer-II on board geostationary satellite Fengyun-2.
9. Advanced Geostationary Radiation Imager on board geostationary satellite Fengyun-4.
10. The Spinning Enhanced Visible and InfraRed Imager (SEVIRI) on board MSG.
11. Sentinel-1 Ground Range Detected.
12. Hyperspectral Infrared Atmospheric Sounder-II on board polar satellite Fengyun-3.

Source: Author's own elaboration.

All RS ET models reported carry over a certain degree of complexity, which implies specific algorithms, parameterization and associated risks of uncertainty. Though, a more complex model is not necessarily more accurate. We have seen that SSEBop (considered one of the relatively simplest models presented) can perform similarly to the other more complex models, on extended spatio-temporal scales.

An attempt to evaluate the selected RS ET models, in terms of their degree of complexity, ranks ALEXI-DisALEXI, ETLook, ETMonitor and ETWatch as "high", followed by SEBAL and METRIC as "moderate", and then followed by SSEBop and PT-JPL as "low".

Some of these models have been used for various water resources management applications in a few countries of the NENA Region, while two applications (SIMS and IrriWatch) have interested specifically on-farm irrigation management.

Some of the above RS ET models have generated data that are reported in databases or portals (here indicated also as platforms) made freely available to the public and accessible from the web. The platforms presented in the webinars series and discussed in this publication are: USGS FEWSN (Famine Early Warning Systems Network with data mostly from SSEBop); WaPOR (with ET data derived from ETLook); GloDET (with ET data derived from DisALEXI); EEFlux (with ET data derived from METRIC); OpenET (with ET data derived from an ensemble of algorithms including SEBAL, METRIC, SSEBop, ALEXI-DisALEXI, among others); and ECOSTRESS (with ET derived from PT-JPL). Some highlights on the 'cloud' platform of ETWatch (ETWatch Cloud) are provided as well.

Distinctive features of the various platforms discussed in this publication are summarized in the following synoptic table.

Database - Portal	Model used	ET of departure	Minimum Time resolution	Spatial resolution	Year of time series	Geographical coverage	Minimum latency	Major use
FEWS NET	SSEBop	instantaneous	Decadal	1 km	2003	Global	3 days	Drought monitoring
						Continental		
WaPOR	ETLook	daily	Decadal	250m	2009	Continental Basin	3 days	Water Accounting
				100m				Water Productivity
				30m				
GloDET	ALEXI	half-day	Daily	375m	2013	By project	2 days	Water Management
	DisALEXI	half-day		30m				
EEFlux	METRIC	instantaneous	Daily	30m	1984	Global (on user demand)	~3 days following the most recent Landsat overpass	Water Management Irrigation

OpenET	Ensemble ¹	instantaneous	Daily	30m	2016	Western United States of America	2 days	Water Management Irrigation
ETWatch Cloud	ETWatch	instantaneous	Daily	250m-1 km	2000	Basin	~2 days	Integrated water resources assessment
		daily		30m		By project	following the most recent	
		monthly		16m		North China	satellite	Water Management Irrigation Water Accounting Water Productivity
		yearly		10m 5m			overpass	

Notes: 1. The ensemble includes the following models: ALEXI-DisALEXI (version 0.0.27); METRIC (specifically eeMETRIC version 0.20.15); PT-JPL (version 0.2.1); SEBAL (specifically geeSEBAL version 0.2.1); SIMS (version 0.0.20); and SSEBop (version 0.1.5).

Source: Author's own elaboration.

It is important to recall that the databases and portals carry over the uncertainty of the RS ET models from which they derive the ET products. In fact, a key discussion of this publication is about the issue of uncertainties involved in the RS-based determination of ET.

We need to be aware that the RS determination of ET is subject to several sources of error that need to be considered comprehensively. Typically, and among others, we may have: spatial and temporal error in the assessment of cloud, aerosol, dust, and smoke contamination of the atmosphere affecting the surface net radiation; the non-uniform underlying land surface affecting wind patterns, roughness and Land Surface Temperature (LST); daily variation of the atmospheric stability conditions affecting the aerodynamic conductance; insufficient spatial and temporal representation of some meteorological variables like wind speed and vapor pressure of the atmosphere, which influence aerodynamic and canopy conductance, respectively; etc.

Furthermore, the determination of the RS input variables for ET computation is mostly instantaneous at the time of the satellite overpass. Therefore, additional sources of uncertainty are in the time integration of ET over the daytime hours, and in the time interpolation of daily ET values over the period in between two satellite overpasses (e.g. like in the case of Landsat having eight days of revisit cycle). Additionally, some computations might require trained and knowledgeable operator skills while others might include processing for 'data sharpening', 'data fusion' and 'cloud masking', among others.

It is evident that the complexity of the various nested algorithms to derive ET, the adequacy of these algorithms to describe the various processes involved, the quite intertwined sources of errors involved in the input variables, the knowledge and skill of the operator, etc., requires a comprehensive uncertainty assessment of ET model performance and of the data they provide in databases. This is accomplished by comparisons against reliable field ET measurements or another model considered being of a higher standard. Several statistical methods can be adapted, from the sensitivity and regression analysis to the method of moments.

The variability of uncertainty in ET by the various models was observed to depend on several factors, including the extent of parameter calibration for a given terrain landscape and field, the accuracy of the input variables and their capacity to represent the actual conditions at the given scale, the uniformity of the land surface being scanned by the satellite sensors, and the spatial and time scales evaluated.

It was also observed some inconsistency in the degree of uncertainty with the period of the year (e.g. during the season) and with various climatic conditions (e.g. arid, sub-humid, etc.). In short, notwithstanding the good

performance in given conditions, there is no guarantee that the expected model accuracy remains consistent throughout space and time. Therefore, one way to look at the various models is on relative terms.

Being mindful of the magnitude of uncertainty allows one to properly identify and select the determination method most suitable for a given application, so that uncertainties are likely to be within acceptable limits for sound quantitative analysis leading to appropriate decisions. Therefore, the identification by the users of the type of application they will be using the RS ET data for (including the most appropriate spatial and temporal scales, if one-source or two-source type of model, etc.), will guide in selecting the likely model/method of RS ET determination with an expected uncertainty (or achievable accuracy) that falls within the acceptable limits, and thus to select the model/method that best fits the purpose.

While this simple logical framework appears straightforward, in reality there are still open questions on: (i) the acceptable limits of uncertainty for a given application; and (ii) the expected uncertainty (or achievable accuracy) by the various models/methods of RS ET determinations.

In fact, there is a need to investigate thoroughly with the various water users, decision makers and stakeholders in general, the acceptable limits of ET uncertainty for their applications. On the other side, the best RS ET determinations show uncertainty in the range of 10–20 percent. Furthermore, it has been observed that, overall, the RS ET uncertainty tends to decrease going from smaller to larger spatial scales and from shorter to longer time scales.

The importance of accurate representation of local conditions to reduce errors in RS ET determinations cannot be understated, particularly in complex landscapes having drastic changes in the micrometeorological variables and land surface properties. In fact, where the landscape is mostly uniform (e.g. flat and extensive field crops) and the meteorological conditions are fairly even (e.g. clear sky, moderate wind) the likelihood is higher to obtain accurate ET with any model, but when the terrain is significantly variable in elevation, slope, aspect, wetness, vegetation cover, etc., and the meteorological conditions are substantially uneven (e.g. variable humidity and temperature of the near-surface air, cloudy conditions, fluctuations in wind speed, etc.) the likelihood to obtain accurate ET is reduced and accuracy will depend on the specific model and how well it recognizes and incorporates the land/atmosphere variability.

The most difficult cases are represented by environments characterized by high cloudy conditions where all models requiring LST are mostly excluded from accurate ET estimation.

In regions having extensive cloudiness, major attempts to obtain ET is through those models that use microwave radar to estimate soil-surface moisture content (e.g. ETMonitor and ETWatch). This approach is however prone to error due to the coarse scale of the microwave radar (25 km pixel size) and due to the interference of the vegetation covering the soil.

Difficult tasks remain the time integration over the day and the interpolation between days of satellite overpasses.

It is part of the research nature that modeling groups tend to describe and project their models in the most positive ways and present comparisons that show the most promising results. However, we strongly encourage all modeling groups to expand the scope of their work towards producing dependable estimates of uncertainties in RS ET products that may vary with location, vegetation type and time of year. These estimates, which are probably best known or estimated by the model developers and operators, will be invaluable in guiding users of RS ET data on expected uncertainties and biases when employed to estimate water consumption for different purposes.

This places a large burden on developers and users alike, but we recognize that estimation of error and bias is imperative to the acceptance and adoption of spatially and remotely derived estimates of ET into operational practice.

We need to be aware of the challenges, tradeoffs and limitations we are facing when dealing with RS ET determinations. The complexity of the systems we are dealing with cannot be a justification for not becoming

more aware of such technologies and their challenges, tradeoffs and limitations and thereby proceeding blindly into the decision-making process involving the sustainable management of such a precious resource as water.

Therefore, RS ET models must continue to be explored, evaluated, scrutinized, tested, and refined.

The future of RS ET determination appears to be bright, offering continuously new opportunities. The missions and technology of satellites are unfolding at a rapid pace so that remote sensing applications are broadening, accuracy is increasing, and spectral, temporal and spatial resolutions are becoming more granular. Among the flagships programmes for the near future we can mention: ECOSTRESS and SBG, from the National Aeronautics and Space Administration (NASA, United States of America); Copernicus, from the European Commission (EU); WaPOR phase II (and III), from FAO; Hydrosat, from a private company; LSTM, from the European Space Agency; and TRISHNA, from a joint development by the French Space Agency (CNES) and Indian Space Research Organization (ISRO).

It is valuable that programmes around space science are very active and that a large number of competing groups of RS ET developers are offering methods and data that can be inter-compared and contrasted. This should make it easier and more apparent in recognizing 'truth'. It is upon the user to seize these opportunities wisely.



©FAO



1. INTRODUCTION

Evapotranspiration (ET) represents the key variable in linking ecosystem functioning, carbon and climate feedback, agricultural management, and water resources (Fisher *et al.*, 2017). Particularly in agricultural and other vegetated lands, ET nearly always represents the largest share of water outflow, identified as the 'consumptive' fraction of water used by the system.

Quantifying ET in space and time, thus, is extremely relevant for water resources management applications, including: monitoring water consumption by various land use systems; water allocation, transfer and regulations; management of irrigation at the scheme and on-farm levels; determination of crop water productivity; prediction of yield through models; assessment of agricultural drought indexes; performing water balance and water accounting within hydrologic systems at a wide range of scales; development of effective strategies of adaptation to climate changes.

Occurring when liquid water is converted to the vapor phase, ET is regulated by complex land-plant-atmosphere interactions that are primarily impacted by weather and additionally influenced by variability in topography, wind patterns, soil moisture and vegetation type. As a result, ET is the most challenging to be quantified among all variables of the hydrological cycle.

In fact, despite the significant advance in ET science and applications over the last decades (e.g. Baldocchi, 2005; Anderson *et al.*, 2011; Mueller *et al.*, 2013; Zhang *et al.*, 2016), there is still a knowledge gap in hydrological and climatological dynamics due to insufficient capabilities in the determination and monitoring of ET from local to global scales (Fisher *et al.*, 2017).

At local or field scale, several methods and instrumentations for ET determination have been developed over time, that include: soil-moisture measurements for water depletion monitoring; weighing lysimeters; the Penman Monteith equation; the Bowen-ratio/energy balance; the Eddy covariance; and the Large Aperture Scintillometer; (e.g. Howell *et al.*, 1991; Baldocchi *et al.*, 2001; Fisher *et al.*, 2011; Liu *et al.*, 2011).

However, these methods are generally complex, expensive, and often focused on limited field scales, and are therefore mostly confined to academic and research environments. Scaling them up to larger areas becomes prohibitive due to cost. For large scales (e.g. irrigation schemes, watershed, sub-national, national and basin scales) the only feasible and affordable methods for ET determination are through satellite remote sensing (RS), where the spatial distribution of ET is revealed.

Although the various satellites missions do not meet fully the spatial, temporal, spectral, and accuracy requirements for a complete ET-based science and applications (Fisher *et al.*, 2017), the progress and advances in the availability of moderate resolution earth observations over recent years, along with the development of sophisticated algorithms, allows the determination of the spatial distribution of ET.

A review of the literature has led to the identification of several models, of which the following have been selected as most operational for RS determination of ET:

- ▶ SEBAL (Surface Energy Balance Algorithm for Land; Bastiaanssen *et al.*, 1998a, 1998b)
- ▶ METRIC (Mapping Evapotranspiration at high Resolution with Internalized Calibration; Allen *et al.*, 2007a and 2007b)
- ▶ ALEXI/DisALEXI (Atmosphere-Land Exchange Inverse; Anderson *et al.*, 1997, 2004 and 2011)
- ▶ SSEBop (Simplified Surface Energy Balance – Operational; Senay *et al.*, 2007 and 2013; Senay 2018a, 2018b)
- ▶ PT-JPL (Priestley-Taylor from Jet Propulsion Lab; Fisher *et al.*, 2008)
- ▶ ETLook (Bastiaanssen *et al.*, 2012)

- ▶ ETMonitor (Hu and Jia, 2015)
- ▶ ETWatch (Wu *et al.*, 2008, 2011 and 2020)

As can be expected, each method has specific advantages and limitations, spatial and temporal resolutions, strengths and weaknesses, uncertainties and best fitting domains of application.

Moreover, most of the above ET algorithms have been used to generate ET databases or portals (here indicated also as platforms) over different time series that have been made freely available to the public and accessible from the web, like USGS FEWSN (Famine Early Warning Systems Network with data mostly from SSEBop), WaPOR (with ET data derived from ETLook), GloDET (with ET data derived from DisALEXI), EEFlux (with ET data derived from METRIC), OpenET (with ET data derived from an ensemble of algorithms including SEBAL, METRIC, SSEBop, ALEXI-DisALEXI, among others), and ECOSTRESS (with ET derived from PT-JPL).

Confronted with this quite ample and diversified offer of RS ET models and platforms, users are concerned with operational issues such as: proper spatial and temporal resolution for given applications; accuracy of the ET determinations provided by the various models and databases; methods to conduct a qualitative (and at least partially quantitative) error analysis of RS-ET determinations for the various algorithms/models; modalities to test the RS ET with field ET measurements; criteria to know which ET data sources best fit one's purpose.

Against this backdrop, the FAO Regional Initiative on Water Scarcity for the Near East and North Africa (WSI) of the NENA Region, with the support of the Sida Project (FAO, 2017), and in consultations with various countries' stakeholders in the region, partners, and major experts in the RS ET domain, elaborated a plan of webinars addressing these various issues.

More specifically, the main objectives of the webinar series were the following:

1. updating and upgrading the knowledge regarding current RS ET determination, the most common and adopted algorithms and approaches, and the latest advances;
2. increasing the capacity of key water professionals in the assessment of RS ET uncertainty and related acceptable limits for their field of application;
3. building awareness on the strengths, limitations and fits-for-purpose for the range of RS ET models and databases available;
4. providing the participants with a complete and advanced set of documentation on the various topics treated during the webinar series.

The webinars were accompanied by 'suggested readings' providing basic background material promoting proficient attendance and relevant discussion session. Recording of the webinars, copies of the presentations and any other additional pertinent documentation is available on the following *Dgroup* link.¹⁰


The major outcomes of the webinars series, along with further insights and an enriched literature review, are reported in the present publication.

Chapters 2 and 3 attempt to provide a comprehensive outlook and a comparative analysis of the selected RS ET models, including inputs requirements, spatial-temporal and spectral resolutions, critical steps prone to errors, expected accuracy, strengths and weakness, and best fit for various applications.

Similarly, chapters 4 and 5 analyse and compare the identified database or portals (platforms) on the basis of their distinctive features, including spatial and temporal resolutions, geographical coverage, length of the time series, and other peculiarities.

Chapter 6 provides some field applications of certain RS ET models, and in particular some that have interested the NENA Region and the on-farm irrigation management. Moreover, this chapter illustrates two examples of operational platforms that integrate the RS ET determinations into a decision support system for irrigation management and scheduling, and that account for other agronomic, engineering and economic factors.

¹⁰ Water Accounting & Water for Food - D Group. <https://dgroups.org/fao/wateraccounting/library/sqff8vmt?o=lc>.



A relatively extended treatment on the subject of “uncertainty” related to RS ET determinations is then found in chapter 7. Here, a background on methods addressing uncertainty and some insights on the risks of errors related to the selected RS ET models are reported. Chapter 7 devotes also discussions on the limits of uncertainty that can be considered acceptable for specific purposes and on the way to decompose major sources of uncertainty in RS ET determinations. This chapter assumes particular relevance to increase the awareness of the reader about the challenges faced by RS ET determinations.

Chapter 8 gives just a brief background on some pertinent European, United States of America and other international RS flagships programmes for the near future, considering that the activities around space science, including missions and technology of satellites, are very dynamic.

The publication then closes with some concluding remarks in chapter 9, where critical reflections, inferences and key messages are offered, along with some prospects for the future directions of RS ET determination.

Finally, an extensive number of relevant references is provided in chapter 10.



©FAO



2. BACKGROUND ON THE SELECTED RS ET MODELS

The RS ET models presented in the webinar series can be grouped into different categories, depending on the core algorithms used (e.g. surface energy balance, Penman-Monteith, psychrometry), the way the 'surface' is characterized (e.g. single layer or two-layer, also referred to as single-source or two-source), the spatial resolution and coverage (e.g. coarse or fine resolution, with global or local coverage), and a few other distinguishing factors.

Furthermore, the various RS ET models may not fall rigidly into only one category. Often, they adopt a mix of approaches, as well as various RS data sources and data fusion, to provide the best results.

One important aspect to consider in RS ET determination is that high or moderate resolution satellites can only take a 'snap-shot' image at one (or more) given instant of the day. Therefore, the determination of ET requires that ET estimated from an image to be integrated over the day-time and over the number of days between satellites overpasses. The various models often differentiate in their approaches to time-integration.

This section will present first the conceptual grounds of core algorithms and then a brief synoptic view and distinctive features of each RS ET model.

2.1 The Surface Energy Balance (SEB)

In RS of ET we cannot determine directly the flux of water, for instance like the eddy covariance method. However, we can derive it indirectly through conducting an energy balance over the land surface. In an energy balance, the exchange of energy between the land surface and the overlying atmosphere, and the underlying ground, involves four important processes of energy exchange, namely:

- ▶ Absorption and Emission of 'natural' electromagnetic radiation by the surface
- ▶ Thermal conduction of heat energy into the ground
- ▶ Turbulent transfer of heat energy towards or away-from the surface within the atmosphere
- ▶ Latent heat of evaporation, including the energy required for evaporation of water from bare soil and free water present at the surface and the energy required for transpiration of water stored in the soil through plants. In rare cases, there may be latent heat of condensation of atmospheric water vapor onto the surface (i.e. negative evaporation).

Each of these processes is expressed as an *energy flux density*, i.e. the rate of transfer of energy normal to a surface per unit area and per unit of time. Energy flux density can be expressed as $J\ m^{-2}\ s^{-1}$ (where 'J' is for Joule) which is equivalent to $W\ m^{-2}$ (where 'W' is for Watt).

Considering that the land surface can be of a finite depth (e.g. including the depth of the vegetation canopy), the energy balance can be written as

$$dQ/dt = R_n - G - H - \lambda E \quad (1)$$

where:

- ▶ Q is the total heat energy stored in the unit surface layer ($J\ m^{-2}$);

- ▶ R_n is the *net surface irradiance* (commonly referred to as the *net radiation*). It represents the gain (or loss) of energy by the surface from radiation ($W\ m^{-2}$);
- ▶ G is the *ground heat flux*. It is the loss of energy by heat conduction through the lower boundary of the surface layer ($W\ m^{-2}$). G is negative when energy flows from soil to the surface;
- ▶ H is the *sensible heat flux*. It represents the loss of energy by the surface as heat transfer to the atmosphere ($W\ m^{-2}$). H is negative when sensible heat energy flows from the atmosphere to the surface;
- ▶ λE is the *latent heat flux*. It represents a loss of energy from the surface due to evaporation ($W\ m^{-2}$)
- ▶ t is time (s).

Eq. (1) is relevant when the depth of the surface layer is significant (e.g. in the case of forest vegetation where the tree canopy and stem can absorb and hold significant heat energy during the day). For crop surfaces, generally the depth of the surface layer (vegetation canopy) can be considered negligible (theoretically as infinitely thin), so that the heat storage (Q) is zero and Eq. (1) reduces to

$$R_n - G - H - \lambda E = 0 \quad (2)$$

or

$$\lambda E = R_n - G - H \quad (3)$$

Eq. (3) provides λE as the residual of the surface energy balance, and is used by RS models that are based on SEB to derive the amount of water evapotranspired, E , (expressed in kg), after dividing the latent heat flux for λ , the latent heat of vaporization, expressed in $J\ kg^{-1}$.

We look now into the derivation of the righthand-side terms of Eq. (3).

- ▶ **R_n** is computed by subtracting all outgoing radiant fluxes from all incoming radiant fluxes, i.e.

$$R_n = R_{s\downarrow} - \alpha R_{s\downarrow} + R_{L\downarrow} - R_{L\uparrow} - (1-\epsilon_o) R_{L\downarrow} \quad (4)$$

where:

$R_{s\downarrow}$ = incoming short-wave radiation, both direct and diffused ($W\ m^{-2}$)

α = surface albedo (dimensionless)

$R_{L\downarrow}$ = incoming long-wave radiation ($W\ m^{-2}$)

$R_{L\uparrow}$ = outgoing long-wave radiation ($W\ m^{-2}$)

ϵ_o = broad-band surface thermal emissivity (dimensionless)

Similar to [$\alpha R_{s\downarrow}$] representing the reflected portion of the incoming short-wave radiation ($R_{s\downarrow}$), $(1-\epsilon_o) R_{L\downarrow}$ represents the reflected portion of the incoming long-wave radiation ($R_{L\downarrow}$).

Putting Eq. (4) into the RS context, the *incoming short-wave radiation* ($R_{s\downarrow}$) is estimated assuming clear-sky conditions (a prerequisite also to the determination of land surface temperature), as a function of time, day of year, location, terrain slope and aspect. Furthermore, $R_{s\downarrow}$ and $\alpha R_{s\downarrow}$ must account for the sun angle from the zenith and the RS sensor angle with respect to the land surface, and the atmospheric transmissivity whose estimates vary with atmospheric thickness (elevation), and suspended aerosols and water vapor. While RS databases for $R_{s\downarrow}$ are available on the Internet (see, for example, this database by the Committee on Earth Observation Satellites - CEOS),¹¹ the specific equations to account for all primary influencing variables of $R_{s\downarrow}$ are well described in literature (e.g. Chen and Ohring, 1984; Koepke *et al.*, 1985; Duffie and Beckman, 1991; Vermote *et al.*, 1997; Allen *et al.*, 2007a, 2007b) and have adequate accuracy. In fact, '*calculated*' $R_{s\downarrow}$ for clear sky conditions is often considered to have the same or even better accuracy than '*measured*' $R_{s\downarrow}$ due to its reliance on reproducible geometry and atmospheric conditions, whereas measured R_s can be plagued by sensor calibration, levelness and sensor maintenance (Allen, 1996; ASCE-EWRI, 2005).

¹¹ CEOS Database. 2023. <https://database.eohandbook.com/measurements/overview.aspx>

The *surface albedo* (α), is the ratio of reflected to incident short-wave radiation (mostly solar) at the surface, integrated across the shortwave spectrum (0.2 to 3.2 μm). The reflected short-wave radiation is detected by the satellite sensors in selected bands. For instance, bands 1–5 and 7 of *Landsat*, bands 1–7 of MODIS and bands 1–9 of *Advanced Spaceborne Thermal Emission and Reflection Radiometer* (Allen *et al.*, 2011b). When deriving albedo, weighting coefficients are then applied to each band to account for scattering, absorption, relative humidity, etc. (e.g. see Tasumi *et al.*, 2008 and Berk *et al.*, 1999 for further insights). RS-based derivation of α can be found in the databases of the CEOS as indicated above for $R_{\text{s}\downarrow}$. However, it is usually important that estimated albedo, as well as $R_{\text{L}\downarrow}$ and $R_{\text{L}\uparrow}$, be coincident, i.e. occurring at the same instant in time as the calculation of the SEB.

The *incoming long-wave radiation* ($R_{\text{L}\downarrow}$) is the downward thermal radiation flux originating from the atmosphere. $R_{\text{L}\downarrow}$ is generally the least certain radiation component in RS because it is not measured by RS. $R_{\text{L}\downarrow}$ is usually computed using the Stefan–Boltzmann equation:

$$R_{\text{L}\downarrow} = \epsilon_{\text{a}} \sigma T_{\text{a}}^4 \quad (5)$$

where:

ϵ_{a} = apparent atmospheric emissivity (dimensionless)

σ = Stefan–Boltzmann constant ($5.670374 \times 10^{-8} \text{ W m}^{-2} \text{ K}^{-4}$)

T_{a} = near surface air temperature where T_{a} is used as a surrogate temperature for the total integrated effective atmospheric emitting temperature (K)

In most RS determinations, the surface temperature (T_{s}) is used as proxy for T_{a} or to estimate T_{a} in Eq. (5), and empirical equations have been developed for ϵ_{a} (e.g. Bastiaanssen, 1995; Allen *et al.*, 2007a).

The *outgoing long-wave radiation* ($R_{\text{L}\uparrow}$) is the upward thermal radiation flux originating from the land surface and is also computed using the Stefan–Boltzmann equation:

$$R_{\text{L}\uparrow} = \epsilon_{\text{o}} \sigma T_{\text{s}}^4 \quad (6)$$

where:

ϵ_{o} = broad-band surface thermal emissivity (dimensionless)

σ = Stefan–Boltzmann constant ($5.670374 \times 10^{-8} \text{ W m}^{-2} \text{ K}^{-4}$)

T_{s} = land surface temperature (K)

In the case of $R_{\text{L}\uparrow}$, estimates are more accurate than those for $R_{\text{L}\downarrow}$ because T_{s} is measured by RS. The surface emissivity (ϵ_{o}) varies with the nature of the surface, soil and vegetation. In RS determinations of ϵ_{o} , empirical equations are used to account for soil and vegetation through *leaf area index* (LAI), e.g. like those developed by Tasumi (2003). $R_{\text{L}\downarrow}$ and $R_{\text{L}\uparrow}$ derivations can also be found in the databases of the CEOS. The thermal emissivity of various surfaces (ϵ_{o}) can be found in the MODIS UCSB Emissivity Library.¹²

G depends on the surface temperature (T_{s}), the temperature gradient establishing below the surface (dT/dx), and the thermal conductivity (κ) of the ground (typically soil and vegetation). While the theoretical basis of heat transfer through conduction is expressed by Fourier's law

$$Q_{\text{h}} = \kappa \frac{dT}{dx} \quad (7)$$

where:

Q_{h} = heat flux density (W m^{-2})

κ = thermal conductivity ($\text{W m}^{-1} \text{ K}^{-1}$)

$\frac{dT}{dx}$ = temperature gradient (K m^{-1})

¹² MODIS UCSB Emissivity Library, 1999. <https://www.icesb.ucsb.edu/modis/EMIS/html/em.html>

in RS applications, because dT/dx is unknown, G is computed as a proportion of R_n through empirical equations like the one proposed by Bastiaanssen (2000)

$$\frac{G}{R_n} = (T_s - 273.15)(0.0038 + 0.0074 \alpha)(1 - 0.98 NDVI^4) \quad (8)$$

where:

T_s = land surface temperature (K)

α = surface albedo (dimensionless)

NDVI = Normalized Difference Vegetation Index

G is then derived by multiplying the results of Eq. (8) times Eq. (4). Additional equations have been developed and adapted to specific surface conditions (e.g. the one by Singh *et al.*, 2008 and 2009 for maize fields), or as the one of Brutsaert (1982) and Stull (1988) to express G as a function of H , rather than function of R_n . See Purdy *et al.* (2016) for a review of algorithms to estimate G .

H is derived through the aerodynamic transport equation (the flux-gradient equation in analogy to the Ficks' law of diffusion), expressing the vertical flux of sensible heat from a surface as directly proportional to the vertical gradient of temperature and inversely proportional to the aerodynamic resistance, i.e.

$$H = \rho_a c_p \frac{dT}{r_{ah}} \quad (9)$$

where:

ρ_a = air density (kg m^{-3})

c_p = specific heat of air at constant pressure ($\text{J kg}^{-1} \text{K}^{-1}$)

dT = near-surface temperature difference between the surface and a near-surface height or between two near-surface heights. In traditional modeling, dT is estimated as $T_s - T_a$, with r_{ah} representing the aerodynamic resistance between the surface and some height above the surface, for example, at 2 m

r_{ah} = aerodynamic resistance to heat transfer between the surface to near-surface height or between two near-surface heights (s m^{-1}) as described below.

H is the most critical energy flux to solve in the SEB (Eqs. 1, 2 and 3) via RS, due to the quite complex nature of the variables dT and r_{ah} involved in Eq. (9) and the dependency of r_{ah} on wind speed and turbulence.

In fact, dT should be the difference between the 'aerodynamic' temperature of the surface (T_{aero}) and the air temperature at some height above the surface (T_a). Both these temperatures cannot be derived easily through RS. Campbell and Norman (1998) indicated that an uncertainty of 1°C in $T_{aero} - T_a$ can result in a 50 W m^{-2} uncertainty in H , which is approximately equivalent to an evaporation rate of 1 mm day^{-1} . Actually, satellites measure the bulk 'radiometric' temperature of the surface (T_s) and not the 'aerodynamic' temperature (T_{aero}). These can be different from one another by several degrees (Friedl *et al.*, 2002; Kustas *et al.*, 2007) Furthermore, the determination of T_s via RS has its own uncertainties due to atmospheric attenuation or contamination and radiometric calibration of the sensors (Allen *et al.*, 2007a). In addition, the air temperature above the surface (T_a) is unknown.

To solve for such complexity, Bastiaanssen (1995) proposed to express dT as a linear function of T_s , corrected for the lapse temperature due to elevation, i.e.

$$dT = a + bT_{s_datum} \quad (10)$$

where:

a and b = empirically determined constants for a given satellite image and thermal conditions

T_{s_datum} = radiometric surface temperature adjusted to a common elevation for each image pixel, using a digital elevation model and the lapse temperature due to elevation

The approach and equations described so far are the basis for most 'one-source' RS ET models, i.e. treating the 'surface' as a single uniform layer (no distinction between 'bare-soil surface' and 'vegetated surface' within the satellite image). In fact, the temperature gradient dT in Eq. (9), calculated through Eq. (10), is conceived to

describe a vertical temperature gradient between the two near-surface heights that are both taken sufficiently above 'd+z_o', where a 'blended' zone having sufficient turbulent mixing prompts a single temperature gradient (dT), thereby reducing the need to separate bare-soil from vegetation (Allen *et al.*, 2007a).

Regarding the aerodynamic resistance to heat transfer, r_{ah}, the complexity is in its dependency on wind speed, atmospheric stability, and surface roughness (Brutsaert, 1982). The traditional formulation for r_{ah} where the endpoints are the surface where T_s is measured and some z₂ height above the surface where T_a is measured is

$$r_{ah} = \frac{\left[\ln\left(\frac{z_2-d}{z_{om}}\right) - \Psi_{sm} \right] \left[\ln\left(\frac{z_2-d}{z_{oh}}\right) - \Psi_{sh} \right]}{u_* k^2} \quad (11a)$$

where 'd' is the surface's *zero-plane displacement* height (the height from the ground at which the mean wind velocity is zero due to large obstacles such as crop canopies and 'z_{om}' and 'z_{oh}' are the surface's *roughness length* for momentum and heat transfer (the heights at which the mean wind velocity is zero due to substrate roughness). Parameters Ψ_{sm} and Ψ_{sh} are integrated stability functions between the surface and z₂ height that account for buoyancy or nonbuoyancy boosts or retardation to the turbulent transport of momentum (m) and sensible heat (h) fluxes.

The Bastiaanssen assumption of Eq. (9) and Eq. (10) requires a corresponding r_{ah} that represents the aerodynamic resistance between the two heights z₁ and z₂, rather than from the surface itself:

$$r_{ah} = \frac{\ln\left(\frac{z_2}{z_1}\right) - \Psi_{sh}(z_2) - \Psi_{sh}(z_1)}{u_* k} \quad (11b)$$

where:

and = heights above 'd+z_{oh}' of the vegetation where the endpoints of dT are defined

= friction velocity (m s⁻¹)

K = von Karman's constant (0.41).

For most of the day time, stable or unstable atmospheric conditions are usually establishing and Ψ_{sm} and Ψ_{sh} are estimated by calculating the Monin-Obukhov length (L). L is the height at which forces of buoyancy (or stability) and mechanical mixing (or instability) are equal, and is calculated as a function of heat and momentum fluxes:

$$L = \frac{\rho_a c_p u_*^3 T_s}{kgH} \quad (12)$$

where:

g = gravitational acceleration (= 9.807 m s⁻²), and the other terms are already defined in previous equations.

When L < 0, the atmospheric condition is unstable; when L > 0, the atmospheric condition is stable; and when L = 0, the atmospheric condition is neutral.

Therefore, the friction velocity in Eq. 11b () is calculated using the logarithmic wind law for neutral or nonneutral atmospheric buoyancy conditions:

$$u_* = \frac{ku_z}{\ln\left(\frac{z-d}{z_{om}}\right) - \Psi_{sm}} \quad (13)$$

where:

u_z = wind speed (m s⁻¹) at height z (m)

z_{om} = momentum roughness length (m).

Functions for estimating Ψ_{sm} and Ψ_{sh} from L are provided in general biophysical texts (Brutsaert, 1982; Campbell and Norman 1998) and in Allen *et al.*, (2007a). These functions for $\Psi = f[L]$ typically use formulations by Paulson (1970) and Webb (1970). Furthermore, it must be realized that the momentum roughness length (z_{om}) depends on the vegetation characteristics, and it is often derived as a function of the leaf area index (LAI) (e.g. Brutsaert, 1982; Bastiaanssen, 1998a; Tasumi, 2003).

It must be noted that in order to calculate L (Eq. 12), the sensible heat flux (H) is needed (Eq. 9), and in order to calculate H, the aerodynamic resistance (r_{ah}) corrected for atmospheric stability through L is needed. In other words we have two unknowns and, therefore, the problem is solved through numerical iteration, starting with an assumption of neutral conditions for the first iteration (see also Allen *et al.*, 2007a, and 2011b, for further details on the derivation of r_{ah}).

The complexity described above essentially doubles where there are reasons for utilizing 'two-source' RS ET models, i.e. treating the 'surface' as two components (distinguishing 'bare-soil surface' from 'vegetated surface'). In this case, the SEB is adapted to account for separate fluxes from both 'soil' (here indicated with subscript 's') and the 'canopy' (here indicated with subscript 'c').

The net radiation R_n is thus obtained as

$$R_n = R_{n_s} + R_{n_c} \quad (14)$$

where:

R_{n_s} = soil net radiation ($W m^{-2}$)

R_{n_c} = canopy net radiation ($W m^{-2}$)

with

$$R_{n_s} = H_s + \lambda E_s + G \quad (15)$$

and

$$R_{n_c} = H_c + \lambda E_c \quad (16)$$

where:

H_s = sensible heat flux from the soil ($W m^{-2}$)

H_c = sensible heat flux from the crop ($W m^{-2}$)

λE_s = latent heat flux from the soil ($W m^{-2}$)

λE_c = latent heat flux from the crop ($W m^{-2}$)

$$H_s = \rho_a c_p \left(\frac{T_s - T_a}{r_{ah}} \right) \quad (17)$$

and

$$H_c = \rho_a c_p \left(\frac{T_c - T_a}{r_{ah}} \right) \quad (18)$$

where:

T_s = soil surface aerodynamic temperature (K)

T_c = canopy surface aerodynamic temperature (K)

T_a = air temperature usually at 2m above 'd+z_{oh}', (K)

r_{ah} = aerodynamic resistance to heat transfer from surface to height of T_a ($s m^{-1}$).

The criteria to disaggregate the two sources (soil and vegetation) are generally based on the knowledge of the LAI or of the NDVI. Different solutions are proposed in the literature for such disaggregation (Norman *et al.*, 1995; Kustas and Norman 1999, 2000; Anderson *et al.* 2005).

SEB uses the RS surface temperature as a valuable metric because varying soil moisture conditions yield a distinctive thermal signature: moisture deficiencies in the root zone lead to vegetation stress and elevated canopy temperatures, while depletion of water from the soil surface layer causes the soil component of the scene to heat up rapidly (Anderson *et al.*, 2007a).

Evapotranspiration computations based on SEB, though, are restricted to clear sky conditions, i.e. it requires thermal infrared radiation measurements from cloud free images, in addition to atmospheric transmissivity corrections, in order to produce accurate land surface temperature (LST) maps. Furthermore, thermal infrared radiation tends to be more sensitive to atmospheric water vapor than visible and near-infrared radiation (Lillesand and Kiefer, 2000).

In fact, while the SEB is a reliable approach that is based on sound physics (e.g. Anderson *et al.* 2005; Allen *et al.*, 2010a; Allen *et al.*, 2011a; Bastiaanssen *et al.*, 2008), cloud cover is considered a serious hindrance to RS ET applications in various parts of the world (Bastiaanssen *et al.*, 2012). Cloud cover reduces the number of clear images to be processed and thereby extends time periods between clear images where assumptions of linearity or curvilinearity in ET are expressed as a fraction of net radiation (Bastiaanssen *et al.*, 1998a) or as a fraction of reference ET (Allen *et al.*, 2007a) must be assumed for the periods between images.

2.2 The Penman-Monteith (PM) model

To circumvent the problem of cloud-cover interference indicated for the SEB approach, the Penman-Monteith (P-M) model (Monteith, 1963, 1964) can be adopted, i.e.

$$\lambda E = \frac{\Delta (Rn - G) + \frac{\rho_a C_p (e_s - e_s RH)}{r_a}}{\Delta + \gamma \left(1 + \frac{r_s}{r_a}\right)} \quad (19)$$

where:

Δ = slope of the relationship between saturation vapor pressure and temperature (kPa °C⁻¹)

e_s = saturation water vapor pressure at the air temperature (kPa)

RH = relative humidity at air temperature (%)

γ = psychrometric constant (kPa °C⁻¹)

r_s = surface resistance (s m⁻¹)

and the other terms already defined in previous equations.

While Rn and G terms are computed as for the SEB, Eq. 19 requires the determination of the vapor pressure deficit, the aerodynamic resistance (r_a) and the surface resistance (r_s).

The vapor pressure deficit is derived by using meteorological data (T_a and RH), usually taken by other RS sources.

The aerodynamic resistance (r_a) is derived through numerical iteration, as in the case of the SEB, to account for boundary layer stability (ψ), though this time H is derived as residual of the energy balance ($H = Rn - G - E$) with the initial estimate of E and friction velocity (u_*) derived for a neutral atmospheric condition. The surface temperature (T_s) required for the computation of the Monin-Obukhov length (Eq. 12) is either obtained by LST maps from other RS data or estimated from the meteorological data by iteration using the aerodynamic equation for H.

When the modeling of E occurs as dual-source (maintaining a distinction between the E of the soil from the E of the vegetation), the aerodynamic resistance in the PM equation is also distinguished between soil (r_{a-s}) and vegetation, or canopy, (r_{a-c}). Similarly, the surface resistance (r_s) is disaggregated into the soil surface resistance (r_{s-s}) and the vegetation (or canopy) surface resistance (r_{s-c}), which will lead to a separation of the soil latent heat of evaporation (E_s) from the canopy latent heat of evaporation (E_c).

The PM equation for the two-source modeling approach is then reformulated as follows:

$$\lambda E_s = \frac{\Delta (Rn - G)_s + \frac{\rho_a C_p (e_s - e_s RH)}{r_{a-s}}}{\Delta + \gamma \left(1 + \frac{r_{s-s}}{r_{a-s}}\right)} \quad (20)$$

$$\lambda E_c = \frac{\Delta (Rn)_c + \frac{\rho_a C_p (e_s - e_s RH)}{r_{a-c}}}{\Delta + \gamma \left(1 + \frac{r_{s-c}}{r_{a-c}}\right)} \quad (21)$$

The Shuttleworth–Wallace dual-source model (Shuttleworth and Wallace, 1985) is a well-established approach, based on the PM equation, to solve for the two latent heat fluxes. The LAI and/or NDVI are used to separate the bare soil surface from the vegetated surface. It is important to note that because surface temperatures of soil and canopy may be substantially different from one another, as may be the albedos, the values for $(R_n)_s$ and $(R_n)_c$ will generally vary substantially from one another. The soil and canopy surface resistances are influenced by the moisture content in the top soil and in the root zone, respectively. Microwave radiometry (e.g. Synthetic Aperture Radar – SAR; Advanced Microwave Scanning Radiometer–Earth Observing System – AMSR-E) can provide continuous surface top-soil moisture information as it is little influenced by cloud cover. However, revisit times and/or spatial resolutions of microwave imagery are generally large. With additional modeling, the root-zone soil moisture can be derived and thus provide the adjustment for r_{s-c} . Several algorithms have been developed to parameterize these surface resistances (e.g. Clapp and Hornberger, 1978; Avissar *et al.*, 1985; Camillo and Gurney, 1986; Stewart, 1988; Dolman, 1993; Bastiaanssen *et al.*, 2012).

A reduced version of the Penman-Monteith is represented by the Priestley-Taylor (1972) equation for the determination of the potential evapotranspiration (ET_p) for extensive areas of well-watered vegetation, obtained by the product of equilibrium evaporation (E_0) and the Priestley-Taylor constant ($\alpha=1.26$).

2.3 The Satellite Psychrometric Approach (SPA)

The Satellite Psychrometric Approach (SPA) follows an analogy with the principles of psychrometry for the determination of the water vapor content of the air.

In psychrometry, the instrument used (psychrometer) consists of two thermometers with one thermometer-bulb kept continuously wet (wet-bulb) while the other thermometer-bulb is measuring the ambient air temperature (dry-bulb). The wet-bulb thermometer registers a lower temperature than the dry-bulb thermometer as a result of the cooling effect of evaporation, under equilibrium heat exchange condition. The difference between the dry- and wet-bulb readings along with a psychrometric constant is used to determine the water vapor pressure of the air:

$$e_a = e_s - \gamma(T_d - T_w) \quad (22)$$

where: e_a is actual vapor pressure (kPa); e_s is the saturation vapor pressure at the temperature of the wet bulb (kPa); T_w is the air temperature measured by the wet-bulb thermometer (K); T_d is the air temperature measured by the dry-bulb thermometer (K); and γ is the psychrometric constant (kPa K⁻¹).

The relative humidity (RH) is a measure of the dryness of the air and is obtained by dividing both sides of Eq. (22) by e_s , expressed in fraction as

$$RH = \frac{e_a}{e_s} = \frac{e_s}{e_s} - \frac{\gamma}{e_s}(T_d - T_w) = 1 - \frac{\gamma}{e_s}(T_d - T_w) \quad (23)$$

The RS modeling of ET based on SPA (Senay, 2018a, 2018b) adopts an analogy between the 'dryness of the air' (RH) and the 'dryness of the surface' expressed as ET fraction (ETf), i.e.

$$ETf = 1 - \gamma^s(T_s - T_c) \quad (24)$$

where ETf represents the ratio between actual and maximum ET, nominally varying between 0 and 1; γ^s is denoted as a "surface psychrometric constant" (SPC) based on the aerodynamic properties of a dry-bare surface (K⁻¹); T_s is the satellite-derived land surface temperature (LST, K); and T_c is the cold/wet limit surface temperature (K).

Satellite measurements of LST are used to estimate both the equivalent dry-bulb ($T_{d,e}$) at any pixel and the wet-bulb ($T_{w,e}$) surface reference temperatures. The equivalent of the psychrometric constant in Eq. (22) and Eq. (23) becomes the Surface Psychrometric Constant (SPC or γ^s) in Eq. (24).

The SPC is computed as

$$\gamma^S = \frac{c_p \rho_a}{Rn \cdot r_{ah}} \quad (25)$$

where all terms are defined in the previous equation, but with the specification that γ^S is determined over bare soil and specified as 110 sm^{-1} when Rn is under clear-sky condition. Higher SPC values are used when gray-sky conditions are used for Rn (Senay *et al.*, 2022).

By knowing the reference ET (ET_o), it is possible to derive the actual ET (ET_a) as

$$ET_a = ET_f \cdot ET_o = [1 - \gamma^S(T_s - T_c)] \cdot ET_o \quad (26)$$

Depending on the reference crop being considered, ET_o may refer either to the reference-grass of the FAO-PM equation (Allen *et al.*, 1998) or to the alfalfa crop of the ASCE equation (ASCE-EWRI, 2005). If grass reference is used, then scaling factor (1.2 - 1.3) would be applied to scale grass reference to alfalfa type.

Eq. (26) is a simplification of the previous modeling approach as it solves for ET_a with a reduced number of variables.

2.4 Specific peculiarities of the selected models

Eight RS ET models were selected for the webinar series. This section provides a synoptic view of each one, highlighting their key peculiarities. Major literature is included so that the reader can look at further details, have additional insights and expand the knowledge on the model.

2.4.1 SEBAL

SEBAL (Surface Energy Balance Algorithm for Land) is a RS ET model developed by Bastiaanssen (1993-1995), who pioneered the era of RS ET determinations. The International Association of Hydrological Sciences (IAHS) Blue Book Series - Special Report 2 - was the first public document defining and explaining all small steps in energy balance modelling that have been followed by many scientists since then. SEBAL is further elaborated by Bastiaanssen *et al.* (1998a, 1998b, 2005) and follows the core algorithms of the SEB illustrated in chapter 2.1.

A major break-through for SEBAL was the linear Eq. (10), proved to hold quite solidly (e.g. Wang *et al.*, 1995; Franks and Beven, 1997; Farah, 2001), including the solution for deriving the parameter 'a' and 'b'.

A first step is to apply Eq. (10) in two specific conditions of a given satellite image: (i) on pixels when $H=0$, i.e. $dT=0$, which in SEBAL is obtained for T_s taken over a water body surface or a well-vegetated/well-irrigated field, and corresponding to the 'cold' pixels of the image; (ii) when $\lambda E=0$, which is obtained for T_s taken over dry soil, and corresponding to the 'hot' pixels of the image.

Accordingly, we have:

$$(i) \quad H=0 \text{ (cold pixels)} \quad a + b \cdot T_{s_datum_cold} = 0 \quad (27)$$

$$(ii) \quad \lambda E=0 \text{ (hot pixels)} \quad Rn = H_{hot} + G \quad (28)$$

using Eq. (9) for H and substituting it in Eq. (25), we obtain

$$Rn = \rho_{a-hot} c_p \frac{dT_{hot}}{r_{ah-hot}} + G \quad \rightarrow \quad dT_{hot} = \frac{(Rn-G)r_{ah-hot}}{\rho_{a-hot} c_p} \quad (29)$$

$$\text{so that} \quad a + b \cdot T_{s_datum_hot} = \frac{(Rn-G)r_{ah-hot}}{\rho_{a-hot} c_p} \quad (30)$$

Different criteria are developed to select the 'cold' and 'hot' pixels, either based on the operator experience or through automated algorithms (Allen *et al.*, 2013a).

Using Eq. (27) and Eq. (30), we can solve for 'a' and 'b' parameters (two equations with two unknowns). However, while the parameters 'a' and 'b' are considered constant for all pixels of a satellite image, r_{ah} varies from pixel to pixel due to the heterogeneity of the landscapes, including the variation in momentum surface roughness (z_{om}), and variability in wind speed near the ground. H represents a convective process and the buoyancy caused by H reduces r_{ah} . This circularity of r_{ah} affecting H and H affecting r_{ah} can be solved by means of the Monin-Obukhov similarity theorem, as reported in chapter 2.1.

The determinations of landcover maps (e.g. crop-cover maps), LAI or NDVI, take care of the surface roughness issue. To solve for spatial wind speed variability near the ground, one can start considering the wind speed to be spatially constant at a blending height (e.g. about 200 m above ground level), where wind speed is presumed not to be substantially affected by local surface heterogeneities (Allen *et al.*, 2010b). Therefore, the wind speed at the blending height is computed by upward extrapolation of a known near-surface wind speed using a logarithmic wind profile and the associated surface roughness. The wind speed at each pixel is then obtained by similarly downward extrapolation, using z_{om} estimated for each pixel from the land-cover map.

Thus, solving for dT and r_{ah} to get H, and using Rn and G, as illustrated in chapter 2.1, we can thus compute λE without any a priori information of the crop such as type, age, planting density, root depth etc. However, this value of λE is only instantaneous. To integrate the instantaneous value of λE over the whole day, SEBAL assumes the evaporative fraction (Λ) of the available energy to be constant during the day (Bastiaanssen *et al.*, 2005), i.e.

$$\Lambda = \frac{\lambda E}{(Rn - G)} \quad (31)$$

so that

$$\lambda E = \Lambda \cdot Rn_{24h} \quad (32)$$

where Rn_{24h} is the 24-h integrated value of Rn, and G describes the seasonal cycle of soil temperature changes.

The assumption of constant Λ in SEBAL seems to hold mostly for environmental conditions where advection does not occur and soil moisture does not significantly change (e.g. Brutsaert and Sugita 1992; Crago 1996; Franks and Beven 1997; Farah 2001).

This time integration for the day of the satellite overpass, and for the days between satellite overpasses, affect the accuracy of λE (and therefore ETa) determinations.

Landsat and Sentinel missions provide the infrared and visible bands used for albedo (α) and vegetation index calculations. Thermal infrared radiation for the determination of land surface temperature (T_s) is taken from low resolution MODIS, Sentinel and VIIRS satellites. It is expected that new missions for thermal determinations (such as *cubesats*) will become available in the period 2023 to 2025 for filling the gap in high resolution thermal data for on-farm crop management.

According to Bastiaanssen *et al.* (2005), the overall accuracy of ET from SEBAL is +/-15 percent, for single-day events (satellite overpasses) and for scales of the order of 100 ha, while the seasonal differences are smaller (1 to 5 percent) due to reduction in the random error.

Several improvements of SEBAL have been introduced from the time of its original version. The reader is referred to the following suggested reading for further insights on the model: Teixeira *et al.* 2009, Jafaar and Ahmad, 2020. It is recommended to visit this web link for the latest version of the SEBAL.¹³

¹³ GitHub, Inc. 2023. Water Accounting - PySEBAL. https://github.com/wateraccounting/PySEBAL_dev

2.4.2 METRIC

METRIC (Mapping Evapotranspiration at high Resolution with Internalized Calibration) is the RS ET model developed by Allen *et al.* (2007a) and Kilic *et al.* (2016) with its original foundation in SEBAL (Bastiaanssen *et al.*, 1998a). METRIC follows the core algorithms of SEB illustrated in chapter 2.1.

The distinctive feature of METRIC is in the use of ground weather-based reference ET (ET_{ref} , calculated on an hourly basis according to ASCE-EWRI, 2005, for alfalfa1) to (i) establish the energy balance conditions for the 'hot' and 'cold' calibration pixels, used to compute the 'a' and 'b' parameters of Eq. (10), and (ii) to derive the reference ET fraction ($ET_{ref}F$) used to convert the instantaneous ET values into daily values.

In essence, the use of ET_{ref} serves as a proven upper limit on ET as governed by energy availability (Allen *et al.*, 1998; ASCE-EWRI, 2005). The latent heat of evaporation (λ) is used for conversion between ET and λE .

Regarding the derivation of the parameters 'a' and 'b' in Eq. (10), METRIC does not assume $\lambda E=0$ for the 'hot pixel' (expected to represent λE from dry bare soil) as does the traditional SEBAL method, but rather allows for a possible 'residual' soil evaporation (λE_{hot}) that may occur due to recent precipitation events, so that

$$H_{hot} = (Rn - G)_{hot} - \lambda E_{hot} \quad (33)$$

where λE_{hot} is calculated according to the soil water balance procedure of the FAO-56 I&D Paper (Allen *et al.*, 1998) and Rn and G are values for the 'hot pixels'.

Similarly, METRIC does not assume $H=0$ for the 'cold pixel' as does the traditional SEBAL method, but rather allows for a possible 'residual' positive or negative sensible heat flux (H_{cold}), so that

$$H_{cold} = (Rn - G)_{cold} - \lambda E_{cold} \quad (34)$$

where λE_{cold} is the estimated latent heat flux at the cold pixels, calculated using ET_{ref} increased by 5 percent to account for large populations of fields having a wet soil surface beneath the full vegetation canopy (Wright, 1982), and using λ for converting ET in λE , i.e.

$$\lambda E_{cold} = 1.05 \cdot ET_{ref} \cdot \lambda \quad (35)$$

where ET_{ref} is the ASCE-EWRI (2005) alfalfa reference that is generally 20 to 40 percent greater than the FAO56 ET_o reference representing clipped grass. Where the vegetation is not fully developed, NDVI measures complement the calculation to account for reduction in λE_{cold} (Allen *et al.*, 2013b).

Using Eq. (9) for cold and hot pixels, one obtains

$$dT_{cold} = a + b \cdot T_{s_datum_cold} \quad (36)$$

$$dT_{hot} = a + b \cdot T_{s_datum_hot} \quad (37)$$

where $T_{s_datum_cold}$ and $T_{s_datum_hot}$ represent delapsed surface temperature at the cold and hot pixels. The delapsing, as in SEBAL, removes artifacts from T_s caused by the effects of elevation change. From Eq. (36) one can derive the parameter 'a' as

$$a = dT_{cold} - b \cdot T_{s_datum_cold} \quad (38)$$

and from Eq. (37) one can derive the parameter 'b' as

$$b = \frac{(dT_{hot} - a)}{T_{s_datum_hot}} \quad (39)$$

Substituting 'a' of Eq. (38) into Eq. (39) and solving, one obtains

$$b = \frac{dT_{hot} - dT_{cold}}{T_{s_datum_hot} - T_{s_datum_cold}} \quad (40)$$

Regarding the derivation of the reference ET fraction ($ET_{ref}F$), METRIC uses the following equation

$$ET_{ref}F = \frac{ET_{inst}}{ET_{ref}} \quad (41)$$

Where ET_{inst} is the computed instantaneous ET for each pixel and ET_{ref} is the standardized reference ET computed (hourly) according to ASCE-WERI (2005) for alfalfa, at the time of the satellite image.

METRIC derives the daily ET (ET_{24}) assuming that $ET_{ref}F$ calculated according to Eq. (41), which is at the time of the satellite image, is the same as the 24 h average $ET_{ref}F$, i.e.

$$(ET_{ref}F)_{Sat_time} = (ET_{ref}F)_{24h_avg} \quad (42)$$

Therefore, actual ET over the entire day (ET_{24h}) is computed according to

$$ET_{24h} = ET_{ref}F \cdot ET_{ref_24h} \quad (43)$$

where:

ET_{24h} = the daily actual ET for the day of the satellite image

ET_{ref_24h} = the daily reference ET for the day of the satellite image (as integration of the hourly ET_{ref})

and $ET_{ref}F$ is as derived from Eq. (41).

Thus, in the case of agricultural vegetation, METRIC uses Eq. (41), $ET_{ref}F$, instead of Eq. (31) of SEBAL, Λ , to obtain ET_{24h} . This generally produces an improvement in accuracy as the assumption of constant Λ during the day can under predict the actual ET in arid climates where afternoon advection or increased afternoon wind speed may increase ET in proportion to the available energy ($R_n - G$), as reported by Allen *et al.* (2007a). In the case of nonagricultural land uses such as forest and rangeland, METRIC follows SEBAL with the use of Λ , because of the assumption that natural vegetation generally exercises midafternoon stomatal control that causes the 24-hour total ET to tend to follow trends in $R_n - G$.

Some versions of METRIC are constructed with additional algorithms for calculating solar radiation in mountainous and other complex terrain and for estimating the impacts of terrain on aerodynamic roughness and wind speed (Allen *et al.*, 2013b). These additional algorithms improve the accuracy of ET estimates in those systems.

To obtain the actual ET_{24h} for the days between satellites overpasses, METRIC interpolates $ET_{ref}F$ between the satellites images (similarly to the interpolation for crop coefficients along the season) and then multiplies it by the ET_{ref_24h} of each day. Typical interpolations between $ET_{ref}F$ values can be carried out as linear or as curvilinear (e.g. a spline function) to better fit the seasonal $ET_{ref}F$ trend, as for the case of crop coefficients (Wright, 1982).

The assumption is that the ET for any pixel will increase and decreases on any particular day in the same proportion that ET_{ref} increases or decreases due to weather conditions. Therefore the value for $ET_{ref}F$ can be assumed to be relatively consistent from day to day. This approach has been found to be relatively accurate for estimating actual ET_{24h} for both clear and cloudy days in between the clear-sky satellite image dates (Tasumi *et al.*, 2005).

Essentially, the use of locally available weather data or gridded weather data to derive ET_{ref} (calculated on hourly base according to ASCE-WERI, 2005, for alfalfa), in turn used in Eq. (33), (35), (41), (42) and (43), provides the 'internal calibration' of METRIC for each satellite image (Allen *et al.*, 2007a). Such 'internal calibration' incorporates biases in individual components that are systematically biased over an image. It thereby eliminates the need for atmospheric correction of T_s and for albedo measurements (using radiative transfer models), and reduces the uncertainties in estimating aerodynamic stability correction and surface roughness, among others. Incorporating all systematic biases into the calculation of H , in turn cancel out, in large part, the biases in R_n and G (Allen *et al.*, 2007a) when calculating λE as residual of the SEB (Eq. 3).

According to Allen *et al.* (2007a, 2007b), METRIC is designed to produce high-resolution and accurate ET maps for regions smaller than a few hundred kilometers in scale. However, to achieve such accurate results highly qualified 'users' may be required to operate METRIC. This is the case for several other RS ET models. The expected accuracy in ET by METRIC can be of +/- 10 percent with a qualified and experienced operator. The

version of METRIC as part of the OpenET platform utilizes an automation scheme described by Allen *et al.*, (2013a) and modified by ReVelle *et al.* (2019), that tends to produce relatively good accuracy (Melton *et al.*, 2022).

The satellite data for METRIC are provided primarily by the thermal-based Landsat satellite, but can be supplemented by a combination of VIIRS thermal and Sentinel 2 short-wave data when Landsat encounters extensive periods of cloudiness. For regional ET, MODIS and VIIRS can be used, with modification to calculations for surface reflectance. Local weather data are used for ET_{ref} and wind speed. Typical spatial resolution is 30 m (sharpening the 60 m thermal band) while the temporal resolution is of 8 days (provided they are clear-sky) when using a combination of Landsat 7 and 8 or Landsat 8 and 9.

Several improvements to METRIC have been introduced from the time of its original version. The reader is referred to the following suggested reading-link for further insights on the model: <https://openetdata.org/methodologies/>.

It is recommended to visit the following web link for the latest version of the METRIC that is available in Python script.¹⁴

2.4.3 ALEXI - DisALEXI

ALEXI (Atmosphere-Land Exchange Inverse) is a RS ET model developed by Anderson *et al.* (1997; 2007a; 2007b), following some of the core algorithms of the SEB (as illustrated in chapter 2.1), though presenting few innovative features as compared to SEBAL and METRIC.

The disadvantage to diagnostic modeling is that the output record often suffers large spatial and temporal gaps due to cloud cover, impacting the critical thermal band satellite input data. Recent advances have implemented the use of land surface temperature (LST) derived from the 37 GHz channel on routinely available passive microwave radiometers (AMSR-E, AMSR-2, SSMI, SSMIS; Holmes *et al.*, 2009). This allows for “all-sky” retrievals of LST to be implemented within the ALEXI component of the modeling system, albeit at coarser spatial resolutions (on the order of 10 – 25 km).

ALEXI incorporates methods for addressing the spatiotemporal limitations of diagnostic modeling.

Distinctive features:

- ▶ ALEXI is based on a two-source land-surface representation (the TSEB), which treats the land surface as a composite of soil and vegetation elements with different temperatures, fluxes, and atmospheric coupling. This results in a single model formulation that can be applied to a wide range of canopy and moisture stress conditions, including partially vegetated surfaces.
- ▶ ALEXI inherently uses the high-temporal resolution (hourly) information provided by geostationary satellites to reduce sensitivity to sensor bias and to provide time-continuous flux predictions over continental scales. For global applications, it uses day-night temperature differences from polar orbiting satellites.
- ▶ Techniques have been developed for predicting fluxes on cloudy days (gap-filling technique) when thermal satellite imagery is not available, and for extrapolating instantaneous fluxes estimated at discrete imaging times to full hourly coverage at each grid cell in the modeling domain.

In ALEXI, the two-source energy balance (TSEB) partitions the composite surface radiometric temperature (T_{RAD}) into characteristic soil and canopy temperatures (T_s and T_c , respectively), based on the local vegetation cover fraction $f(\theta)$, apparent at the thermal sensor view angle,

$$T_{RAD}(\theta) \approx f(\theta) \cdot T_c + [1 - f(\theta)] \cdot T_s \quad (44)$$

with

$$f(\theta) = 1 - \exp\left(\frac{-0.5 \cdot \Omega(\theta) \cdot F}{\cos \theta}\right) \quad (45)$$

where F is the leaf area index, and $\Omega(\theta)$ is the vegetation clumping factor apparent at view angle θ .

¹⁴ GitHub, Inc. 2023. WSWUP - Pymetric. <https://github.com/WSWUP/pymetric>

Therefore, ALEXI evaluates the soil and canopy energy budget separately, as indicated in chapter 2.1, with the Eq. (11), (12), (13), (14) and (15).

Because angular effects are incorporated into the decomposition of T_{RAD} (Eq. 44), ALEXI can accommodate thermal data acquired at off-nadir viewing angles and can therefore be applied to geostationary satellite images.

The R_n and G computation in ALEXI follows Eq. (4), (5), (6) and (8), but is applied to the two-sources components separately (soil and crop), and differing for the empirical parameterization (see Anderson *et al.*, 2007a and 2007b for further details).

What is quite unique, instead, are the solutions adopted for H and λE .

Consider first the sensible heat fluxes (Figure 1). For regional-scale applications of the TSEB model in ALEXI, meteorological boundary conditions in air temperature, T_A , must be specified at the spatial resolution of the thermal data (typically 5-10 km). Due to localized feedback between the land and atmosphere, this input field cannot be spatially interpolated with adequate accuracy from standard synoptic measurements having typically large spacing (e.g. 100 km). To overcome this limitation, the TSEB model has been coupled with an atmospheric boundary layer (ABL) model, thereby simulating land-atmosphere feedback and its effect on local air temperature internally.

Thus, the TSEB is applied at two times during the morning ABL growth phase (approximately $t_1 = 1.5$ and $t_2 = 5.5$ h after local sunrise), using radiometric temperature data obtained from a geostationary platform like GOES or Meteosat at spatial resolutions of 5 – 10 km.

The ABL model in ALEXI relates the rise in air temperature in the mixed layer to the time-integrated influx of sensible heat (between H_1 at t_1 and H_2 at t_2) from the land surface, assuming a linear functional form for $H(t)$ during this morning interval, i.e.

$$\int_{t_1}^{t_2} H(t) dt = \frac{1}{2} (H_2 t_2 - H_1 t_1) \quad (46)$$

Furthermore, McNaughton and Spriggs (1986) provides a conservation equation relating the rise in potential temperature (θ_m) with height (z) of the mixed layer to the time-integrated sensible heating from the surface (Eq. 44) as

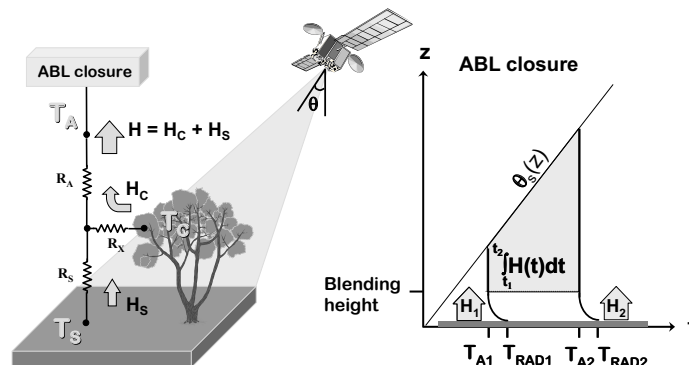
$$\int_{t_1}^{t_2} H(t) dt = \rho C_p (z_2 \theta_{m2} - z_1 \theta_{m1}) - \rho C_p \int_{z_1}^{z_2} \theta_s(z) dz \quad (47)$$

where $\theta_s(z)$ represents an early morning ABL potential temperature. The ABL is intended to start at an effective blending height, assumed to be at 50 m above ground level. Moreover, the mixed layer potential temperature (θ_m) and the air temperature (T_a) are related near the land surface through the following equation

$$\theta_m = T_a \left(\frac{100}{p} \right)^{\frac{R}{c_p}} \quad (48)$$

where: R is the universal gas constant; c_p is the specific heat capacity of air at constant pressure; p is the air pressure.

Figure 1: Schematic diagram representing the two-source land-surface scheme (left) and the time-integrated ABL closure component (right) of the ALEXI mode



Source: Anderson M.C., Norman J.M., Mecikalski J.R., Otkin J.A. and Kustas W.P. 2007a. A climatological study of evapotranspiration and moisture stress across the continental United States based on thermal remote sensing.

The surface and ABL components of the model iterate until the time-integrated sensible heat flux estimates from both components (Eq. 44 and Eq. 45, respectively) converge (energy-closure).

It is important to note that, as a result of this approach, ALEXI uses only time-differential temperature signals, thereby minimizing flux errors due to absolute sensor calibration and atmospheric and spatial effects (Kustas *et al.*, 2001).

Regarding the latent heat fluxes, we have

$$\lambda E = \lambda E_C + \lambda E_S \quad (49)$$

with

$$\lambda E_C = \alpha_c f_g \left(\frac{\Delta}{\Delta + \gamma} \right) Rn_c \quad (50)$$

and

$$\lambda E_S = \lambda E - \lambda E_C \quad (51)$$

where:

f_g = the fraction of green vegetation;

$\alpha_c f_g \left(\frac{\Delta}{\Delta + \gamma} \right) Rn_c$ = a modified Priestley-Taylor (PT) equation for transpiration (λE_C);

α_c = the PT coefficient, adjusted for stress as described below;

and the other terms already defined in previous equations.

The TSEB has a built-in mechanism for detecting thermal signatures of stress in the soil and canopy. A modified Priestley-Taylor (PT) relationship, applied to the divergence of net radiation within the canopy (Rn_c), provides an initial estimate of canopy transpiration (λE_C), while the soil evaporation rate (λE_S) is computed as a residual to the system energy budget. If the vegetation is stressed and transpiring at significantly less than the potential rate, the PT equation will overestimate E_C and the residual λE_S will become negative. Condensation onto the soil is unlikely at midday on clear days, and therefore $\lambda E_S < 0$ is considered a signature of system stress. Under such circumstances, the PT coefficient is throttled back until $\lambda E_S = 0$ (expected under dry conditions). Both λE_C and λE_S will then be some fraction of the potential ET rates associated with the canopy and soil components of the scene; these ratios are integral to the soil moisture estimation scheme.

At each GOES observation time, the TSEB simultaneously balances energy budgets associated with the canopy, the soil and the composite land-surface system.

Gapfilling and extrapolation to daily total fluxes

The extrapolation of instantaneous satellite-based flux estimates to daily totals assumes that the ratio of ET to solar radiation (f_{sun}) remains constant during the day. Of several scaling fluxes tested, Cammalleri *et al.* 2014 found insolation to provide the best performance on average using flux data from towers sampling a range in cover and climate conditions. However, other scaling fluxes could be easily applied and evaluated within the ALEXI framework.

Gap-filling of daily ET between clear days, when direct retrievals can be obtained, is achieved by interpolating f_{sun} to daily timesteps and multiplying by daily insolation derived from reanalysis datasets or geostationary imagery. Because the revisit frequency from geostationary inputs is relatively high, we can use this time-series information to filter for undetected clouds, which can corrupt the temperature rise signal used in ALEXI and add noise to flux estimates. Currently a Savitsky-Golay smoothing filter with a 2nd order smoothing polynomial is used to interpolate f_{sun} to daily timesteps.

A disadvantage to this gap-filling scheme is that moisture updates will not occur until the first clear day following a precipitation event. In other words, there may be a few days lag before the impact of rainfall over a given pixel is reflected in the available water pools of that pixel. The average frequency of update varies spatially and temporally across the domain according to the regional cloud cover climatology. As an example, Anderson *et al.* (2007a) indicated that, on average, the moisture pools in 75 percent of the U.S. domain are updated at least once every 6 days, while 95 percent are updated at least every 20 days.

Needless to say that rigorous flagging of cloud-contaminated pixels is critical to obtaining accurate flux estimates.

Input data required to execute ALEXI are listed in Table 1. Primary outputs from ALEXI are instantaneous values of T_A , G , R_n , R_{n_c} , R_{n_s} , E , E_c , E_s , H , H_c , and H_s at times t_1 and t_2 .

Table 1: Primary ALEXI input data sources

Data	Purpose	Source	Product Resolution
Clear sky:			
T_{RAD1}, T_{RAD2}	Surface temperature change	GOES	5–10 km
LAI	Assign $f(\theta)$, h_c , d , z_0 , ε	MODIS	1 km
Landcover type	Assign h_c , d , z_0 , α , s	UMD global	1 km
Wind	Aerodynamic resistances	ASOS/AWOS	40 km ^a
Lapse rate profile	ABL growth model	Radiosonde	40 km ^a
$\theta_s(z)$, $q_s(z)$	Atmospheric corrections	Radiosonde	40 km ^a
Cloud amount	Cloud mask	GOES	10 km
S_{di} , L_{di}	Hourly net radiation	GOES	20 km
Cloudy sky:			
Soil texture (0–5 cm, 5–200 cm)	Assign AWC	STATSGO	1 km

Source: Author's own elaboration.

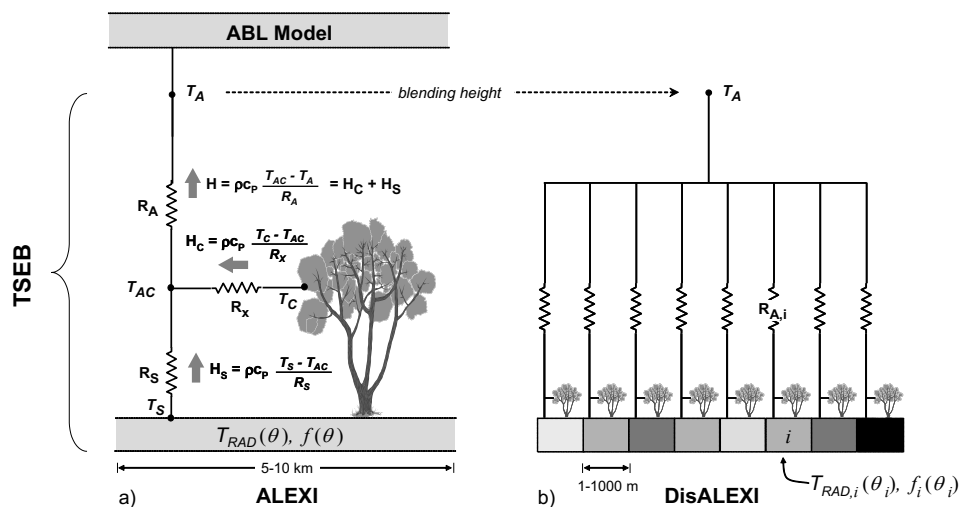
The accuracy of ALEXI-derived fluxes is difficult to assess directly due to the scale mismatch between the ALEXI pixel size (5-10 km) and the footprint of the surface flux measurement (typically 100 m – 1 km).

Disaggregation of ALEXI to measurement scales is described below.

DisALEXI

The coarse-scale flux estimates by ALEXI (constrained to operate on spatial scales of 5–10 km) can be spatially disaggregated to micrometeorological scales (typically of 100 m) using a flux-disaggregation technique referred to as DisALEXI (Norman *et al.*, 2003; Anderson *et al.* 2004). This technique uses air temperature diagnoses from ALEXI along with higher resolution TIR imagery available from aircraft or polar orbiting systems such as Landsat, MODIS, or VIIRS (Figure 2).

Figure 2: Schematic diagram representing the ALEXI (a) and DisALEXI (b) modeling schemes



Note: The schematic diagram, highlights fluxes of sensible heat (H) from the soil and canopy (subscripts “s” and “c”) along gradients in temperature (T), and regulated by transport resistances R_A (aerodynamic), R_X (bulk leaf boundary layer) and R_S (soil surface boundary layer). DisALEXI uses the air temperature predicted by ALEXI near the blending height (T_A) to disaggregate 10-km ALEXI fluxes, given vegetation cover ($f(\theta)$) and directional surface radiometric temperature ($T_{RAD}(\theta)$) information derived from high-resolution remote-sensing imagery at look angle θ .

Source: Anderson M.C., Kustas W.P., Norman J.M., Hain C.R., Mecikalski J.R., Schultz L., González-Dugo M.P., Cammalleri C., d’Urso G., Pimstein A. and Gao F. 2011. *Mapping daily evapotranspiration at field to continental scales using geostationary and polar orbiting satellite imagery*. *Hydrol. Earth Syst. Sci.*, 15: 223-239.

The boundary conditions (air temperature at the blending height and ET fluxes) are then iteratively adjusted at the ALEXI pixel scale, until the DisALEXI ET field reaggregates to the ALEXI baseline flux (convergence of T_A and closure of energy fluxes between ALEXI and DisALEXI).

The disaggregation operated by DisALEXI provides high spatial resolution assessment of moisture flux and stress conditions, though the temporal resolution is constrained by the overpass frequency of the polar orbiting satellite. Fusing ET from multiple thermal sensors provides a means for improving temporal sampling capabilities at the critical field scale (Xue *et al.*, 2022).

Together, ALEXI and DisALEXI facilitate scalable flux and moisture stress mapping using thermal imagery from a combination of geostationary and polar orbiting satellites, zooming in from the national scale to sites of specific interest (Anderson *et al.*, 2011).

Based on multiple data fusion analyses using daily tower flux measurements over different vegetation cover types and climatic conditions, typical root-mean-square-deviation errors for DisALEXI ET fluxes are on the order of 1 mm d⁻¹.

2.4.4 SSEBop

SSEBop (Simplified Surface Energy Balance – Operational) is a RS ET model developed by Senay *et al.* (2013, 2020) following the Satellite Psychrometric Approach (SPA) described in chapter 2.3.

The equation for calculating actual evapotranspiration (ET_a) is

$$ET_a = ETf \cdot K \cdot ET_o \quad (52)$$

where: ETf is the ratio between actual and maximum ET, nominally varying between 0 and 1;

K is a maximum ET scaling factor (to convert ET_o from grass to alfalfa; average at 1.2);

and ET_o is the grass reference evapotranspiration (in mm) taken as the FAO-PM equation (Allen *et al.*, 1998); if ET_o is taken as the ASCE equation (ASCE-EWRI, 2005) for alfalfa crop, then the K scaling factor is not used in Eq. (52)

As seen earlier, ETf is calculate as

$$ETf = [1 - \gamma^s (T_s - T_c)] \quad \text{Eq. (24) from chapter 2.3}$$

where: γ^s is the "surface psychrometric constant" (SPC), expressed in K⁻¹;

T_s is satellite-derived land surface temperature (LST), expressed in K;

T_c is the cold/wet limit surface temperature (also expressed in K).

The distinctive feature of SSEBop is in the SPC (γ^s) being considered a constant function of the location and of the day of the year (as it is mainly driven by net solar radiation). In other terms, it can be predetermined using Eq. (25).

Furthermore, as demonstrated in Senay *et al.* (2013), γ^s is the inverse of the difference (dT) between the hot/dry limit surface temperature (Th), corresponding to E=0, and the cold/wet limit surface temperature (Tc), corresponding to H=0; i.e.

$$dT = Th - Tc \quad \Rightarrow \quad Tc + dT = Th \quad (53)$$

By substituting 1/dT in Eq. (24), we obtain

$$ETf = \left[1 - \frac{(T_s - T_c)}{dT} \right] \quad (54)$$

$$\Rightarrow \quad ETf = \left[\frac{(Tc + dT) - T_s}{dT} \right] \Rightarrow$$

$$\Rightarrow \quad ETf = \left[\frac{T_h - T_s}{dT} \right] \quad (55)$$

Eq. (24), Eq. (54) and Eq. (55) are equivalent and provide the basis to explain the physical principles and working mechanisms of the SSEBop model.

The use of Eq. (55), though, eliminates the need to determine the hot/dry pixel reference limit (T_h) as dT is derived by the inverse of Eq. (25). To solve Eq. (55), we are thus left with the need of getting T_s (derived through satellite LST) and T_c (the cold/wet limit surface temperature).

A key consideration for the application of the psychrometric analogy in RS ET determination is that measurements of T_s and T_c should be in close proximity. In a satellite image, finding well-distributed cold/wet pixels (to derive T_c) in the proximity of actual dry pixels (the LST T_c) is often a significant challenge (only a few pixels may qualify for wet/cold reference). Therefore, SSEBop introduces an important simplification to derive T_c , consequent to the stable and strong relationship between air temperature and satellite-based LST at the wet surface. Such simplification considers T_c as a 'regional' variable (Senay, 2018b) and consists in estimating T_c from daily T_{max} (in K) of the air over well-watered and well-vegetated surfaces, at the location and day of the satellite overpass, through a conversion factor c (Senay *et al.*, 2013, 2016, 2017), i.e.

$$T_c = c \cdot T_{max} \quad (56)$$

Due to the complexity of hydro-climatic regions, where elevation, slope, and aspect can bring marked differences in air and surface temperatures within short distances, it is recommended to use gridded T_{max} in Eq. (56), instead of weather-station based T_{max} (Senay *et al.*, 2017, Senay, 2018b).

Furthermore, for localized applications, user can develop local-specific "c" values, for each satellite image, through

$$c = \frac{T_{s_cold}}{T_{max}} \quad (57)$$

where T_{s_cold} is the satellite-based T_s at the cold pixel where $NDVI > 0.8$ and T_{max} is the corresponding daily maximum air temperature at the same location and period (Senay *et al.*, 2013).

SSEBop is considered one of the simplest surface energy balance models for large-scale ET estimation as it directly solves for latent heat flux without the need to solve for the other fluxes of the surface energy balance equation (R_n , H , and G). For such simplification, in fact, the model has received some criticisms (Senay, 2018b).

However, most of the tests carried out on SSEBop have shown that the loss of accuracy due to the simplifications introduced is within the same order of magnitude of uncertainty of several other RS ET models that have a larger number of parameters (see chapter 7 for further insights on error analysis).

Finally, it is important to highlight that SSEBop, like METRIC, anchor ET_a to ET_o in order to remain within realistic boundaries of daily ET fluxes. Furthermore, the potential integration of Landsat 8 and Sentinel-2 data for estimating ET with SSEBop on higher temporal and spatial resolution has been attempted with good results, where errors were contained between 10 percent and 17 percent (Singh *et al.*, 2020).

2.4.5 PT-JPL

PT-JPL (Priestley-Taylor Jet Propulsion Laboratory) model was developed by Fisher *et al.* (2008). This modelling approach is conceived by having two major terms as part of the actual ET (ET_a) determination: (i) the potential ET of a surface (ET_p), setting the upper boundary of ET flux, and (ii) a set of eco-physiological constraining functions, reducing ET_p to ET_a .

ET_p is formulated through the Priestley-Taylor (1972) equation, which is a reduced version of the Penman-Monteith equation (see chapter 2.2), eliminating the need to parameterize stomatal and aerodynamic resistances, i.e.

$$ET_p = \alpha \cdot \frac{\Delta}{\Delta + \gamma} R_n \quad (58)$$

where: α is the Priestley-Taylor constant (=1.26); Δ is the slope of the saturation vapor pressure curve vs near surface air temperature ($kPa \cdot ^\circ C^{-1}$), dependent also on water vapor pressure (e_a); γ is the psychrometric constant

($\text{kaP}^\circ\text{C}^{-1}$); and R_n is net radiation (W m^{-2}). ETp is here expressed in energy terms, but can be converted into water mass by dividing it by the latent heat of evaporation (λ).

The PT-JPL model subdivides the total surface ETa in three ET contributions, i.e. from the soil (ETs), from the canopy (ETc), and from the water intercepted by the surface (canopy and soil) (ETi), each with its pertinent constraining functions, so that

$$\text{ETa} = \text{ETs} + \text{ETc} + \text{ETi} \quad (59)$$

where:

$$\text{ETs} = [f_{wet} + f_{SM} \cdot (1 - f_{wet})] \cdot \alpha \cdot \frac{\Delta}{\Delta + \gamma} (Rn_s - G) \quad (60)$$

$$\text{ETc} = (1 - f_{wet}) \cdot f_g \cdot f_T \cdot f_M \cdot \alpha \cdot \frac{\Delta}{\Delta + \gamma} Rn_c \quad (61)$$

$$\text{ETi} = f_{wet} \cdot \alpha \cdot \frac{\Delta}{\Delta + \gamma} Rn_c \quad (62)$$

with the various constraining functions and additional variable as follow:

f_{wet} is the relative surface wetness and expressed as relative humidity (RH) elevated to the 4th power (RH^4);

f_g is the green canopy fraction, obtained by the ratio of two additional functions (f_{PAR_A}/f_{PAR_i}), where f_{PAR_A} is the fraction of the photosynthetic active radiation (PAR) absorbed by the green vegetation cover (function of the leaf area index - LAI) and f_{PAR_i} is the fraction of the PAR intercepted by the total vegetation cover (green + non-green); f_{PAR_A} is expressed as linear function of the SAVI (soil adjusted vegetation index) and f_{PAR_i} is expressed as linear function of the NDVI (normalized difference vegetation index);

f_T is the plant temperature constraint and calculated as $\exp\left[-\left(\frac{T_{max}-T_{opt}}{T_{opt}}\right)^2\right]$, with T_{max} the maximum air temperature and T_{opt} the optimum plant growth temperature;

f_M is the plant moisture constraint and calculated as ($f_{PAR_A}/f_{PAR_{Amax}}$);

f_{SM} is the soil moisture constraint and calculated as $\text{RH}^{\left(\frac{\text{VPD}}{\beta}\right)}$, with VPD the saturation vapor pressure deficit of the atmosphere and β defining the relative sensitivity of RH to VPD;

Rn_s is the soil net radiation; Rn_c is the canopy net radiation ($R_n - Rn_s$); and G is soil heat flux.

Further details on the parameterization and algorithms' calculations are found in Fisher *et al.* (2008).

As we can see, the PT-JPL model (like S5EBop) avoids calculating the latent sensible heat flux (H) and invests most of its algorithms in the constraining functions that reduce ETp to ETa . Three of these constraints relate to the plant: leaf area index (LAI), the green fraction of the canopy that is actively transpiring (f_g), the plant temperature constraint (f_T), and the plant moisture constraint (f_M). One of them relates to the soil (f_{SM}) and one to the atmospheric relative humidity (RH). Furthermore, the novelty of these constraining functions is that, while remaining eco-physiological in nature, they are developed without using soil moisture, stomatal resistance and wind speed data, which are generally unavailable or often prone to large modeling errors. Moreover, ETp can be replaced with any preferred choice of ETp such as Penman-Monteith; this is how PT-JPL is being used in the OpenET project (Melton *et al.*, 2022).

In fact, PT-JPL requires five general data inputs to derive ETa : R_n ; air temperature (T_a); 3) vapour pressure of the atmosphere (e_a); surface reflectance in the red (R) band; and surface reflectance in the near infrared (NIR) band. All of these inputs can be derived via satellite, and particularly from a single-source like MODIS (MODerate-resolution Imaging Spectroradiometer).

Recently, PT-JPL is incorporating measurements of T_s from ECOSTRESS to reach the spatial resolution of 70 m (Fisher *et al.*, 2020). Similarly, it can incorporate Landsat vegetation cover information (from the Red and Near-Infra-Red bands) to reach the 30 m resolution. Due to R_n as the major driver of the energy fluxes, PT-JPL remains highly sensitive to LST measurements, and to a lesser extent on NDVI.

It can be considered a three-source model (as opposed to the two-source ALEXI model) as it can disaggregate the contribution to the total ETa in the soil (ETs), canopy (ETc), and water intercepted by the surface (ETi), components.

Tests of the PT-JPL performance against field determinations showed very good accuracy of the modeled ETa (Vinukollu *et al.*, 2011; Chen *et al.*, 2014; Ershadi *et al.*, 2014). Apparently, the parameters already entered the model do not require further site calibration (Fisher *et al.*, 2008).

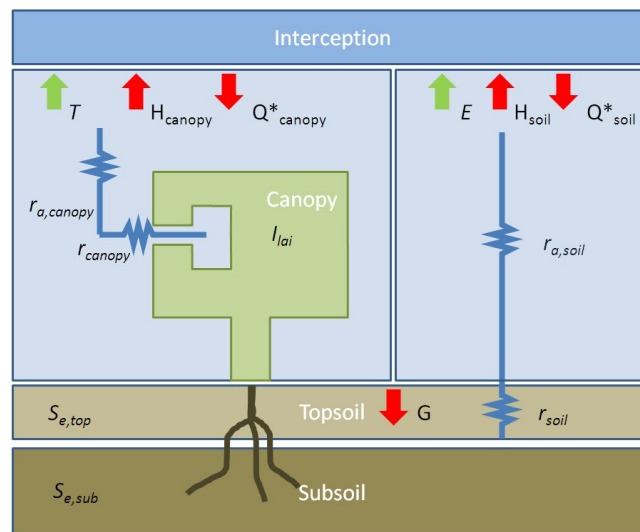
2.4.6 ETLook

ETLook is a model based on the P-M equation developed by Pelgrum *et al.* (2010) and Bastiaanssen *et al.* (2012) and designed to be applied also in the presence of cloudy conditions and across several scales, from field to continental level. It has gone through several refinements and represents the core ET model for the FAO Portal WaPOR.¹⁵ Though, the current version of ETLook uses soil moisture based on LST and is therefore not able anymore to operate under cloudy conditions.

The ETLook algorithm is a two-source model and solves the P-M equation for soil evaporation (E) and crop transpiration (T) separately. A third component is derived by the model to account for the precipitation interception by the canopy (I).

The main concepts of the ETLook model are schematically illustrated in in Figure 3.

Figure 3: Graphical conceptualization of ETLook



Note: Two sources for energy exchange are identified: canopy and soil. The 'Interception' of rainfall by the canopy (which evaporates) is accounted for reducing the available energy for transpiration from the canopy (T). Q' is the symbol equivalent of net radiation (Rn) and is also distinguished for the two sources (Q*_canopy and Q*_soil). Similarly, the sensible heat flux is distinguished for the two sources (H_canopy and H_soil). G is the soil heat flux. The canopy component is characterized by the 'size' of the T source (expressed through LAI) and the 'intensity' of T source (expressed through the canopy and aerodynamic resistances, r_canopy and r_a,canopy respectively). The soil component is characterized by two sub-components, the topsoil and the subsoil. The subsoil moisture content is pertinent to the water uptake by the root-zone and going into T, while the topsoil is pertinent to E. The resistances to the E flux are expressed through the surface resistance (r_a,soil) and the aerodynamic resistance (r_a,soil).

Source: FAO. 2018. *WaPOR Database Methodology: Level 1. Remote Sensing for Water Productivity Technical Report: Methodology Series*. Rome, FAO. 72 pages. Licence: CC BY-NC-SA 3.0 IGO.

¹⁵ WaPOR 2.1. 2019. https://wapor.apps.fao.org/home/WAPOR_2/1

The precipitation interception by the canopy (I) is derived first to account for the energy that would be consumed to evaporate the water intercepted. The interception is made as a function of the vegetation cover (C_{veg}), Leaf Area Index (LAI) and precipitation (P). This interception (in mm of water) is expressed as

$$I = 0.2 \cdot LAI \left(1 - \frac{1}{1 + \frac{C_{veg}P}{0.2 LAI}} \right) \quad (63)$$

which assumes that a water film of maximum 0.2 mm is stored per unit LAI . The energy required to evaporate the intercepted water is subtracted from the total energy available for T .

The ETLook model solves two versions of the P-M equation: one for the soil evaporation (λE) and one for the canopy transpiration (λT):

$$\lambda E = \frac{\Delta (Rn_{soil} - G) + \frac{\rho_a C_p (e_a - e_a RH)}{r_{a,soil}}}{\Delta + \gamma \left(1 + \frac{r_{s,soil}}{r_{a,soil}} \right)} \quad (= \text{Eq. 20 from chapter 2.2})$$

$$\lambda T = \frac{\Delta (Rn_{canopy}) + \frac{\rho_a C_p (e_a - e_a RH)}{r_{a,canopy}}}{\Delta + \gamma \left(1 + \frac{r_{s,canopy}}{r_{a,canopy}} \right)} \quad (= \text{Eq. 21 from chapter 2.2})$$

The net radiation Rn is described by the radiation balance Eq. (4) of chapter 2.1, where the net long wave radiation (net R_L), i.e. the difference between the incoming ($R_{L\downarrow}$) and outgoing ($R_{L\uparrow}$) long wave radiation, is computed using the formulation described in FAO report no 56 (Allen *et al.*, 1998), where net R_L is a function of the air temperature (T_a), actual vapor pressure (e_a) and transmissivity (τ).

The separation of Rn in the soil and crop contributions is operated through the leaf area index (LAI) according to

$$Rn_{soil} = Rn \cdot \exp(-\alpha \cdot LAI) \quad (64)$$

$$Rn_{canopy} = Rn \cdot [1 - \exp(-\alpha \cdot LAI)] \quad (65)$$

Where α is the light extinction coefficient for net radiation (often set at 0.6).

The soil heat flux (G), required to calculate evaporation from the soil surface, is derived with a formulation similar to one of FAO report no 56 (Allen *et al.*, 1998).

While the aerodynamic resistances ($r_{a,soil}$ and $r_{a,canopy}$) are calculated resembling the basic concepts reported in chapter 2.1 (introducing the stability correction through the Monin-Obukhov length and required iterations to solve for the stability correction), the way the surface resistances ($r_{s,soil}$ and $r_{s,canopy}$) are derived is among the distinctive features of ETLook.

The soil resistance ($r_{s,soil}$) is modelled using the minimal soil resistance ($r_{s,soil,min}$) and relative soil moisture content (S_e) by means of a constant power function, i.e.

$$r_{s,soil} = r_{s,soil,min} \cdot (S_e^{top})^{-2.1} \quad (66)$$

The canopy resistance is expressed as a function of the LAI , minimum stomatal resistance and a number of reduction factors, according to Jarvis (1976) and Stewart (1988), i.e.

$$r_{s,canopy} = \left(\frac{r_{s,canopy,min}}{LAI_{eff}} \right) \cdot \left(\frac{1}{S_t \cdot S_p \cdot S_r \cdot S_m} \right) \quad (67)$$

where:

$r_{s,canopy,min}$ is minimum stomatal resistance (in $s \cdot m^{-1}$);

LAI_{eff} is an effective leaf area index (adimensional), introduced because the canopy is assimilated to a big-leaf and therefore the surface resistance requires an adjustment of the LAI through the following equation

$$LAI_{eff} = \frac{LAI}{0.3 \cdot LAI + 1.2} \quad (68)$$

S_t is the temperature stress, function of minimum, maximum and optimum temperatures as defined by Jarvis (1976);

S_v is the vapor pressure stress induced due to persistent vapor pressure deficit;

S_r is the radiation stress induced by the lack of incoming shortwave radiation;

S_m is the soil moisture stress originating from a lack of soil moisture in the root zone.

All the reduction factors are adimensional and scaled between 0 (maximum stress) and 1 (no stress).

It must be highlighted that λE and λT are determined providing directly the daily values, i.e. the daily values are not the day-time integration of the instantaneous values, like it is the case for the model previously described.

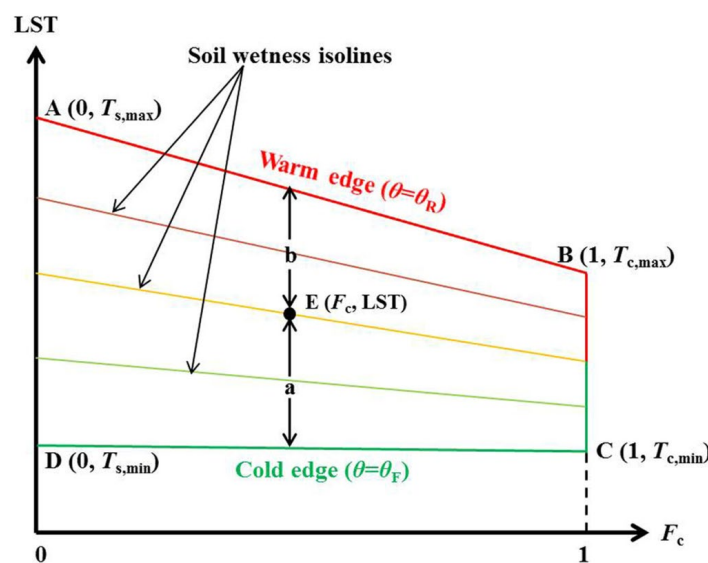
Key input data for ETLook are: surface soil moisture, spectral vegetation index, surface albedo, atmospheric optical depth, land use and land cover (LULC, used for determination of the minimum stomatal resistance and obstacle height), soil physical properties, and meteorological data (e.g. air temperature, relative humidity and wind speed) obtained either from field meteorological stations or from gridded satellite data.

Evidently, soil moisture is key for the calculation of both E and T, respectively, and their derivation represents an additional distinctive feature of ETLook. The so-called trapezoid method (Yang *et al.*, 2015) is used to derive the soil moisture, making use of visible and LST information from satellite images.

The concept behind the trapezoid method indicates that soil moisture can be diagnosed by exploiting the relationship between LST and the vegetation coverage (F_c), as provided by the satellite thermal infrared band and the visible and near-infrared spectrum, respectively. In fact, at high value of F_c generally corresponds low value of LST and high surface soil moisture, and vice versa.

The envelope of all points of the relationship LST vs F_c is indicated as the F_c /LST space, and theoretically represented by a trapezoid, as reported in Figure 4.

Figure 4: A sketch of the trapezoidal vegetation coverage/land surface temperature (F_c /LST) space. See text for explanation



Source: Yang Y., Guan H., Long D., Liu B., Qin G., Qin J. and Batelaan O. 2015. *Estimation of surface soil moisture from thermal infrared remote sensing using an improved trapezoid method*. Remote sensing, 7: 8250-8270.

Four critical points, related to four extreme conditions, define the trapezoid of Figure 4 (Yang *et al.*, 2015):

A is the bare soil LST ($F_c = 0$) under completely dry conditions;

B is the full-vegetation LST ($F_c = 1$) under completely dry conditions;

D is the bare soil LST ($F_c = 0$) with no water stress;

C is the full-vegetation LST ($F_c = 1$) with no water stress.

Points A and B constitute the warm edge of the trapezoid space, along which the pixels have the largest water stress for the entire range of F_c (from 0 to 1) and where the soil moisture is assumed to be minimum (indicated also as residual soil water content, θ_r). Accordingly, soil evaporation (λE) and vegetation transpiration (λT) are assumed to be equal to zero.

On the other side, points C and D constitute the cold edge of the trapezoid, along which the pixels have no water stress for the entire range of F_c (from 0 to 1) and where the soil moisture is assumed to be maximum, i.e. at field capacity (θ_f). Accordingly, λE and λT are assumed to occur at their potential.

It can be easily visualized that isolines of constant LST along the entire F_c range can be interpolated between the A-D edge and the B-C edge of the trapezoid (Figure 4), along which corresponding constant soil moisture availability can be derived.

While LST is obtained from the thermal infrared band, F_c is calculated through the NDVI, as obtained from the visible and near-infrared band, according to the following equation:

$$F_c = \left(\frac{NDVI - NDVI_{min}}{NDVI_{max} - NDVI_{min}} \right)^n \quad (69)$$

where the coefficient n is a function of leaf orientation and distribution within the canopy (value generally suggested is 2).

For a general pixel within the trapezoid space (point E of Figure 4), and having a defined value of F_c , a difference can be derived between the pixel LST and the cold edge LST (indicated as a in Figure 4), as well as between the pixel LST and the warm edge LST (indicated as b in Figure 4). The interpolation for the variables a and b is calculated as:

$$a = LST_E - LST_{cold\ edge} \quad (70)$$

$$b = (1 - F_c) \cdot (LST_{S,max} - LST_{C,max}) + LST_{C,max} - LST_E \quad (71).$$

The relative soil moisture (θ) for each pixel, the fraction between actual and saturated soil moisture content and expressed as a percentage, can be calculated as:

$$\Delta\theta = \frac{b}{a+b} \quad (72)$$

Evaluation of ETLook (e.g. FAO and IHE Delft, 2019; Blatchford *et al.*, 2020) indicates the reliability of the model for a longer period (e.g. a year) and larger areas (e.g. a sub-basin). It appears that the 250m and 100m pixels are less suitable for detecting ET of vegetables and fruit crops in smaller fields as compared to 30 m pixels.

Furthermore, ETLook version 2 is overestimating ET in dry, hot and water-stressed conditions, likely due to the estimation of the soil moisture content (using the trapezoidal method) with relatively coarse spatial resolution. ETLook version 3 tackles this problem in two ways: (i) by increasing the spatial resolution of LST using thermal sharpening, and (ii) by including stability functions, in particular for calculating the aerodynamic resistance for non-neutral conditions where turbulence is created by buoyancy.

However, ET underestimations are observed also under irrigation where advection conditions may develop (e.g. like the case of Egypt).

Nevertheless, ETLook is undergoing continuous spatial and temporal refinements and new versions are expected so that the degree of uncertainty will also continue to reduce.

2.4.7 ETMonitor

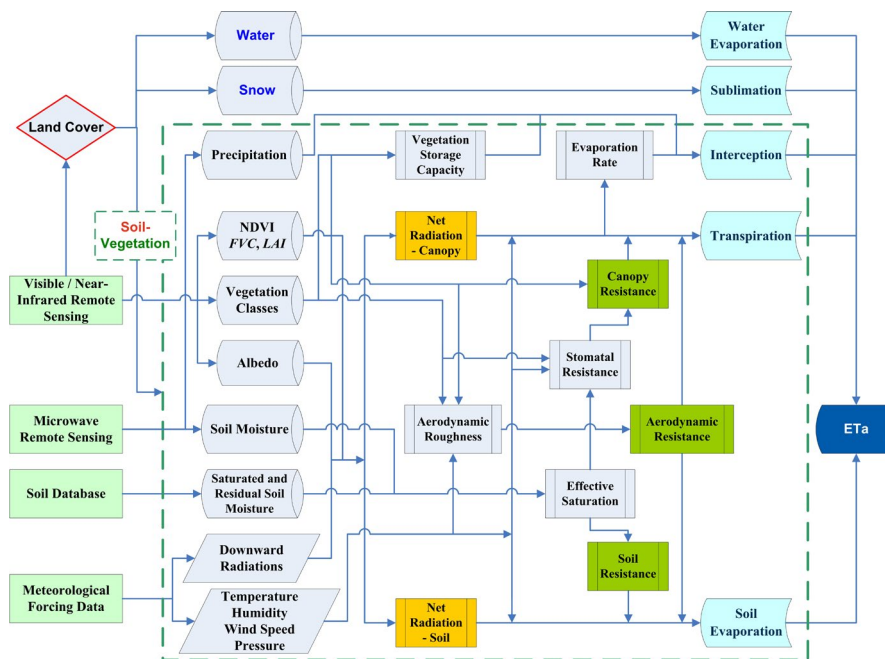
ETMonitor has been developed by Hu and Jia (2015) to estimate the daily actual evapotranspiration (ET_a) on large basins, having a spatial resolution of 1 km for the global standard model (Zheng *et al.*, 2022).

ETMonitor uses microwave and optical remote sensing observations as input data to Penman-Monteith based algorithms (see chapter 2.2), specifically the Shuttleworth–Wallace dual-source model (Shuttleworth and Wallace, 1985), for calculating soil evaporation and vegetation transpiration separately at a regional scale. Therefore, ETMonitor provides daily ET_a data, with no gaps due to clouds.

Considering the diverse landscapes and multi-climatic features of large basins, ETMonitor was conceived to cover several hydrological processes, including evaporation from bare soil and water surfaces, evaporation of canopy rainfall interception, transpiration from grasses, crops and forests, and sublimation of snow and glaciers (Hu and Jia, 2015; Zheng *et al.*, 2022).

The flow chart of the different states and processes involved in ETMonitor is sketched in Figure 5.

Figure 5: Flowchart of the ETMonitor model



Source: Hu G. and Jia L. 2015. *Monitoring of evapotranspiration in a Semi-Arid Inland River Basin by Combining Microwave and Optical Remote Sensing Observations*. Remote sensing, 7: 3056-3087 doi:10.3390/rs70303056.

Like ETLook, ETMonitor also separates the energy fluxes of the soil-vegetation system into two sources, soil and vegetation. In ETMonitor, however, these two sources are part of a unique bi-dimensional system and where the aerodynamic mixing of the soil-vegetation system is assumed occurring at a mean-canopy source-height within the canopy.

In fact, ETMonitor uses the Shuttleworth–Wallace equation (allowing for a bi-dimensional system, like soil and crop combined), which is a variant form of the Penman–Monteith equation (considered one-dimensional, i.e. either the crop closed canopy or the bare soil), and expressed as:

$$\lambda E = C_S \cdot PM_S + C_C \cdot PM_C \quad (73)$$

where: the subscripts S and C are for soil and canopy, respectively; PM_S and PM_C are variables related to soil evaporation and canopy transpiration (having the unit of $W \cdot m^{-2}$), respectively, and expressed as:

$$PM_S = \frac{\Delta \cdot (R_n - G) + (\rho \cdot C_p \cdot VPD - \Delta \cdot r_{a,S} \cdot R_{n,C}) / (r_{a,a} + r_{a,S})}{\Delta + \gamma [1 + r_{s,S} / (r_{a,a} + r_{a,S})]} \quad (74)$$

$$PM_C = \frac{\Delta \cdot (R_n - G) + [\rho \cdot C_p \cdot VPD - \Delta \cdot r_{a,C} \cdot (R_{n,S} - G)] / (r_{a,a} + r_{a,C})}{\Delta + \gamma [1 + r_{s,C} / (r_{a,a} + r_{a,C})]} \quad (75)$$

where R_n is the net radiation at the top of canopy, R_s is the net radiation at the top of soil, G is conductive heat flux at soil surface, all have the unit of $W \cdot m^{-2}$; $r_{a,a}$ ($s \cdot m^{-1}$) is the aerodynamic resistance between the canopy source height and the reference height above the canopy, $r_{a,S}$ ($s \cdot m^{-1}$) ($r_{a,C}$ ($s \cdot m^{-1}$)) is the aerodynamic resistance between the soil (canopy) and the canopy source height; $r_{s,S}$ ($s \cdot m^{-1}$) is the soil surface resistance, $r_{s,C}$ ($s \cdot m^{-1}$) is the bulk canopy surface resistance.

C_S and C_C (dimensionless) are the surface resistance coefficients for soil and canopy, respectively, and calculated as follows:

$$C_S = \left\{ 1 + \frac{R_S \cdot R_a}{[R_C \cdot (R_S + R_a)]} \right\}^{-1} \quad (76)$$

and

$$C_C = \left\{ 1 + \frac{R_C \cdot R_a}{[R_S \cdot (R_C + R_a)]} \right\}^{-1} \quad (77)$$

The terms R_a , R_s , and R_c (having the unit of $Pa \cdot K^{-1} \cdot s \cdot m^{-1}$) are the total aerodynamic resistances to vapor transport for the whole soil-vegetation canopy system, for the soil and for the vegetation, respectively. They are derived from the corresponding surface resistance (r_s) and aerodynamic resistance (r_a), as follows:

$$R_a = (\Delta + \gamma) \cdot r_{a,a} \quad (78)$$

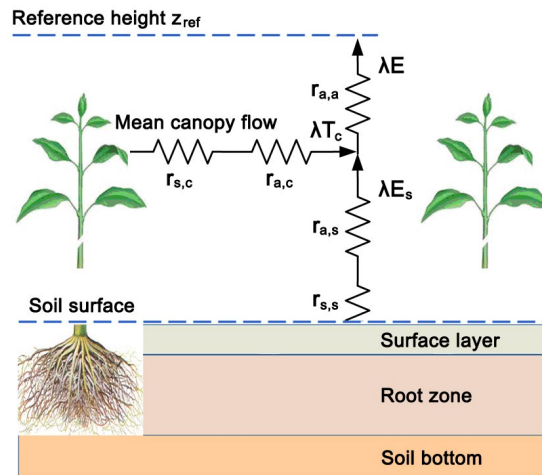
$$R_S = (\Delta + \gamma) \cdot r_{a,S} + \gamma \cdot r_{s,S} \quad (79)$$

$$R_C = (\Delta + \gamma) \cdot r_{a,C} + \gamma \cdot r_{s,C} \quad (80)$$

The canopy source height is taken at $d + z_{o,m}$ (in m), with d (in m) and $z_{o,m}$ (m) are the zero plane displacement height and the aerodynamic roughness length, respectively, for momentum transfer of the whole soil-vegetation canopy system (see also chapter 2.1). In ETMonitor, a machine learning model using Random Forest (RF) algorithm was developed and applied to estimate the conductive heat flux at soil surface G (Zheng *et al.*, 2022).

These resistances and latent heat fluxes of the bi-dimensional soil-canopy system are sketched in Figure 6.

Figure 6: Schematic representation of the relevant resistances and latent heat fluxes of the soil-vegetation canopy system considered in ETMonitor



Source: Hu G. and Jia L. 2015. *Monitoring of evapotranspiration in a Semi-Arid Inland River Basin by Combining Microwave and Optical Remote Sensing Observations*. Remote sensing, 7: 3056-3087 doi:10.3390/rs70303056.

The use of the dual-source Shuttleworth–Wallace equation is a distinctive feature of ETMonitor, while the surface and aerodynamic resistances are parameterized similarly to what is done in ETLook.

For instance, the derivation of the atmospheric stability correction follows the iterative approach (see also chapter 2.2) and the partitioning of fluxes between soil and canopy is made function of LAI. The soil surface resistance to vapor flux is parameterized through the same power function of ETLook (see Eq. 66, except that the power set at -3 instead of -2.1. The relative water content of soil surface layer is derived from the observations by the passive microwave radiometer and is downscaled to 1 km resolution using a machine learning algorithm by taking NDVI, albedo, DEM and soil properties as input and the algorithm is trained by combination with in-situ soil moisture measurements. The canopy surface resistance is parameterized using Jarvis-Stewart type of equation, similar to ETLook (see Eq. 67).

ETMonitor derives the interception of different vegetation types using as a basis the Gash analytical model (Gash *et al.*, 1995; Van Dijk and Bruijnzeel, 2001), but reformulated and adapted to remote sensing inputs (Cui and Jia, 2014; Cui *et al.*, 2015; Zheng and Jia, 2020) and called RS–Gash model.

The sublimation of snow and ice is derived using the Penman combination equation (Penman, 1948), in which G was taken as the conductive heat flux at the interface between the snowpack and the soil surface and calculated as a constant proportion of R_n received at the snow surface following the study of Wang *et al.* (2017).

The evaporation from the water surface is derived using the classical Penman equation (Penman, 1948), with surface resistance equal to zero.

ETMonitor has also been refined for high resolution ET (at 250 and 30 m), adopting different data-fusion algorithms, for particular use in agriculture.

Calibration of the major model parameters and model validation were carried out in a regional scale (the Heihe River basin in China, the Kingdom of the Netherlands and Thailand) and in global scale using flux tower measurements and for inter-comparison with other models (Cui and Jia, 2014; Hu and Jia, 2015; Zheng *et al.*, 2019a; Zheng and Jia, 2020; Zheng *et al.*, 2022). ETMonitor has been applied in a few projects in China, The Kingdom of the Netherlands and Morocco.

The level of accuracy is considered good, though continuous improvements are ongoing particularly for the soil moisture determination at high spatial resolution (e.g. using machine learning methods to downscale the microwave information) and input data quality. Furthermore, a dedicated information platform on ETMonitor and its results is under development.

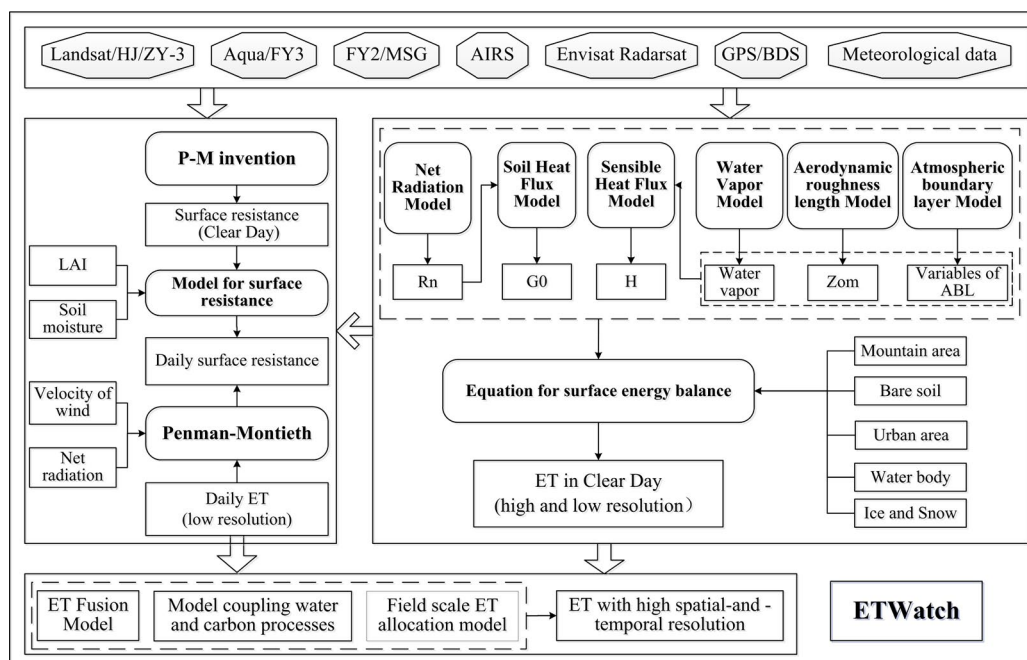
2.4.8 ETWatch

ETWatch has been developed by Wu *et al.* (2008, 2012, 2020), integrating the surface energy balance, aerodynamic theory and water balance to determine ET at a resolution from 5m to 1km. It uses multiple sources of satellite data (Wu *et al.*, 2020) including optical, thermal, microwave, together with geostationary and ground meteorological observation data to characterize the earth surface. As an integrated package of algorithms, ETWatch is designed to estimate regional ET at different resolutions and spatiotemporal scales for basin water resources management and agricultural irrigation management, including basin level ET with 1km/250m resolution and irrigation district ET with 5-30m resolution.

ETWatch was initiated in 2005. At that time the SEBAL model (Bastiaanssen *et al.*, 1998a) was programmed and used to generate ET data for the Hai Basin. In order to produce high quality data for the Hai basin, additional algorithms and methods were developed such as seasonal lapse rates of air temperature, atmospheric boundary conditions, aerodynamic roughness at urban and mountain area, and so on. Radar data were introduced to quantify the surface roughness. Therefore, the first version of ETWatch was gradually formed. From its initial version, algorithms and methods as well as parameters in ETWatch have been continuously refined, replaced and replenished.

ETWatch is now characterized by a high degree of complexity in managing and processing the multi-type data, as well as by having the algorithms of the various components of the model highly parameterized with multi-source data to quantify fluxes between surface and atmospheric boundary layer, in the attempt to make the model more accurate and reduce the complex influence of multicollinearity problem. ETWatch is embedded with various algorithms for specific land surfaces such as water and ice surface, and bare land. A typical flow chart of ETWatch is represented in Figure 7.

Figure 7: Typical ETWatch processes flowchart



Source: Wu B.F., Xiong J. and Yan N.N. 2008. *ETWatch for monitor regional evapotranspiration with remote sensing*. *Advances Water Sci.*, 19(5): 671–678.

To solve the mismatching issue between the complex underlying surface within pixel of remote sensing and the homogeneous underlying surface hypothesis, ETWatch developed new surface resistance algorithm based on the canopy stomatal conductance, replacing the empirical value of the maximum stomatal conductance with a mathematical model to reflect the spatial heterogeneity of vegetation types and the influence of the atmospheric environment, reducing the impact of heterogeneous surface on the model (Xu et al, 2020,2021).

As it can be seen in the flowchart of Figure 7, ETWatch can use both satellite and ground meteorological data, including air temperature, air pressure, air humidity and wind speed, typically interpolated into daily maps at 250m/1 km resolution. The sunshine duration is extracted using FY2 geostationary satellite cloud product. Nevertheless, where the quality of ground data and their spatial interpolation is unsatisfactory, only gridded data are used. The model also develops multiple data fusion and ET allocation algorithms to integrate data at different resolutions, reaching spatial scales down to field scale at 5 m (Wu *et al.*, 2011).

While the reader is referred to Wu *et al.* (2012; 2020), Zhuang *et al.* (2016), and Xu *et al.* (2018, 2021) for the detailed description of the various updates and algorithms of ETWatch, some examples of corrections and equations are reported here for the sake of illustrating the extent of complexity and parameterization of the model.

For instance, to conduct atmosphere correction for the calculation of net radiation, ETWatch has embedded the atmospheric radiative transfer models derived by Stein and Zaanvoordijk (1999) and Vermote *et al.* (1997). For better estimation of net radiation, ETWatch developed a new satellite -based net radiation approach integrating FY2 cloud classification product derived sunshine duration, which increases the spatial representation compared with interpolated sunshine hour method (Wu et al, 2017).

Concerning the determination of land surface temperature, the split-window algorithm proposed by Wan and Li (1997) and Mao *et al.* (2005) is used to eliminate the effects resulting from atmospheric water vapor on the transmittance of long wave radiation through the atmosphere. ETWatch proposed an optimized algorithm to derive near-surface actual vapor pressure from MODIS profile data, NDVI and surface data, and improves the estimation of instantaneous VPD calculation (Zhang *et al.*, 2014).

$$VPD = e^*(T_a) - e_a \quad (81)$$

$$e^*(T_a) = 0.6108 \cdot \exp \left[17.27 \cdot \frac{T_a}{237.3 + T_a} \right] \quad (82)$$

$$T_a = T_s - k_{12} \cdot W - k_{11} \cdot NDVI - k_{10} \quad (83)$$

$$e_a = 0.126 \times 10^6 \cdot a \cdot \left(1 + \frac{T_a}{273.15} \right) \quad (84)$$

where k_{12} is a constant determined by statistical analysis, and k_{10} , k_{11} are regression coefficients.

Regarding the surface energy balance equations, the instantaneous surface soil heat flux ($G_{0,i}$) is estimated using the following equation (Wu *et al.*, 2020):

$$G_{0,i} = R_{n,i} \cdot \left[T_s \cdot (a_1 - a_2 RVI + a_3 RVI^2) \cdot (b_1 + b_2 \alpha_3 + b_3 \alpha_4) \cdot e^{\frac{-0.25}{\cos(s_{oz})}} \right] \quad (85)$$

where: $R_{n,i}$ is the instantaneous net radiation; T_s is the surface temperature, RVI is the radar vegetation index; s_{oz} is the solar zenith angle; a_1 , a_2 , a_3 , b_1 , b_2 , b_3 , α_3 and α_4 being empirical parameters requiring calibration. The daily soil heat flux is then obtained from the daily integral of the instantaneous surface soil heat flux, with diurnal variation of the surface temperature simulated with land surface temperatures from multiple temporal satellite passages (Wu *et al.*, 2020).

The sensible heat flux (H) is estimated using the following equation:

$$H = \frac{\rho_a C_p (T_s - T_a) (e_s^* - e_s) (1.2 + 0.3 \cdot LAI)}{r_{c,min} (e_s - e_a) \cdot F_1^{-1} \cdot F_2^{-1} \cdot F_3^{-1} \cdot F_4^{-4}} \quad (86)$$

where: ρ_a , C_p , T_s , T_a , LAI, e_s^* , e_s and e_a have been already defined earlier; $r_{c,min}$ is the minimum canopy resistance, and F_1 , F_2 , F_3 , and F_4 are constraining factors linked to photosynthetic active radiation, soil moisture affecting canopy water stress, VPD, and the air temperature, respectively.

Furthermore, to express a comprehensive and effective roughness length ($z_{0,m}$) for the calculation of the aerodynamic resistance on large scale, four components are accounted for: the vegetation ($z_{0,m}^v$); the terrain ($z_{0,m}^T$); the non-vegetation obstacles ($z_{0,m}^r$); and the change of the vegetation canopy structure ($z_{0,m}^{nir}$).

These four components of the roughness length are calculated as follows (Wu *et al.*, 2020):

$$z_{0,m}^v = \left[b_1 + b_2 \cdot \left(\frac{NDVI}{NDVI_{max}} \right) \right]^{b_3} \quad (87)$$

where b_1 , b_2 , and b_3 are empirically determined coefficients;

$$z_{0,m}^T = \frac{slope - a}{b} \quad (88)$$

where the terrain slope is derived from the 90m digital elevation model (DEM) data from Shuttle Radar Topography Mission (SRTM) aggregated to 1 km spatial resolution, and a and b are empirically determined coefficients;

$$\log(z_{0,m}^r) = -1.221 + 0.0906 \cdot \sigma_0 \quad (89)$$

where σ_0 represents the radar backscattering coefficient data acquired from Sentinel-1 and aggregated to 1 km spatial resolution using the nearest neighbor method;

$$z_{0,m}^{nir} = e^{c_1 \cdot \frac{k_2}{k_0} + c_2} \quad (90)$$

where: c_1 and c_2 are empirically determined coefficients; k_0 is the weighting factor of the isotropic scattering component; and k_2 is the weighting factor based on surface scattering and the shadow casting theory (see Wu *et al.*, 2020 for further details).

The total roughness length ($z_{0,m}$) is then calculated as:

$$z_{0,m} = (z_{0,m}^v + z_{0,m}^{nir}) \cdot z_{0,m}^T + z_{0,m}^r \quad (91)$$

From the above, it is evident that ETWatch is a complex computational model requiring multiple sources data and to reduce the uncertainties of input data, a demanding calibration procedure of the numerous parameters is involved. As an example, the characteristic of the atmospheric boundary layer height is a key factor in the ET process, ETWatch developed new method to derive atmospheric boundary layer height (ABL) from MODIS and AIRS atmospheric profile data (Feng *et al.*, 2015), which reduces the sensitivity of ETWatch to the thermal character of ground, such as air temperature and LST data, then improves the accuracy of ET model. Planetary boundary layer parameterization is validated from several meteorological stations equipped with weather balloons. Furthermore, for an effective validation platform, a combination of ground-flux network and hydrological modelling is required.

After calculating clear day surface resistance, daily surface resistance is derived by inverting the Penman-Monteith (P-M) equation, and it is scaled at daily level accounting for the LAI, soil moisture, wind speed and radiance. The P-M equation is then used again to derive daily ET in cloudy conditions, which overcomes the influence of cloudy and rainy days. The daily surface resistance ($r_{s,daily}$) is thus calculated as (Wu *et al.*, 2020):

$$r_{s,daily} = \frac{r_{s,clear} \cdot LAI_{clear} \cdot Rn_{clear} \cdot SM_{clear} \cdot U_{clear}}{Rn_{daily} \cdot SM_{daily} \cdot U_{daily} \cdot LAI_{daily}} \quad (92)$$

where: $r_{s,clear}$ is the bulk stomatal resistance of the well-illuminated leaf on the clear-day and obtained by P-M inversion; LAI_{clear} is the LAI calculated using clear-day satellite data and adopted as a scalar to relate surface resistance with environmental constraints such as air temperature and vapour pressure deficit (VPD); SM_{clear} is the soil moisture content retrieved from the microwave radar information; LAI_{daily} is the daily Leaf Area Index (LAI) values (irrespective if under clear or cloudy day); and SM_{daily} is the daily soil moisture content also retrieved from the microwave radar information (irrespective if under clear or cloudy day). U is wind speed; and R_n is net radiation calculated at clear and daily.

Therefore, ETWatch provides preset values of model parameters and achieves its best performance when customized for specific basins, with parameters to be re-calibrated case by case.

The overall accuracy of ETWatch is then the result of many concurring factors, internal and external to the model itself. For example, satellite data availability is a prime concern due to the frequent presence of clouds. In fact, the most difficult part of temporal-scaling is the ET estimation during cloudy and rainy weather (spatial and temporal scaling still remains a major challenge).

A major performance assessment of ETWatch was conducted in Hai river basin, Turpan Basin, the Loess Plateau and Hei river basin (in China), covering multiple regions of China dryland where the results of ETWatch were validated against various methods, including soil moisture depletion, lysimeters, eddy covariance and classical water balances (Wu *et al.*, 2012, 2020). There were some concerns with the comparison between ETWatch and the eddy covariance (EC) showing significant deviation on a daily scale, with EC presenting problems of closure with typical errors often of 15-20 percent. Better comparisons were found with the other methods.

Overall, the results of the validation in Hai river Basin indicated that (i) annual ET data were more reliable (deviations of 3.8 percent) than the daily ET data, and (ii) basin-scale ET data were more reliable (deviation of 1.8 percent) than those of single pixels (Wu *et al.*, 2012). In Hei river basin, the overall deviation between the annual ETWatch results and ground-based water balance measurements was 1 percent for the entire basin and 9.44 percent for small watersheds (Wu *et al.*, 2020).

Cloud cover and the long intermittence between consecutive high resolution thermal images (i.e. the low

frequency of high-resolution Landsat images) is a likely cause of a lower accuracy of ET measurements at the field scale, rather than the methodology per se. Though, data fusion errors (not quantified) could have contributed as well. ETWatch has developed a pixel level downscaling method based on remote sensing vegetation indices, phenology, and surface resistant (Tan, et al 2017, 2019). To break the bottleneck of thermal infrared remote sensing that cannot monitor the evapotranspiration of fragmented plots with low resolution, and realizes the evapotranspiration monitoring at the block level of 5-10 meters, ETWatch developed field scale ET allocation method considering the soil moisture and crop growth condition (Ma, et al 2021).

ETWatch is now proposed in two versions, the standalone software and the 'cloud' version with APIs for modules (Wu, et al 2021) (ETWatch.cn). For specific basins and/or regions, the standalone software provides users with functions of data preprocessing, batch processing of ETWatch algorithms, internal calibration of model parameters, data quality control and result analysis.

ETWatch.cn cloud provides open-access, free to use cloud computation capability for any users who want to do ET calculation for their regions of interest. Every module of ETWatch model and water resources management methods were packaged in APIs, ETWatch.cn helps users to build their own applications with self-customized APIs of ET calculation and single components such as net radiation, sunshine duration and sensible heat flux. The applications are equipped with a flexible-sized cloud storage that can automatically download satellite data. Users can upload their own data to fulfill their purposes. ETWatch cloud platform is open to upload and manage self-developed APIs by users who develop their own models while keeping the copyright, which makes the calculation procedure more flexible and open to satisfy different needs.



©FAO



3. COMPARATIVE ANALYSIS OF THE SELECTED RS ET MODELS

The individual RS ET models described in chapter 2 are compared here in terms of their distinctive features, peculiarities, relative strengths and weaknesses and primary types of application, in order to help the reader to become more aware of what the present-day modeling landscape can offer and what the models might be that best fit a given purpose.

A first attempt to organize a comparative analysis is to categorize and separate models based on their primary reliance on Surface Energy Balance (SEBAL, METRIC and ALEXI/DisALEXI) and on psychrometry (SSEBop) from the others. This is because these SEB-based and psychrometry models all require satellite-based determination of Land Surface Temperature (LST), and this can be feasibly done only when there are clear views of the land surface, i.e. when there are the conditions of a cloud-free sky. Even thin clouds such as cirrus and jet contrails can influence the LST measurement due to their emission of thermal radiation.

Impacts of clouds and their masking. Cloudiness in a satellite image will severely limit the ability to produce ET estimates from that image. This applies to both LST-based models and short-wave based models. Several techniques for cloud masking are available to identify cloudy and cloud-free pixels of a satellite image,¹⁶ often using spectral disaggregation and the so-called *convolutional neural network* (CNN; e.g. Hughes and Kennedy, 2019). Cloud masks are also offered as a product of certain satellites, like the one of MODIS generated at 1-km and 250-m spatial resolutions. It is important to note that a cloud mask typically applies to the specific satellite image and time that it is collected. This is because clouds tend to continually move, so that the locations of clouds must be paired with the spectral information collected at the same time. Some cloud identification approaches employ the use of thermal imagery, if available for the satellite, in addition to shortwave imagery.

However, notwithstanding the various techniques, some uncertainties can remain when assessing the "clearness" of an image due to the influence of aerosols, dust, and smoke contamination of the atmosphere. This contamination, which is often invisible to the human eye and may even be difficult to detect in any of the shortwave bands, can impact both shortwave reflectance and LST determination. It can therefore impact estimates of the surface net radiation.

The resulting satellite image, after screening for cloud cover (e.g. high-altitude clouds, dense clouds, cirrus clouds, cloud-shadows, opaque clouds, etc.), haze, and different atmospheric vapor concentrations, thereby often suffers from large spatial gaps that may then create large temporal gaps for specific locations. Thus, a high potential for cloudy conditions can create a serious weaknesses of models that are based on SEB that requires the determination of LST. Models that are based on optical imagery only are also plagued by cloudiness. However, there tends to be a larger population of shortwave (only) satellites (for example, Sentinel 2 and SPOT) so that the likelihood of minimizing long time periods between a clear look at a location may be reduced. As indicated in chapter 2.4.3, recent advances in "all-sky" retrievals of LST have used the 37 GHz channel on routinely available passive microwave radiometers (Holmes *et al.*, 2009), although the tradeoff is coarser spatial resolution (on the order of 10 – 25 km).

Where cloudy conditions are significant and prevalent, one might be better off using the shortwave-only models that are based on the P-M equation (either single source or double source) such as ETMonitor. A special case is ETWatch as it implements a combination of the two methods (SEB and P-M) so that the model can derive certain parameters during the clear-sky conditions and use them during cloudy conditions. However, in this case a more appropriate spatial scale may be at the regional level (1 km or more). Nevertheless, these

¹⁶ EOS Data Analytics, Inc. 2023. Cloud Mask: What makes a difference for data accuracy. <https://eos.com/blog/cloud-mask/>

models make use of the NDVI derived from the NIR and Red wave lengths that are also affected by cloudy conditions, but are affected to a lesser degree by haze and aerosols. Therefore, the major advantage of using these P-M based models is partially due to their capacity to use microwave radiometers and to then derive missing parameters from different sources. The introduction of data processing (e.g. fusion and sharpening) having different scales and temporal resolution may constitute a major weakness. Another weakness of the P-M-based models can be the lack of LST United States of America that may preclude detection of effects of water stress and consequent lowering of ET.

SEBAL and METRIC models. Within the domain of the SEB-based models, we can say that their strength is in their ability to estimate actual ET rates, even during periods of water shortage, when they are locally calibrated. Application of SEB for field-scale ET estimates remains restricted to satellites that have high spatial resolution of LST determinations, down to 60 m with Landsat 7 and 100 m with Landsats 8 and 9, albeit a 16 day repeat orbit for each system.

More specifically, we can say that the highest spatial resolution with minimal data sharpening is generally obtained by SEBAL and METRIC, where ET estimates are produced at the 30-m scale of the shortwave images (although, ETLook can also provide images at 10m scale using thermal sharpened LST data from Landsat or VIIRS). However, the ET estimates are degraded to some degree by the 60 to 100-m spatial scale of the original LST information. In traditional applications, SEBAL and METRIC have been applied to single Landsat scenes where their calibrations are scene and date-specific. Therefore, their area of implementation is often confined to only about 25 000 square kilometers in extent. More recently, the implementation of SEBAL and METRIC on cloud-based computing platforms such as Google Earth Engine, where the calibration of the models, while still conducted scene-by-scene, is fully automated. This allows for the processing of hundreds of Landsat images at a time over a larger spatial range and over a larger range in time.

Both SEBAL and METRIC employ a similar approach to overcome the problem of inferring the surface aerodynamic temperature from the surface radiometric temperature (or LST) and the challenge of directly estimating the temperature difference between two near-surface air temperatures, assigned to two arbitrary heights above the surface to derive the sensible heat flux (H). The establishment of the temperature difference is done via inversion of the function for H at two known evaporative conditions in the model using the *calibration through inverse modeling at extreme conditions* (CIMEC) technique (see chapter 2.4.2; Allen et al., 2010a). This approach requires the identification of 'hot' and 'cold' pixels within the area of pertinence. This implies a certain level of skill by the operator in selecting these reference pixels. The effort to automate the procedure (Allen et al., 2013a) has not completely eliminated uncertainty risks associated to these hot/cold pixel selections. However, extensive testing of SEBAL and METRIC model results by the OpenET Consortium in the United States of America indicates relatively accurate and performance of the automation schemes (Melton et al., 2022). If this critical step of the procedure is not properly conducted, it may constitute the main weakness of SEBAL and METRIC models.

However, once the calibration step is properly enacted, the CIMEC approach generally guarantees a valid 'internal' calibration. By using locally available weather data within the calibration, a number of computational biases common to SEB models are corrected (Irmak et al., 2012), including: atmospheric correction; albedo calculation; net radiation calculation; surface temperature from the satellite thermal band; air temperature gradient function used in sensible heat flux calculation; aerodynamic resistance including stability functions; soil heat flux function; and wind speed field.

As with all ET models that produce ET estimates from the higher resolution polar-orbiting satellites such as Landsat and Sentinel 2, where spatial resolution ranges from 10- to 30-m, these two SEB one-source models derive ET on an instantaneous basis, and therefore they have to interpolate and integrate ET over the entire days between satellite revisits. The basic assumption for this integration is that the ratio between actual ET and the available energy ($\Lambda = R_n - G$, in the case of SEBAL), or reference ET over alfalfa (ET_{ref} , also indicated as ET_{ref} in the case of METRIC), at the time of the satellite overpass remains constant over the day and varies only gradually from one satellite image date to the next. It seems that the selection of Λ is more appropriate for rainfed conditions while ET_{ref} is more appropriate for irrigated crops in arid climates, as the use of alfalfa-based reference ET (ET_{ref}) allows one to better capture effects of regional advection of H and dry air, which can be substantial in irrigated deserts (Allen et al. 2007b).

Here in fact, we may state that a major strength of METRIC is in its 'anchoring' the SEB using CIMEC and the application of an ET ratio relative to ground weather-based reference ET calculated hourly for purposes of interpolation over time. This strength is however exercised provided well-calibrated and well-maintained weather stations exist in the area of interest. Gridded values of ETr (also used by SEBAL) are an alternative when local weather stations are lacking. However, gridded weather data sets can be biased by the incorporation of weather data collected over dry surfaces so that ETr is overestimated.

Time integration. In addition to the daily integration, where instantaneous estimates of ET at the overpass time are translated into ET estimates for the overpass day, SEB-based models, as with VI-based models, have the challenge of interpolating ET between satellite overpass dates to construct monthly and seasonal ET maps. In addition to the inaccuracies that might occur in the interpolation method (these are typically based on the ratio of ET divided by Rn-G (\wedge) or ETr (ETrF)), they all suffer from the inability to capture specific evaporation that may occur from episodic precipitation and irrigation events occurring between the satellite overpass dates (Allen *et al.*, 2010a). Ratios of (\wedge) or ETrF tend to be closely related to the amount of vegetation present, which, in turn, tends to vary slowly and continually between overpass dates. The interpolated (\wedge) or ETrF values for each day between overpass dates mimic the evolution of the vegetation. The (\wedge) or ETrF for each day are then multiplied by Rn-G or by ETr for each day to capture the effects of changing weather (sunny or cloudy, windy or calm, humid or dry, hot or cool). This method tends to work well and it is very similar to the use of crop coefficients that are multiplied by ET.

The low temporal interpolation of models like SEBAL and METRIC, which at best (with no clouds) is eight days using Landsat, may be avoided at the expense of the spatial resolution. For example, using MODIS or VIIRS instead of Landsat, one can gain a nearly daily temporal resolution, but loses the spatial resolution that will change from 30 m to 375 m with VIIRS or 1 km with MODIS (or 500 m with some sharpening procedure). This change of spatial scale may severely limit the application of the models for field-scale water monitoring and management. Thus, RS ET models that better fit purposes such as agricultural (e.g. water allocation, irrigation), aquifer depletion from pumpage, watershed water accounting, among others, often require a higher spatial resolution, like SEBAL and METRIC, but also DisALEXI, all of which tend to use thermal-based Landsat imagery.

The ALEXI-disALEXI model. With regard to the two-source ALEXI SEB model, we have seen (chapter 2.4.3) that H is derived differently from SEBAL and METRIC. The rise in air temperature (T_A) of the atmospheric mixed layer between two times in the morning (approximately at 1.5 hr and 5.5 hr after local sunrise and derived departing from the radiometric temperature data) is related to the time-integrated influx of sensible heat over the two times. The sensible heat flux is derived through an atmospheric boundary layer (ABL) model that simulates land-atmosphere feedback and its effect on local air temperature. The surface and ABL components of ALEXI iterate until there is convergence towards energy-closure. Although the complexity of the model is significant, it is important to note that ALEXI uses only time-differential temperature signals, thereby minimizing flux errors due to absolute sensor calibration and atmospheric and spatial effects (Kustas *et al.*, 2001).

However, it is clear that ALEXI can be applied only for RS ET determination at regional scales (5-10 Km), and relies on satellites that can give multiple shots per day for the diurnal aspect (such as the geostationary ones). An important application of ALEXI has been in drought indices determination, such as the evaporation stress index (ESI).

The post-ALEXI model DisALEXI produces a disaggregation of the fluxes down to a scale of 30 m (when using Landsat), though the temporal resolution is constrained by the overpass frequency of the satellite (e.g. 8-16 days when using Landsat). In DisALEXI, the boundary conditions (T_A and ET) are iteratively adjusted until convergence of T_A and closure of energy fluxes between ALEXI and DisALEXI are achieved. DisALEXI can thus be applied to fit the same purposes of SEBAL and METRIC to produce field-scale (30 m) ET. Based on the experience of the large US OpenET computations (Melton *et al.*, 2022), DisALEXI can struggle in areas having frequent and distinct transitions between irrigated and arid land uses. This occurs during the disaggregation and ET distribution phase. In addition, DisALEXI tends to be impacted to a greater extent by bias in LST retrievals caused by atmospheric correction uncertainties than are the CIMEC-driven SEBAL and METRIC models.

While the complexity of ALEXI/DisALEXI can be seen as a weak point for these models, their strength is in the two-source development (separating crops from soil) and the fact that they offer a consistent set of RS ET modeling approach in scaling the continuum from the national scale to sites of specific interest.

SSEBop. While ALEXI/DisALEXI brings in a higher complexity as compared to SEBAL and METRIC, SSEBop goes in the opposite direction. For instance, user-directed selection of the hot and cold reference pixels for a study area is not required. In fact, Senay *et al.* (2013) argue that under clear skies the hot and cold boundary conditions do not vary significantly among years, and more importantly the difference between the hot and cold reference values can be assumed constant for a given location and day of year (e.g. the values for the cold pixel temperature can be estimated from daily maximum air temperature along with a psychrometric-based calculation for wet-bulb temperature). An additional assumption of SSEBop is that the latent heat flux (λE) varies linearly between hot and cold reference pixels.

SSEBop is considered one of the simplest thermally-based one-source models, as it directly solves for λE without the need to solve for H and G, and thus require a reduced number of calculations. Its substantial simplification is also considered as one of its weaknesses, although several tests have shown that the loss of accuracy due to the simplifications is within the same order of magnitude of uncertainty as several other RS ET models that have a larger number of parameters (see chapter 7). In fact, Chen *et al.* (2016) determined that uncertainty in the simplification of the model did not significantly affect how well SSEBop estimates ET at a regional scale. Also McShane *et al.* (2017) concluded that SSEBop is a simple model, having reduced data requirements and greater ease of implementation without a substantial loss of accuracy in estimating ET. The reduced loss of accuracy, notwithstanding the simplification, is considered a SSEBop's strength.

It is important to highlight that SSEBop, like METRIC, can anchor ET to ET_r in order to remain within realistic boundaries of daily ET fluxes, and that Landsat and Sentinel-2 data can be integrated within SSEBop to obtain higher temporal and retain spatial resolution. Although greater accuracy is possible with the incorporation of ground-based data, no ground-based data are required. Weather data are obtained from gridded data sets that may be subject to the aridity biases as previously discussed.

We need to recognize that the initial development of SEBop was for the purpose of drought monitoring and famine early warning in regions having sparse ground-based data, mapping of water use by different land cover classes, and estimation of ET in the United States of America at regional to continental scales with default spatial resolution of 1 km, using mostly MODIS data (McShane *et al.*, 2017). Although it can scale down its ET determinations, more tests may be required to consolidate its accuracy at higher granular scales and in new regions.

PT-JPL. Among the non-SEB based models, a special case is represented by the PT-JPL model (Fisher *et al.* 2008). The major two terms are (i) the potential ET of a surface (ET_p), setting the upper boundary of ET flux, and (ii) a set of eco-physiological constraining functions, reducing ET_p to actual ET (see chapter 2.4.5).

The net radiation (R_n) is the major driver for ET_p while the constraining functions, reducing ET_p to ET, are related to plant temperature, plant moisture and soil moisture, where canopy and soil surfaces are distinguished through a green canopy cover fraction relationship. While these constraining functions remain eco-physiological in nature, they are developed without using the actual eco-physiological constraining data such as the soil moisture, stomatal resistance and wind speed (which are generally unavailable or often prone to large modeling errors). In fact, they are derived using air temperature (T_a), vapour pressure of the atmosphere (e_a), and surface reflectance in the red (R) and in the near infrared (NIR) bands, all obtained through satellite sources, or from field weather stations if appropriate.

Beyond MODIS and VIIRS, PT-JPL can use Landsat and ECOSTRESS to retrieve LST measurements to reach a higher spatial resolution (Fisher *et al.* 2020). The LST measurements assume relevance for the determination of R_n , a major driver of the energy fluxes. Thus, PT-JPL, like the SEB models, is impacted by clear sky conditions in the determination of LST and NDVI.

We can see that PT-JPL can be also considered to be a relatively 'simple' model, in a similar fashion to SSEBop. In fact, the parameters already entered into the model do not seem to require further site calibration. This

has been substantiated by the numerous tests against field ET determinations under a variety of land surface covers (see chapter 2.4.5). In fact, PT-JPL is one of the top performing models in the OpenET system.

As such, PT-JPL can fit the ET monitoring purposes over the continuum from local to global scale (like ALEXI/DisALEXI). However, for local scales it is recommended to conduct further local tests of validation to confirm that the model parameters do not require further site calibration.

PM-based models. The initial versions of ETLook, ETMonitor and ETWatch distinguish themselves from the previous models because, among others, they attempt to solve the problem of cloudiness to derive ET by following an approach different from the cloud masking used in SEB based models. Instead, these models adopt the Penman-Monteith (P-M) equation on a daily basis (see chapters 2.2, 2.4.6, 2.4.7 and 2.4.8).

Nevertheless, the P-M equation is a combination of (i) the energy and (ii) the aerodynamic terms, so that Rn is required for the 1st term and the surface and aerodynamic resistances (r_s and r_a) are required for the 2nd term, respectively. While Rn may be parameterized without the LST requirement, the r_a is derived in the usual numerical iteration (as in the case of the SEB model), though with H (instead of E) derived as residual of the energy balance (H=Rn-G-E), with the initial estimate of E and friction velocity (u.) for a neutral atmospheric condition. The derivation of r_s differentiates these three models that are based on the P-M equation.

The initial versions of ETLook and ETMonitor use passive microwave radiometer (AMSR-E) imagery to derive continuous surface soil moisture as it is little influenced by cloud cover. The root-zone soil moisture can then be derived through additional modeling (water balance, etc.) and thus providing the adjustment for the r_s .

ETWatch, instead, adopts the approach of deriving E during the clear sky days, based on the integration of surface energy balance and aerodynamics, and obtaining r_s by inverting the P-M equation. The r_s from the clear-sky days is then used with the P-M approach during cloudy conditions (see chapter 2.4.8).

Additional distinctive features of these original models are that ETLook derives soil evaporation (E) and canopy transpiration (T) using the P-M equation in both situations (as the two sources are in parallel), while ETMonitor derives the two sources of evaporation using the modified P-M equation to account for the two sources as part of a single integrated system, i.e. using the Shuttleworth-Wallace dual-source model (see chapter 2.4.7). ETWatch, instead, remain as single source model.

To draw some inferences on the strength and weakness of these P-M based models, it is necessary at this point to provide some sensible considerations. The transition from a SEB modeling approach to a P-M one introduces a significant addition of parameters, which increases the complexity of the models. The trade-offs in terms of gains and losses of accuracy need to be carefully assessed. Furthermore, the soil-surface moisture obtained through microwave has a quite coarse spatial resolution (25 km), so that substantial sharpening and data fusion computation is required to bring the ET estimates to reasonable operational scales. This same coarseness makes it impossible to monitor soil wetness caused by irrigation of an individual field and to incorporate that wetness into the r_s estimate.

ETMonitor has in fact developed a quite elaborate parameterization for operating on large basin scales. The parameterization of ETWatch and the various procedures for data sharpening and fusion, with substantial multiple sources of satellite data, is even more sophisticated, particular for deriving ET of each arable parcel based on water balance. Both models rely on a heavy calibration of the various parameters within the area of interest. The complexity of these models is one of their weaknesses, while the capacity to be used under cloudy conditions is their strength.

ETLook is a special case as its recent version has abandoned the use of deriving soil moisture through microwave radiometry and has introduced the trapezoid method (see chapter 2.4.6), which makes use of visible and LST information. The requirement of LST as input has defeated the initial intent of using the P-M equation to address ET under dominant cloudy conditions. In fact, the initial version of ETLook was utilized in the monsoon region of the Indus Basin, dominated by continuous cloudy conditions (Bastiaanssen *et al.*, 2012).

Therefore, ETMonitor may be better suited to fit regions with a high presence of cloudy conditions, while ETWatch can function under both cloudy and clear-sky conditions. The reliability of ETLook, instead, remains

for longer periods (e.g. a year) and larger areas (e.g. a sub-basin). Similar to the case of PT-JPL, it is recommended that validation tests also be conducted for ETLook for local conditions.

Summary of features of models. To conclude this chapter, the different features of the selected models are summarized and reported in Table 2.

Table 2: Distinctive features of the selected models

Model	Conceptual approach	Input variable	Sources ^(*)	Output spatial scale	Output temporal scale ^(*)	Major application
SEBAL	Residual Surface Energy Balance 1-source ($\lambda E = R_n - H - G$)	LST	VIIRS, Landsat,	30 m (Landsat)	1 day (VIIRS, MODIS)	District Water Balance
		Albedo, NDVI	ECOSTRESS,			
		Land surface elevation	Sentinel, Landsat	375 m (VIIRS)	8 days (Landsat)	Irrigation Crop yield
		Cloud cover (LandSAF)	SRTM, Copernicus	1 Km (MODIS)		
		Ta, RH, wind	MSG			Carbon sequestration
			CFSR, GEOS			
METRIC	Residual Surface Energy Balance 1-source ($\lambda E = R_n - H - G$)	LST	Landsat or VIIRS	30 m (Landsat)	8 days (Landsat)	ET from parcels > 5ha
		Albedo	Landsat, Sentinel 2			
		Land surface elevation	SRTM - DEM	30 m (VIIRS LST sharpened using Sentinel 2)		District Water Balance
		Land Cover Type	NLCD or ESA WorldCover			Irrigation
		NDVI or LAI	Landsat, Sentinel 2			Basin Water Balance
	ET _r , Wind speed	Weather Stations or NLDAS or CFSV2 or GridMET				

ALEXI-DisALEXI	Residual Surface Energy Balance 2-source ($\lambda E = R_n - H - G = \lambda E_c + \lambda E_s$)	LST	GOES (for ALEXI) LANDSAT (for DisALEXI)	5-10 km (ALEXI) 30 m (DisALEXI)	1 day (ALEXI) 8 days (DisALEXI)	Continental ET Monitoring; Drought Indexing (ALEXI)
		Albedo	MODIS (for ALEXI) Landsat (for DisALEXI)			Local ET Monitoring; District Water Balance;
		NDVI or LAI	MODIS (for ALEXI) Landsat (for DisALEXI)			Irrigation (DisALEXI)
		Land Cover	NLCD			
		Ta profile & other meteorological inputs	CFSR			
SSEBop	Psychrometric Approach 1-source	LST	MODIS or Landsat	30 m (Landsat)	1 day (MODIS)	Continental Drought Indexing,
		Ta	PRISM or Chelsa/WorldClim	1 Km (MODIS)	8 days (Landsat)	ET monitoring
		Albedo	MODIS or Landsat			Crop Water Use Assessment
		Land surface elevation	SRTM - DEM			
		NDVI	MODIS or Landsat			
		ETr	GRIDMET/GDAS			
PT-JPL	Priestley-Taylor 3-source including interception evaporation	LST	ECOSTRESS, MODIS, VIIRS or Landsat	3 m (Planet) 30 m (Landsat)	1 day (MODIS) 2-5 days (ECOSTRESS)	Local to Global scale ET monitoring
		Albedo	MODIS or Landsat			
		NDVI or LAI	Landsat, MODIS, VIIRS, Planet, Sentinel-2	70 m (ECOSTRESS)	8 days (Landsat)	
		meteorological inputs	GEOS-FP, MODIS, CFSR for Ta, RH	1 Km (MODIS)		

ETLook	Penman-Monteith 2-source	LST	MODIS, VIIRS, Sentinel-3 or Landsat	10m (Sentinel-2)	1 day	Field-scale to continental ET monitoring Agricultural water management
		Albedo		30 m (Landsat)	(inputs are interpolated/extrapolated between observations)	
		NDVI	MODIS/VIIRS/Sentinel-3 or Landsat/Sentinel-2	375m (VIIRS)		
			MODIS, VIIRS, ProbaV, Sentinel2 and 3, Landsat	1 Km (MODIS, Sentinel-3)		
		Land surface elevation	Copernicus DEM or SRTM DEM			
	meteorological inputs	GEOS-5, ERA5, ¹ Gridded Meteostations				
ETMonitor	Shuttleworth-Wallace (modified PM) 2-source	Surface/Top Soil Moisture	AMSR-E	1 Km (MODIS)	1 day (MODIS)	Regional & National ET monitoring Basin Water Balance
		Albedo	GLASS or MODIS			
		NDVI	MODIS			
		Land Cover	Variable sources			
		Land surface elevation	Variable DEMs			
		Soil physical properties	Variable maps			
		meteorological inputs	Gridded or Weather Stations			

Note: 1. The 5th generation ECMWF Reanalysis for the Global Climate and Weather data.



©FAO



4. BACKGROUND ON THE SELECTED RS ET DATABASES/ PORTALS

Some of the RS-ET models presented in chapter 2.4 are part of monitoring programmes that have generated ET databases over different time series and that have been made freely available to the public and accessible from the web.

In this chapter we are briefly addressing five of these databases (and portals): USGS FEWS NET (Famine Early Warning Systems Network with ET data mostly from SSEBop); WaPOR (with ET data derived from ETLook); GloDET (with ET data derived from ALEXI-DisALEXI); EEFlux (with ET data derived from METRIC); and OpenET (with ET data derived from an ensemble of algorithms including SEBAL, METRIC, SSEBop, ALEXI-DisALEXI, and PT-JPL among others). The reader is referred to the specific web-link to gain further insights and updates on the respective data base and/or portals. Furthermore, the reader is recommended to visit also the web site of ECOSTRESS (see also chapter 8).

4.1 USGS FEWS NET

FEWS NET (Famine Early Warning Systems Network) is a data portal provided by the United States Geological Survey (USGS) in support of drought monitoring efforts of Africa, Central and South Asia, Latin America and Caribbean, and the Middle East.²⁸

Several climatological data are present in the portal, including among others: monthly and annual precipitation (from CHIRPS 2 - Climate Hazards group InfraRed Precipitation with Station data); monthly mean of maximum temperatures, obtained by combining geostationary satellite thermal infrared (TIR) observations with sets of in situ station observations (from CHIRTSmax Climate Hazards group InfraRed Temperature with Station data); decadal, monthly and annual actual evapotranspiration (from SSEBop). The spatial scale is of predominantly 5km for precipitation and temperature, and of 1km for evapotranspiration. The time series are dating back to 1981 for precipitation, to 1983 for maximum temperature, and to 2003 for actual evapotranspiration.

As vegetation cover, the Normalized Digital Vegetation Index (NDVI) is also reported on dekad basis (when derived from MODIS; and dating back to 2002) and every five days (when derived from VIIRS; and dating back to 2012), and with a spatial resolution of 250m.

Data are provided as raster in GeoTIFF format.

The latency (lag time between access to data on the portal and actual time of the data determination) is three days.

Further reading on methods and data validation of FEWS NET can be found in Brown (2008), Ross *et al.* (2009) and FEWSNET.²⁹

²⁸ USGS - science for a changing world. <https://earlywarning.usgs.gov/fews>

²⁹ USGS - science for a changing world. International programs. <https://www.usgs.gov/international-programs/fews-net>

4.2 WaPOR

WaPOR (Water Productivity Open-access of Remote sensing data) is the FAO's portal to assist countries in monitoring water productivity, identifying water productivity gaps, and proposing solutions to reduce these gaps. It is the output of a project funded by the Ministry of Foreign Affairs of the Kingdom of the Netherlands.³⁰

WaPOR makes available a time series (dating back to 1st of January 2009) of basic variables such as: qualitative Land Cover Classification (LCC); Evaporation (E); Transpiration (T); water Interception (I); the integrated actual evapotranspiration and interception (ETIa); Net Primary Production (NPP); Total Biomass Production (TBP); Phenology; Reference Evapotranspiration (RET); Precipitation (P); and Water Productivity (WP) expressed as both 'Gross Biomass WP' [$=TBP/(E+T+I)$] and 'Net Biomass WP' [$=TBP/T$]. Quality layers are available that inform on time passed between valid observations for key input data Land Surface Temperature (LST) and Normalized Digital Vegetation Index (NDVI), and also on the reliability of the land cover classification at level 3. Both 'Gross Crop WP' [$[(TBP \cdot HI \cdot AoT)/(1-\theta)]/(E+T+I)$] and 'Net Crop WP' [$[(TBP \cdot HI \cdot AoT)/(1-\theta)]/T$] can be calculated on-line by users of the portal, accounting for the HI of the specific crop, the ratio between above-ground and total biomass production (AoT), and the moisture content of the harvested product (θ).

E, T, I, and therefore ETIa, are derived from ETLook.

The database is reported at three ground resolutions:³¹

- ▶ level 1 (250 m), covering Africa and Near East;
- ▶ level 2 (100 m), covering (i) the countries of Morocco, Tunisia, Egypt, Ghana, Kenya, Niger (the), Sudan, South-Sudan, Mali, Benin, Ethiopia, Rwanda, Burundi, Mozambique, Uganda, Sri Lanka, Iraq, West Bank and Gaza Strip, Yemen, Jordan, Syrian Arab Republic (the)n Arab Republic and Lebanon; and (ii) the river basins of Niger (the), Nile, Awash and Jordan and Litani.
- ▶ level 3 (30 m), covering Irrigation schemes and rainfed areas in Egypt, Ethiopia, Mali, Lebanon, Kenya, Mozambique Iraq, Libya, Rwanda, Senegal, Tunisia, Yemen, Sri Lanka and Sudan.

The development of the operational methodology and input data variables used to calculate water and land productivity was originally granted through an open tender to the FRAME Consortium whose members are Vito, eLEAF, the International Institute for Geo-Information Science and Earth Observation at the University of Twente, the University of Twente and the WaterWatch Foundation.

The minimum temporal resolution is decadal, and variables are also integrated at monthly, seasonal, and annual scales.

Data are provided as raster in GeoTIFF format.

The latency is three days.

Further reading on methods and data validation of WaPOR can be found in FAO (2018, 2020) and FAO and IHE Delft (2019).

³⁰ FAO. 2023. Land and Water. WaPOR - FAO portal to monitor Water Productivity through Open access of remotely sensed derived data. <https://www.fao.org/land-water/databases-and-software/wapor/en/>

³¹ The coverage of the database is continuously expanding and it is expected to include global coverage at level 1 in 2023. For an updated list of areas and countries covered at different levels of resolution, please visit wapor.apps.fao.org or the project website: <https://www.fao.org/in-action/remote-sensing-for-water-productivity/en/>

4.3 GloDET

GloDET (Global Daily ET) is a free portal hosted by the Daugherty Water for Food Global Institute (DWFI), at the University of Nebraska, providing global daily evapotranspiration (ET) spatial datasets at 375 meter resolution, calculated by the ALEXI two-source energy balance model.³²

The effort is a collaboration between DWFI, and researchers at USDA-ARS, NASA and ESSIC at the University of Maryland. The ALEXI ET at 375 m resolution can be subsequently downscaled to 30 meter resolution using the PyDisALEXI (Anderson *et al.*, 2011; Schull *et al.*, 2017).³³

In Nebraska, RS-ET data are periodically checked against eddy covariance towers equipped with the SmartFlux system developed by LI-COR Biosciences that are measuring ground ET for different crop types and climate conditions in the central plains of the United States of America.³⁴ These eddy covariance towers represent a collection of equipment being part of the "Parallel 41 Flux Network" only for Nebraska and Iowa, at this stage, the two sources of data (GloDET data sets and eddy covariance ET of the Parallel 41 Network) are being integrated to provide high-quality spatial information on daily crop water use.³⁵

Some of the ET time series of GloDET date back to 2013, however the various time series differ in their starting time because they depend on the duration of the project and funding. In fact, the geographical coverage is for the time being limited to the MENA Region, and to some areas of Brazil and United States of America. The database itself cannot be considered a monitoring time series of ET in these areas, but rather a repository of data.

Data are provided in GeoTIFF raster format and the latency is two days.

Further reading on methods and data validation of GloDET can be found at the GloDET Website.³⁶

4.4 EEFlux

EEFlux (Earth Engine Evapotranspiration Flux) is a tool system providing the METRIC RS model data on-demand, including among others, Landsat scene-sized imagery on: albedo, NDVI, Digital Elevation Model (DEM), Land cover, LST, alfalfa reference ET (ET_r), grass reference ET (ET_o) and actual ET (ET_a) derived from the EEFlux version of METRIC. More specifically, ET_a is expressed in terms of ET_r fraction (ET_rF), i.e. $ET_rF = ET_a / ET_r$. Thus, the uniqueness and advantage of EEFlux is that data generation is on-demand rather than being from a database.

The tool system has been developed by the consortium of the University of Nebraska-Lincoln, the University of Idaho and the Desert Research Institute, with initial funding support by Google, Inc.

EEFlux uses the full archive of Landsat images collection that is housed in the Google Earth Engine so that ET_a maps can date back to 1984 with geographical coverage for nearly every land area of the Globe. The various calculations and data processing take advantage of the Google cloud computing system.

ET_a is derived as residual of the surface energy balance, following the METRIC approach, first at the instant of the satellite overpass and then integrated over the day. Data are provided as rasters in GeoTIFF format, at a ground resolution of 30 m and every 8 to 14 days (depending on the time of subsequent satellites' launching). Furthermore, the Landsat scenes available include an assessment of the percent cloud cover, as determined by the USGS Earth Resources Observation System (EORS) data centre. As of now, the EEFlux web site does not provide the time interpolation between the dates of the satellite overpass. This task is left to the user.

³² University of Nebraska. GloDet. <https://glodet.nebraska.edu/#/>

³³ GitHub, Inc. 2023. Bucricicket - ProjectMAS. <https://github.com/bucricicket/projectMAS/tree/master/pydisalexix>

³⁴ LI-COR, Inc. 2023. Eddy Covariance Systems. https://www.licor.com/env/products/eddy_covariance/

³⁵ University of Nebraska. Parallel 41 Flux Network. <https://parallel41.nebraska.edu/#/>

³⁶ University of Nebraska. GloDet. <https://glodet.nebraska.edu/#/>

For the automated calibration of the surface energy balance of the RS images, EEFlux uses gridded weather data from two sources: the North American Land Data Assimilation System (NLDAS) for the United States coverage; and the Climate Forecast System Version 2 (CFSV2) for the rest of the globe. Calibration is performed automatically using the statistical procedure by Allen *et al.* (2013a) that applies population statistics to NDVI and LST for agricultural areas within a Landsat image. These statistics are used to identify suitable candidates for the hot and cold calibration pixels of METRIC.

The latency is about three days following the most recent Landsat overpass.

Further reading on methods and data validation of EEFlux can be found in Allen *et al.* (2015), Nisa *et al.* (2021) and at this link.³⁷

4.5 OpenET

OpenET[™] is developed by several partners to provide daily, monthly and annual ET data, at a spatial resolution of 30 meters, covering the western United States of America (for the time being).³⁸

The actual ET available includes data from an ensemble of six satellite-driven ET models, as well as a single 'ensemble ET' value determined from multiple satellite-driven models that use the Google Earth Engine as a shared platform for data processing, cloud computing and web development.

The models currently included in OpenET are: ALEXI-DisALEXI (version 0.0.32); METRIC (specifically eeMETRIC version 0.20.26); PT-JPL (version 0.2.1); SEBAL (specifically geeSEBAL version 0.2.2); SIMS (version 0.1.0); and SSEBop (version 0.2.6).³⁹

The basis for using an 'ensemble' ET value (from the six models above) is that the ensemble facilitates the identification and removal of outlier values, and the mean of the remaining ensemble values is expected to offset some of the individual model's biases and, therefore, to likely provide a more accurate estimate of actual ET than any one model on its own, across a diversity of crops and vegetation types. Nevertheless, there may be cases when a single model, or a subset of models, may be consistently more accurate than the ensemble, so that users may choose whether to use the ensemble ET value or an individual model or a subset of the models. The OpenET team is currently conducting accuracy assessments to characterize the accuracy of both the individual models and ensemble ET value, using data from more than 142 eddy covariance sites across the U.S. (Melton *et al.*, 2022).

While Landsat data is the most relevant input to the models, OpenET includes inputs also from Sentinel-2, Geostationary Operational Environmental Satellite (GOES), Suomi National Polar-orbiting Partnership (Suomi NPP), Terra, Aqua and other satellites.

OpenET also uses weather station measurements across the western United States of America that are integrated into assimilation systems to produce spatially distributed or gridded weather datasets, such as gridMET,⁴⁰ Spatial California Irrigation Management System (Spatial CIMIS),⁴¹ Daily Surface Weather and Climatological Summaries (DAYMET),⁴² PRISM,⁴³ and Land Data Assimilation System (LDAS).⁴⁴

Similar to EEFlux, the fraction of reference ET ($ET_{oF} = ET_a / ET_o$) is used to derive daily ET_a for each satellite

³⁷ EEFlux. 2022. <https://eeflux-level1.appspot.com/>

³⁸ OpenET. <https://openetdata.org/>

³⁹ gridMET. Climatology Lab. <https://www.climatologylab.org/gridmet.html>


⁴⁰ gridMET. Climatology Lab. <https://www.climatologylab.org/gridmet.html>

⁴¹ State of California. 2023. CIMIS. <https://cimis.water.ca.gov/SpatialData.aspx>

⁴² Oak Ridge National Laboratory. DAYMET. <https://daymet.ornl.gov/>

⁴³ Northwest Alliance for Computational Science & Engineering (NACSE), based at Oregon State University. 2023. PRISM Climate Group. <https://prism.oregonstate.edu/>

⁴⁴ Land Data Assimilation System. 2023. NLDAS-2 Forcing Dataset Information. <https://ldas.gsfc.nasa.gov/nldas/v2/forcing>



overpass. One minor difference is that OpenET uses grass reference ET (ET_o), as opposed to alfalfa reference ET (ET_r). The daily values of ET_{oF} are then linearly interpolated for all days in between clear satellite overpass dates, and pixel-by-pixel. The ET_{oF} are then multiplied by the daily ET_o values to obtain the daily time series of ET_a for every pixel, which are further aggregated to monthly and annual time periods. The data latency varies between 2 and 16 days from the day of satellite overpass (except under cloud cover).

Currently, monthly and daily data products are available from the OpenET Data Explorer, although the daily data are only available in 'Raster View' for selected pixels, due to the very large number of agricultural fields and growing length of the data record available from OpenET. Data can be downloaded from the Data Explorer in comma separated value (CSV) data formats, as well as various image formats. Data will also be available in the near future from the OpenET Application Programming Interface (API), which will facilitate automated data retrieval in multiple formats, including CSV, JavaScript Object Notation (JSON), GeoJSON, and GeoTIFF data formats.

Further reading on methods and data validation to date for OpenET can be found at the link.⁴⁵ The OpenET framework, data processing, and Phase I of the OpenET Accuracy Assessment is described by Melton *et al.* (2022), also available in the Journal of the American Water Resources Association as an open access paper at this link.⁴⁶

⁴⁵ OpenET. <https://openetdata.org/>

⁴⁶ John Wiley & Sons, Inc. 2023. OpenET: Filling a Critical Data Gap in Water Management for the Western United States. <https://onlinelibrary.wiley.com/doi/full/10.1111/1752-1688.12956>





5. COMPARATIVE ANALYSES OF THE SELECTED RS ET DATABASES/PORTALS

The databases/portals (here after indicated as platforms) presented in chapter 4 are here compared in terms of their distinctive features, peculiarities and major use, in order to orient the reader towards selecting a platform that better suits his/her needs.

In addition, we include references to the platform of ETWatch Cloud, although not elaborated in chapter 4. In fact, the peculiarity of ETWatch is in its multi-scale operation for multiple uses, like for watershed water resources allocation, water productivity assessment, and irrigation management. It allows users to rapidly and easily set up an ET generation project for any region of interest by invoking APIs directly to produce ET data using a web browser or local integrated development environment. This means that ETWatch Cloud can provide a highly scalable and interoperable ET generation tool for stakeholders from the ET community, helping to facilitate the application of remote sensing-based ET algorithms for water management in the hydrology sector.

The first aspect to consider is the RS ET model that provides ET to the database or portal, as the implications associated with each model are reflected in the related platform. The reader is referred to chapter 3 for comparisons among RS ET models and a list of data inputs, spatial and temporal scales and general types of application.

For different operational reasons and purposes, the temporal and spatial resolutions reported for the platforms are not necessarily the same of those that the RS ET models are able to provide. Examples are the FEWS NET platform which reports ET at decadal time resolution and 1 km spatial resolution, although its RS ET model (SSEBop) can provide higher resolutions. Similarly, WaPOR reports ET data aggregated at decadal time resolution from the daily values obtained through its RS ET model (WaPOR ETLook).

According to the author of ETWatch, the ETWatch Cloud reports ET data at daily/monthly temporal resolutions, 1km-250m and 10-30m spatial resolutions, and can even provide higher resolutions, such as 5m, for irrigation areas and cropland parcels.

One important distinctive feature among platforms is in how many years back a platform can extend in the time series, i.e. the year when the time series of ET has started. ETWatch could go back to 2000, SSEBop ET time series dates back to 2003, followed by WaPOR (back to 2009), GloDET (back to 2013) and OpenET (back to 2016 for the western United States of America).

A special case is represented by the web-based EEFlux, which cannot be considered to be a database (like the other platforms) but instead can only process on-demand the ET of selected Landsat scene areas all the way back to 1984, i.e. when the 1st thermally-equipped mission of Landsat was launched and corresponding to the image collection of the Google Earth Engine which is generally world-wide. Users of EEFlux must download individual images of ET or ETrF (ET divided by ETr) and then perform the time integration themselves.

Another important feature of a platform is the geographical area that it can cover. The ET product provided can be available around the globe (covering most of the world), like FEWS NET and EEFlux, or continental, like WaPOR (although, coverage is continuously expanding and it is expected to also have a global geographical coverage in the near future), or regional, like OpenET (covering for the time being mostly the Western United States of America) and ETWatch Cloud (where the geographical area can be set up by users, mostly covering the drylands in the northern part of China), or for specific areas depending on the projects implemented, like

GloDET and ETWatch Cloud. More than a database, GloDET can rather be considered to be a repository of data from projects developed in the MENA Region and in some areas of Brazil and the United States of America (see chapter 4.3).

Depending on the use of the ET product, the platforms can be distinguished for the total time elapsed between when data are acquired by the satellite(s) and when the ET data are made available to the user (this elapsed time is called latency). All platforms have reached a latency that generally does not go beyond 2-3 days, which is generally considered satisfactory for most user applications (except than for irrigation scheduling with drip and micro-sprinkler methods, requiring daily ET information).

In terms of major use of the selected databases and portals, FEWS NET has been conceived mostly for drought monitoring, WaPOR for water accounting and water productivity and the others for water and irrigation management.

It is important to consider that, beyond a required registration as a user, the platforms reported here are all free of charge and of open access and most of the data are downloadable as 'tiff' format, ready to be used with GIS software.

In addition to major ET products, the platforms may provide several ancillary products (e.g. NDVI, ETo, precipitation, DEM and LST, among others). The reader is referred to chapter 4, and to the web sites for the various databases and portals, to identify all ancillary products available.

Thus, depending on the specific purpose, the user can select the best fitting platform in terms of the most appropriate temporal and spatial scale, if the interest is on present periods or there is a need to go back in time to observe trends, and if the area of specific interest is covered by the selected platform.

The distinctive features of the various databases and portals discussed above are summarized in the synoptic table 3.

Table 3: Comparison of key features among the RS ET databases and portals

Database - Portal	Model used	ET of departure	Minimum time-resolution	Spatial resolution	Year of time series	Geographical coverage	Minimum latency	Major use
FEWS NET ¹	SSEBop	instantaneous	Decadal	1 km	2003	Global Continental	3 days	Drought monitoring
WaPOR ²	ETLook	daily	Decadal	250m 100m 30m	2009	Continental Basin	3 days	Water Accounting Water Productivity
GloDET ³	ALEXI DisALEXI	half-day half-day	Daily	375m 30m	2013	By project	2 days	Water Management
EEFlux ⁴	METRIC	instantaneous	Daily	30m	1984	Global (on user demand)	~3 days following the most recent Landsat overpass	Water Management Irrigation
OpenET ⁵	Ensemble [*]	instantaneous	Daily	30m	2016	Western United States of America	2 days	Water Management Irrigation

ETWatch Cloud ⁶	ETWatch	instantaneous daily monthly yearly	Daily	250m-1km 30m 16m 10m 5m	2000	Basin By project North China	~2 days following the most recent satellite overpass	Integrated water resources assessment Water Management Irrigation Water Accounting Water Productivity
-------------------------------	---------	---	-------	-------------------------------------	------	------------------------------------	---	---

Notes: 1. USGS - science for a changing world. USGS FEWS NET Data Portal. <https://earlywarning.usgs.gov/fews>

2. FAO. WaPOR 2.1. 2019. https://wapor.apps.fao.org/home/WAPOR_2/1

3. University of Nebraska. GloDet. <https://glodet.nebraska.edu/#/>

4. EEFlux. 2022. <https://eeflux-level1.appspot.com/>

5. OpenET. 2023. <https://openetdata.org/>

6. ETWatch. 2020. <https://www.etwatch.cn>

Source: Author's own elaboration.

* The ensemble includes the following models: ALEXI-DisALEXI (version 0.0.27); METRIC (specifically eeMETRIC version 0.20.15); PT-JPL (version 0.2.1); SEBAL (specifically geeSEBAL version 0.2.1); SIMS (version 0.0.20); and SSEBop (version 0.1.5).

It remains to be stressed that the databases and portals carry over the uncertainty of the RS ET models they derive the ET products from. Therefore, the user is always recommended to test and validate the ET data from the platform with some valid and verified ground reference data or through cross validation. The reader is thus referred to chapter 7 to gain further insights on the uncertainties of the various models and to chapter 7.3, to better frame the limits of uncertainty he/she can accept vis-à-vis the specific purpose of the ET use.



©FAO

6. SOME FIELD APPLICATIONS

The RS models presented in chapter 2.4 have been used in several water resources management applications. In this chapter we are summarizing some of these applications, presented during the webinar series, and in particular some that have interested the Near East and North Africa region and two that interested specifically on-farm irrigation management.

6.1 Experience from the NENA Region

A Python version of SEBAL (pySEBAL), processing images from Landsat-8, was used by Caiserman *et al.* (2021) to determine ET of crops in the plain of Marvdasht, in the Fars Province of **Islamic Republic of Iran (the)**. Sentinel-2 images were used for crop mapping. The objective was to identify situations of high water consumption by irrigated crops to advice political decision-making to revise cropping pattern towards the reduction of water consumption and groundwater depletion, while sustaining food security. Such reduction in water consumption, and a possible corresponding increase in water productivity, is a necessity for Islamic Republic of Iran (the) in view of its population growth and the increase of drought frequency over the last two decades, expected to further increase as results of future climate change scenarios. The authors observed an underestimation by pySEBAL ET of the order of 10 percent for most of the cases. This underestimation was confirmed through both farmer surveys and comparison with FAO-56 method. They concluded that PYSEBAL seems to underestimates the reality, but at the same time the model seems robust enough in its application in the plain of Marvdasht, as the uncertainty of pySEBAL (in the way it was determined) remains low.

Islamic Republic of Iran (the) was also the subject of another study, this time on the Urmia Lake Basin (ULB) where the METRIC model was operated for the RS ET determination (using Landsat thermal resolution of 100 m) to gain more insights on the basin hydrology and water resources management, as the lake was subject to rapid progressive shrinking due to multiple factors, including climate change and overuse of water by agriculture. The study was conducted by Tasumi (2019), on the western area of the basin, who also investigated the accuracy of the model, providing local refinements related to terrain characteristics. The estimation of the RS ET accuracy was assessed by comparison with the ET estimated using the FAO-56, as a widely accepted method for field ET estimation. Thus, assuming that the difference between the ET obtained through FAO-56 and the ET obtained by METRIC is the estimation error of METRIC, some of the statistical indicators for accuracy were determined for apple, grape, and bare soils. Specifically: for apple orchard, the mean bias error (MBE), the mean absolute error (MAE) and the root mean square error (RMSE) were 0.20, 0.57 and 0.73 mm d⁻¹, respectively; for grape vine, MBE, MAE and RMSE were 0.16, 0.72 and 0.84 mm d⁻¹, respectively; and for bare soil, MBE, MAE and RMSE were 0.36, 0.59 and 0.68 mm d⁻¹. The author found that MBE, MAE and RMSE tended to be similar among the three different land use types, suggesting that the error range in METRIC tends to be constant, rather proportional to the amount of ET occurring. The ET RMSE for apple orchard (having the highest ET of the three land use type, i.e. avg=5.29 mm d⁻¹) was equivalent to 14 percent of the average ET, while for bare soil (very low ET, i.e. avg=0.41 mm d⁻¹) RMSE was of 166 percent (which is expected for such very low ET value). The conclusion of the study was that the estimation accuracy of METRIC in the ULB was comparable to other similar applications and that the estimation of ET in this region was successful.

Owaneh and Suleiman (2018) tested two RS ET models (ALARM and SEBAL) against the ET of a lysimeter in **Jordan**. A potato crop of 1.5 ha was cultivated from January to May 2016, with the lysimeter located at the center of the field. The RS ET was derived for three Landsat-8 images: on March 22 (partially cloudy but not for the area of the potato field); on April 7 (clear sky); and on April 23 (clear sky). Six pixels of the images covered the main area of the potato field surrounding the lysimeter (surface area of approximately 7 m² and 2.5 m deep). Complementing field measurements included: hourly solar radiation, temperature, wind speed and humidity

from an automated weather station; LAI derived with a portable ceptometer (Decagon LP-80) to obtain values (direct or interpolated) on the date of the Landsat-8 images; canopy height. The two models under study are both based on the SEB approach (Eq. 3), calculate R_n and G in the same way, but they differ significantly in the calculation of the sensible heat flux (H): SEBAL derives dT (the difference between two near-surface heights) as a linear function of the surface temperature (Eq. 10 in chapter 2.1) through the 'hot pixel' and 'cold pixel' to derive the intercept and the slope of the linear function; ALARM, instead, derives dT (as previously mentioned) after converting the radiometric temperature in aerodynamic temperature, having no need to identify hot or cold pixels, though requiring the vegetation temperature profile and the satellite's sensor zenith view angle. Furthermore, leaf area index (LAI), canopy height, fractional cover and leaf angle distribution along the canopy are also required to obtain the roughness length for sensible heat (z_{oh}). The evaporation fraction (Λ) was used to integrate the instantaneous ET value at the time of overpass over the day. A first ET comparison was conducted by keeping the standard assumptions and empirical relationships used by each model and averaging the ET of the six pixels surrounding the lysimeter. The daily ET for the three date increases from 5.00 to 7.48 mm for the lysimeter, from 4.00 to 5.60 mm for SEBAL, and from 4.38 to 5.11 mm for ALARM. The results of the comparison at each date showed that ALARM underestimated the daily lysimeter ET by 8 percent on March 22, by 16 percent on April 7 and by 33 percent on April 23, while SEBAL underestimated the daily lysimeter ET by 4 percent on March 22, by 15 percent on April 7 and by 37 percent on April 23. A second comparison was conducted after: accounting for the variability in LAI among the six pixels; removing the night-time ET of the lysimeter; selecting manually the hot and cold pixels in SEBAL, rather than automatically; and using a locally derived relationship between LAI and NDVI. The new daily ET for the three dates increased from 4.74 to 6.85 mm for the lysimeter, varied from 4.43 to 4.97 mm for SEBAL, and increased from 4.82 to 5.34 mm for ALARM. The results of the second comparison showed that the modified ALARM overestimated ET by 1 percent on March 22 and underestimated ET by 6 percent and by 22 percent on April 7 and on April 23, respectively. The modified SEBAL underestimated ET by 0.7 percent, by 10 percent and by 35 percent on March 22, April 7, and April 23, respectively. Some of the conclusions indicate that: the extent of underestimation by the two models increases with the increase of ET; ALARM requires air temperature for each pixel; the selection of the hot and cold pixels in SEBAL is crucial to the accuracy of ET.

Remote sensing determinations of ET were carried out in **Syrian Arab Republic (the)** over a palm and olive mix orchard in the Palmyra oasis. RS ET and field eddy-covariance ET were carried out during the years 2003, 2004 and 2005 by a team of scientists of the Arab Center for the Studies of Arid Zones and Dry Lands (ACSAD). The RS ET was derived using the SEB approach (Eq. 3) with: LST, albedo and NDVI coming from MODIS; incoming solar radiation coming from Solar Data Intelligent System (from METEOSAT). The net radiation (R_n) calculation followed Eq. (4), with typical parameterization for the incoming and outgoing long-wave radiation. The sensible heat flux (H) calculation followed Eq. (9), with typical parameterization and stability correction for the aerodynamic resistance (r_{ah}), while dT (difference between two near-surface heights) was derived after converting the radiometric temperature in aerodynamic temperature through the ALARM model (Analytical Land and Atmosphere Radiometric Model) developed by Crago (1998) and Suleiman and Crago (2002a; 2002b). The soil heat flux (G) was taken as 20 percent of R_n . It can be realized that the calculation procedure does not follow strictly any of the model described in this report, nevertheless it is still a SEB approach and represents one of the few cases of RS ET determination in the country. The average daily ET from RS and field eddy-covariance, for 152 days, resulted in 5.61 mm and 5.67 mm, respectively. The RMSE was 11.45 percent and the MBE was -0.5 percent indicating a slight underestimation (due to underestimation in R_n). These very encouraging results provided an important contribution to the water resources management of the Palmyra oasis. The same team of scientists at ACSAD compared the reference ET (ET_o) provided by WaPOR and the ET_o calculated through the Penman-Monteith (PM) equation with field meteorological data coming from a well maintained agro-meteorological station, operated by the University of Damascus. The PM calculation was carried out through the FAO software 'ETo calculator' and its comparison with WaPOR ET_o spanned the period 30 November 2020 – 31 August 2021. The comparison showed a very close matching during the winter period while an overestimation by WaPOR, of about 15 percent, was observed during the warmer seasons (from May to August). Nevertheless, the overall RMSE was of 0.85 mm d⁻¹. This can be considered a very good result with very important implications for the irrigated agriculture of the country (and of the NENA Region as well), due to the very limited presence of agro-meteorological field stations and often not well maintained.

Studies conducted in **Tunisia** aimed at correlating wheat yield (a strategic crop for the country's food security) with the evaporative stress index (ESI), with rainfall (P), with leaf area index (LAI) and with land surface temperature (LST), derived through satellite remote sensing over the years 2002-2013. The area under investigation was within the northern part of the country where more than 90 percent of durum wheat production in Tunisia comes from. The crop is cultivated under rainfed conditions and, therefore, the most limiting factor for wheat yield and its inter-annual variability is due to insufficient and irregular rainfall patterns over time and space, which is reflected in the crop water status. The degree of correlation between yield and the RS indexes provides insights on the crop response to soil moisture for yield forecast purposes. Yield data were obtained from the statistical department of the Ministry of Agriculture. ESI was computed as a standardized anomaly of the ET Ratio (ET/ETR), where ET was derived through the ALEXI surface energy balance model. ESI effectively integrates information on both LST and LAI, which are critical inputs to the physically-based modeling system. Daily rainfall was obtained from CHIRPS (v 1.8 dataset). LAI maps were obtained from MODIS at 1km ground resolution, with gap-filling according to Gao *et al.* (2008). LST was also obtained from MODIS. The results of the study indicated that ESI provided the earliest signal of yield anomalies, with correlations reaching maximum values during the booting/heading growth stage. Correlation strength was regionally variable, with higher correlations in semi-arid regions and lower correlation in coastal governorates where rainfall is more reliable year-to-year. During the dry year of 2002, LST recorded the highest anomalies, capturing the impacts of the drought on canopy and soil temperatures. In contrast, during the wet years of 2003 and 2004, LAI anomalies showed the highest value during the grain filling period, one of the most sensitive stages of the wheat crop. Standardized CHIRPS anomalies were able to explain the yield variability in relation to rainfall variability in the early growing phases of the crop (seedling-tillering). In fact, a higher effectiveness of precipitation was observed when occurring at the beginning of the crop season (crop establishment) as compared to subsequent rainfall. This result is consistent with the findings of Laatiri *et al.* (2010) that demonstrated the substantial effect of the autumn precipitation on wheat yield and the lower contribution of the spring rainfall, in northern Tunisia. Overall, ESI appears to be a very good indicator to explain wheat yield variability, though its performance is higher in semi-arid governorates where soil moisture is the most important factor limiting crop yields. It is hypothesized that a combination of multiple indicators, including ESI, LAI, LST and P, may provide an improved yield estimate in terms of timing and accuracy, and this will be a topic of future research.

6.2 SIMS (Satellite Irrigation Management Support)

With support from the NASA Applied Science Program, Melton *et al.* (2012) have developed the NASA Satellite Irrigation Management Support (SIMS) framework, synthesizing data from multiple sensors to enhance the utility and accessibility of satellite data to derive crop ET for irrigation management and scheduling.

For the time being, SIMS crop ET (ET_{c-SIMS}) data are available across the Western United States of America, where agriculture is typically the largest user of water, groundwater is rapidly depleting in multiple basins that support agricultural production, and electricity used for pumping is accelerating. Over time, it is expected that SIMS would cover the entire United States of America and eventually extend to other regions of the world. In the interim, the SIMS application programming interface (API), currently allows the user to define any area of interest globally, specify a crop type, and retrieve a time series of satellite derived basal crop coefficient (K_{cb}) values calculated from satellite measurements of the crop growth stage and condition. The API parameterizes the SIMS equations using the crop type specified by the user, and can be applied over any agricultural area globally.

Two key considerations are at the base of the SIMS rationale: (i) an effective irrigation schedule requires that near real-time information is available to the agricultural producer and, therefore, the estimates of crop ET (ET_c) should adopt algorithms compatible with full automation; (ii) rather than deriving ET_c through the surface energy balance approach (requiring RS data in the thermal band that are only available at field scales from Landsat at

present), ET_c can be obtained from the NDVI (requiring RS data in the red and near-infrared bands) using a well-established and robust method (Allen *et al.*, 1998), i.e. by the product of reference evapotranspiration (ET_o) and specific crop coefficients (K_c), highly suitable for irrigation scheduling, with ET_o derived from either agricultural weather networks (e.g. the California Irrigation Management Information System –CIMIS–, the Columbia-Pacific Northwest region meteorological network –AgriMet–, and the Arizona Meteorological Network –AZMET) or other sources of gridded meteorological data.

SIMS currently uses Google Earth Engine to automate the processing of the satellite inputs and to integrate the satellite and surface observations in near real-time, but can also be run on any local or cloud-based compute resource.

More specifically, ET_c is derived through the following equation (following Allen *et al.*, 1998)

$$ET_c = ET_o \cdot K_c \quad (93)$$

with ET_o being the reference ET calculated by the PM equation using solar radiation (Rs), air temperature (Ta), relative humidity (RH), wind speed (u) and according to the FAO-PM formulation (Allen *et al.*, 1998), and with

$$K_c = K_s \cdot K_{cb} + K_e \quad (94)$$

where K_{cb} is the basal crop coefficient representing the ratio between crop transpiration and ET_o , K_e is a soil evaporation coefficient representing the ratio between soil evaporation and ET_o (Allen *et al.*, 1998, 2005; Allen, 2011) and K_s is a dimensionless stress coefficient whose value (ranging from 1, no stress, and 0, full stress) is dependent on available soil water in the root zone and soil and crop salinity related characteristics (Allen *et al.*, 1998).

SIMS derives ET under well-watered (unstressed) conditions with minimal soil evaporation using satellite data to account for the current crop stage, condition and fractional cover, and a gridded soil water balance model to account for soil evaporation resulting from precipitation, such that:

$$ET_{c-SIMS} = ET_o \cdot (K_{cb} + K_e) \quad (95)$$

Two steps are involved in SIMS K_{cb} derivation: (i) first, to convert satellite NDVI to crop fractional canopy cover (F_c) based on a generalized empirical equation derived in literature (Trout *et al.*, 2008; Johnson and Trout, 2012); (ii) then, to convert F_c to K_{cb} by considering a vegetation density coefficient (K_d), as developed by Allen and Pereira (2009), and further described by Pereira *et al.* (2020) and Wang *et al.* (2021), which accounts for the cases when plant density or leaf area fall below full ground cover, often when LAI < 3.

SIMS relates F_c to NDVI by the following equation after Johnson and Trout (2012):

$$F_c = 1.26 \cdot NDVI - 0.18 \quad (96)$$

Then, according to Allen and Pereira (2009), K_{cb} relates to F_c and K_d through the following equation:

$$K_{cb} = K_{c,min} + K_d \cdot (K_{cb,full} - K_{c,min}) \quad (97)$$

with

$$K_d = \min \left[1, M_L \cdot F_{c,eff}, F_{c,eff}^{\left(\frac{1}{1+h}\right)} \right] \quad (98)$$

where: $K_{cb,full}$ is the estimated K_{cb} during nearly full ground cover (or LAI >3); $K_{c,min}$ is the minimum K_{cb} for bare soil (taken equal to 0.15 for typical agricultural conditions); $F_{c,eff}$ is the effective fraction of ground covered or shaded by vegetation near solar noon (ranging from 0.01 to 1); M_L is a multiplier on $F_{c,eff}$ describing the effect of canopy density on shading and on maximum relative ET per fraction of ground shaded (ranging from 1.5 to 2); and h is the mean height of the vegetation in m. As a simplification, SIMS uses F_c rather than $F_{c,eff}$ to calculate K_d .

To derive NDVI, SIMS uses data from Landsat 8 and Landsat 9 (and data from Landsat 5 and 7 for studies prior to November 2011 and December 2021, respectively), and Sentinel-2A/2B. SIMS is able to ingest Landsat Collection 2, Level 2 surface reflectance data products from USGS, as well as top-of-atmosphere (TOA) reflectance data

from USGS, and then apply fully automated atmospheric corrections using the LEDAPS (Masek *et al.*, 2006) and L8SR (Roy *et al.*, 2014) software packages to calculate top-of-canopy (TOC) surface reflectance and screen out clouds within the satellite scene.

After the automated atmospheric correction, cloud masking, and gap-filling procedures, SIMS maps of F_c and K_{cb} are derived every eight days and interpolated to a daily timestep at spatial resolutions of 30 m. After deriving K_e from precipitation using a soil water balance model (Allen *et al.*, 1998), ET_{c-SIMS} is derived through Eq. (95).

However, in scheduling irrigation, other factors beyond ET_c need to be considered, including soil type, salinity and leaching fraction, irrigation system type, distribution uniformity, root zone soil moisture, among others. Therefore, information from SIMS has been integrated with a browser-based irrigation management decision support system that serves water managers and agricultural producers. Presently, SIMS is integrated with the CropManage platform,⁴⁷ developed by the University of California, Division of Agriculture and Natural Resources.

SIMS has also been included in the suite of models available from OpenET (openetdata.org; see chapter 6.5) due to the ET_c reliability and accuracy across irrigated agricultural lands. While a more comprehensive uncertainty discussion of remote sensing based ET models and inter-comparisons between models and field data will be reported later in chapter 7, here we highlight the results of some of the SIMS accuracy assessments conducted in field trials.

Relative to actual ET measured in commercial fields of 15 major California crops (including vegetables, field crops, trees and vines), and over six years, SIMS has shown a mean absolute error (MAE) within +/-10 percent, for seasonal total ET_c of well-watered crops, and within +/-15 percent for all crops (Pereria *et al.*, 2020).

On a daily basis, MAE increases to 16 percent for annual crops and 21.7 percent for perennial crops. ET_c errors on seasonal scale are reduced to 8 percent when K_s and K_e are calculated via soil water balance models (Allen *et al.*, 1998). In fact, SIMS tends to underestimate ET_a during the initial development stage of field crops due to the effects of soil evaporation, since irrigation is not currently considered by the gridded soil water balance model. Overall, SIMS shows the highest ET_c accuracy for well irrigated crops during the mid- to late-season, when the crop canopy is fully established.

We may thus conclude that the major strengths of SIMS are computational efficiency, full automation over large areas, and the ability to derive consistent, reasonably accurate canopy cover and ET_c values under well irrigated conditions. Finally, the integration of SIMS with CropManage provides growers (both on personal computers and smart phone Apps) with a complete set of information to make data-driven decisions about irrigation (and nutrient) management.

6.3 IrriWatch

IrriWatch is a commercial web-based platform (operated on both personal computer and smart-phone Apps) developed by Wim Bastiaanssen to provide farm managers, food processors and agricultural supply chain with daily guidance in key on-farm processes such as irrigation, fertilizers and crop protection.⁴⁸ It also serves public agencies responsible for irrigation schemes to monitor water consumption and to support irrigation priority setting and water allocation decisions. It also estimates net soil carbon capture for carbon trade purposes being part of climate-smart agriculture and regenerative agriculture.

IrriWatch analyses every 10 m x 10 m of user-defined fields, with a daily revisit time, using RS data coming from Landsat, EcoStress, VIIRS and Sentinel and advance data processing techniques (such as irrigation tiles). The primary engine of IrriWatch is SEBAL (see chapter 2.4.1) converting satellite measurements of crop temperature, vegetation cover, solar radiation and other crop parameters into actual crop evapotranspiration (and transpiration separately) and related parameters.

⁴⁷ University of California. CropManage. <https://cropmanage.ucanr.edu/>

⁴⁸ IrriWatch. 2022. <https://irriwatch.com/en/>

Focusing on the Irrigation component, the IrriWatch technology senses soil moisture content and actual soil water potential checked against the crop critical value, beyond which stress is triggered, and provides irrigation scheduling advice for every 10m x 10m. Furthermore, weather forecasts in combination with today's satellite measurements of soil moisture status are then used to forecast soil moisture conditions for the next eight days to be compliant with irrigation systems of South Asia.

In practice, IrriWatch provides every morning a daily irrigation advice to growers, ranking fields requiring irrigation based on the priority to needed water (urgent irrigation; irrigation; no irrigation; over-irrigation; no vegetation) using color code. A minimum value required to replenish daily crop water use will be recommended for each field needing irrigation. In addition, a maximum value will be provided to refill the root zone to a certain pre-defined moisture level to be set by the farm managers. This can be near field capacity but also near to the point of easily available soil moisture in case deficit irrigation is practiced. But the final decision of how much water to actually apply is made by growers and their consultants that can factor in additional agronomic and economic conditions.

Instead of a uniform irrigation amount, it is thus possible to modify the irrigation by management zones. This recognizes local crop and soil variability. In fact, it is possible to upload local soil maps to consider differences of soil physical characteristics such as storage of soil moisture.

Users of IrriWatch can subscribe for three types of "packages": (i) *Premium*, providing maps of soil water potential, soil moisture and ET values, along with information on daily crop production and information on irrigation scheduling and irrigation performance; (ii) *Dryland*, meant for rainfed farmers with information on crop production, the impact of droughts, soil moisture in the root zone and crop fertilizer status and (iii) *Climate Smart Agriculture* that includes greenhouse gas emissions, carbon capture in soil and the resource efficiencies of light, water and Nitrogen .

Expected levels of ET accuracy are within the range of ± 5 percent on a seasonal basis.

As up the present, IrriWatch is serving more than 200 000 individual fields across more than 60 countries around the world.

Further information on IrriWatch can be found on its portal.⁴⁹

⁴⁹ IrriWatch. 2022. <https://irriwatch.com/en/>





7. UNCERTAINTY REVIEW ON RS ET DETERMINATIONS

The present chapter addresses, in part, the issue of uncertainties involved in satellite remote sensing (RS)-based determination of evapotranspiration (ET). Uncertainties (also referred to as error) are unavoidable in all types of models and in any other kind of determinations and measurements. Being aware of the magnitude of uncertainty allows one to properly identify and select the determination method most suitable for a given application, so that uncertainties are likely to be within acceptable limits for sound quantitative analysis leading to appropriate decisions. In fact, the issue of error and uncertainty is generally the first question asked regarding a model or method for determining ET. Decision-makers and policymakers ask "how good is the method" or "how accurate is the method" or "how far off can the estimates be?" These very important questions are in regard to uncertainty and reproducibility.

After illustrating some of the most adopted methods for analyzing uncertainty, the chapter will provide some results of tests conducted to compare RS ET determinations with field ET measurements, which are, in turn, subject to error. The results of these comparisons will then be discussed within the context of the various models presented in chapter 2.4.

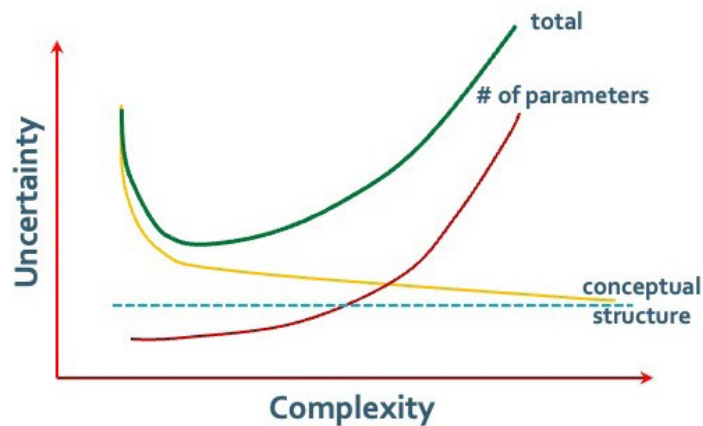
The chapter will close with a special session devoted to the elaboration of some criteria for determining what acceptable limits of uncertainty are for given types of applications.

7.1 Background on methods for addressing and applying uncertainty analysis

It is appropriate to start this chapter by recalling that the RS determinations of ET are based on mathematical models, and therefore they are a 'simplification' of reality. A real system (e.g. hydrological, social, agricultural, biological, etc.) is extremely complex, and through 'modeling' we try to identify and formulate a set of algorithms that best simulate those 'status' (or structural components) and 'processes' that best capture most of the real system, accounting of course for the objective of the modeling work.

The more we simplify the system (through its structure conceptualization), the higher the risk of system misrepresentation by the model, and therefore the higher the uncertainty. Similarly, the more we increase the model complexity in order to more closely represent the real system (e.g. incorporating more processes and algorithms), the larger the risk of uncertainty due to the introduction of increasing numbers of parameters, each of which can have its own error and uncertainties. The qualitative relationship between uncertainty and complexity in modeling is graphically expressed in Figure 8 (Passioura, 1996; Affholder *et al.*, 2012).

Figure 8: Relationships between uncertainty and complexity in modeling



Note: The yellow line represents the change in uncertainty of the model conceptual structure with increasing complexity. The red line represents the change in uncertainty with the increase of the model number of parameters. The green line represents the total change in uncertainty of the model (inclusive of conceptual structure and number of parameters).

Source: Passioura J.B. 1996. *Simulations models: science, snake oil, education, or engineering?* Agron. J., 88: 690-694. Affholder F., Tittone P.A., Corbeels M. and Roux S. (2012). Ad hoc modeling in agronomy: what have we learned in the last 15 years? Agron. J., 104(3): 735-748.

It is evident that there is an optimal balance between a sufficiently complex representation of the model (its conceptual structure) and the number of parameters required for such a complex representation. While on the one hand, it is not an easy task to identify such an optimal balance, on the other hand, it is clear that a very sophisticated model for a system is not necessarily better than a simpler model in regard to the accuracy of results.

We observed in chapter 2 that there is a relatively large number of models, each determining ET with multiple purposes (e.g. drought monitoring, water resources management, irrigation scheduling, etc.), addressing different scales (farm-field, basin, global), and having different conceptual structures (e.g. Surface Energy Balance; Penman Monteith, Psychrometric Satellite Approach, etc.) requiring different numbers of parameters.

We will now provide an overview of the most common methodological approaches to analyze the uncertainty in the ET determinations of these RS models, considering that uncertainty stems from three major sources: inadequate model structure, poorly defined parameters within the model's algorithms (e.g. inadequate calibration), and model input errors. To have everybody on the same page, the reader should be acquainted with a few terms, notations and definitions, such as those reported in Box 1.

Box 1 – Some terms, notations and definitions in uncertainty analysis

Error: is the difference (or deviation) between the measured value and the 'true value' of the variable being measured. As in reality the 'true value' is unknown, we generally refer to the *expected value* of a measured quantity (x), determined as its *best estimate* (x_{best}) associated with an *error* ($\pm\delta x$) so that the *expected value* lies somewhere between ($x_{\text{best}} - \delta x$) and ($x_{\text{best}} + \delta x$), with an associated *confidence*, or *level of probability* (e.g. 95 percent). Thus,

$$x = x_{\text{best}} \pm \delta x \text{ with a given level of probability}$$

where x_{best} and δx are obtained through repeated measurements of the same quantity, and the *level of probability* is obtained by knowing the statistical law governing the measurement process (e.g. 'Gaussian', 'Binomial' or 'Poisson' probability distributions).

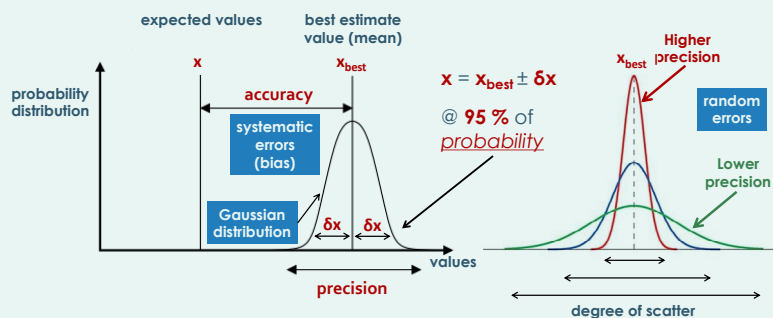
Precision: is the closeness of agreement between values obtained by repeated measurements. A measurement is precise if the readings cluster closely together (low extent of reading scatter), without reference to the *true* value. It is associated with the *random error*, i.e. reading fluctuations in either direction (+/-) of the measured value. To increase the precision requires increasing the number of repeated measurements.

Accuracy: is the closeness of agreement between a *measured value* and a *true* or *expected* value. It is associated with the *systematic error* (or *bias*), i.e. reproducible inaccuracies that are consistently in the same direction. To increase the accuracy requires calibration against a standard or reference value.

A way to visualize low and high degrees of measurement precision and accuracy, in the different combinations, is provided by the following sketch:



A way to visualize the different variables involved in the precision and accuracy determinations with repeated measurements (values) obeying a Gaussian probability distribution is provided by the following figure:



The Gaussian (or normal) probability function is expressed by the **standard deviation** (s)

$$s = \sqrt{\frac{\sum_{i=1}^n (x_i - \bar{x})^2}{(n - 1)}}$$

► **Box 1 continue**

with: x_i being the individual measurements, \bar{x} is the mean of the repeated measurements, calculated as

$\bar{x} = \frac{\sum_{i=1}^n x_i}{n}$ and representing the best estimate (x_{best}) of the expected value (x), and n is the total number of repeated measurements.

For the same number of measurements, the higher the precision the smaller the standard deviation.

For a large enough sample, approximately 68 percent of the readings will be within one standard deviation of the mean value, 95 percent of the readings will be in the interval $x \pm 2s$, and nearly all (99.7 percent) of readings will lie within 3 standard deviations from the mean.

Uncertainty: the interval within which the *expected value* can be considered to lie with a given level of confidence or probability. It represents the degree of confidence we have in our measurements (or the doubt that exists about the result of the measurements), and is influenced by accuracy (systematic error or bias) and precision (random errors) of the measurement, as well as by the measurement method. Thus, the *expected value* (x) should be expressed as

$$x = x_{\text{best}} \pm \text{uncertainty} \approx \bar{x} \pm \text{uncertainty}$$

The uncertainty of the expected value can be also expressed as percent $\left(\frac{\text{uncertainty}}{x_{\text{best}}} \cdot 100 \right)$

In the case of repeated measurement, with a well calibrated instrument (to minimize the systematic error), the uncertainty is expressed as the *standard deviation of the mean*, often called the *standard error (SE)*

so that

$$SE = \frac{s}{\sqrt{n}}$$

$$x = \bar{x} \pm 2SE \text{ at a level of confidence of 95 percent}$$

The term **error** (without being qualified, e.g. random or systematic) is often used as synonym of uncertainty as it generally refers to SE.

The **number of significant figures** when reporting a measurement value has to be properly defined as it implies an approximate relative uncertainty, i.e.:

1 significant figure suggests a relative uncertainty of about 10 percent to 100 percent

2 significant figures suggest a relative uncertainty of about 1 percent to 10 percent

3 significant figures suggest a relative uncertainty of about 0.1 percent to 1 percent

Source: The Language of Measurement' published by the Association for Science Education (ASE), ISBN 978086357424545)

Some considerations need to be highlighted when dealing with ET determinations by RS. First of all, they cannot be assimilated specifically and completely to laboratory or field measurements and, strictly speaking, they cannot provide 'repeated measurements' of the same quantity under the same conditions. Moreover, the ET determination is the modeling resulting from the use of multiple input variables, such as measurements of radiation of different bands of the solar and thermal spectrum (e.g. **in the visible, infrared, near-infrared, etc.) derived** from multiple sensors (e.g. **multi-spectral optical sensor, thermal radiometers, etc.) and often installed on different satellites. Therefore, there is a need to estimate a compounded uncertainty on ET resulting from the propagation of errors for each individual measurement.**

As an example, if we have a model formulating λE as a function of a certain number of input variables ($x_1, x_2, x_3, \dots, x_n$), i.e.

$$\lambda E = f(x_1, x_2, x_3, \dots, x_n) \quad (99)$$

for which we would like to determine the error ($\delta\lambda E$), with each variable x ($x_1, x_2, x_3, \dots, x_n$) having their own error δx ($\delta x_1, \delta x_2, \delta x_3, \dots, \delta x_n$) based on **technical specifications or experience**, then, the overall error in λE can be obtained as (Taylor, 1982).

$$\delta\lambda E = \sqrt{\left(\frac{\partial\lambda E}{\partial x_1}\right)^2 \delta x_1^2 + \left(\frac{\partial\lambda E}{\partial x_2}\right)^2 \delta x_2^2 + \left(\frac{\partial\lambda E}{\partial x_3}\right)^2 \delta x_3^2 + \dots + \left(\frac{\partial\lambda E}{\partial x_n}\right)^2 \delta x_n^2} \quad (100)$$

However, the assumption behind Eq. (100) is that the errors (δx) follow the Gaussian probability distribution and are independent of each other (i.e. they are uncorrelated), and this is not necessarily the case in RS measurements. For example, error in spatial registration of a satellite image will impact albedo derived from shortwave bands in a similar way as it impacts surface temperature derived from longwave bands. Similarly, the vegetation index NDVI used to estimate aerodynamic roughness can be impacted by error in shortwave bands or error in atmospheric corrections similar to how albedo is impacted. We'll see later how to estimate the propagation of errors avoiding the risk of any possible correlations between errors.

One important implication of Eq. (100) is that generally, depending on their magnitude, only a few of its terms (causing errors of high magnitude) are the main contributors to the overall uncertainty, so that other terms (causing errors of low magnitude) can generally be ignored. In fact, if one of the terms causes uncertainty that is more than three times greater than that for the other terms, then it can be considered to be the term that is determining the largest uncertainty. This shortcut allows saving time in model development and calibration without losing substantial accuracy in the estimate and overall uncertainty.

The number of sensors on the various satellites used for RS of ET is quite large and the reader is referred to the websites such as those of the Committee on Earth Observation Satellites (CEOS), of the National Air and Space Administration (NASA) and the European Space Agency (ESA) for specific instruments and measurements.⁵⁰

Methods to determine uncertainty. When there are doubts regarding the correlation of parameters and error, we can use the 'method of moments', which does not require the specification of the probabilistic distributions of the repeated measurements (Rushidi and Kafrawy, 1988). This method calculates the uncertainty in the output (e.g. $H, \lambda E$) using the propagation of the partial derivatives of output vs. the input variables and their respective covariance (Hansen, 1982).

Using as an example the same λE function of Eq (99), the method of moments estimates the compounded error in λE , resulting from the propagation of error from the input variables, as

$$\delta\lambda E = \sqrt{\sum_{i=1}^n \left\{ \left[\left(\frac{\partial\lambda E}{\partial x_1} \delta x_1 \right)^2 + 2 \cdot r_1^2 \cdot \left(\frac{\partial\lambda E}{\partial x_1} \delta x_1 \right) \left(\frac{\partial\lambda E}{\partial x_2} \delta x_2 \right) \right]_1 + \left[\left(\frac{\partial\lambda E}{\partial x_2} \delta x_2 \right)^2 + 2 \cdot r_2^2 \cdot \left(\frac{\partial\lambda E}{\partial x_2} \delta x_2 \right) \left(\frac{\partial\lambda E}{\partial x_3} \delta x_3 \right) \right]_2 + \dots \right\}} \quad (101)$$

where the new terms introduced ($r_1^2, r_2^2, r_3^2, \dots, r_n^2$) are the coefficients of determination of the cross-correlations between input variables taken as pairs of all combinations.

The method of moments has been utilized by Fisher *et al.* (2008) to analyze the error propagation on λE , as derived through the PT-JPL model, and the sensitivity analysis of the model, with four input variables: net radiation (R_n), Normalized Difference Vegetation Index (NDVI), maximum air temperature (T_{max}), and atmospheric water vapor pressure (e_a). Attributing 10 percent and 25 percent error for each of the four input variables, the resulting compounded error on E was 11.3 percent and 28.3 percent, respectively. Subsequently, the authors varied the error (set at 10 percent) of only one input at a time, while holding the error for the other inputs constant at zero. The major result of the uncertainty analysis was the heavy dependency of PT-JPL on the accuracy of R_n . NDVI was second in total error contribution. Minimal error contribution was coming from T_{max} and e_a .

⁵⁰ CEOS. 2023. <https://ceos.org/>

CEOS. 2023. The CEOS Database. CEOS EO Handbook - Catalogue of Satellite Instruments. <https://database.eohandbook.com/database/instrumenttable.aspx>

CEOS. 2023. The CEOS Database. CEOS EO Handbook - Measurements. <https://database.eohandbook.com/measurements/overview.aspx>

NASA. Earth Data - Open Access for Open Source. <https://www.earthdata.nasa.gov/>

The European Space Agency. <https://www.esa.int/>

It is important at this point to clarify the difference (and similarity) between 'sensitivity analysis' and 'uncertainty analysis'. In a broad meaning, a sensitivity analysis (Saltelli *et al.*, 2008) aims to describe how much the model output values are affected by (i.e. how sensitive the model is to) relative changes in model input values. More specifically, the sensitivity analysis aims to identify the relative contribution of each error source to the overall uncertainty in the model prediction and therefore to pinpoint which variables are most influential in the determination of ET. The analysis can examine the effects of changes in a single input variable, assuming no changes in all other inputs, or it examines the combined effects of multiple sources of error.

The uncertainty analysis (Morrison, 2021), instead, attempts to describe the compounded uncertainty of model predictions as affected by multiple sources of uncertainty in model input. The quantification is often performed by estimating statistical quantities of interest such as probability distribution, mean and standard deviation that describe the likely error and uncertainty in inputs and in model algorithms and parameters.

In fact, sensitivity and uncertainty analyses are run in tandem, where the sensitivity analysis is used to reduce the number of variables to be involved in the uncertainty analysis (Saltelli *et al.*, 2000). Several methods are available to perform sensitivity and uncertainty analysis, including Maximum Likelihood (Rossi, 2018), Monte Carlo (Kroese *et al.*, 2014), and the method of moments previously described, each one with its own merit and drawbacks.

The most commonly used method in modeling appears to be the Monte Carlo method, which simulates numerical values that follow a parameterized probability distribution through repeated random sampling (e.g. like random errors following the Gaussian probability distribution). It is considered very powerful as it can simulate almost any type of uncertainty, particularly when associated with a valid random generator, because the nowadays high processing capacity of computers allows very large numbers of simulation runs. However, when the per-pixel distributions of ET appear to be non-Gaussian (Cawse-Nicholson *et al.*, 2020) and therefore precision and accuracy may not be sufficiently adequate metrics to describe uncertainty, an alternative method can be the one of "quantiles" (Cawse-Nicholson *et al.*, 2020).

The method of moments, though, is also a powerful technique as being very efficient and not requiring the specification of the probabilistic distributions of the uncertainties in input variables (Rushidi and Kafrawy, 1988). It is usually based on a multivariable Taylor expansion of the system function that, in the case of the RS ET models, is truncated at the second-order moment (i.e. beyond the mean, it takes into consideration variance and covariance), as the higher-order moments (e.g. skewness and kurtosis) are considered to be negligible.

Sources of model errors. We need to be aware that the RS determination of ET is subject to several sources of error that need to be considered comprehensively. Typically, and among others, we may have: spatial and temporal error in the assessment of cloud, aerosol, dust, and smoke contamination of the atmosphere affecting the surface net radiation; the non-uniform underlying land surface affecting wind patterns, roughness and Land Surface Temperature; daily variation of the atmospheric stability conditions affecting the aerodynamic conductance; insufficient spatial and temporal representation of some meteorological variables like wind speed and vapor pressure of the atmosphere, which influence aerodynamic and canopy conductance, respectively; etc.

Here we provide the magnitudes of accuracy for some typical RS measurements or determinations.

Uncertainty in Land Surface Temperature (LST) measurements. The thermal band of MODIS (1 km resolution) provides an expected absolute accuracy of surface temperature in the range of 0.3-0.5 K over oceans and of 1 K over land (MODIS Brochure, 2000). Sekertekin and Bonafoni (2020) reported an accuracy of LST derived from Landsat varying between 0.1 K to 0.4 K (with a typical mean accuracy value of 0.25 K).

Uncertainty in Radiation measurement. According to Sai Krishna *et al.* (2014), the daily net radiation under clear sky derived from Clouds and Earth's Radiation Energy Systems (CERES) has a typical accuracy of 17-25 W m⁻² for downward long-wave radiation, and 73-89 W m⁻² for downward short-wave radiation, while Mira *et al.* (2016) reported a global uncertainty in surface net radiation (Rn) derived from Landsat in the range of 40-100 W·m⁻².

Error in radiation measurements can vary over time with atmospheric conditions such as haze, aerosols and humidity, and the means to measure and to correct for these. In addition, the detection of clouds and cloud shadows, even thin clouds, can introduce errors in radiation measurements, especially when cloud detection is automated, which is required for most web-based RS systems.

Uncertainty in time integration/interpolation of ET. The determination of the RS input variables for ET computation is mostly instantaneous at the time of the satellite overpass. Therefore, additional sources of uncertainty are in the time integration of ET over the daytime hours, and the typical time interpolation of daily ET values over the period in between two satellite overpasses (e.g. like in the case of Landsat having 8 days of revisit cycle).

The important passage of up-scaling the instantaneous ET to daily values has been addressed differently by different authors. For example, originally Bastiaanssen *et al.* (2005) assumed the instantaneous ratio between the latent heat (λE) and the available energy ($R_n - G$), indicated as evaporative fraction (Λ), to be constant during the day (see chapter 2.4.1). Similar assumption was retained by Allen *et al.* (2007a), with the major difference that the instantaneous ratio was taken between actual ET and the reference ET (E_{Tr}), indicated as the reference ET fraction (E_{TrF} ; see chapter 2.4.2). Recall that E_{Tr} refers to the reference ET using alfalfa (ASCE-EWRI, 2005) and E_{To} refers to reference ET using grass (Allen *et al.*, 1998) and that there is a relationship between the two (see chapter 2.4.2 or later description).

The use of reference ET fraction instead of the evaporative fraction is considered an improvement in the accuracy of ET determinations, particularly under arid climates, due to afternoon advection or increased afternoon wind speed, which tend to increase ET and not being captured if considering the available energy only (Allen *et al.*, 2007a). However, this improvement has not been observed under land use different from irrigated agriculture (e.g. Cammalleri *et al.*, 2014).

Additionally, error in weather parameters input to the calculation of E_{Tr} (or of E_{To}), either from point ground measurements or from gridded weather data sets, can introduce some uncertainty in the reference ET estimate and therefore into the final ET estimate. The error produced by daily upscaling of E_{TrF} and error produced by the reference ET (either E_{Tr} or E_{To}) determinations are estimated to be on the order of +/- 10 percent and are generally considered to be randomly distributed around 0.0 (Allen *et al.*, 2011a).

Additional methods based on 'fraction' with respect to other climatic variables, like extraterrestrial solar radiation (SR), incoming shortwave radiation (R_s) and net radiation (R_n), among others, have been proposed and tested over time (e.g. Ryu *et al.*, 2012; Cammalleri *et al.*, 2014; Liu, 2021). The overall conclusion on the daily ET up-scaling from instantaneous values was that all methods can be accurate as their performance will depend on the variability of the sky transmissivity around the time of the satellite overpass and on the availability of data for the area of interest (Liu, 2021).

Nevertheless, where possible, the E_{TrF} remains a solid method as it is anchored to the reference ET. In fact, SEBAL, METRIC, SSEBoP and PT-JPL all utilize the "fraction of reference ET" (either E_{TrF} or E_{ToF}).

The second important passage of interpolating between consecutive satellite overpasses has been illustrated by Allen *et al.* (2010a). These authors indicate that this interpolation of ET information between image dates represents '*at least half the total effort in producing a quantitative ET product*'. While the numerical interpolation, per se, is not a problem (splines have shown to be perfectly feasible for this purpose), a major challenge in the interpolation is to capture evaporation that may take place following episodic precipitation and/or irrigation events occurring between overpass dates. In fact, the ET retrieval may be biased 'high' or 'low' when the overpass respectively 'follows' or just 'precedes' one of these events. To account for these biases, one approach is to adjust the 'background' soil evaporation of the processed images. The 'background' evaporation for bare soil is computed using a gridded FAO-56 two-stage evaporation model of Allen *et al.* (1998) with modification to account for 'flash' evaporation from the soil skin (Allen 2010) or some other soil evaporation model such as Hydrus⁵¹ or DAISY.⁵² The soil evaporation model is on a daily time step using spatially distributed precipitation, reference ET, and soil properties. In addition to the background evaporation, the interpolation also involves the treatment of clouded areas of images, using cloud masking techniques. The reader is referred to Allen *et al.* (2010a), Kjaersgaard *et al.* (2011), and Singh *et al.* (2020), for further details on the method addressing the interpolation challenges.

⁵¹ Finite element model for simulating the one-dimensional movement of water, heat, and multiple solutes in variably saturated media.

⁵² Danish Soil-Plant-Atmosphere System model.

Georegistration error. In addition to the radiometric sensor and atmospheric error, additional errors in RS readings can come from errors in spatial registration. In other words, how well each particular pixel is mapped to the correct actual area on the earth. The spatial error varies with satellite and location. Common expected spatial error for Landsat, for example, ranges from 12 to 15 m prior to about year 2021 and 8 m beginning in year 2021 (Storey *et al.*, 2019). The processes of georeferencing (alignment of imagery to its correct geographic location) and orthorectifying (correction for the effects of relief and view direction on pixel location) are components of geometric correction necessary for the accurate positioning of an image. Imagery can be positioned relative to the datum, topography, or other data types, including reference data and additional geospatial layers. Landsat Level-1 products, for example, are precision registered and orthorectified through the use of ground control points and a digital elevation model (DEM). The Landsat Level-1 products are termed “terrain-corrected” and the majority of images can be used as delivered by the USGS. Collection 1 images are classified into tiers based on quality and processing level.⁵³

Georegistration error, especially when interest is for parcel-sized ET estimation, can cause sensor data from outside a parcel to be incorrectly utilized to represent inside that parcel. The amount of error will depend on the similarity of vegetation status between inside and outside the parcel. Landsat Tier 1 products are consistently georegistered within ≤ 12 m (Young *et al.*, 2017). This represents only one-half of a standard 30-m pixel, so that, in general, the impact on parcel-sized ET should be small. Other satellites, however, can have much larger georegistration error, including level 3 products from MODIS and VIIRS.

Some computations might require trained and knowledgeable operator skills while others might include additional processing for ‘data sharpening’, ‘data fusion’, ‘cloud masking’, among others, which are themselves models with their own parameters. Thus, it is evident that the complexity of the various nested algorithms to derive ET, the adequacy of these algorithms to describe the various processes involved, the quite intertwined sources of errors involved in the input variables, along with the implicit assumption of the probability distributions for the input values, requires one to go beyond the sensitivity and uncertainty analysis and may require some degree of subjectivity.

A comprehensive uncertainty assessment of ET model performance, and particularly of the data they provide in databases, benefits by a comparison with reliable field ET measurements or against another model considered to be of a higher standard.

Field ET measurement error. Although there is not a standardized field reference to test RS ET models, the eddy covariance (EC) micrometeorological measurement is often considered to be a ‘golden’ standard method for field ET determination, provided it is well calibrated, well maintained and operated by highly qualified technicians. However, the EC method is not without errors and/or systematic bias (Allen *et al.*, 2011b).

Some of the critical issues to be aware of when comparing RS ET with EC data are: (i) the extent of energy balance closure with the EC flux-measurements (possibly only 80 to 90 percent); (ii) the EC fluxes footprint to evaluate possible pixel-to-footprint mismatch. Energy balance closure refers to the frequent inability of the sum of the EC measurements of the latent energy of evaporation (λE) and sensible heat flux (H) to equal the sum of the net radiation (R_n) and soil heat flux (G) measurements, and to therefore “close” the energy balance (see Eq. 1 in chapter 2). The frequent inability for $\lambda E + H$ to equal $R_n - G$ is usually considered to be caused by the inability for the high frequency sonic anemometer, temperature and humidity measurements to adequately account for the entire vertical fluxes of λE and H . The λE and H measurements are typically adjusted by multiplying each measurement by a constant needed for their sum to equal $R_n - G$. However, there is always uncertainty as to whether λE should be corrected more than or less than H , and thus there is always uncertainty on the “correction” made to λE and its equivalent ET. Generally, EC measurements where the average energy balance closure is less than 85 percent should be avoided (Allen *et al.*, 2011b; Melton *et al.*, 2022).

The EC footprint is defined as the spatial area that contributes λE and H fluxes that are measured at the location of the EC system, which is typically located 2 to 5 m above the ground. This area is also referred to as the “source area” for the two fluxes and the amounts of fluxes are largest toward the center of the source area. The size and shape of the footprint area and the distribution of λE and H fluxes within the area can be estimated

⁵³ USGS - science for a growing world. 2023. Landsat Collection 1. <https://www.usgs.gov/landsat-missions/landsat-collection-1>

using footprint models (Kljun *et al.*, 2015). When comparing EC or other ET measurements to RS of ET data, the RS pixels lying within the area should be weighted according to the amount of LE flux originating from each pixel.

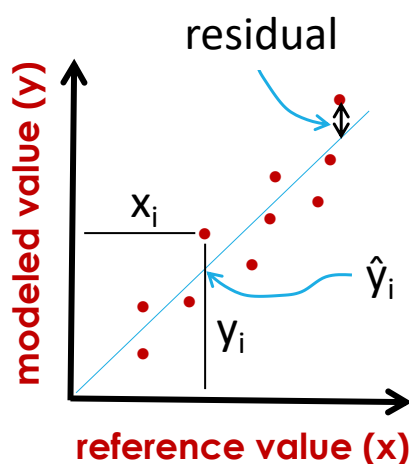
Other than using footprint models (e.g. Kljun *et al.*, 2015), one can assess the EC footprint area using flux measurements at several heights on the same tower, and with more stations about 200m in the surrounding of the main flux tower. However, these measurements are very expensive and are generally reserved for research settings. It is important that the flux measurements of the main EC instrumentation be within the fully adjusted atmospheric boundary layer.

Precision weighing lysimeters have often been used for testing ET model performance (Allen *et al.*, 2007b) and can be used to compare against RS of ET models. One challenge with lysimeters, however, is that they measure relatively small areas on the order of 1 to 20 m², whereas the smallest pixel size of a satellite-based ET estimate will be nearly 1000 m² for a 30 m pixel size and 10 000 m² for a 100 m thermal pixel size. Therefore, the 10 000 m² (1 ha) or larger area sampled from the RS of ET must have vegetation and ET characteristics that are identical to those of the smaller lysimeter. This is often difficult to accomplish and often research-grade lysimeters are placed in land parcels that are smaller than 1 ha. In addition, in order to guarantee that one entire satellite pixel lies completely within the field interior, one needs a parcel nearly 4 ha in size. Thus, the main critical issues to be aware of with lysimeters are: (i) the variability in vegetation type and amount and availability of soil moisture of a sufficiently large area surrounding the lysimeter; (ii) tendencies for vegetation inside a lysimeter to be more dense or less dense or of shorter or taller height than vegetation outside the lysimeter; this can cause the ET measured by the lysimeter to be unrepresentative of the area sampled from the RS of ET model (Allen *et al.*, 2011b); and (iii) possible negative ET occurring during dew or frost formation (e.g. ET becomes negative at night). Similarity in soil water available to the vegetation requires that the soil profile inside the lysimeter itself to be well representative of the soil moisture, and at sufficient depth, of the surrounding area.

Assuming that the field ET measurements can be proven to be of good quality, we are going to review here some of the most common methods and indicators providing the assessment of the RS ET performance and related uncertainty, making use of regression analysis.

Some notations we need to consider in the regression of our interest are reported in Figure 9.

Figure 9: Linear regression between modeled values (e.g. RS ET) and reference values (e.g. Field ET)



Source: Author's own elaboration.

The modeled values and the reference values are reported along the Y axis (e.g. RS ET data) and the X axis (e.g. field ET data), respectively. The straight line is the regression (forced to be linear) between the Y values and X values. The dots represent the location in the data space as derived from the number (n) of individual pairs of

Y and X values, indicated as y_i and x_i , respectively. The mean of the entire set of Y and X values is indicated as \bar{y} and \bar{x} , respectively. The regressed values associated to the pair values along the straight line are indicated as \hat{y}_i . Adopting the previous notation, we can now abstract a set of statistical indicators of performance for the modeled regression.

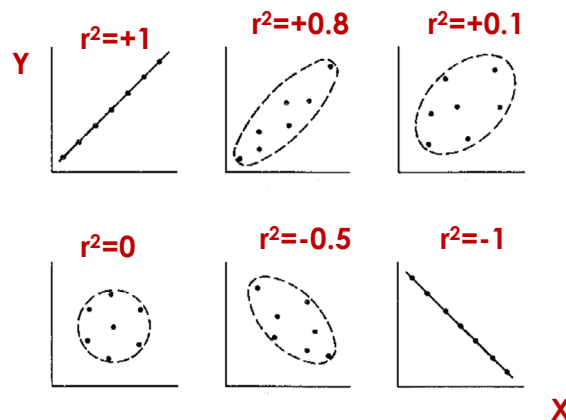
Coefficient of determination (r^2) represents (for the specific case of a linear regression, as in Figure 9) the goodness of fit of the data to the linear equation. It tells us how strong the linear relationship is between **Y** & **X**. It is calculated as:

$$r^2 = 1 - \frac{\sum_{i=1}^n (y_i - \hat{y}_i)^2}{\sum_{i=1}^n (y_i - \bar{y})^2} \quad (102)$$

Its value is the square of the correlation coefficient (r) that varies from +1 (perfect positive correlation) to -1 (perfect inverse correlation).

Examples of r^2 values are visually represented in Figure 10

Figure 10: Examples of r values that can be encountered in regression analysis



Source: Author's own elaboration.

Absolute Error (AE) is the absolute difference between the modeled value (y_i) and the reference value (x_i), and it is calculated as:

$$AE = |y_i - x_i| \quad (103)$$

Relative Error (RE) is the ratio between the Absolute Error (AE) and the reference value (x_i).

Mean Absolute Error (MAE) is an arithmetic average of the absolute error, representing an overall measure of error between paired observations. It is measured as:

$$MAE = \frac{\sum_{i=1}^n |y_i - x_i|}{n} \quad (104)$$

Mean Relative Error (MRE) is the ratio between the Mean Absolute Error (MAE) and the mean reference value (\bar{x}).

Mean Absolute Percentage Error (MAPE), expresses in percentage the average difference between the modeled value and the reference value, and it is calculated as:

$$MAPE = \frac{100\%}{n} \sum_{i=1}^n \left| \frac{y_i - x_i}{x_i} \right| \quad (105)$$

Mean Bias Error (MBE) corresponds to the MAE without taking the absolute value of differences between the model estimate and measurement, i.e.

$$MBE = \frac{\sum_{i=1}^n (y_i - x_i)}{n} \quad (106)$$

Root Mean Square Error (RMSE), also referred to as Root Mean Square Deviation or Difference, (RMSD), is the standard deviation of the residuals (distance of the data point from the regression line), which is a measure of the differences between the values resulting from the regression (\hat{y}_i) and the values resulting from the ET model (y_i). It is calculated as:

$$RMSE = \sqrt{\frac{\sum_{i=1}^n (\hat{y}_i - y_i)^2}{n}} \quad (107)$$

The RMSE is an actual measure of the ET model uncertainty, including precision (random errors) and accuracy (systematic errors). A perfect fit between ET modeled data and field ET data would give a RMSE=0. For normally distributed data, 68 percent of 'expected' values will be within ± 1 RMSE, 95 percent within ± 2 RMSE, and 99 percent within ± 3 RMSE.

The unit of the RMSE is the same as for the Y and X values. To abstract from its specific units, but more specifically to compare different models results and scales, we generally use the **Normalized Root Mean Square Error (NRMSE)** that can be expressed as a fraction or percent. The normalization is generally obtained by dividing the RMSE by the mean of the Y values (\bar{y}).

Index of Agreement (d) by Willmott (1981) is considered to be a standardized measure of the degree of model prediction error and is calculated as the ratio between the mean square error and the potential error:

$$d = 1 - \frac{\sum_{i=1}^n (y_i - \hat{y}_i)^2}{\sum_{i=1}^n (|\hat{y}_i - \bar{y}| + |y_i - \bar{y}|)^2} \quad (108)$$

The index of agreement varies between zero (no agreement at all) and 1 (perfect agreement). Furthermore, Willmot (1981) recommended using a statistical procedure that re-samples a single data set to create several simulated samples (called '*bootstrapping*' method) to evaluate the confidence interval and significance associated with the d index.

Nash-Sutcliffe Efficiency coefficient (NSE) by Nash and Sutcliffe (1970) is used to assess the predictive skill of a model, expressed as a function of the error variance of the modeled values and the variance of the observed values. It is calculated as:

$$NSE = 1 - \frac{\sum_{i=1}^n (y_i - x_i)^2}{\sum_{i=1}^n (x_i - \bar{x})^2} \quad (109)$$

A qualitative rating of model performance used for the FAO model AquaCrop, and that can be used for any model, is reported in table 4 (Raes *et al.*, 2017)

Table 4: Qualitative rating of model performance

Performance Rating	Statistical Indicator		
	r^2	NRMSE (%)	d
Very good	≥ 0.90	$\leq 5\%$	≥ 0.90
Good	0.80 – 0.89	6 – 15 %	0.80 – 0.89
Satisfactory	0.70 – 0.79	16 – 25 %	0.65 – 0.79
Unsatisfactory	< 0.70	$> 25\%$	< 0.65
Total range	0-1	0-100 %	0-1

Source: Raes D., Steduto P., Hsiao T.C. and Fereres E. 2017. *AquaCrop 6.0 - Reference Manual. Chapter 2: User guide.* FAO, Rome.

The qualitative rating for NSE can be considered to be the same as the one for d in table 4.

The indices above assume that all errors occur within the model predictions and that the reference measurements (field measurements) are error free. In reality this is not the case, and to be fully fair and correct, we need to consider also the error in the measurements. While the above indexes are still valid for an assessment of model performance, the 'method of moments' is recommended for comprehensive analytics in 'variables regression problems', where errors are considered in both measurements and model predictions.

7.2 Overview of the selected RS ET models' uncertainty

With the background overview on uncertainty analysis provided in the previous chapter, here we'll review major uncertainty assessments carried out on the models in chapter 2.4. We will refer primarily to peer-reviewed articles describing assessments, bearing in mind that each assessment may have had limited scope, geographic area, climate and vegetation type. Each assessment will have, no doubt, included some measurement error, either random error that would impact the precision of the measurement or a systematic error that may have introduced some higher or lower bias in the measurement. These errors are very difficult to qualify and quantify. Only a few very experienced and qualified experts exist in the world who are able to thoroughly evaluate an ET measurement system and elucidate and quantify the probable error and its behavior.

Also important to bear in mind is that the various assessment studies span more than two decades and tested a specific version of a model, whereas models typically continue to evolve over time as refinements and new data sources occur. Some assessments have been carried out by the model developers, whereas others are more independent.

SEBAL

Bastiaanssen *et al.* (1998b) have provided the first results of the model validation of ET determination using large-scale field experiments conducted in Spain, Niger (the), China and Egypt. Different field methods of ET determination were used, including eddy covariance, airborne turbulent flux measurements, soil moisture profiles measurements and surface and groundwater hydrological models.

The resulting accuracy of SEBAL varied with the scale and the field ET method used to test the model. The authors observed the highest accuracy, within the range of 90-99 percent, when the model ET was compared against the airborne flux and soil moisture measurements, while the lowest accuracy (81 percent) resulted from the comparison against the groundwater hydrological model. The accuracy was in the range of 92-95 percent when the model was compared against the surface hydrological model, and in the range of 85-95 percent when compared against the eddy covariance.

Teixeira *et al.* (2009) carried out a local calibration (in Brazil) of several SEBAL parameters in order to study the impacts on the accuracy of the model. The study area was characterized by irrigated crops (wine grape, table grape, mango orchards) and natural vegetation. Several field agro-meteorological stations and other field instrumentations were utilized to obtain the data to test and revise the following parameters: surface albedo; surface temperature; surface and atmospheric emissivity; roughness length for momentum transport; net radiation; soil heat flux; air temperature gradient; sensible heat flux; latent heat flux; and photosynthetically active radiation (PAR).

The instantaneous values of the energy fluxes from the revised SEBAL were compared against those obtained from Bowen-ratio and eddy covariance towers. The linear regressions between the modeled and reference fluxes reported coefficients of determination (r^2) of 0.94, 0.93, 0.83 and 0.81 for R_n , λE , H and G , respectively. The corresponding root mean square errors (RMSE) were found to be 17.5 $W m^{-2}$, 33.8 $W m^{-2}$, 41.8 $W m^{-2}$ and 13.3 $W m^{-2}$,

respectively. When the comparison was conducted with daily values, the regression for the evapotranspiration (ET) showed a r^2 of 0.91 and a RMSE of 0.38 mm d⁻¹.

SEBAL prediction of ET has been also tested against weighing lysimeters and scintillometers. The difference between modeled-ET and lysimeter-ET, on a monthly scale and for a sugarbeet crop, was found to be in the range ± 16 percent and ± 20 percent (depending on the year of observation). These differences were reduced to about four percent (or less) if ET was computed on a seasonal scale (Bastiaanssen *et al.*, 2005). This latter reduction suggests that much of the estimation error was random in nature and therefore decreased with the repeated sampling occurring over time.

De Bruin *et al.* (1995) and Hemakumara *et al.* (2003) tested SEBAL ET against scintillometers in Sri Lanka and Indus Basin. Errors were variable, ranging from four percent to 32 percent for 10-day ET values. Errors reduced to three percent when ET values were compared on a monthly basis.

Errors tend to reduce with longer time integration caused by the partial cancellation of the random error as well as integration over a larger spatial scale. This was also noted for the METRIC model by Allen *et al.*, (2007a,b). For instance, the SEBAL ET for the period June 1999 to June 2000 for the two river basins in Sri Lanka was found to be between one percent and 11 percent different from the water balance ET (Bastiaanssen and Chandrapala, 2003). The same authors indicated an average deviation in annual ET for large catchments in Pakistan and Sri Lanka of about four percent. This same value has also been reported by Mohamed *et al.* (2004) in estimating the monthly evaporation of the vast swamps of the upper Nile Basin in South Sudan.

Bastiaanssen *et al.*, (2005), thus, claim that the overall accuracy of ET from SEBAL for single-day events and for scales of the order of 100 ha is ± 15 percent, considering that space and time integration further improves the accuracy. Moreover, the catchment-scale studies conducted in Pakistan, Sri Lanka and South Sudan reveal an overall ET accuracy of four percent on an annual basis.

METRIC

Allen *et al.* (2007a, b) reported the first test of the model comparing METRIC ET against high quality ET measurements obtained from both weighing and drainage lysimeters, at Kimberly and Montpellier (Idaho), United States of America, respectively.

The comparison with the drainage lysimeters was conducted for four months in 1985 with an irrigated forage crop. Deviations in weekly ET during the crop season showed a large variability, going from -14 percent (observed in October) to 28 percent (observed in July), with an average deviation of 18 percent over the period July-October. When assessed on a monthly basis, the deviation went from -18 percent (observed in the month of August) to 22 percent (observed in September), with an average deviation of 16 percent over the same period. However, the seasonal difference between METRIC ET and lysimeters, calculated by summing the ET over the 4 month period, was only 4 percent. This is due, again, to a reduction in the random error components present the model, in addition to those of the lysimeter measurements.

The comparison with the weighing lysimeter, measuring ET from irrigated sugarbeets, was conducted on eight dates of 1989. Excluding one of the dates, considered to be affected by inadequate field size and placement of the thermal pixel of Landsat, the deviations of the daily ET of an individual date varied from -23 percent on May 4 to 34 percent of September 25, with an average deviation of 14 percent. Also in this case, the deviation decreased when the comparison was conducted over the entire crop season and, for this particular comparison, showed to be less than 1 percent without any recalibration.

In a regional study to estimate the evapotranspiration (ET) from the western part of Urmia Lake Basin (Islamic Republic of Iran (the)), Tasumi (2019) compared the ET obtained by METRIC with an independent estimation of ET obtained using the FAO-56 approach, for apple, grape and bare soil over the period 2014 through 2016. Taking the difference between daily ET of FAO-56 and daily ET of METRIC as the estimation error of METRIC, mean bias error (MBE) for apple, grape, and bare soils was 0.20, 0.16, and 0.36 (mm d⁻¹), respectively, the mean absolute

error (MAE) was 0.57, 0.72, and 0.59 (mm d⁻¹), respectively, and the Root Mean Square Error (RMSE) was 0.73, 0.84, and 0.68 (mm d⁻¹), respectively. Expressing the RMSE in percentage of average ET, the accuracy for the well-watered apple resulted in 14 percent (the highest accuracy observed). The accuracy decreased for grapes which had intermediary soil moisture conditions, and was poor for dry soil due to the very low evaporation rates. When the accuracy assessment was carried out on a monthly time scale, the MBE ranged from 0.1 to 8.3 mm mo⁻¹, MAE was between 9.0 to 16.0 mm mo⁻¹ and RMSE was between 10.8 to 20.5 mm mo⁻¹.

He *et al.* (2017) investigated the accuracy of METRIC ET over irrigated almond in the San Joaquin Valley, California. The comparison was carried out against field ET obtained as a residual of the energy balance ($\lambda E = R_n - H - G$), where R_n , H and G were measured with a flux tower where the eddy covariance method was used to derive H . The diurnal value of field ET was provided every half hour, allowing the comparison for the instantaneous value of METRIC ET, in addition to the comparison of daily and monthly values. The instantaneous METRIC ET at the time of the Landsat overpass (around 10:30 a.m.) was regressed with field measurements over a total of 46 Landsat overpass cloud-free days, from 2009 to 2012. The regression had a r^2 of 0.74, a RMSE of 0.11 mm hr⁻¹ and a mean relative difference (MRD) of 21 percent. When aggregated at daily time scale, r^2 increased to 0.87, the RMSE was 0.80 mm day⁻¹ and the MRD remained the same. However, when the comparison of ET was conducted by selecting the images of the satellite overpasses occurring during the growing season only (34 cloud-free days), higher accuracy was found, where: for the instantaneous ET value, r^2 slightly decreased to 0.71, RMSE increased to 0.45 mm hr⁻¹ and the MRD decreased to 11 percent; for daily ET values, r^2 remained the same, RMSE was reduced to 0.53 mm/day and mean relative difference (MRD) lowered to 8.0 percent. When the comparison was conducted with ET values aggregated at a monthly time scale, METRIC ET expressed its highest accuracy, i.e. r^2 of 0.90, RMSE of 12.08 mm mo⁻¹ and a RMD of 9.7 percent.

Choi *et al.*, (2009) used Landsat imagery collected during the Soil Moisture Atmosphere Coupling Experiment (SMACEX) in 2002 and compared METRIC model results with observations from a network of EC flux towers over soybeans and corn in Iowa, United States of America. The METRIC model yielded RMSE of 38 W/m² over all EC flux sites combined, assuming a Bowen ratio-based energy balance closure technique for EC.

Several other accuracy assessments of METRIC were conducted with various crops, and the mean absolute difference (MAD), evaluated against field measurements, was found to range between 16 percent for monthly ET values over irrigated meadow (Allen *et al.*, 2007b) to 20 percent for daily ET values over olive (Paço *et al.*, 2014), although the MAD decreased to 4 percent when comparing seasonal ET values (Allen *et al.*, 2007b). Furthermore, RMSE of 1.1 mm d⁻¹ was reported by Lian *et al.* (2015) over spring wheat fields, while French *et al.* (2015) found a RMSE of 1.9 mm d⁻¹ over cotton and Jin *et al.* (2018) observed a RMSE of 1.4 mm d⁻¹ over pistachio.

The lists of METRIC performance assessments against field data are extensive and continue to add over time. So far, it can be stated that the overall model accuracy is expected to vary from 85 percent, for daily ET values, to 95 percent for seasonal ET values, provided a skillful operator of METRIC is assured. For the fully automated version of METRIC (named eeMETRIC) in the OpenET platform, the accuracy of METRIC was found to average about 3 percent for total growing season weighted mean ET assessed over 15 EC sites representing 40 total growing seasons (Melton *et al.*, 2022).

ALEXI/DisALEXI

Both models associated with ALEXI/DisALEXI, the regional-scale (5 km) ALEXI and the higher-resolution (10-100 m) disaggregated version DisALEXI, have gone through various degrees of validation, including comparisons with flux towers and aircraft in the United States of America and Europe with satisfactory results (NASA-JPL, 2018).

Anderson *et al.* (2007b) compared the λE determined by ALEXI (including the algorithm for gap-filling of cloudy days) with the λE obtained by all towers of the SMACEX study noted above for METRIC, conducted in a watershed of Iowa, the United States of America. The results of this comparison indicated an error of about 20 percent in ET at the hourly time scale and of ≤ 15 percent at daily time scale.

The various tests have indicated that ALEXI is more suitable for spatial scales of 5-10 km, where the land surface influence on the mean atmospheric conditions and on the boundary layer growth is observed to be effective (Anderson *et al.*, 2004). Therefore, to compare ET at a regional scale with ground-based flux measurements it is appropriate to disaggregate the large-scale fluxes. DisALEXI (Norman *et al.*, 2003) is the disaggregated high-resolution version of ALEXI.

Anderson *et al.* (2004) applied DisALEXI to remote sensing data obtained from aircraft at 24 m resolution, over 4 days, during the 1997 Southern Great Plains field experiment. The resulting λE from the model was compared with the λE measured with eddy covariance and the differences were within 12 percent.

DisALEXI, using Landsat data, was tested against measurements on irrigated cotton and rainfed grass in semi-arid, advective environments, obtained during the field campaign 'Bushland evapotranspiration and Agricultural Remote sensing Experiment' (BEAREX) of 2008 (Anderson *et al.*, 2012). The comparison between λE data of DisALEXI with the two lysimeters and eight eddy covariance data showed an error of \approx 17 percent on an instantaneous scale at the Landsat overpass time. The error was reduced to \approx 11 percent when the comparison was conducted at a daily scale.

DisALEXI was tested over vineyards in California (Knipper *et al.*, 2018), specifically on two drip-irrigated Pinot noir vineyard sites in Central Valley during the 2013-2016 growing seasons. These sites are being monitored as part of the Grape Remote-Sensing Atmospheric Profile and evapotranspiration eXperiment (GRAPEX). ET determined by the model was compared against the ET measured by eddy covariance flux-towers (one for each vineyard). Data sharpening (Gao *et al.*, 2012) and data fusion (Gao *et al.*, 2006) were used to generate daily ET maps at 30 m resolution. The comparison resulted in relative errors of 17 percent and 12 percent at daily and weekly time scale, respectively.

After the launch of the ECOSystem Spaceborne Thermal Radiometer Experiment on Space Station (ECOSTRESS) in June 2018, DisALEXI has been applied as one of the RS models to derive ET over large areas. More specifically, a model version revised by the Jet Propulsion Lab of NASA (DisALEXI-JPL) has been adopted to produce ET at the ECOSTRESS resolution of 70 m, and using the LST as input, the most recently available acquisition of Landsat 8, and different visible to shortwave infrared (VSWIR) input processing approaches. DisALEXI-JPL has been applied to cover the entire continuous U.S. (CONUS) and has been evaluated by comparing its ET determinations against the ET measurements taken at 26 eddy covariance sites across the United States of America, over a variety of landcover classes (Cawse-Nicholson *et al.*, 2021). The results of the comparison reported a $r^2 = 0.80$ and $RMSE = 0.81 \text{ mm d}^{-1}$.

Overall, ALEXI and DisALEXI have demonstrated to have good accuracy in a number of ET determinations. This is in part due to the time differential temperature approach (day-minus-night LST differences from MODIS/VIIRS) used in ALEXI to predict the morning LST rise. By coupling a time-integration computation with an atmospheric boundary layer (ABL) model implemented over the morning period of ABL growth, near-surface air temperature is computed internally rather than used as a model input (Cammalleri *et al.*, 2012).

SSEBop

Senay *et al.* (2013) tested SSEBop estimates of actual ET over diverse ecosystems across the contiguous the United States of America (CONUS), using the MODIS and Global Data Assimilation System (GDAS) data streams. The validation test was conducted for 1 km pixels, at monthly and seasonal time scales, against monthly datasets from 45 eddy covariance sites of AmeriFlux for the year 2005 and for different land cover types. While SSEBop was able to capture the seasonality of ET, with a strong correlation for individual stations (r^2 between 0.70 and 0.97), overestimation and underestimation of absolute values varied from station to station and from season to season.

SSEBop ET was also tested against lysimeters ET measurements in the semi-arid High Plain of Texas (Senay *et al.*, 2014). SSEBop used a total of 14 Landsat-5 cloud-free images acquired during the growing season (March to

October) of the years 2006 and 2007. Field ET was derived from cultivated large monolithic precision weighing lysimeters located at the US Department of Agriculture-Agricultural Research Service (USDA-ARS) Conservation and Production Research Laboratory (CPRL) in Bushland, Texas. Two of the lysimeters were irrigated and two were under dryland conditions. The modeled and observed daily ET values were evaluated by differentiating the "irrigated" and "dryland" lysimeters and considering four aggregation periods, i.e. 1-day, 2-day, 3 day and "seasonal". The results of the comparison showed an overall strong linear relationship, with r^2 values ranging from 0.87 to 0.97 (higher for the "irrigated" lysimeters). Generally, the performance between irrigated and dryland fields was comparable with an overall under-estimation bias of around 11 percent. Furthermore, the RMSE, expressed as percent of the mean values, reduced progressively from 28 percent to 24 percent, to 16 percent and to 12 percent when passing from 1-day, to 2-day, to 3-day, and to "seasonal" aggregation periods, respectively. The random error contribution to the total error was reduced from 86 to 20 percent, while the bias contribution increased from 14 to 80 percent when aggregated from daily to seasonal scale, respectively.

An uncertainty analysis conducted on SSEBop by Chen *et al.* (2016) utilized eddy covariance flux data from 42 selected AmeriFlux tower sites, from 2001 to 2007, to test the model performance in determining monthly ET. Overall, ET estimates by SSEBop accounted for about 86 percent of the monthly ET measurements over all land uses, though performing best for cropland where it accounted for 92 percent variability with an RMSE of 13 mm/month. Furthermore, the uncertainty analysis showed that error in land surface temperature (LST) within ± 1 K (0.35 percent) can lead to ET errors having a range of 20 percent. This is the case for most globally available LST data at 1-Km resolution, though in arid or semiarid climatic conditions errors in LST may increase up to ± 5 K (Hulley *et al.*, 2012). In fact, it was highlighted that SSEBop is most sensitive during the non-growing season and in more arid regions, where ET errors might go up to 30 percent. It was also observed that lower uncertainty (e.g. ≈ 5 mm/month) is associated with a coarser spatial resolution (e.g. ≈ 14 Km), while higher uncertainty (e.g. ≈ 10 – 15 mm mo^{-1}) is associated to finer resolution (e.g. ≈ 1 – 8 km).

These findings imply that SSEBop may be more suitable for ET prediction at regional scale. However, the OpenET study of Melton *et al.*, (2022) indicates relatively good accuracy by the 2021 version of SSEBop at the field scale when applied with Landsat imagery. Accuracy at higher spatial resolution may be improved if the accuracy in the input variables and in key model parameters is adequately improved.

The daily ET determinations by SSEBop for irrigated and non-irrigated farmlands in the mid-western the United States of America were compared with eddy covariance measurements during the 2001 growing season over three sites planted with maize and soybean (Sing and Senay, 2016). The results showed an r^2 of 0.92 and a RMSE of 84 mm over the season.

In generating ET maps for nine irrigation districts in California over 31 years (1984–2014), SSEBop processed a total of 3396 Landsat images (Landsat 5, 7, and 8) to generate monthly and annual ET data for each district (Senay *et al.*, 2017). To validate the model performance, its ET determinations were compared against the global estimates of monthly land ET, over the period 1984–2011, from the Max Planck Institute (MPI) in Germany. These MPI ET estimates, available at ≈ 50 -km spatial resolution, are compiled using a machine learning approach to upscale eddy covariance measurements (FLUXNET), meteorological data, climate data, and the fraction of absorbed photosynthetic active radiation data (Jung *et al.* 2009; Jung *et al.* 2010). The result of the comparison showed r^2 up to 0.88 and RMSE as low as 14 mm/month.

SSEBop is currently used by the US Geological Survey (USGS) Famine Early Warning System Network (FEWS NET) to routinely provide multitemporal ET and ET anomalies for drought monitoring and early warning purposes. In one of the operationalizations of global ET determinations (Senay *et al.*, 2020), SSEBop was evaluated using field ET data measured at 12 eddy covariance flux tower sites (provided by FluxNet) selected over six continents: two in Europe, two in North America, two in South America, two in Asia, two in Africa and two in Australia. The time period for the EC data was 2003–2014, based on the availability of flux tower measurements and the comparison of ET was on a monthly basis. Overall, the result of the comparison showed an r^2 as high as 0.76 (with the exception of a site in South America, with an $r^2 = 0.008$), while the RMSE ranged between 7.5 mm/month and 43.7 mm/month. The strongest correlations occurred in Australia ($r^2 = 0.76$, RMSE = 13.6 mm/month) and Europe ($r^2 = 0.67$, RMSE = 15.8 mm/month), while the lowest correlations were in South America (r^2

= 0.008, RMSE = 43.7 mm/month). While the observed overall bias for SSEBop ET ranged from 3 percent to 50 percent, in both negative and positive directions, the measured EC flux tower ET was also subject to biases and uncertainties, as indicated by relatively large energy balance closure error at some sites.

However, SSEBop seemed to under-estimate in Europe and Asia, but partly over-estimate in Africa and Australia. Despite the concerns with SSEBop ET biases and energy balance closure error with EC flux tower data, SSEBop ET captured the temporal variability and anomalies so that it can be used for drought monitoring and early warning applications from 1 km decadal to basin-scale annual estimates. Nevertheless, a comprehensive investigation using complete water budgets and more quality-controlled EC station datasets is recommended.

PT-JPL

The PT-JPL model has been selected (among others) by the ECOSystem Spaceborne Thermal Radiometer Experiment on Space Station (ECOSTRESS) mission of the National Aeronautics and Space Administration (NASA) of the United States of America and it has been tested across a wide range of ecosystems, climate and land covers (NASA-JPL, 2018).

Using the net radiation, air temperature and air vapor pressure deficit measurements at 16 FLUXNET sites in various regions worldwide and over the years 2000-2003, Fisher *et al* (2008) tested the ET accuracy of PT-JPL on a monthly scale. Apart from two sites reporting an r^2 of 0.55 and 0.78, respectively for tropical evergreen broadleaf forest and for cold-temperate deciduous broadleaf, all other 14 sites had an r^2 ranging from 0.81 to 0.96. When data from all sites were combined, the r^2 was 0.90 with a RMSE of 16 mm/month. When the ET comparison was made on an annual scale, r^2 was 0.94 with a RMSE of 12 mm/month. Furthermore, Fisher *et al.* (2008) separated the systematic RMSE from the random (or unsystematic) RMSE so that the PT-JPL accuracy resulted in $\pm 4 \text{ mm yr}^{-1}$ with a precision of 68 mm yr^{-1} .

Vinukollu *et al.* (2011) carried out an inter-comparison of the PT-JPL latent heat fluxes with 12 eddy-covariance towers across the U.S. over the period 2003-2006. The eddy-covariance sites had different land uses, including cropland, grassland, evergreen needle-leaf forest, deciduous broadleaf forest, mixed forests and woody savannas. The results of the comparison at a monthly scale, using the data of all sites, showed a relatively low regression coefficient ($r^2 = 0.54$) a mean RMSE of $\approx 20 \text{ Wm}^{-2}$, and a mean bias of $\approx -6 \text{ Wm}^{-2}$. The authors highlighted the difficulties and challenges encountered in conducting the inter-comparisons between satellite ET and eddy covariance ET, including the mismatch between instantaneous values of the satellite and hourly values of the eddy covariance, the difference in spatial scales (and heterogeneity of the land surface) between the satellite footprint and the eddy-covariance tower footprint, and the lack of energy balance closure of the eddy covariance measurements.

Chen *et al.* (2014) compared the PT-JPL ET with the measured ET at 23 eddy covariance sites within or around China, covering diverse terrestrial biomes, including cropland, grassland, evergreen and deciduous broadleaf forests, evergreen and deciduous needle-leaf forests, and mixed forests. The results showed a good performance of the PT-JPL model, with an $r^2 = 0.80$, a slope of the regression line of 1.05, and a RMSE = 0.5 mm d^{-1} .

In evaluating the performance of four commonly applied satellite ET models against measured ET of 20 FLUXNET towers, Ershadi *et al.* (2014) highlighted the overall good performance of PT-JPL. The eddy covariance sites encompassed a number of biomes including cropland, grassland, shrubland, evergreen needle-leaf forest and deciduous broadleaf forest, spanning a period of high-quality data between 1.5 and 10 years. In order to provide high-quality data, the eddy covariance values used in the comparison were filtered to daytime only (to avoid negative net radiation and nighttime condensation), for a number of meteorological conditions (e.g. rain events, frozen periods, etc.), and other quality-control checks. The results of the comparison across all biomes showed a mean $r^2 = 0.70$, a mean RMSE = 66 Wm^{-2} and mean relative error (the RMSE normalized by the mean values of observed data) = 0.37.

ETLook

The initial version of ETLook used radar microwave radiation to estimate the soil moisture of the top soil and in turn the evaporation component (E) of the surface ET. The first model validation with field measurements was conducted using this version of ETLook to determine the actual ET in the Indus Basin (Bastiaanssen *et al.*, 2012) at 1 km ground resolution. A first challenge was then to downscale the 25 km ground resolution data of the Advanced Microwave Scanning Radiometer (AMSR-E) on the Aqua Satellite, obtained from the National Snow and Ice Data Center (NSIDC). Most of the additional satellite data input were derived from MODIS, while the source of meteorological data varied between the countries of the Indus Basin. Specifically data from 65 meteorological station were used in Pakistan (provided by the Pakistan Meteorological Department) while the data for India, China and Afghanistan were abstracted from the National Oceanic and Atmospheric Administration (NOAA) National Climatic Data Center (NCDC). Modeled annual ET was compared with measured values obtained in the same basin by the Pakistan Agricultural Research Council (1982) over the period 1975-1980, including soil moisture and lysimeter data, and by Ahmad (2002) over the period 2000-2001, including ET data obtained with a Bowen ratio energy balance system. The result of the comparison over irrigated crops for the year 2007 showed an r^2 of 0.70, and an annual RMSE of 163 mm. The relative error (RE) between ETLook and measured ET values ranged from -1.9 percent to -28 percent with an average of -11.5 percent, indicating a tendency of the model to underestimate ET.

The same authors (Bastiaanssen *et al.*, 2012) presented the results of the comparison of ETLook with the annual ET data provided by the Australian Water Resources (AWR) for the year 2005, showing an r^2 of 0.70 and an RMSE of 112 mm. The RE between the ETLook and AWR ET values ranged from -40 percent to 36 percent. They also presented the results of the comparison of ETLook with ET measured with eddy covariance flux measurement station in China for the year 2009. The results of the comparison showed an r^2 of 0.92, an RMSE of 11 mm, and an RE of 9.5 percent.

When ETLook was adopted by the WaPOR project in FAO, a new version of the model was developed, using the 'trapezoid' method and no longer used microwave data to derive the top soil moisture (see chapter 2.4.6), and additional validations were carried out. The quality assessment of WaPOR 1.0, conducted by FAO and IHE Delft (2019), concluded that the ET obtained via ETLook is reliable for a longer period (e.g. a year) and larger areas (e.g. a sub-basin), and that the quality reduces with a higher aridity, systematically underestimating (20-60 percent) seasonal crop ET in comparison with eddy covariance measurements.

After further development of the ETLook model (WaPOR 2.0), including an improved parameterization of the soil moisture content and of the reference ET (ET₀), along with the use of the EU Copernicus land cover classification rather than the previous Globcover (used in WaPOR 1.0), an additional quality assessment was carried out by FAO and IHE Delft (2020). The actual ET from ETLook was compared to the in-situ actual ET measured with eddy covariance flux towers at a 10-day (dekad) and monthly scale over 14 locations, encompassing different climatic zones ranging from the equatorial to warm temperate, to semi-arid to arid. The results of the comparison showed an r^2 ranging from 0.119 to 0.924 and an RMSE ranging from 0.4 mm d⁻¹ to 2.2 mm d⁻¹. The variations among the sites appears to be linked to the quality of NDVI and LST data, as a better performance of ETLook is observed when these variable have high quality and when the sites are water limited rather than energy limited. From the performance assessment conducted in Africa, it was concluded that ETLook appears to overestimate ET in dry irrigated areas (e.g. in irrigation areas of the Nile Delta). The overall mean average percent error on daily and monthly scale is 40.4 percent and 26.3 percent, respectively, while on annual basin scale is 29.5 percent (Blatchford *et al.*, 2020).

ETMonitor

Hu and Jia (2015) validated ETMonitor in the Heihe River basin, located in the arid region of northwest China. The daily land surface soil moisture was derived from the Advanced Microwave Scanning Radiometer (AMSR-E) on

the Aqua satellite, at 25 km spatial resolution and 4 days temporal resolution, obtained from the National Snow and Ice Data Center (NSIDC). Using the bilinear resampling method, the soil moisture data were downscaled to 1 km, which is considered the operational ground resolution at basin scale. Also the meteorological data, derived at 5 km ground resolution from the Weather Research and Forecasting model (WRF) simulation, had to be downscaled to 1 km. The estimated daily ET by ETMonitor was then evaluated against ET measurements, during the period 2009-2011, at three eddy covariance flux sites differing in vegetation type (cropland, alpine meadow and forest), cover and climatic conditions. The results of the comparison showed an r^2 of 0.70, 0.82 and 0.87 for forest, cropland and alpine meadow, respectively, and an RMSE of 17.9 Wm^{-2} , 18.9 Wm^{-2} and 24.8 Wm^{-2} , for forest, alpine meadow and cropland, respectively.

In attempting to generate global daily ET at 1 km spatial resolution during the period 2008-2012, and utilizing as much as possible open accessed remote sensing data, Zheng *et al.* (2016, 2017) tested ETMonitor against high-quality ground ET measurements obtained from 10 eddy covariance observation sites, with landcover of forest, shrubland, grassland, and cropland. Overall, the estimated ET shows good accuracy when compared with ground observations, with $r^2 = 0.74$, Bias = -0.05 mm d^{-1} , RMSE = 0.87 mm d^{-1} . Nevertheless, the performance varied from site to site, with r^2 ranging from 0.36 to 0.93, the bias ranged between -0.74 mm d^{-1} and 0.88 mm d^{-1} , and RMSE ranging from 0.34 mm d^{-1} to 1.40 mm d^{-1} .

In estimating ET in Thailand (a tropical monsoon area) based on earth observation products from 2001 to 2015 (Zheng *et al.*, 2019a and 2019b), the ETMonitor algorithm was improved and the modeled daily ET at 1 km spatial resolution was tested against the ground ET measured at six eddy covariance flux towers. The estimated daily ET agreed well with the ground observations, with mean bias error (MBE) ranging from -0.44 to 0.89 mm d^{-1} , root mean square error (RMSE) ranging from 1.08 to 1.58 mm d^{-1} , and r^2 ranging from -0.004 and 0.28 . Overall, ETMonitor performed better over cropland.

Sriwongsitanona *et al.* (2020) tested seven global remote-sensing ET products across Thailand, where ETMonitor was one of them, adopting a water balance based on high-quality hydrological data from 1,743 gauged rainfall stations and 172 streamflow stations across the country. The water balance equation was expressed as

$$ET_{\text{WB}} = P - Q - \Delta S \quad (110)$$

where ET_{WB} is the ET derived through the water balance, P is the precipitation, Q is the stream flow and ΔS is the change in water storage of the system over time. The innovative aspect of this approach is that the Gravity Recovery and Climate Experiment (GRACE) was adopted to represent monthly ΔS in terms of the terrestrial water storage change. Thus, the monthly ET validation was conducted by inverting the water balance equation 109 where ET is the one obtained by remote sensing (ET_{RS}), i.e.

$$\Delta S = P - Q - ET_{\text{RS}} \quad (111)$$

so that the monthly ΔS obtained through the inverted water balance equation 110 is compared with the monthly ΔS obtained through GRACE (ΔS_{GRACE}). The annual modeled ET is instead validated directly against the ET_{WB} (Eq. 110) using ΔS_{GRACE} . The results of the comparison were excellent for ETMonitor, which showed an $r^2 = 0.98$ and a Nash-Sutcliffe coefficient (NSE) = 98.42 percent for annual ET. The monthly comparison between ΔS from remote sensing and ΔS_{GRACE} showed an $r^2 = 0.60$ and a NSE = 67.02 percent.

ETWatch

Wu *et al.* (2012) have tested ETWatch in the complex terrain of the Hai Basin, by comparing the modeled ET with field ET measurements obtained with a variety of methods, including soil moisture depletion at three locations, one lysimeter, six eddy covariance systems (EC), three large aperture scintillometers (LAS), and the water balance at six sub-watersheds.

For the comparison of seasonal ET (during 2005 in 20 fields) between ETWatch and the soil moisture depletion method, the overall correlation showed an $r^2 = 0.88$. The RMSE was 16 mm for the whole season, and the average relative error (RE) was + 4 percent, indicating a slight seasonal ET overestimation by ETWatch. The comparison

with the lysimeter, during the year 2003, was more complex to be analyzed due to the disturbance by rain during the winter months. Thus, limiting the season to the period July 1st to September 30th, ET estimated by ETWatch for maize was 324 mm while 304 mm were recorded by the lysimeter, thus showing a -6.6 percent deviation. Furthermore, it was observed that ETWatch performed better in maize than in wheat and predicted a 9 percent lower ET for the annual cycle of 365 days. The comparison with EC over the years 2003-2005 was limited to a few fragmented data periods due to weather conditions. A high correlation ($r^2 = 0.91$) was observed over wheat and maize crops. The total ET for 10 days measured by the EC system over wheat and maize was 19.9 mm, whereas ETWatch predicted 19.2 mm, thus showing a difference of -3.7 percent. The daily absolute average ET deviation by ETWatch was 8.7 percent, whereas for two days the error was larger than 15 percent. A more comprehensive comparison with EC data set, generated from the Chinese Ecosystem Research Network and GEF funded sites, showed an r^2 ranging from 0.64 to 0.79, with one site showing the largest deviation (30 percent) over a period of 40 days. The comparison with LAS, between 2007 and 2009, showed a range of deviation between +1.15 percent and -4.7 percent for the daily ET and between +4.3 percent and +11.8 percent for the monthly ET. The water balance method was conducted between 2002 and 2005 in six sub-watersheds of the Hai Basin, which altogether represent about 25 percent of the entire basin surface area. The deviations between ETWatch and the water balance annual ET estimates ranged between -15.4 percent and +16.9 percent. When the annual ET was integrated for the entire Hai Basin, the deviation of ETWatch was +1.8 percent.

ETWatch was also tested after the elaboration of a method for downscaling ET from 1-km to 30-m resolution (Tan *et al.*, 2019). The test was conducted over the period between April to October 2003, at four EC sites in the Zhangye Oasis of the Gansu Province in China, and encompassing cropland, wetland and sparse grass. The overall results of the comparison of daily downscaled ET from ETWatch against the EC ET showed an r^2 ranging from 0.80 to 0.91, the mean bias ranging from 0.17 to 0.72 mm d⁻¹, the RMSE ranging from 0.23 and 0.69 mm d⁻¹ and the index of agreement (d) ranging from 0.93 and 0.98.

An improved version of ETWatch for continuous ET determinations at regional scale, using algorithms acquiring satellites data from multiple sources, was validated using ground observations from the Heihe River Basin of northwest China (Wu *et al.*, 2020). Field ET measurements were collected during the period 2008-2014 using six EC and automatic weather stations encompassing different land surface types, including alpine meadow, irrigated oases, and sparse vegetation. Furthermore, additional field annual ET during the period 2012-2013 were derived through the water balance method. The validation results for daily ET at 1 km resolution against EC data at the six stations showed an r^2 ranging between 0.71 and 0.84, a mean absolute error (MAE) ranging between 0.229 and 0.582 mm d⁻¹, a RMSE ranging between 0.278 and 0.768 mm d⁻¹, and the Nash–Sutcliffe efficiency coefficient (NSE) ranging from 0.70 and 0.83. When the ET comparison was scaled to monthly values, the r^2 ranged between 0.78 and 0.99 and the RMSE ranged between 1.02 and 5.47 mm/month. The comparison of annual ET values by ETWatch with the water balance estimates, conducted on the entire Heihe River Basin and one small watershed, resulted in deviation of +1 percent and +9.44 percent, respectively.

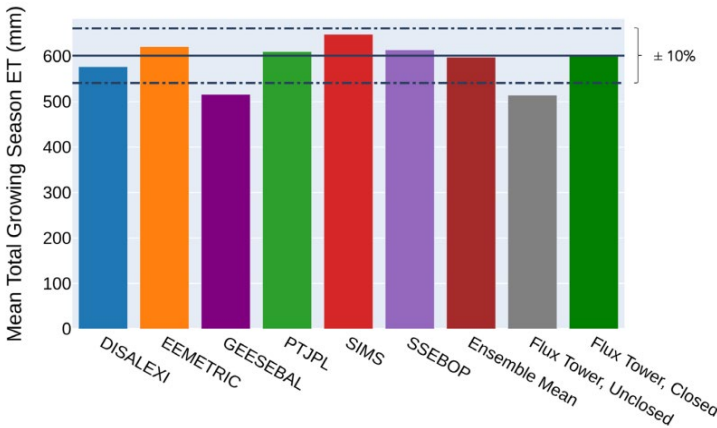
7.2.1 Some highlights on model inter-comparisons

The previous section has provided some descriptions and examples of specific model performance with associated values of some statistical indicators. The variability of uncertainty in ET by the various models was observed to depend on several factors, including the extent of parameter calibration for a given terrain landscape and field, the accuracy of the input variables and their capacity to represent the actual conditions at the given scale, the uniformity of the land surface being scanned by the satellite sensors, and the spatial and time scales evaluated. There was also some inconsistency on the degree of uncertainty with the period of the year (e.g. during the season) and with various climatic conditions (e.g. arid, sub-humid, etc.). In short, notwithstanding the good performance in given conditions, there is no guarantee that the expected model accuracy remains consistent throughout space and time.

One way to look at the various models is on relative terms. In other words, given the same conditions monitored by more than one model can provide a comparative assessment of their individual performance. This has not always been possible and here some of these multiple model inter-comparisons are reported.

A first opportunity has been offered by the OpenET platform that has provided a series of tests on various models.⁵⁴ Figure 11 shows the comparison between the seasonal ET derived by the six models adopted by OpenET, and by the ensemble of all six models, against the mean seasonal ET measured by EC at 15 sites and over 40 crop seasons in the Western United States of America (Melton *et al.*, 2022). Apart from GESEBAL (Google Earth Engine-SEBAL), all other model determinations are within ± 10 percent of the mean of all EC measurements, corrected for energy balance closure.

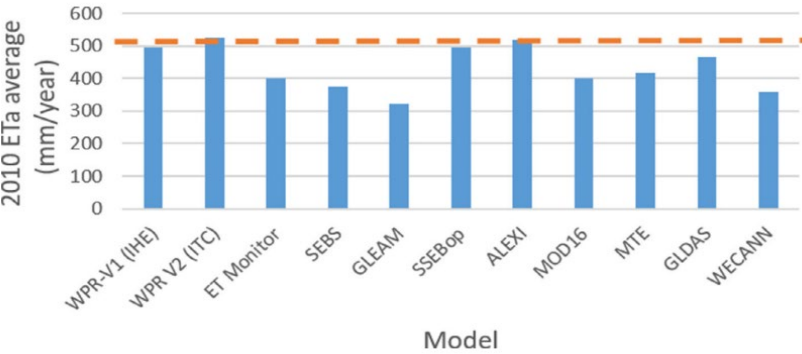
Figure 11: Total growing season weighted mean ET (n = 15 sites with 40 total growing seasons) for six satellite-driven ET models, the ensemble mean ET, and ET calculated from the closed and unclosed energy balances at each flux tower site



Source: Melton F.S., Huntington J., Grimm R., Herring J., Hall M., Rollison D., Erickson T. et al. 2022. *OpenET: Filling a Critical Data Gap in Water Management for the Western United States*. J. Amer. Water Resour. Association, 58 (6):

A similar multi-model inter-comparison was provided by Blatchford *et al.* (2020) in evaluating the yearly ET determination for the WaPOR extent (Africa and MENA Region) compared to WaPOR values (indicated as WPR in ET of Figure 12).

Figure 12: Comparison of ETa obtained from various models and ETa-WPR (represented by the orange dashed line) used as reference to compare the other model performances



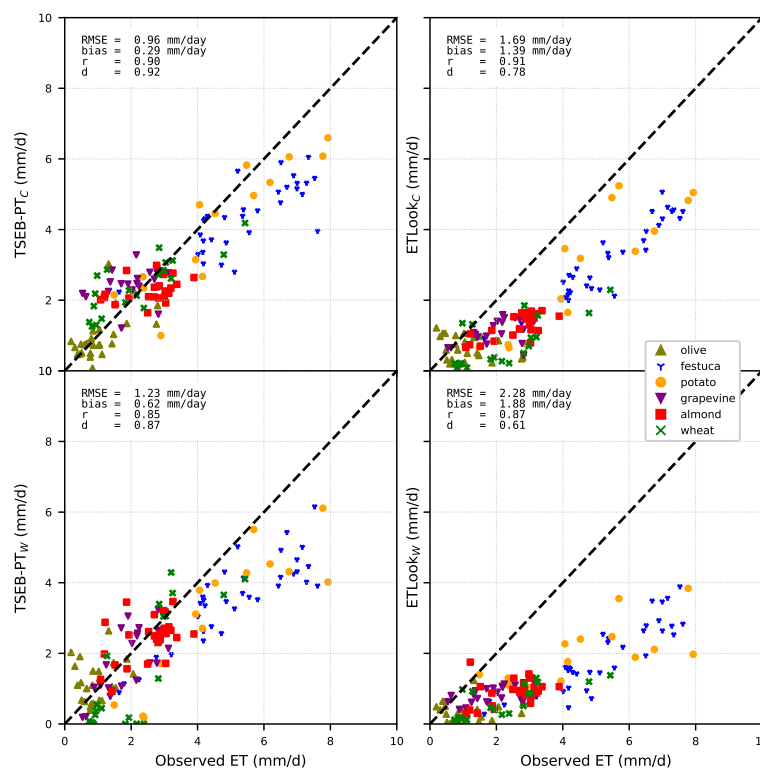
Source: Blatchford M.L., Mannaerts C.M., Njuki S.M., Nouri H., Zeng Y., Pelgrum H., Wonink S. and Karimi P. 2020. *Evaluation of WaPOR V2 evapotranspiration products across Africa*. Hydrol. Process., 34 (15): 3200–3221.

⁵⁴ OpenET. 2023. <https://openetdata.org/>

It appeared that the best performance was expressed by the ETLook of the version 2 of WaPOR, along with SSEBop and ALEXI. SEBAL and METRIC models were not included in the comparison.

An additional inter-comparison between ETLook and the Two Source Energy Balance – Priestley Taylor (TSEB-PT) model was conducted in Tunisia (over olive) and Spain (over almond, grapevine, festuca, wheat and potato), during the period 2017-2019 (DHI-Gras and Compluting, 2022). The field measurements of ET were conducted with EC over irrigated almond, and rainfed olive and wheat and with lysimeters over potato, festuca and grapevine, all under irrigation. The result of the inter-comparison are reported in Figure 13

Figure 13: Scatterplot between the *in situ* decadal ET (observed ET) and estimated decadal ET by TSEB-PT (left graph) and ETLook (right graph). Subscripts 'w' and 'c' refer to WaPOR-like and Copernicus input data source, respectively



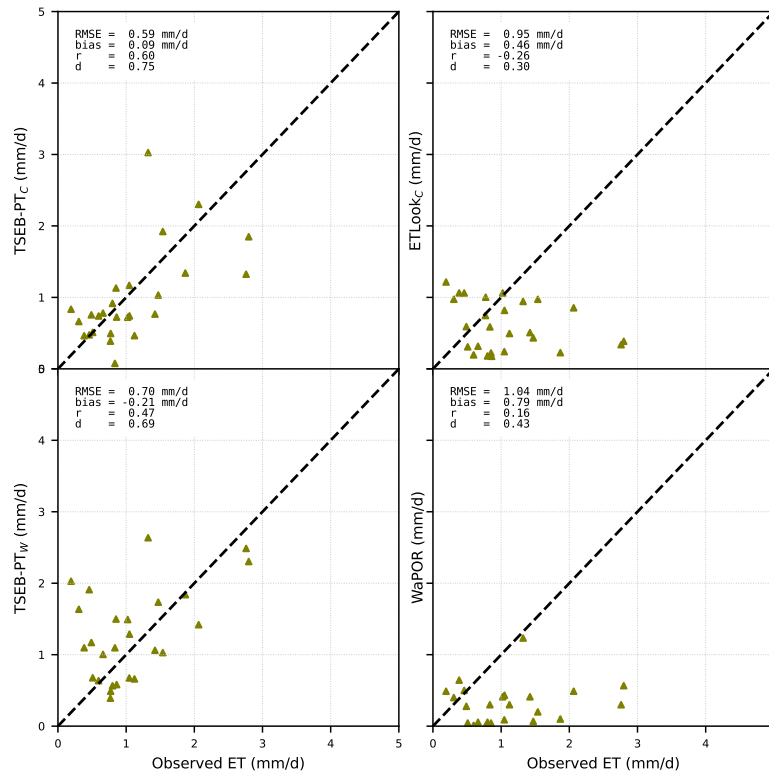
Source: DHI-Grass and Compluting 2022. *Increasing Crop Water Use Efficiency at Multiple Scales Using Sentinel.*

Evapotranspiration. ET4FAO D4.2 – Final Report. https://et4fao.dhigroup.com-/ET4FAO_Final_Report.pdf. While ETLook shows a systematic and larger underestimation, as compared to TSEB-PT, its performance increases when input data from Copernicus are adopted. Nevertheless, the improvement is not realized when isolating challenging crops such as the olive grove in Tunisia (Figure 14).

Further ET model inter-comparisons were conducted by ICARDA (data not yet published) on a pomegranate orchard in Egypt. The *in situ* ET was derived as the residual of the energy balance where the sensible heat flux (H) was measured via EC and the soil heat flux (G) was obtained through the soil heat flux plate method. The results of the cumulative ET by ETLook (WaPOR), SSEBop, METRIC (EEFlux), ALEXI (GloDET) and the *in-situ* measurements, for the period March 2018-March 2019, is reported in Figure 15.

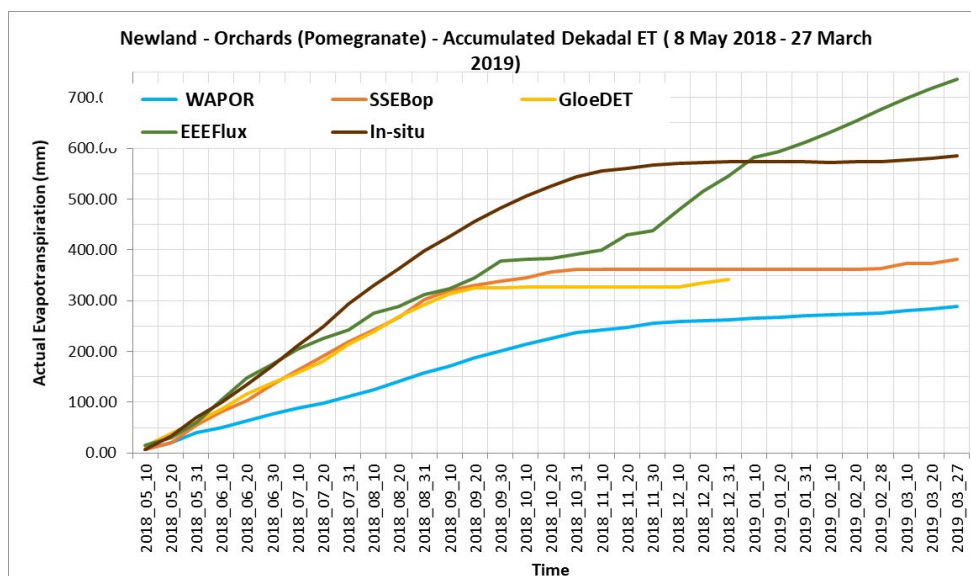
With the apparent exception of METRIC (labeled as EEFlux) for some periods of the growing season, all other models seem to underestimate the *in situ* ET determinations.

Figure 14: Scatterplot between the *in situ* decadal ET and estimated decadal ET by TSEB-PT (left graph) and ETLook and WaPOR (right graph). Subscripts 'w' and 'c' refer to WaPOR-like and Copernicus input data sources, respectively. The WaPOR ET product was downloaded from the FAO Portal



Source: DHI-Grass and completing 2022. *Increasing crop water use efficiency at multiple scales using sentinel evapotranspiration*. ET4FAO D4.2 – Final Report. https://et4fao.dhigroup.com/-ET4FAO_Final_Report.pdf.

Figure 15: Cumulative ET of pomegranate orchards cultivated in the Newland area of Egypt, as determined by ETLook (WaPOR), SSEBop, METRIC (EEFlux), ALEXI (GloDET) and *in-situ* (ICARDA, unpublished)



Source: Swelam A., Govind A., Abdallah M., Steduto P. and Taha A. 2019. *Validation of remote sensing evapotranspiration data of selected crops in the Nile Delta*. 3rd World Irrigation Forum (WIF3), 1-7 September 2019, Bali, Indonesia.

7.3 On the acceptable limits of uncertainty towards best fit-for-purpose

We would like to close chapter 7, on the uncertainty review on RS ET determinations, by addressing an operational dimension of uncertainty. An important reminder here is that "*all measurements, however careful and scientific, are subject to some uncertainties*" (Taylor, 1982). This is valid not only for *measurements* but for any determination, direct, indirect, through modeling, or any other approach. Therefore, the two most relevant questions we should ask to ourselves, in dealing with uncertainty, are: how much uncertainty is generally associated to a determination that I need? Is such uncertainty acceptable for my application?

A typical and simple example is the case of the weighing uncertainty of a scale. If the scale is used to weigh gold to sell, then one needs a very low uncertainty (say ± 1 mg). If instead the scale is used to weigh apples to be sold at the farmers' market, one can accept a higher degree of uncertainty (say ± 100 g). Knowing the acceptable weighing uncertainty for a given application (selling gold or apples) will allow one to make a better decision on which scale on the market best fits the purpose.

The same reasoning applies to the uncertainty of RS ET determinations, whose higher or lower uncertainty becomes acceptable depending on the type of application the ET determinations will be used for. Therefore, a simple logical framework in dealing with uncertainty is: *first* identify the type of application (the domain) you will be using the RS ET data for; *second* define the limits of uncertainty that are acceptable for the identified application; *third* select the model/method of RS ET determination with an expected uncertainty (or achievable accuracy) that falls within the acceptable limits, i.e. select the model/method that best fit the purpose.

While this simple logical framework appears straightforward, in reality there are still open questions on: (i) the acceptable limits of uncertainty for a given application; and (ii) the expected uncertainty (or achievable accuracy) by the various models/methods of RS ET determinations.

In fact, there is a need to investigate thoroughly with the various water users, decision makers and stakeholders in general, what are the acceptable limits of ET uncertainty for their application. Furthermore, the various RS ET models are being continuously improved, calibrated and refined, so that they may achieve different degrees of accuracy and therefore be selected in principle for multiple applications, or not be able to achieve at all the acceptable limits due to intrinsic limitations.

As a first attempt to provide a categorization of the type of applications, the quantitative order of magnitude of water involved per application, and the corresponding acceptable limits of uncertainty are reported in Table 5.

Table 5: Draft categorization of application type, order of magnitude of water amount per application, approximated acceptable limits of uncertainty per application, and likely classes of RS ET model and satellite to be used

Application type	Order of magnitude of water amounts involved	Approximate acceptable uncertainty (\pm or %)	Likely RS ET model classes to be used ⁽¹⁾	Likely satellite classes to be used
National Water Balance	Million Cubic Meters (on a yearly basis)	5 – 10%	SEB or thermal-PM	Geostationary MODIS/VIIRS Landsat/S2
River Basin Water Balance	Million Cubic Meters (on a yearly basis)	5 – 10%	SEB or thermal-PM	MODIS/VIIRS Landsat/S2
Irrigation District Allocation	ThoUnited States of Americans Cubic Meters (on a yearly basis)	5 – 15 %	SEB or thermal-PM or SIMS	MODIS/VIIRS Landsat/S2
Seasonal Crop Water Use per Parcel	Hundreds Cubic Meter	10 – 15 %	SEB or thermal-PM or SIMS	Landsat/S2
On-farm Irrigation Management	Variable from a few to several mm depending on the period of crop cycle considered and on irrigation method	\pm 1 mm/day \pm 5 mm/week \pm 5-20 mm/month \pm 50-100 mm/year	SEB	Landsat/S2
Ground Water Use	Variable Million Cubic Meters	5 – 15 %	SEB or thermal-PM	Geostationary MODIS/VIIRS Landsat/S2
Inter-basin allocation (compliance with water rights/water regulation)	Variable Million Cubic Meters	5 – 10 %	SEB	MODIS/VIIRS Landsat/S2

⁽¹⁾ **Note:** SEB = surface energy balance (SEBAL, eeMETRIC, disALEXI) or other LST driven models (SSEBop, PT-JPL); thermal-PM = Penman-Monteith method using thermally derived land surface temperature to inform the PM parameters; SIMS = vegetation-index-based estimation of crop coefficient.

Source: Author's own elaboration.

An additional question that can be asked in estimating acceptable uncertainty and error in a RS ET model (or any model for that matter) is what amount of error will cause severe damage to the water management, water balance or water regulation system? In other words, if a regulation entity must begin to curtail groundwater pumping to a sustainable, long term level, how much error in the ET estimate will create severe economic damage? Will a substantial overestimation of ET result in too many water users being incorrectly curtailed from pumping or irrigating? This creates both economic and personal/emotional harm to those incorrectly curtailed. By the same token, will a substantial underestimation of ET result in too much water consumption that result in unrecoverable aquifer depletion?

Even though RS of ET methods do have error and uncertainty, one can ask what the alternative to estimating total water consumption over an area is. Clearly, and at the present time, parcel-by-parcel measurement of ET (or well-by-well metering) is cost prohibitive. Application of the traditional crop coefficient x reference ET approach may be too general and it may overstate ET because its standardized form and crop coefficients assume full water availability, which may not be the case. A basin water balance may be too general for managing diverse water users within the basin.

Therefore, as cycling through these questions and deliberations, one may need to conclude that RS of ET models, although they have uncertainty and potential bias, may be a primary solution and means to assess water consumption on large scale. Selection of an appropriate model will require study and effort.

A semi-empirical decomposition of uncertainty for RS of ET. As discussed earlier, a number of factors affect the accuracy of daily, monthly and annual values for spatial ET estimates produced by RS of ET. These factors include user capabilities in the case of manually operated models, such as the manual versions of METRIC and SEBAL, and they include the user's ability to review and confirm the good performance of a model. These capabilities depend on user experience and understanding of the RS model and its physical processes, familiarity with the vegetation types in a region, and familiarity with expected ranges of ET according to energy availability for evaporating water.

The accuracy of RS of ET interpolated over several days also depends on the number of clear-sky satellite images per month and year, types of vegetation, and the time of year.

A way of accounting for these additional factors (user skills and interpolation) in expressing the accuracy in RS ET can be done through estimating the accuracy in the daily reference ET fraction (ET_rF ; chapter 2.4.2), intended to normalize relative errors as fraction of reference ET. A semi-empirical expression of RS ET accuracy has been proposed by Rick Allen (personal communication) and derived from the following equation that parses the final estimate of accuracy into three components:

$$\text{Accuracy} = \left(1.0 + \frac{ET_rF_{\text{representation error}}}{n}\right) \left(1.0 + ET_rF_{\text{image_systematic error}} + \frac{ET_rF_{\text{image_random error}}}{\sqrt{n}}\right) - 1.0 \quad (112)$$

where: parameter n represents the number of cloud-free images processed during a month of interest, or a growing season of interest, or a year of interest for a particular location or parcel; $ET_rF_{\text{representation error}}$ represents the ability of any particular image date to specifically represent the net, integrated and averaged ET_rF over a month, or over a growing season or year; $ET_rF_{\text{image_systematic error}}$ represents systematic user error in ET_rF ; $ET_rF_{\text{image_random error}}$ represents random user or model error that results in over- and under- estimation of ET_rF that is expected to vary from image date to image date.

ET_rF is the actual ET expressed as a fraction of reference ET for a specific date and location (pixel or parcel), and generally ranges from 0 (no ET) to about 1.0 (for the alfalfa reference) and to about 1.4 (for the grass reference). The reference ET can be either the standard grass ET_o or it can be an alfalfa reference ET (ET_r) that is used in METRIC. Alfalfa reference ET is generally 20 to 40 percent greater than ET_o due to the taller and leafier alfalfa characteristics and generally, alfalfa reference ET can be used to represent a maximum ET value based on available environmental energy. In the above equation, the use of either grass reference ET or alfalfa ET is valid.

The $(1.0 + ET_rF_{\text{representation error}}/n)$ expression represents the expected error in the monthly or growing season ET_rF estimate under perfect model estimation, but where the time integrated ET, by necessity, is estimated based on one or more periodic satellite image dates. Division of $ET_rF_{\text{representation error}}$ by n considers the reduction in representation error as more image dates are processed per month or growing season. This is similar to repeated sampling. ET_rF varies during the growing season as crops grow and more fully cover the ground. Generally, a Landsat image is made available every eight days if two Landsat satellite systems are in orbit. However, the cloudiness of images or parts of images reduces the number of clear dates per month to as few as one or two for representing the ET_rF (or ET_oF) for that month. Cloudiness can reduce the number of clear views by Landsat to as few as 5 to 20 over a growing season. $ET_rF_{\text{representation error}}$ is estimated to contribute as much as 0.5 (50 percent error) to the error for the growing season average ET_rF if only a single image date is used to represent the season-long ET_rF . Of course, using a single image date to represent the growing season

is not advised. $ETrF_{\text{representation error}}$ is estimated to be 0.15 for a single image date used to represent monthly ETrF. Increasing the number of image dates is expected to improve the definition of the ETrF curve during a month or during the year by more accurately following the progression of ETrF as crops develop during the spring or during the growing season and as they senesce in the fall. $ETrF_{\text{representation error}}$ also applies to the variation in ETrF over time caused by surface wetting by individual irrigation events on individual fields.

The second parenthetical expression in Eq. 112 estimates an adjustment to the overall error in the ETrF estimate introduced by any systematic and random user error or model error. Systematic user error in ETrF ($ETrF_{\text{image_systematic_error}}$) can be caused by a lack of understanding by the user of a need to impose limits on model output due to energy availability to evaporate water, or by the tendency for the RS ET model to consistently over- or under- calibrate ET images.

Random user or model error ($ETrF_{\text{image_random_error}}$) represents an over- or under- estimation of ETrF that is expected to vary from image date to image date. The division of the $ETrF_{\text{image_random_error}}$ term by the square root of n represents the reduction in random error expected from the impact of repeated sampling over multiple locations (fields) for the same crop type or over multiple image dates for any particular location. This term represents the error of the mean that reduces with the square root of the number of observations (McDonald, 2015). $ETrF_{\text{image_random_error}}$ includes the reduction in uncertainties in ETrF that may stem from a random error in calibration or processing of individual images, including RS ET model calibration. $ETrF_{\text{image_systematic_error}}$ and $ETrF_{\text{image_random_error}}$ are additive. Variable n in Eq. 112 can represent the number of clear images for one location or field, or it can represent the number of fields that are sampled and aggregated into a single estimate of ET.

The reader is encouraged to read ANNEX II for an applicative example of semi-empirical decomposition of RS ET uncertainty using METRIC.



©FAO



8. PROSPECTS FOR THE NEAR FUTURE

The missions and technology of satellites are unfolding at a rapid pace so that remote sensing applications are broadening, accuracy is increasing, and spectral, temporal and spatial resolutions are becoming more granular.

The programmes around space science are very active and it is challenging to be updated on everything is on-going.

Here we are providing just some brief background on four flagships programmes for the near future, with particular attention to the determination of ET: (i) ECOSTRESS from the National Aeronautics and Space Administration (NASA, United States of America); Copernicus from the European Commission (EU); WaPOR phase II from FAO; and Hydrosat (private company).

Obviously, the reader is highly recommended to visit the web pages of these programmes for a more comprehensive and updated information.

8.1 ECOSTRESS

The ECOSTRESS mission (The **ECO**system **S**paceborne **T**hermal **R**adiometer **E**xperiment on **S**pace **S**tation) was built by NASA's Jet Propulsion Laboratory and was launched to the International Space Station on June 29, 2018 (Fisher *et al.*, 2020).⁵⁵ The primary measurements are in the thermal infrared, which are combined with ancillary meteorological and surface reflectance data to produce data products for surface temperature, ET, vegetation water use efficiency (WUE), and the Evaporative Stress Index (ESI). ET and ESI are derived through the PT-JPL model, while the Gross Primary Production (GPP) for WUE is derived through the Breathing Earth System Simulator (BESS; Jiang and Ryu, 2016; Jiang *et al.*, 2020).

The surface temperature is measured through a multispectral thermal infrared radiometer (Prototype HypsIRI Thermal Infrared Radiometer - PHYTIR) capturing instantaneous scenes of 400 km² with wavelength ranging 8-12.5 μm , 38x69 m ground resolution and 1-5-day repeat in low Earth orbit (LEO). However, the data are further processed for the users to reach an operational ground resolution of 70 m., except than the poles, the coverage of ECOSTRESS is essentially global (50S-50N).

The distinctive feature of ECOSTRESS is the combination of high spatial resolution and high temporal resolution in the thermal bands, at least relative to Landsat.

Several applications of ECOSTRESS data are continuously developing within domains from agriculture, to natural forests, volcanoes, urban sector, coastal ecology, geology, etc.

⁵⁵ NASA. Jet Propulsion Laboratory. California Institute of Technology. ECOSTRESS. <https://ecostress.jpl.nasa.gov/>

8.2 Copernicus

Copernicus is the European Union's Earth observation and monitoring flagship programme offering information "services", specifically designed to meet user requirements, drawing from satellite Earth Observation and in-situ (non-space) data such as airborne, seaborne and ground-based measurement sensors⁵⁶. While the satellite data cover the whole globe, they suit also local and regional needs.

The Programme is coordinated and managed by the European Commission in cooperation with partners such as the European Space Agency (ESA) and the European Organization for the Exploitation of Meteorological Satellites (EUMETSAT).

The different dedicated satellites serving the Copernicus programme are part of a constellation (the Sentinel family), eight of which have been already launched and recurrent satellites will be launched to ensure the operational continuity of the Sentinels beyond 2030. In addition to the Sentinel family of satellites, Copernicus uses additional contributing missions to make the earth observation and monitoring more comprehensive.

Copernicus delivers near-real-time data that are analyzed and processed to monitor trends and changes, to derive maps, identify features and anomalies and extract statistical information, which are addressing six thematic streams of "services": the Copernicus Atmosphere Monitoring Service (CAMS), the Copernicus Marine Environment Monitoring Service (CMEMS), the Copernicus Land Monitoring Service (CLMS), the Copernicus Climate Change Service (C3S), the Copernicus Emergency Management Service (CEMS) and the Copernicus Security Service. The information provided by the services is free and openly accessible to all users.

The "services" of main interest for agriculture are : (i) the one on land monitoring (CLMS), particularly through its components on 'Land cover and land use mapping' provided through satellite data of Sentinel 1 and 2; (ii) the ESA satellite ground segment, particularly for the data on land surface temperature coming from Sentinel 3 and land surface reflectance coming from Sentinel 2; and (iii) C3S for the access to global, near-real-time surface and atmospheric meteorological parameters.

Regarding Sentinel 2, there are two twins polar-orbiting satellites (sun-synchronous) equipped with a multi-spectral optical sensor detecting 13 spectral bands (in the visible, in the near infrared and in the short-wave infrared). The spatial resolution can be 10 to 20 m, depending on the spectral band, with a revisit time at the equator of 5 days (with both satellites operating).

Also for Sentinel 3 there are two twins near-polar orbiting satellites (sun-synchronous), but equipped with different sensors, of which the one of interest for ET is the Sea and Land Surface Temperature Radiometer (SLSTR), which is a dual view scanning radiometer with 3 spectral bands in the thermal infrared and 6 in the visible, near and short-wave infrared. The spatial resolution is 1 km for the thermal bands with a revisit time of 1 day (under clear sky and both satellites operating).

However, new monitoring missions are planned for the near future (Copernicus 2.0) of which the key one for the determination of ET is the Land Surface Temperature Monitoring (LSTM) mission. The LSTM mission, expected to be launched not before the end of 2028, has the objective of providing high spatio-temporal resolution Thermal Infra-Red (TIR) observations over land and coastal regions.

The two satellites of the LSTM mission will be equipped with multi-spectral sensor detecting 11 spectral bands (5 in the thermal infrared, 4 in the visible and near infrared, and 2 in the short-wave infrared). The spatial resolution will be of 50 m (37 at nadir), with a revisit time of 2 days at the equator (under clear sky and both satellites operating). The targeted accuracy in ET is 15 percent mm d^{-1} (threshold 20 percent) and a precision of 5 percent (threshold 10 percent) over a field scale of 0.5 ha.

In waiting for the launch of the LSTM mission, there have been determinations of ET using data from the SLSTR radiometer on Sentinel-3 and the optical observations from multispectral instrument (MSI) on Sentinel-2. This approach was developed by Guzinski and Nieto (2019) to derive ET at 20m resolution in an agricultural

⁵⁶ Copernicus. <https://www.copernicus.eu/en>

landscape in Denmark and Italy, using a Two-Source Energy Balance (TSEB) modeling scheme (Norman *et al.*, 1995 and Kustas and Norman, 1999). To reach the fine resolution ET estimates, the thermal observations by SLSTR (at 1 km resolution) have been sharpened using the optical observations taken by MSI (at 20 m resolution), some additional ancillary RS data (e.g. DEM), and a machine learning algorithm based on the data sharpening approach of Gao *et al.* (2012), followed by flux disaggregation using the scheme of Guzinski *et al.* (2014).

The higher resolution ET maps were compared in part against field eddy covariance measurements and in part against ET maps obtained from Landsat. Results indicated, on the one side, the overall applicability of the proposed methods to be used with Sentinel-2 and Sentinel-3 images to obtain high-resolution ET estimates and, on the other side, the inherent limitations of these methods in terms of achievable accuracy. Guzinski and Nieto (2019) pointed out that while the methodologies proposed are valuable for filling in data gap, the accuracy is considerably less than what would be possible with high-resolution thermal infrared (TIR) observations, indicating the need for direct high-resolution TIR to complement the existing capabilities of the Sentinel satellite constellation.

These findings were confirmed also in another study of Guzinski *et al.* (2020) where the sharpening method of the TIR of Sentinel 3 with the optical MSI observation of Sentinel 2 was used to derive ET through METRIC, Priestley-Taylor TSEB (Kustas *et al.*, 2016), and the End-member-based Soil and Vegetation Energy Partitioning (ESVEP, Tan and Li, 2017), and comparing ET against field eddy covariance. This was followed by another study, Guzinski *et al.* (2021), where the methodology was applied at the country extent and evaluated against flux tower measurements and ET estimates from the FAO WaPOR database (wapor.apps.fao.org/). Although with a relative RMSE of instantaneous latent heat flux of around 30 percent in agricultural areas, the proposed methodology is a sound solution to the lack of high spatio-temporal resolution of TIR observation for ET modeling and can fill this data gap until the next generation of thermal satellites are launched.

8.3 WaPOR Phase II

The basic features of WaPOR have been described in chapter 4.2.⁵⁷

The WaPOR II, launched in June 2019 and expected to continue at least until 2025, is an extension of the phase 1 of WaPOR which intended to provide mainly actionable information at three levels (250 m, 100 m and 30 m), to cover river basins, countries and irrigation schemes. Key data and information provided, among others, are actual evapotranspiration and interception (ETIa) and water productivity (WP) of agricultural land.

The phase 2 of WaPOR is also taking advantage of the various quality assessments periodically conducted to improve methods and accuracy. Some functionalities of the portal have been updated (such as the ability to explore, overlay and compare the United States of America and external partners' data sources) and new ones have been added (such as cumulated time series, direct comparison on the charts between different areas or different period). New and higher quality documentation is also provided.

This second phase of WaPOR intends to support partner countries in monitoring and improving water and land productivity, of rainfed and irrigated agriculture, through three project components:⁵⁸

(i) continue to expand the coverage of the WaPOR database, containing data related to biomass production, evapotranspiration and agricultural land and water productivity in Africa and the Near East, ensuring an uninterrupted data availability dating back to 2009 and that will continue to be archived in quasi real-time.⁵⁹ The data at 30m resolution will be created for partner countries aiming at specific field applications, such as

⁵⁷ FAO. 2023. WaPOR, remote sensing for water productivity. <https://www.fao.org/in-action/remote-sensing-for-water-productivity/en/>

⁵⁸ FAO. 2023. WaPOR, remote sensing for water productivity. WaPOR data. <https://www.fao.org/in-action/remote-sensing-for-water-productivity/wapor-data/en>

⁵⁹ FAO. WaPOR 2.1. 2019. https://wapor.apps.fao.org/home/WAPOR_2/1

monitoring pest and diseases of crops or developing high-precision irrigation scheduling. The input data of WaPOR database continue to be processed and provided by a Consortium comprising eLEAF and VITO;

(ii) focus on a large capacity development programme to enhance the capacity of local stakeholders of partner countries to make use of the WaPOR database in the elaboration of practical solutions to locally-identified issues, and end-users to put them in practice. The capacity development will also cover policy-relevant applications that support sustainable water management, water governance and agricultural policies. The capacity development efforts will account for long-term sustainability, focusing on partner countries that can continue to provide services after the end of the project;

(iii) co-design and co-develop user-centered solutions and practical tools to effectively improve agricultural land and water productivity at different scales. Such solutions and tools might vary from practical ICT solutions to improve agricultural production systems (e.g. monitoring of the health of specific crops in the fields), to de-risk investments (e.g. credit and insurance), to support water management (e.g. modernization of irrigation systems), to water governance (e.g. water accounting and auditing) and agricultural policies in river basins and countries, etc. With this component, and in combination with capacity development efforts, the project aims to create a community of practice.

Partner countries in WaPOR phase 2 are Algeria, Mali, Tunisia, Iraq, Jordan, Palestine, South Sudan, Ethiopia, Egypt, Kenya and Mozambique. Local stakeholders include research institutes, universities, policy-makers, extension service officers, water user groups, irrigation scheme managers, local and international NGOs, relevant private companies, and others.

The international partners are IHE-Delft Institute for Water Education and the International Water Management Institute (IWMI).

The intended outcome of the project (continued to be funded by the Ministry of Foreign Affairs of the Kingdom of the Netherlands) remains the *increased capacity of FAO members in monitoring terrestrial biomass production and evapotranspiration to assess land and water productivity in rainfed and irrigated agriculture, and contribute to sustainable crop production intensification adapted to a changing climate.*

8.4 Hydrosat

Hydrosat is a space and data analytics company providing geospatial intelligence for agriculture, food security, public safety, climate and environment, through high resolution thermal imagery monitored globally, with a major focus on the determination of water consumption of land (evapotranspiration) (Fisher et al 2022).⁶⁰


A major driver behind the establishment of Hydrosat is the need to fill the gap in simultaneous high resolution of spatial and temporal scales of thermal measurements, necessary to adequately capture the large variability and dynamics of the processes involved in land-vegetation-water-atmosphere exchange.

The targeted spatial resolution is set at 10 m and 50 m pixels in the Visible and Near-Infrared (VNIR-seven bands) and in the Long Wavelength Infrared (LWIR-multiple bands), respectively, with daily revisits (and multiple time per days in the long-term).

To achieve these resolutions, Hydrosat is launching a constellation of 16 sun-synchronous satellites, progressively starting from 2024 (at 500-550 km altitude – Low Earth Orbit), hosting a new generation of thermal sensor with accuracy of LWIR measurements equivalent to that of Landsat.

The innovative feature of the thermal sensor mounted on the Hydrosat satellites is in the elimination of the cryocooling, required by traditional thermal sensors like the one of Landsat, Sentinel 3 and ECOSTRESS, among others. Cryocooling is very expensive, energy intensive and utilizes large mass and volume.

⁶⁰ HYDROSAT, Inc. 2022. <https://www.hydrosat.com/>



The thermal sensor of Hydrosat is based on the “microbolometer” technology, measuring radiant heat by means of a material having a temperature-dependent electrical resistance and typically used as a detector in thermal cameras. The sensor is compact (about the size of a coffee can), accurate, low-cost, and without the need of cryocooling. The drawback of the microbolometer is in the long response time, which restitutes blurred images in fast moving objects.

While the microbolometer technology is consolidated and already used on remote sensing (e.g. installed in the Thermal Emission Imaging Spectrometer –THEMIS– mounted on board of the NASA’s Mars Odyssey, launched in 2001), the long integration time causing the blurry effect was not resolved, until Hydrosat overcame the problem through a breakthrough solution (not yet publically disclosed). The Hydrosat microbolometer was tested over time and is being readied for space launch.

In this way, the 16-satellite constellation will enable an unprecedented high-spatial, multi-spectral VNIR and LWIR measurements, on a daily temporal resolution. This will represent a game-change for different agricultural and ecosystem applications, including vegetation health, crop water stress, irrigation recommendations, and yield forecast.

A series of analytic products regarding these applications are already provided by the Hydrosat platform currently through their ‘Fusion Hub’, which provides surface temperature at 20 m pixel, obtained through the fusion of satellite data inputs from MODIS, VIIRS, Landsat, ECOSTRESS and the Harmonized Landsat-Sentinel (HLS).

While Hydrosat intends to provide insightful products for commercial and government customers, it offers an Academic Data Use Policy, which allows making data freely available, provided they are not used for commercial purpose.



©FAO



9. CONCLUDING REMARKS

In this final chapter, we provide some reflections, draw some inferences, and convey some key messages about the described and reviewed RS ET models, related databases and portals, and the uncertainty impacts. We'll also look ahead at the near-future perspectives as well, as models continue to evolve, as their use increases and additional testing occurs.

As clearly stated by Fisher *et al.* (2017), "*ET is a keystone climate variable that uniquely links the water cycle (evaporation), energy cycle (latent heat flux), and carbon cycle (transpiration-photosynthesis tradeoff)*". In agriculture and other vegetated systems, the determination of ET is crucial for several applications including, among others, water accounting, enforcing water regulations, sustainable water resources allocation and management (irrigation in primis), and analysis of ecosystem functioning. Furthermore, the imperative of knowing ET is amplified by the anticipated impact of climate change. It is the ET process that transforms liquid water into vapor and causes water to leave the water resource system. Because of the volumes of ET required to produce vegetation are large, ET has a very large impact on liquid water resources.

It is clear that satellite remote sensing (RS) represents the most suitable method to capture the large variability in ET over large areas and over time. Nevertheless, the determination of ET through RS comes with several challenges, and making the readers aware of these challenges is among the objectives of this publication.

In this regard, we wish to distinguish between at least two types of readers and users of this publication: one type that is interested in the possibility of applying a RS ET model; and one type that is interested in using the ET data provided by the databases and portals (platforms) associated with the RS ET models. To make reliable choices regarding the model or the platform to select, both of these reader types need to identify the *purpose* for which the ET data are going to be used and the various assumptions, theory and data sources from which the ET data are being, or have been, derived. In fact, the *purpose* may be a primary determinant in the selection of the most appropriate spatial and temporal scales, the preference or suitability of a complete surface energy balance model, a one-source or two-source type of model, and the uncertainties in model parameterization and how that model addresses those uncertainties, that can be considered acceptable. In turn, the assumptions, theory and data sources will be determinant in deciding on the suitable RS ET model to use and in understanding the likelihood and risks of exposure to errors that can possibly occur.

We have observed that in general there is an inverse relationship between spatial scales and temporal scales for the satellite imagery of interest. This is particularly true for satellites providing thermal infrared radiation, i.e. instantaneous thermal images with higher spatial resolution (e.g. with 60 m – 100 m pixels, like those of Landsat) that have a 16 day interval between two overpasses for the same satellite. Vice versa, daily (or twice-a-day) instantaneous thermal images (like from MODIS or VIIRS) have 1 km and 375 m pixel sizes. We have also the case of geo-stationary satellites (like GOES and Meteosat) that monitor the land surface temperature nearly continuously, but at a spatial scale of 2-10 km.

The future prospect is to hopefully reduce (if not to eliminate) the trade-off between space and time resolutions through missions of new generation of satellites (e.g. VIIRS that is already retrieving LST at 375m every day; Sentinel 3 that retrieves the LST at 300 m ground resolution every 2 days; or ECOSTRESS that has an interval between overpasses of a maximum five days, depending on latitude, with an operational pixel size of 70 m), or using a constellation of satellites carrying a similar type of sensor and that may provide the LST on a 10 m pixel every day (like is anticipated for the *Hydrosat* satellite constellation that may be planned to be launched in 2024, or the LSTM, TRISHNA and SBG missions from 2025 onward).

Overall, the projected spatial and temporal resolutions for a global coverage in the future are down to 10 m and at a one/two-day or even a sub-daily scale, respectively, and are associated with a relative error of less than 10 percent (Fisher *et al.*, 2017). These developments paint a bright future for the use of LST-based RS ET models for producing high resolution ET on a nearly continuous basis.

Presently, the trade-off between space and time resolutions has been in part addressed by several techniques of data fusion (merging and leveraging images of different spatial and temporal resolutions) and data sharpening (to increase the ground resolution of ET maps). In fact, the improvement in ground resolution assumes great relevance for local applications (e.g. irrigation water consumption and scheduling, small watershed water balances, groundwater depletion, etc.).

It is important to recognize that multiple sources of inputs will incrementally feed RS ET models as new satellite missions, with new sensors at higher spectral resolution, are launched so that the practice of data fusion and data sharpening will become more common and more sophisticated while being supported by the higher computing power of the 'cloud'. However, we recognize that these data processing techniques increase the risk of additional biases as well as the confounding of the sources of biases.

The reader can refer to Table 2 in chapter 3 and Table 3 in chapter 5 for information related to the spatial and temporal resolutions of the various RS ET models and platforms, respectively.

In particular (Table 2), we can observe that SEBAL and METRIC remain the most used and applied at the local level worldwide, particularly for agricultural related domains, followed by DisALEXI, SSEBop and PT-JPL. ALEXI and ETMonitor can be considered more suited for covering large scale (from national to continental to global). ETLook and PT-JPL are expected to cover the entire range from field to continental. ETWatch is a special case where the most suitable scale is the basin and the region, but it can scale down also to the irrigation district scale.

All RS ET models presented serve agriculture water management in one way or another. Though, the formulation of each model carries over a certain degree of complexity, which implies specific algorithms, parameterization and associated risks of uncertainty. As seen in chapter 7, a more complex model is not necessarily more accurate. In fact, in the figures 11 and 12 of chapter 7.2.1 we have seen that SSEBop (considered one of the relatively simplest model presented) can perform similarly to the other more complex models, on extended spatio-temporal scales.

An attempt to rank the various models in terms of their relative complexity is reported in Table 6.

Table 6: Tentative ranking of model relative complexity.

RS ET Model	Degree of Complexity
ALEXI/DisALEXI	High
ETLook	High
ETMonitor	High
ETWatch	High
SEBAL	Moderate
METRIC	Moderate
SSEBop	Low
PT-JPL	Low

Source: Author's own elaboration.

In chapter 7, we have seen how different sources of error affect the RS ET models (e.g. the cloudiness and contamination of the atmosphere, the variability of the underlying land surface, wind patterns, vapor pressure of the atmosphere, uncertainty in impacts of surface roughness, atmospheric stability, and geo-registration,

among others).

Furthermore, the RS input variables for ET determination are mostly instantaneous at the time of the satellite overpass, and therefore, additional sources of uncertainty are introduced during the time integration of ET over the daytime hours and in the time interpolation of daily ET values over the interval between two satellite overpasses.

Moreover, some computations like 'data sharpening', 'data fusion' and 'cloud masking' can all propagate further uncertainties, in addition to those introduced by the skill level and knowledge of the operators behind all the various calculations and data handling.

Finally, the estimation or calibration of the algorithms' parameters at a local level remains a challenge for all models. METRIC, ETMonitor and ETWatch rely heavily on parameter or surface energy balance calibration within the area of ET determination. SEBAL, SSEBop, ETLook, PT-JPL and ALEXI/DisALEXI use mostly parameterizations that are based on inputs obtained only by remote sensing and ground-based data sets (where reliable).

This brings us to a fundamental consideration, i.e. the accurate representation of local conditions, particularly in complex landscapes having drastic changes in the micrometeorological variables and land surface properties, such as transitions from hot, dry desert to cool, wet irrigated agriculture. These stark transitions and heterogeneities can play an important role in the accuracy of RS ET determinations (Liu *et al.*, 2021). Where the landscape is mostly uniform (e.g. flat and extensive field crops) and the meteorological conditions are fairly even (e.g. clear sky, moderate wind) the likelihood is higher to obtain accurate ET with any model, but when the terrain is significantly variable in elevation, slope, aspect, wetness, vegetation cover, etc., and the meteorological conditions are substantially uneven (e.g. variable humidity and temperature of the near-surface air, cloudy conditions, fluctuations in wind speed, etc.) the likelihood to obtain accurate ET is reduced and accuracy will depend on the specific model and how it incorporates and recognizes the land/atmosphere variability.

While all RS ET models use, directly or indirectly, Digital Elevation Models (DEMs) to characterize the land conditions, it is worth highlighting differences among RS ET models in their incorporation of the additional land/atmosphere variability. On the one end, some of the RS-ET models based on SEB (SEBAL, METRIC, ALEXI-DisALEXI) incorporate additional land/atmosphere variability through pixel-specific estimation of aerodynamic resistance, which accounts for the structural vegetation and wind characteristics, along with the stability conditions of the atmosphere. On the other end, the RS-ET models based on Priestley-Taylor (PT), Penman-Monteith (PM) or Shuttleworth-Wallace (SW), as is the case for PT-JPL, ETLook, ETWatch and ETMonitor, incorporate the additional land/atmosphere variability through aerodynamic resistance and surface resistance (largely as functions of radiation, air temperature, moisture content of the soil, and vapor pressure deficit of the atmosphere). Conceptually, we can say that the land/atmosphere variability characterizations are much more skewed towards the estimated vegetation responses to the local environmental conditions in the RS ET models based on PT, PM and SW, than those based on SEB. This implies different exposures to risks of error in determining ET. In other words, there is a trade-off in selecting one model or another, depending on how accurately they capture the variability in ET and behavior by the local conditions. The SSEBop model is a special case as it does not use either aerodynamic or surface resistance.

The best RS ET determinations show uncertainty in the range of 10-20 percent. Furthermore, it has been observed that, overall, the RS ET uncertainty tends to decrease going from smaller to larger spatial scales and from shorter to longer time scales.

Thus, the importance and applicability of utilizing high-resolution input data and of the representation of local conditions in heterogeneous croplands, particularly for precision agriculture management, cannot be understated (e.g. Wu *et al.*, 2022). In fact, numerous efforts have been made to develop methods that merge multiple remote sensing data and ground-based measurements to improve the precision of spatial and temporal mapping of ET at regional and global scales (e.g.: Yao *et al.*, 2017; Jiménez *et al.*, 2018; He *et al.*, 2020). The most recent approaches use the machine learning method (Shang *et al.* 2020) and neural networks to integrate satellite-derived evapotranspiration products, eddy covariance observations and ancillary information (Shang

et al. 2021). However, these methods add another layer of complexity and exposure to error and assumptions, and are in experimental stages (not yet operational).

The most difficult cases are represented by environments characterized by high cloudy conditions. All models requiring LST are mostly excluded from accurate ET estimation in regions having extensive cloudiness, and the major attempt to obtain ET is through those models that use microwave radar to estimate soil-surface moisture content (e.g. ETMonitor and ETWatch). This approach is however prone to error due to the coarse scale of the microwave radar (25 km pixel size) and due to the interference of the vegetation covering the soil. The hope is that the next generation of active microwave radar will significantly improve the determinations in cloudy conditions.

The considerations made for the RS ET models remain valid for the databases and portals (platforms) that provide ET data derived from their corresponding model (chapter 5). Also in this case, the selection of the best fitting platform will again depend on the *purpose* for which the ET data are going to be used and the assumed *boundary and underlying conditions* of the land-atmosphere system in which the ET data are being, or have been, derived.


The most critical aspect of the provided RS ET data remains in their associated uncertainty. In fact, none of the ET data provided by the platforms comes with a \pm <uncertainty> (either in absolute or percentage value). This provision is very difficult to produce, especially for those platforms that tend to cover large areas where uncertainty is to vary in space and time. Furthermore, these uncertainties tend to propagate and compound as more computational procedures are incorporated into the model, as previously indicated (e.g. data fusion, data sharpening; could masking, gap-filling and time integration/interpolation). And one does not want to forget the previously mentioned contributions of the skills and understandings of the operator of the model to the overall uncertainty.

It is part of the research nature that modeling groups tend to describe and project their models in the most positive ways and present comparisons that show the most promising results. However, we strongly encourage all modeling groups to expand the scope of their work towards producing dependable estimates of uncertainties in RS ET products that may vary with location, vegetation type and time of year. These estimates, which are probably best known or estimated by the model developers and operators, will be invaluable in guiding users of RS ET data on expected uncertainties and biases when employed to estimate water consumption and regulation. This places a large burden on developers and users alike, but we recognize that estimation of error and bias is imperative to the acceptance and adoption of spatially and remotely derived estimates of ET into operational practice.

Therefore, a way to proceed forward is to always perform some sort of validation or comparison of data provided by a model and/or platform with some 'references' (trusted field measurements of ET; inter-comparison with higher-standard models, etc.). However, these 'references' have in turn their own limitations. As we have seen in chapter 7.1, the validation against eddy covariance measurements suffer from uncertainty due to the lack of energy balance closure and the pixel-to-footprint risk of mismatch, as well as improper handling and locating instrumentation. The validation against lysimeters suffers from uncertainty due to the possible lack of representation by the lysimeter of the field surrounding the lysimeter itself (soil moisture and canopy cover uniformity). The validation on large scale conducted with hydrological models suffers from uncertainty due to often incomplete identification of the boundary conditions, field-to-field variation and lack of satisfactory field data, etc.

In summary, there is not an easy way to select an appropriate model or approach and to put RS ET data into an operational system for management, monitoring or regulation. But this is the reality where progress proceeds incrementally, and therefore the RS ET models must continue to be explored, evaluated, scrutinized, tested, and refined (Fisher *et al.*, 2017). The scrutiny and testing is additionally required for the platforms and the operational products made available either publically (e.g. SIMS) or commercially (e.g. IrriWatch).

We need to be aware of the challenges, tradeoffs and limitations we are facing when dealing with RS ET determinations. The complexity of the systems we are dealing with cannot be a justification for not becoming



more aware of such technologies and their challenges, tradeoffs and limitations and thereby proceeding blindly into the decision-making process involving the sustainable management of such a precious resource as water.

The future of RS ET determination appears to be bright, offering continuously new opportunities. It is valuable that a large number of competing groups of RS ET developers are offering methods and data that can be inter-compared and contrasted. This should make it easier and more apparent in recognizing 'truth'. It is upon the user to seize these opportunities wisely.

10. REFERENCES

- Affholder F., Tilton P.A., Corbeels M. and Roux S. 2012. *Ad hoc modeling in agronomy: what have we learned in the last 15 years?*. Agron. J., 104(3): 735-748.
- Ahmad M.D. 2002. *Estimation of net groundwater use in irrigated river basins using geo-information techniques: A case study in Rechna Doab, Pakistan*. Ph.D. dissertation, 143 pp, Wageningen, Netherlands.
- Allen R.G. 1996. *Assessing integrity of weather data for reference evapotranspiration estimation*. J. Irrig. Drain. Eng., 122(2): 97-106.
- Allen R.G., Pereira L.S., Raes D. and Smith M. 1998. *Crop evapotranspiration-Guidelines for computing crop water requirements*. FAO Irrigation and drainage paper 56. FAO, Rome, 300p.
- Allen R.G., Pruitt W.O., Raes D., Smith M. and Pereira L.S. 2005. *Estimating evaporation from bare soil and the crop coefficient for the initial period using common soils information*. J. Irrig. Drain. Eng., 131(1): 14-23.
- Allen R.G., Tasumi M. and Trezza R. 2007a. *Satellite-based energy balance for mapping evapotranspiration with internalized calibration (METRIC) - model*. J. Irrig. Drain. Eng. ASCE, 133: 380-394.
- Allen R.G., Tasumi M., Morse A., Trezza R., Wright J.L., Bastiaanssen W., Kramber W., Lorite I. and Robison C.W. 2007b. *Satellite-based energy balance for Mapping evapotranspiration with Internalized Calibration (METRIC) - Applications*. J. Irrig. Drain. Eng., 133(4): 395-406
- [[https://doi.org/10.1061/\(ASCE\)0733-9437\(2007\)133:4\(395\)](https://doi.org/10.1061/(ASCE)0733-9437(2007)133:4(395))].
- Allen R.G. and Pereira L.S. 2009. *Estimating crop coefficients from fraction of ground cover and height*. Irrig. Sci., 28: 17.
- Allen R.G. 2010. *Modification to the FAO-56 soil surface evaporation algorithm to account for skin evaporation during Small Precipitation Events*. Memorandum prepared for the UI remote sensing group, revised May 16, 2010, August 2010, 9p.
- Allen R.G., Hendrickx J., Bastiaanssen W.G.M., Kjaersgaard J., Irmak A. and Huntington J. 2010a. *Status and continuing challenges in operational remote sensing of ET*. In: ASABE 5th National Decennial Irrigation Conference Proceedings, edited, Phoenix Convention Center, Phoenix, Arizona.
- Allen R.G., Kjaersgaard J., Trezza R., Oliveira A., Robison C. and Lorite-Torres I. 2010b. *Refining components of a satellite based surface energy balance model to complex-land use systems*. Proceedings of the remote sensing and hydrology symposium, Jackson Hole, Wyo, IAHS. Oct. 2010. 3 p.
- Allen R.G. 2011. *Skin layer evaporation to account for small precipitation events - an enhancement to the FAO-56 evaporation model*. Agric. Water Manage., 99: 8-18.
- Allen R.G., Irmak A., Trezza R., Hendrickx J.M.H., Bastiaanssen W., Kjaersgaard J. 2011a. *Satellite-based ET estimation in agriculture using SEBAL and METRIC*. Hydrol. Process., 25: 4011-4027.
- Allen R.G., Pereira L.S., Howell T.A. and Jensen M.E. 2011b. *evapotranspiration information reporting: I. Factors governing measurement accuracy*. Agric. Water Manage., 98(6): 899-920.
- Allen R.G., Burnett B., Kramber W., Huntington J., Kjaersgaard J., Kilic A., Kelly C. and Trezza R. 2013a. *Automated calibration of the METRIC-Landsat evapotranspiration process*. J. American Water Resources Association, 49(3): 563-576.
- Allen R.G., Trezza R., Kilic A., Tasumi M. and Li H. 2013b. *Sensitivity of Landsat-scale energy balance to aerodynamic variability in mountains and complex terrain*. J. American Water Resources Association, 49(3): 592-604.

- Allen R.G., Morton C., Kamble B., Kilic A., Huntington J., Thau D., Gorelick N., Erickson T., Moore R., Trezza R., Ratcliffe I. and Robison C. 2015. *EEFlux: A Landsat-based evapotranspiration mapping tool on the Google Earth Engine*. ASABE Meeting, Paper Number: 152143511.
- Anderson M.C., Norman J.M., Diak G.R., Kustas W.P. and Mecikalski J.R. 1997. *A two-source time-integrated model for estimating surface fluxes using thermal infrared remote sensing*. *Remote sensing environ.*, 60: 195-216.
- Anderson M.C., Norman J.M., Mecikalski J.R., Torn R.D., Kustas W.P. and Basara J.B. 2004. *A multi-scale remote sensing model for disaggregating regional fluxes to micrometeorological scales*. *J. Hydrometeor.*, 5: 343-363.
- Anderson M.C., Norman J.M., Kustas W.P., Li F., Prueger J.H. and Mecikalski J.M. 2005. *Effects of vegetation clumping on two-source model estimates of surface energy fluxes from an agricultural landscape during SMACEX*. *J. Hydrometeor.*, 6: 892-909.
- Anderson M.C., Norman J.M., Mecikalski J.R., Otkin J.A. and Kustas W.P. 2007a. *A climatological study of evapotranspiration and moisture stress across the continental United States based on thermal remote sensing: 1. Model formulation*. *J. Geophys. Res.*, 112: 1-17.
- Anderson M.C., Norman J.M., Mecikalski J.R., Otkin J.P. and Kustas W.P. 2007b. *A climatological study of evapotranspiration and moisture stress across the continental U.S. based on thermal remote sensing: II. Surface moisture climatology*. *J. Geophys. Res.*, 112: 1-13.
- Anderson M.C., Kustas W.P., Norman J.M., Hain C.R., Mecikalski J.R., Schultz L., González-Dugo M.P., Cammalleri C., d'Urso G., Pimstein A. and Gao F. 2011. *Mapping daily evapotranspiration at field to continental scales using geostationary and polar orbiting satellite imagery*. *Hydrol. Earth Syst. Sci.*, 15: 223-239.
- Anderson M.C., Kustas W.P., Alfieri J.G., Gao F., Hain C., Prueger J.H., Evett S., Colaizzi P., Howell T. and Chávez J.L. 2012. *Mapping daily evapotranspiration at Landsat spatial scales during the BEAREX'08 field campaign*. *Advances in Water Resources*, 50: 162-177.
- ASCE-EWRI. 2005. *The ASCE Standardized Reference evapotranspiration Equation*. ASCE-EWRI Standardization of Reference evapotranspiration Task Committee Report, 216 pp., Reston, Virginia.
- Avissar R., Avissar P., Mahrer Y., Bravdo B.A. 1985. *A model to simulate response of plant stomata to environmental conditions*. *Agric. For. Meteorol.*, 34: 21-29.
- Baldocchi D., Falge E., Gu L.H., Olson R.J., Hollinger D., Running S.W., Anthoni P.M., Bernhofer C., Davis K., Evans R., Fuentes J., Goldstein A., Katul G., Law B.E., Lee X.H., Malhi Y., Meyers T., Munger W., Oechel W., Paw U K.T., Pilegaard K., Schmid H.P., Valentini R., Verma S., Vesala T., Wilson K. and Wofsy S.C. 2001. *FLUXNET: A new tool to study the temporal and spatial variability of ecosystem-scale carbon dioxide, water vapor, and energy flux densities*. *Bulletin of the American Meteorological Society*, 82(11): 2415-2434.
- Baldocchi D.D. 2005. *The Role of Biodiversity on the Evaporation of Forests, in Forest Diversity and Function. In: Temperate and Boreal Systems*. Eds. M. Scherer-Lorenzen, C. Körner and E.-D. Schulze, pp. 131-148, Springer Berlin Heidelberg, Berlin.
- Bastiaanssen W.G.M. 1995. *Regionalization of surface flux densities and moisture indicators in composite terrain: a remote sensing approach under clear skies in Mediterranean climates*. PhD Diss., CIP Data Koninklijke Bibliotheek, Den Haag, the Netherlands; pp 273.
- Bastiaanssen W.G.M., Menenti M., Feddes R.A. and Holtslag A.A.M. 1998a. *A remote sensing surface energy balance algorithm for Land (SEBAL), Part 1: Formulation*. *J. Hydrol.*, 212-213: 198-212.
- Bastiaanssen W.G.M., Pelgrum H., Wang J., Ma Y., Moreno J.F., Roerink G.J. and van der Wal T. 1998b. *A remote sensing surface energy balance algorithm for land (SEBAL)—Part 2. Validation*. *J. Hydrol.*, 212-213: 213-229 [https://doi.org/10.1016/S0022-1694\(98\)00254-6](https://doi.org/10.1016/S0022-1694(98)00254-6)
- Bastiaanssen W.G.M. 2000. *SEBAL-based sensible and latent heat fluxes in the irrigated Gediz Basin, Turkey*. *J. Hydrol.*, 229: 87-100.

- Bastiaanssen G.M.W. and Chandrapala L. 2003. *Water balance variability across Sri Lanka for assessing agricultural and environmental water use*. Agric. Water Manage., 58(2): 171–192.
- Bastiaanssen W.G.M., Noordman E., Pelgrum H., Davids G., Thoreson B. and Allen R. 2005. *SEBAL model with remotely sensed data to improve water-resources management under actual field conditions*. J. Irrig. Drain. Eng., 131(1): 85–93 [https://doi.org/10.1061/(ASCE)0733- 9437(2005)131:1(85)].
- Bastiaanssen W.G.M., Pelgrum H., Soppe R.W.O., Allen R.G., Thoreson B.P. and Teixeira A.H. 2008. *Thermal-infrared technology for local and regional scale irrigation analyses in horticultural systems*. Acta Hort., 792: 33–46.
- Bastiaanssen W.G.M., Cheema M.J.M., Immerzeel W.W., Miltenburg I.J. and Pelgrum H. 2012. *Surface energy balance and actual evapotranspiration of the transboundary Indus Basin estimated from satellite measurements and the ETLook model*. Water Resour. Res., Vol. 48, W11512, doi: 10.1029/2011WR010482.
- Berk A., Anderson G.D., Bernstein L.S., Acharya P.K., Dothe H., Matthew M.W., Adler-Golden S.M., Chetwynd J.H., Richtsmeier S., Pukall B., Allred C.L., Jeong L.S. and Hoke M.L. 1999b. *MODTRAN₄ radiative transfer modeling for atmospheric correction*. In Proceedings of SPIE. SPIE. https://doi.org/10.1117/12.366388.
- Blatchford M.L., Mannaerts C.M., Njuki S.M., Nouri H., Zeng Y., Pelgrum H., Wonink S. and Karimi P. 2020. *Evaluation of WaPOR V2 evapotranspiration products across Africa*. Hydrol. Process., 34 (15): 3200–3221.
- Brown M.E. 2008. *Famine early warning systems and remote sensing data*. Springer Berlin, Heidelberg, 314pp. https://doi.org/10.1007/978-3-540-75369-8.
- Brutsaert W. 1982. *Evaporation into the atmosphere*. D. Reidel Publishing Co: Dordrecht, Holland; pp 300.
- Brutsaert W. and Sugita M. 1992. *Application of self-preservation in the diurnal evolution of the surface energy balance budget to determine daily evaporation*. J. Geophys. Res., 97(D17): 18377–18382.
- Caiserman A., Amiraslani F. and Dumas D. 2021. *Assessment of the agricultural water budget in southern Iran using Sentinel-2 to Landsat-8 datasets*. J. Arid Environ., Volume 188: 104461 https://doi.org/10.1016/j.jaridenv.2021.104461.
- Camillo P.J. and Gurney R.J. 1986. *A resistance parameter for bare-soil evaporation models*. Soil Sci., 141: 95–105.
- Cammalleri C., Anderson M.C., Ciraolo G., D'Urso G., Kustas W.P., La Loggia G. and Minacapilli M. 2012. *Applications of a remote sensing-based two-source energy balance algorithm for mapping surface fluxes without in situ air temperature observations*. Remote sensing of Environ., 124: 502–515; doi:10.1016/j.rse.2012.06.009.
- Cammalleri C., Anderson M.C. and Kustas W.P. 2014. *Upscaling of evapotranspiration fluxes from instantaneous to daytime scales for thermal remote sensing applications*. Hydrol. Earth Syst. Sci., 18: 1885–1894 [doi:10.5194/hess-18-1885-2014].
- Campbell G.S. and Norman J.M. 1998. *The light environment of plant canopies*. In An introduction to environmental biophysics (pp. 247–278. Springer, New York, NY.
- Cawse-Nicholson K., Bravermana A., Kangb E.L., Lib M., Johnsona M., Halversona G., Anderson M.C., Hain C., Gunsona M. and Hook S. 2020. *Sensitivity and uncertainty quantification for the ECOSTRESS evapotranspiration algorithm – DisALEXI*. Int. J. Appl. Earth Obs. Geoinformation: 89 102088 https://doi.org/10.1016/j.jag.2020.102088 Received 31 October 2019.
- Cawse-Nicholson K., Anderson M.C., Yang Y., Yang Y., Hook S.J., Fisher J.B., Halverson G., Hulley G.C., Hain C., Baldocchi D.D., Brunzell N.A., Desai A.R., Griffis T.J. and Novick K.A. 2021. *Evaluation of a CONUS-Wide ECOSTRESS DisALEXI evapotranspiration Product*. IEEE Journal of Selected Topics in Applied Earth Observations and remote sensing, Vol. 14; doi:10.1109/JSTARS.2021.3111867.
- Chen T.S. and Ohring G. 1984. *On the relationship between clear sky planetary and surface albedos*. J. Atmos. Sci., 41: 156–158.

- Chen Y., Xia J., Liang S., Feng J., Fisher J.B., Li X., Li X., Liu S., Ma Z., Miyata A., Mu Q., Sun L., Tang J., Wang K., Wen J., Xue Y., Yu G., Zha T., Zhang L., Zhang Q., Zhao T., Zhao L. and Yuan W. 2014. *Comparison of satellite-based evapotranspiration models over terrestrial ecosystems in China*. Remote sensing Environ., 140: 279–293; <http://dx.doi.org/10.1016/j.rse.2013.08.045>.
- Chen M., Senay G.B., Singh R.K. and Verdin J.P. 2016. *Uncertainty analysis of the Operational Simplified Surface Energy Balance (SSEBop) model at multiple flux tower sites*: J. Hydrol., 536: 384–399 [<https://doi.org/10.1016/j.jhydrol.2016.02.026>].
- Choi M., Kustas W.P., Anderson M.C., Allen R.G., Li F. and Kjaersgaard J.H. 2009. *An intercomparison of three remote sensing-based surface energy balance algorithms over a corn and soybean production region (Iowa, US) during SMACEX*. Agric. For. Meteorol., 149(12): 2082–2097.
- Clapp R.B. and Hornberger (1978). G.M. *Empirical equations for some soil hydraulic properties*. Water Resour. Res., 14: 601–604.
- Crago R.D. 1996. *Comparison of the evaporative fraction and the Priestley-Taylor α for parameterizing daytime evaporation*. Water Resour. Res., 32(5): 1403–1409.
- Crago R.D. 1998. *Radiometric and equivalent isothermal surface temperatures*. Water Resour. Res., 34(11): 3017–3023 <https://doi.org/10.1029/98WR02522>.
- Friedl M., Crago R.D., Kustas W. and Wang Y.Q. 2002. *Investigation of Aerodynamic and Radiometric Land Surface Temperatures*. NTRS-NASA Technical Report n. 20020077956.
- Cui Y.K. and Jia L. 2014. *A modified Gash model for estimating rainfall interception loss of forest using remote sensing observations at regional scale*. Water, 6: 993–1012.
- Cui Y.K., Jia L., Hu G.C. and Zhou J. 2015. *Mapping of interception loss of vegetation in the Heihe River basin of China using remote sensing observations*. IEEE Geosci. Remote sensing Lett., 12: 23–27.
- de Bruin H.A.R., van den Hurk B.J.J.M. and Kohsiek W. 1995. *The scintillation method tested over a dry vineyard area*. Boundary Layer Meteorol., 76: 25–40.
- DHI-Grass and Compluting (2022). *Increasing Crop Water Use Efficiency at Multiple Scales Using Sentinel Evapotranspiration*. ET4FAO D4.2 – Final Report. https://et4fao.dhigroup.com/-/ET4FAO_Final_Report.pdf.
- Dolman A.J. 1993. *A multiple-source land surface energy balance model for use in general circulation models*. Agric. For. Meteorol., 65: 21–45.
- Duffie J.A. and Beckman W.A. 1991. *Solar engineering of thermal process, 2nd edn*. John Wiley and sons: NY.
- Ershadi A., McCabe M.F., Evans J.P., Chaney N.W. and Wood E.F. 2014. *Multi-site evaluation of terrestrial evaporation models using FLUXNET data*, Agric. For. Meteorol., 187: 46–61. <http://dx.doi.org/10.1016/j.agrformet.2013.11.008>.
- FAO. 2017. *Implementing the 2030 Agenda for water efficiency/productivity and water sustainability in NENA countries (GCP/RNE/009/SWE)*. FAO Projects Repository. <https://www.fao.org/in-action/water-efficiency-vena/en/>
- FAO. 2018. *WaPOR Database Methodology: Level 1. Remote Sensing for Water Productivity Technical Report: Methodology Series*. Rome, FAO. 72 pages. Licence: CC BY-NC-SA 3.0 IGO.
- FAO and IHE Delft. 2019. *WaPOR Quality Assessment. Technical report on the data quality of the WaPOR FAO database version 1.0*. Rome, 134 pp. <https://www.fao.org/3/ca4895en/ca4895en.pdf>
- FAO. 2020. *WaPOR database methodology: Version 2 release*, April 2020. Rome. <https://doi.org/10.4060/ca9894en>.
- FAO and IHE Delft. 2020. *WaPOR Quality Assessment. Technical report on the data quality of the WaPOR FAO database version 2*. Rome, 73 pp. <https://www.fao.org/3/cb2208en/CB2208EN.pdf>.

- Farah H.O. 2001. *Estimation of regional evaporation under different weather conditions from satellite and meteorological data. A case study in the Naivasha Basin, Kenya*. Doctoral Thesis Wageningen University and ITC.
- Feng X., Wu B. and Yan N.A. 2015. *Method for deriving the boundary layer mixing height from modis atmospheric profile data*. Atmosphere, 6: 1346–1361.
- Fisher J.B., Tu K.P. and Baldocchi D.D. 2008. *Global estimates of the land–atmosphere water flux based on monthly AVHRR and ISLSCP-II data, validated at 16 FLUXNET sites*. Remote sensing Environ., 112: 901–919.
- Fisher J.B., Whittaker R.H. and Malhi Y. 2011. *ET Come Home: A critical evaluation of the use of evapotranspiration in geographical ecology*. Global Ecology and Biogeography, 20: 1–18.
- Fisher J.B., Melton F., Middleton E., Hain C., Anderson M.C., Allen R., McCabe M., Hook S., Baldocchi D., Townsend P.A., Kilic A., Tu K., Miralles D., Perret J., Lagouarde J.P., Waliser D, Purdy A.J., French A., Schimel D., Famiglietti J.S., Stephens G. and Wood E.F. 2017. *The Future of evapotranspiration: Global requirements for ecosystem functioning, carbon and climate feedbacks, agricultural management, and water resources*. Water Resour. Res., 53(4)
<https://www.researchgate.net/publication/314755599>.
- Fisher J.B. 2018. *ECOSTRESS Science Document no. D-94645*. Jet Propulsion Laboratory, California Institute of Technology, Pasadena, California (USA), pp. 18.
- Fisher J.B., Lee B., Purdy A.J., Halverson G.H., Dohlen M.B., Cawse-Nicholson K., et al. 2020. *ECOSTRESS: NASA's Next Generation Mission to measure evapotranspiration from the International Space Station*. Water Resour. Res., 56, e2019WR026058. <https://doi.org/10.1029/2019WR026058>.
- Fisher J.B., Soenen S., Abello A., Blom B., Byckling K., Changaival B., Devecigil D., Elmes A., Fischer K., Gerace A., Joshi R., Kleynhans T., Lalli K., McGinley R., McGlinchy J., Mills S., Molev A., Montanaro M., Nagarajan A., Noblot N., Owczarski M., Reed J., Rehman E., Rogozin D., Sales M., Tati N., Thomas H., Werner F., Ziliani M., Zuenka K., Zuleta I., Dalby R. and Fossel P. 2022. *Hydrosat: Towards Daily, Field-scale, Global evapotranspiration from Space*. American Geophysical Union, Chicago, IL, USA.
- Franks S.W. and Beven K.J. 1997. *Estimation of evapotranspiration at the landscape scale: A fuzzy disaggregation approach*. Water Resour. Res., 33: 2929–2938.
- French A.N., Hunsaker D.J. and Thorp K.R. 2015. *Remote sensing of evapotranspiration over cotton using the TSEB and METRIC energy balance models*. Remote sensing Environ., 158: 281–294.
- Gao F., Masek J., Schwaller M. and Hall F. 2006. *On the blending of the Landsat and MODIS surface reflectance: predicting daily Landsat surface reflectance*. IEEE Trans. Geosci. Remote sensing, 44: 2207– 2218; <https://doi.org/10.1109/TGRS.2006.872081>.
- Gao F., Morisette J.T., Wolfe R.E., Ederer G., Pedelty J., Masuoka E. and Nightingale J. 2008. *An algorithm to produce temporally and spatially continuous MODIS LAI time series*. IEEE Geosci. Remote sensing Letters, 5(1): 60–64.
- Gao F., Kustas W.P. and Anderson M.C. 2012. *A data mining approach for sharpening thermal satellite imagery over land*. Remote sensing, 4: 3287–3319; <https://doi.org/10.3390/rs4113287>.
- Gash J.H.C., Lloyd C.R. and Lachaud G. 1995. *Estimating sparse forest rainfall interception with an analytical model*. J. Hydrol., 170: 79–86.
- Guzinski R., Nieto H., Jensen R. and Mendiguren G. 2014. *Remotely sensed land-surface energy fluxes at sub-field scale in heterogeneous agricultural landscape and coniferous plantation*. Biogeosciences, 11(18): 5021–5046 <http://www.biogeosciences.net/11/5021/2014/>
- Guzinski R. and Nieto H. 2019. *Evaluating the feasibility of using sentinel-2 and sentinel-3 satellites for high-resolution evapotranspiration estimations*. Remote Sens, Environ., 221: 157–72 <https://doi.org/10.1016/j.rse.2018.11.019>.

- Guzinski R., Nieto H., Sandholt I. and Karamitilios G. 2020. *Modelling high-resolution actual evapotranspiration through Sentinel-2 and Sentinel-3 data fusion*. Remote sensing, 12: 1433; <https://doi.org/10.3390/rs12091433>.
- Guzinski R., Nieto H., Sanchez J.A., López-Urrea R., Boujnah D.M. and Boulet G. 2021. *Utility of copernicus-based inputs for actual evapotranspiration modeling in support of sustainable water use in agriculture*. IEEE journal of selected topics in applied earth observations and remote sensing, 14: 11466–11484. <https://doi.org/10.1109/jstars.2021.3122573>
- Hansen L.P. 1982. *Large sample properties of generalized method of moments estimators*. Econometrica, 50: 1029–1054.
- He R., Jin Y., Kandelous M.M., Zaccaria D., Sanden B.L., Snyder R.L., Jiang J. and Hopmans J.W. 2017. *Evapotranspiration estimate over an almond orchard using landsat satellite observations*. Remote sensing, 9: 436. <https://doi.org/10.3390/rs9050436>.
- He X., Xu T., Xia Y., Bateni S.M. and Zhao J. 2020. *A Bayesian Three-Cornered Hat (BTCH) Method: Improving the terrestrial evapotranspiration estimation*. Remote sensing, 12: 878.
- Hemakumara H.M., Chandrapala L. and Moene A. 2003. *Evapotranspiration fluxes over mixed vegetation areas measured from large aperture scintillometer*. Agric. water manage., 58: 109–122.
- Holmes T.R.H., De Jeu R.A.M., Owe M. and Dolman A.J. 2009. *Land surface temperature from Ka band (37 GHz) passive microwave observations*, J. Geophys. Res., 114 [D04113, doi:10.1029/2008JD010257].
- Howell T.A., Schneider A.D. and Jensen M.E. 1991. *History of lysimeter design and use for evapotranspiration measurements*. Paper presented at the proceedings of the international symposium on lysimetry, ASCE, Honolulu, Hawaii.
- Hu G. and Jia L. 2015. *Monitoring of evapotranspiration in a semi-arid inland river basin by combining microwave and optical remote sensing observations*. Remote sensing, 7: 3056–3087 doi:10.3390/rs70303056.
- Hughes M.J. and Kennedy R. 2019. *High-quality cloud masking of landsat 8 imagery using convolutional neural networks*. Remote sensing, 11, 2591; doi:10.3390/rs11212591.
- Hulley G.C., Hughes C.G. and Hook S.J. 2012. *Quantifying uncertainties in land surface temperature and emissivity retrievals from ASTER and MODIS thermal infrared data*. J. Geophys. Res. Atmos., 117 (23) D23113. <http://dx.doi.org/10.1029/2012jd018506>.
- Irmak A., Allen R.G., Kjaersgaard J., Huntington J., Kamble B., Trezza R. and Ratcliffe I. 2012. *Operational remote sensing of ET and challenges*. In: Irmak, A (ed.). 2012, Evapotranspiration - Remote sensing and modeling, IntechOpen, London, 25p.
- Jaafar H., and Ahmad F. 2020. *Time series trends of Landsat-based ET using automated calibration in METRIC and SEBAL: The Bekaa Valley, Lebanon*. Remote sensing environ., 238: 111034 <https://doi.org/10.1016/j.rse.2018.12.033>.
- Jarvis P.G. 1976. *The interpretation of the variations in leaf water potential and stomatal conductance found in canopies in the field*. Philosophical transactions of the royal society of London B: Biological sciences, 273(927): 593–610.
- Jiang C. and Ryu Y. 2016. *Multi-scale evaluation of global gross primary productivity and evapotranspiration products derived from Breathing Earth System Simulator (BESS)*. Remote sensing environ., 186: 528–547.
- Jiang C., Guan K., Pan M., Ryu Y., Peng B. and Wang S. 2020. *BESS-STAIR: a framework to estimate daily, 30 m, and all-weather crop evapotranspiration using multi-source satellite data for the US Corn Belt*. Hydrol. Earth Syst. Sci., 24: 1251–1273- <https://doi.org/10.5194/hess-24-1251-2020>.
- Jiménez C., Martens B., Miralles D.M., Fisher J.B., Beck H.E. and Fernández-Prieto D. 2018. *Exploring the merging of the global land evaporation WACMOS-ET products based on local tower measurements*. Hydrol. Earth system Sci., 22: 4513–4533.

- Jin Y., He R., Marino G., Whiting M., Kent E., Sanden B.L., Culumber M., Ferguson L., Little C., Grattan S., Paw U K.T., Lagos L.O., Snyder R.L. and Zaccaria D. 2018. *Spatially variable evapotranspiration over salt affected pistachio orchards analyzed with satellite remote sensing estimates*. Agric. For. Meteorol., 262: 178-191.
- Johnson L.F. and Trout T.J. 2012. *Satellite NDVI assisted monitoring of vegetable crop evapotranspiration in California's San Joaquin Valley*. Remote sensing, 4(2): 439-455.
- Jung M., Reichstein M. and Bondeau A. 2009. *Towards global empirical upscaling of FLUXNET eddy covariance observations: validation of a model tree ensemble approach using a biosphere model*. Biogeosciences, 6: 2001-2013.
- Jung M., Reichstein M., Ciais P., Seneviratne S.I., Sheffield J., Goulden M.L., Bonan G., Cescatti A., Chen J., de Jeu R., Dolman A.J., Eugster W., Gerten D., Gianelle D., Gobron N., Heinke J., Kimball J., Law B.E., Montagnani L., Mu Q., Mueller B., Oleson K., Papale D., Richardson A.D., Rouspard O., Running S., Tomelleri E., Viovy N., Weber U., Williams C., Wood E., Zaehle S. and Zhang, K. 2010. *Recent decline in the global land evapotranspiration trend due to limited moisture supply*. Nature, 467: 951-954 [http://dx.doi.org/10.1038/nature09396].
- Kilic A., Allen R., Trezza R., Ratcliffe I., Kamble B., Robison C. and Ozturk D. 2016. *Sensitivity of evapotranspiration retrievals from the METRIC processing algorithm to improved radiometric resolution of Landsat 8 thermal data and to calibration bias in Landsat 7 and 8 surface temperature*. Remote sensing environ., 185: 198-209.
- Kjaersgaard J., Allen R.G. and Irmak A. 2011. *Improved methods for estimating monthly and growing season ET using METRIC applied to moderate resolution satellite imagery*. Hydrol. Process., 25(26): 4028-4036 [DOI: 10.1002/hyp8394].
- Kljun N., Calanca P., Rotach M.W. and Schmid H. 2015. *A simple two-dimensional parameterisation for Flux Footprint Prediction (FFP)*. Geoscientific Model Development, 3713-3695 :1118. <https://doi.org/10.5194/gmd-8-3695-2015>
- Koepke P., Kriebel K.T. and Dietrich B. 1985. *The effect of surface reflection and of atmospheric parameters on the shortwave radiation budget*. Adv. Space Research, 5: 351-354.
- Knipper K.R., Kustas W.P., Anderson M.C., Alfieri J.G., Prueger J.H., Hain C.R., Gao F., Yang Y., McKee L.G., Nieto H., Hipps L.E., Alsina M.M. and Sanchez L. 2018. *Evapotranspiration estimates derived using thermal-based satellite remote sensing and data fusion for irrigation management in California vineyards*. Irrig. Sci., 37: 431-449; <https://doi.org/10.1007/s00271-018-0591-y>.
- Kroese D.P., Brereton T., Taimre T. and Botev Z.I. 2014. *Why the Monte Carlo method is so important today*. WIREs Comput Stat., 6(6): 386-392 <https://doi.org/10.1002/wics.1314>.
- Kustas W.P. and Norman J.M. 1999. *Evaluation of soil and vegetation heat flux predictions using a simple two-source model with radiometric temperatures for partial canopy cover*. Agric. For. Meteorol., 94(1): 13-29 <http://www.sciencedirect.com/science/article/pii/S0168192399000052>.
- Kustas W.P. and Norman J.M. 2000. *A two-source energy balance approach using directional radiometric temperature observations for sparse canopy covered surfaces*. Agron. J., 92: 847- 854.
- Kustas W.P., Diak G.R. and Norman J.M. 2001. *Time difference methods for monitoring regional scale heat fluxes with remote sensing*. land surface hydrol., Meteorol., Climate: observations and modeling, 3: 15 - 29.
- Kustas W.P., Anderson M.C., Norman J.M. and Li F., 2007. *Utility of radiometric-aerodynamic temperature relations for heat flux estimation*. Boundary-Layer Meteorol., 122(1), pp.167-187.
- Kustas W.P., Nieto H., Morillas L., Anderson M.C., Alfieri J.G., Hipps L.E., Villagarcía L., Domingo F. and Garcia M. 2016. *Revisiting the paper "Using radiometric surface temperature for surface energy flux estimation in Mediterranean drylands from a two-source perspective"*. Remote sensing environ., 184: 645-653 - <https://doi.org/10.1016/j.rse.2016.07.024>.
- Laatiri K., Lhomme J.P., Annabi M. and Setter T.L. 2010. *Wheat production in Tunisia: Progress, inter-annual variability and relation to rainfall*. Europ. J. Agronomy, 33: 33-42.

- Lian J. and Huang M. 2015. *Evapotranspiration estimation for an oasis area in the Heihe river basin using landsat-8 images and the METRIC model*. *Water resources Management*, 29: 5157–5170.
- Lillesand T. and Kiefer R.W. 2000. *Remote sensing and image interpretation*. John Wiley and Sons, New York.
- Liu N., Oishib A.C., Miniat C.F. and Bolstad P. 2021. *An evaluation of ECOSTRESS products of a temperate montane humid forest in a complex terrain environment*. *Remote sensing environ.*, 265: 112662 [https://doi.org/10.1016/j.rse.2021.112662].
- Liu S.M., Xu Z.W., Wang W.Z., Jia Z.Z., Zhu M.J., Bai J. and Wang J.M. 2011. *A comparison of eddy-covariance and large aperture scintillometer measurements with respect to the energy balance closure problem*. *Hydrol. Earth Syst. Sci.*, 15: 1291–1306.
- Liu Z. 2021. *The accuracy of temporal upscaling of instantaneous evapotranspiration to daily values with seven upscaling methods*. *Hydrol. Earth Syst. Sci.*, 25: 4417–4433 [https://doi.org/10.5194/hess-25-4417-2021].
- Ma Z., Wu B., Yan N., Zhu W., Zeng H. and Xu J. 2021. *Spatial allocation method from coarse evapotranspiration data to agricultural fields by quantifying variations in crop cover and soil moisture*. *Remote sensing*, 13: 343. https://doi.org/10.3390/rs13030343.
- Mao K., Qin Z., Shi J. and Gong P. 2005. *A practical split-window algorithm for retrieving land-surface temperature from MODIS data*. *Int. J. remote sensing*, 26(15): 3181–3204.
- Masek J.G., Vermote E.F., Saleous N.E., Wolfe R., Hall F.G., Huemmrich K.F., Feng G., Kutler J. and Teng-Kui L. 2006. *A Landsat surface reflectance dataset for North America, 1990-2000*. *IEEE Geosci. Remote sensing letters*, 3(1): 68-72.
- McDonald J.H. 2015. *Standard error of the mean*. *Handbook of biological statistics*. <http://www.biostathandbook.com/standarderror.html>.
- McShane R.R., Driscoll K.P. and Sando R. 2017. *A review of surface energy balance models for estimating actual evapotranspiration with remote sensing at High Spatiotemporal resolution over large extents*. USGS - Scientific Investigations Report 2017–5087, 19p.
- McNaughton K.G. and Spriggs T.W. 1986. *A mixed-layer model for regional evaporation*. *Boundary-Layer Meteorol.*, 74: 262-288.
- Melton F.S., Johnson L.F., Lund C.P., Pierce L.L., Michaelis A.R., Hiatt S.H., Guzman A., Adhikari D.D., Purdy A.J., Roosevelt C., Votava P., Trout T.J., Temesgen B., Frame K., Sheffner E.J. and Nemani R.R. 2012. *Satellite Irrigation Management Support with the Terrestrial Observation and Prediction System: a framework for integration of satellite and surface observations to support improvements in agricultural water resource management*. *IEEE J. Stars*, 5(6): 1709–1721.
- Melton F.S., Huntington J., Grimm R., Herring J., Hall M., Rollison D., Erickson T. et al. 2022. *OpenET: Filling a Critical Data Gap in Water Management for the Western United States*. *J. Amer. Water Resour. Association*, 58 (6): 971–994 - <https://doi.org/10.1111/1752-1688.12956>.
- Mira M., Oliosio A., Gallego-Elvira B., Courault D., Garrigues S., Marloie O., Hagolle O., Guillevic P. and Boulet G. 2016. *Uncertainty assessment of surface net radiation derived from Landsat images*. *Remote sensing environ.*, 175: 251-270.
- MODIS Brochure.2000. https://modis.gsfc.nasa.gov/about/media/modis_brochure.pdf
- Mohamed Y., Bastiaanssen W.G.M. and Savenije H.H.G. 2004. *Spatial variability of evaporation and moisture storage in the swamps of the upper Nile studied by remote sensing techniques*. *J. Hydrol.* 124–116 :277 ..
- Monteith J.L. 1963. *Gas exchange in plant communities*. *Environmental control of plant growth* Evans L.T., ed. Academic Press, New York, pp.95-112 .
- Monteith J.L. 1964. *Evaporation and environment*. *The State and Movement of Water in Living Organism*. 19th Symp. Soc. Exp. Biol., Academic Press, New York, pp. 205-234.

- Morrison F. 2021. *Uncertainty analysis for engineers and scientists: A practical guide*. Cambridge university press, p 378.
- Mueller B., Hirschi M., Jimenez C., Ciais P., Dirmeyer P., Dolman A., Fisher J., Jung M., Ludwig F. and F. Maignan. 2013. *Benchmark products for land evapotranspiration: LandFlux-EVAL multi-dataset synthesis*. Hydrol. Earth Syst. Sci., 17: 3707- 3720.
- NASA-JPL. 2018. *ECOSystem Spaceborne Thermal Radiometer Experiment on Space Station (ECOSTRESS). Level-3 evapotranspiration (ET_ALEXI) Algorithm Theoretical Basis Document*. JPL Publication D-94646.
- Nash J.E. and Sutcliffe J.V. 1970. *River flow forecasting through conceptual models part I – A discussion of principles*. J. Hydrol., 10(3): 282–290 [https://doi.org/10.1016/0022-1694\(70\)90255-6](https://doi.org/10.1016/0022-1694(70)90255-6).
- Nisa Z., Sarfraz Khan M., Govind A., Marchetti M., Lasserre B., Magliulo E. and Manco A. 2021. *Evaluation of SEBS, METRIC-EEFlux, and QWaterModel Actual evapotranspiration for a Mediterranean Cropping System in Southern Italy*. Agronomy, 11: 345. <https://doi.org/10.3390/agronomy11020345>.
- Norman J.M., Xu W.P. and Humes K.S. 1995. *A two-source approach for estimating soil and vegetation energy fluxes in observations of directional radiometric surface temperature*. Agric. For. Meteorol., 77(3-4), pp.263-293.
- Norman J.M., Anderson M.C., Kustas W.P., French A.N., Mecikalski J.R., Torn R.D., Diak G.R., Schmugge T.J. and Tanner B.C.W. 2003. *Remote sensing of surface energy fluxes at 101-m pixel resolutions*. Water Resour. Res., 39(8): 1221, doi:10.1029/2002WR001775.
- Owaneh O.M. and Suleiman A.A. 2018. *Comparison of the performance of ALARM and SEBAL in estimating the actual daily ET from satellite data*. J. Irrig. Drain Eng., 144(9): 04018024 [https://doi.org/10.1061/ASCE\(IR1943-4774.0001335](https://doi.org/10.1061/ASCE(IR1943-4774.0001335).
- Paço T.A., Pôças I., Cunha M., Silvestre J.C., Santos F.L., Paredes P. and Pereira L.S. 2014. *Evapotranspiration and crop coefficients for a super intensive olive orchard. An application of SIMDualKc and METRIC models using ground and satellite observations*. J. Hydrol., 519: 2067–2080.
- Pakistan Agricultural Research Council. 1982. *Consumptive use of water for crops in Pakistan*, pp. 20–30, Islamabad, Pakistan.
- Passioura J.B. 1996. *Simulations models: science, snake oil, education, or engineering?* Agron. J., 88: 690-694.
- Paulson C.A. 1970. *The mathematical representation of wind speed and temperature profiles in the unstable atmospheric surface layer*. Appl. Meteorol., 9: 857-861.
- Pelgrum H., Miltenburg I.J., Cheema M.J.M, Klaasse A. and Bastiaanssen W.G.M. 2010. *ETLook: a novel continental evapotranspiration algorithm. Remote sensing and hydrology*. Proceedings of a symposium held at Jackson Hole, Wyoming, USA. IAHS Publ. 3XX, 2011.
- Penman H.L. 1948. *Natural evaporation from open water, bare soil and grass*. Proc. R. Soc. A, 193: 120–145.
- Pereira L.S., Paredes P., Melton F., Johnson L., Wang T., López-Urrea R., Cancela J.J., Allen R.G. 2020. *Prediction of crop coefficients from fraction of ground cover and height. Background and validation using ground and remote sensing data*. Agric. Water Manag., 241, 106197 - <https://doi.org/10.1016/j.agwat.2020.106197>.
- Priestley C.H.B. and Taylor R.J. 1972. *On the assessment of surface heat flux and evaporation using large scale parameters*. Monthly Weather Review, 100: 81–92.
- Purdy A., Fisher J.B., Goulden M.L. and Famiglietti J.S. 2016. *Ground heat flux: an analytical review of 6 models evaluated at 88 sites and globally*. Journal of Geophysical Research – Biogeosciences, 121: doi:2016/10.1002/JG003591.
- Raes D., Steduto P., Hsiao T.C. and Fereres E. 2017. *AquaCrop 6.0 - Reference Manual. Chapter 2: User guide*. FAO, Rome
- ReVelle P., Kilic A. and Allen R. 2019. *Updated Calibration Description: Spatial Delapsing in automated METRIC applications for OpenET*. In-house report. University of Nebraska-Lincoln and University of Idaho. 9 p.

- Ross K.W., Brown M.E., Verdin J.P. and Underwood L.W. 2009. *Review of FEWS NET biophysical monitoring requirements*. Environ. Res. Lett., 4 024009 (10pp).
- Rossi R.J. 2018. *Mathematical Statistics: An Introduction to Likelihood Based Inference*. John Wiley & Sons, New York, p. 227.
- Roy D.P., Wulder M.A., Loveland T.R., C.E W., Allen R.G., Anderson M.C., Helder D., Irons J.R., Johnson D.M., Kennedy R., Scambos T.A., Schaaf C.B., Schott J.R., Sheng Y., Vermote E.F., Belward A.S., Bindschadler R., Cohen W.B., Gao F., Hipple J.D., Hostert P., Huntington J., Justice C.O., Kilic A., Kovalsky V., Lee Z.P., Lymburner L., Masek J.G., McCorkel J., Shuai Y., Trezza R., Vogelmann J., Wynne R.H. and Zhu Z. 2014. *Landsat-8: Science and product vision for terrestrial global change research*. Remote sensing environ., 145: 154-172.
- Rushidi A.M. and Kafrawy K.F. 1988. *Uncertainty propagation in fault-tree analysis using an exact Method of Moments*. Microelectron. Reliab., 28(6): 945-965.
- Ryu Y., Baldocchi D.D., Black T.A., Detto M., Law B.E., Leuning R., Miyata A., Reichstein M., Vargas R., Amman C., Beringer J., Flannigan L.G., Gu L., Huttley L., Kim J., McCaughey H., Moors E.J., Rambal S., Richardson A.D. and Vesala T. 2012. *On the temporal upscaling of evapotranspiration from instantaneous remote sensing measurements to 8-day mean daily-sums*. Agric. For. Meteorol., 152: 212-222.
- Sai Krishna S.V.S., Manavalan P. and Rao P.V.N. 2014. *Estimation of net radiation using satellite based data inputs*. ISPRS Technical Commission VIII Symposium, 09 – 12 December 2014, Hyderabad, India. <http://doi:10.5194/isprsarchives-XL-8-307-2014>.
- Saltelli A., Tarantola S. and Campolongo F. 2000. *Sensitivity Analysis as an ingredient of Modeling*. Statistical Sci., 15(4): 377-95.
- Saltelli A., Ratto M., Andres T., Campolongo F., Cariboni J., Gatelli D., Saisana M. and Tarantola S. 2008. *Global Sensitivity Analysis: The Primer*. John Wiley & Sons.
- Schull M.A., Hain C., Anderson M.C., Gao F., Neale C.M.U. and Zhan X. 2017. *An Open Source Implementation of the DisALEXI ET Data Fusion Suite*. 4E, Washington State Convention Center.
- Sekertekin A. and Bonafoni S. 2020. *Land Surface Temperature retrieval from Landsat 5, 7, and 8 over rural areas: Assessment of different retrieval algorithms and emissivity models and toolbox implementation*. Remote sensing, 12: 294; <http://doi:10.3390/rs12020294>.
- Senay G.B., Budde M., Verdin J. and Melesse A. 2007. *A coupled remote sensing and simplified surface energy balance approach to estimate actual evapotranspiration from irrigated fields*. Sensors, 7(6): 979. <https://doi.org/10.3390/s7060979>.
- Senay G.B., Bohms S., Singh R.K., Gowda P.H., Velpuri N.M., Alemu H. and Verdin J.P. 2013. *Operational evapotranspiration mapping using remote sensing and weather datasets: A new parameterization for the SSEB approach*. JAWRA, 49(3): 577-591. <https://doi.org/10.1111/jawr.12057>.
- Senay G.B., Gowda P.H., Bohms S., Howell T.A., Friedrichs M., Marek T.H. and Verdin J.P. 2014. *Evaluating the SSEBop approach for evapotranspiration mapping with landsat data using lysimetric observations in the semi-arid Texas High Plains*. Hydrol. Earth Syst. Sci. Discuss., 11: 723-756. doi:10.5194/hessd-11-723-2014.
- Senay G.B., Friedrichs M., Singh R.K. and Velpuri N.M. 2016. *Evaluating landsat 8 evapotranspiration for water use mapping in the Colorado river basin*. Remote sensing environ., 185, 171-185. <https://doi.org/10.1016/j.rse.2015.12.043>.
- Senay G.B., Schauer M., Friedrichs M., Velpuri N.M. and Singh R.K. 2017. *Satellite-based water use dynamics using historical Landsat data (1984-2014) in the southwestern United States*. Remote sensing environ., 202 : 98-112. <https://doi.org/10.1016/j.rse.2017.05.005>.
- Senay G.B. 2018a. *Satellite psychrometric formulation of the Operational Simplified Surface Energy Balance (SSEBop) model for quantifying and mapping evapotranspiration*. Amer. Soc. Agric. Biol. Eng., 34(3): 555-566.

- Senay G.B. 2018b. *Landsat-based illustrative implementation of Satellite Psychrometry for ET Mapping*. U.S. Geological Survey data release. doi.org/10.5066/F7ZS2VR6.
- Senay G.B., Kagone S. and Velpuri N.M. 2020. *Operational global actual evapotranspiration: development, evaluation, and dissemination*. Sensors, 20: 1915 [doi:10.3390/s20071915].
- Senay G.B., Friedrichs M., Morton C., Parrish G.E.L., Schauer M., Khand K., SKagone S., Boiko O. and Huntington J. 2022. *Mapping actual evapotranspiration using Landsat for the conterminous United States: Google Earth Engine implementation and assessment of the SSEBop model*. Remote sensing environ., 275: 113011 [https://doi.org/10.1016/j.rse.2022.113011].
- Shang K., Yao Y., Li Y., Yang J., Jia K., Zhang X., Chen X., Bei X. and Guo X. 2020. *Fusion of Five Satellite-Derived Products Using Extremely Randomized Trees to Estimate Terrestrial Latent Heat Flux over Europe*. Remote sensing, 12: 687.
- Shang K., Yao Y., Liang S., Zhang Y., Fisher J.B., Chen J., Liu S., Xu Z., Zhang Y., Jia K., Zhang X., Yang J., Bei X., Guo X., Yu R., Xie Z. and Zhang L. 2021. *DNN-MET: A deep neural networks method to integrate satellite-derived evapotranspiration products, eddy covariance observations and ancillary information*. Agric. For. Meteorol., 308–309: 108582.
- Shuttleworth W.J. and Wallace J.S. 1985. *Evaporation from sparse crops—An energy combination theory*. Q. J. R. Meteorol. Soc., 111: 839–855.
- Singh R.K., Irmak A., Irmak S. and Martin D.L. 2008. *Application of SEBAL model for mapping evapotranspiration and estimating surface energy fluxes in south-central Nebraska*. J. Irrig. Drain. Eng., 134(3): 273–285.
- Singh R.K., Irmak A., Walter-Shea E.A. and Verma S.B. 2009. *Performance evaluation of soil heat flux models in Great Plains*. World Environmental and Water Resources Congress 2009: Kansas City, MO; 10.
- Singh R.K. and Senay G.B. 2016. *Comparison of four different energy balance models for estimating evapotranspiration in the Midwestern United States*. Water, 8(1): [http://dx.doi.org/10.3390/w8010009].
- Singh R.K., Khand K., Kagone S., Schauer M., Senay G.B. and Wu Z. 2020. *A novel approach for next generation water-use mapping using Landsat and Sentinel-2 satellite data*. Hydrol. Sci. J., 65 (14): 2508–2519.
- Sriwongsitanona N., Suwawonga T., Thianpopiruga S., Williams J., Jia L. and Bastiaanssen W. 2020. *Validation of seven global remotely sensed ET products across Thailand using water balance measurements and land use classifications*. J. Hydrol.: regional studies, 30: 100709; https://doi.org/10.1016/j.ejrh.2020.100709.
- Stein A. and Zaadnoordijk W.J. 1999. *Improved parameter estimation for hydrological models using weighted object functions*. Hydrol. Process., 13: 1315–1328.
- Stewart J.B. 1988. *Modelling surface conductance of pine forest*. Agric. For. Meteorol., 43(1): 19–35.
- Storey J.C., Rengarajan R. and Choate M.J. 2019. *Bundle adjustment using space-based triangulation method for improving the landsat global ground reference*. Remote sensing, 11(14): 1640.
- Stull R.B. 1988. *An introduction to boundary layer meteorology*. Kluwer Academic Publishers, Dordrecht, Boston, London. 666. ISBN 90 277 2768 6; 90 277 2769 4.
- Suleiman A.A. and Crago R.D. 2002a. *Analytical land atmosphere radiometer model*. J. Appl. Meteorol., 41(2): 177–187 https://doi.org/10.1175/1520-0450(2002)0412.0.CO;2.
- Suleiman A.A. and Crago R.D. 2002b. *Analytical land atmosphere radiometer model (ALARM) applied to a dense canopy*. Agric. For. Meteorol., 112(3–4): 151–159 https://doi.org/10.1016/S0168-1923(02)00127-2.
- Tan R. and Li Z.L. 2017. *An end-member-based two-source approach for estimating land surface evapotranspiration from remote sensing data*. IEEE Trans. Geosci. Remote sensing, 55: 5818–5832.
- Tan S., Wu B., Yan N. and Zhu W. 2017. *An NDVI-based statistical ET downscaling method*. Water, 9(12): 995 - doi:10.3390/w9120995.

- Tan S., Wu B. and Yan N. 2019. *A method for downscaling daily evapotranspiration based on 30-m surface resistance*. J. Hydrol., 577: 123882.
- Tasumi M. 2003. *Progress in operational estimation of regional evapotranspiration using satellite imagery*. Ph.D. Dissertation, University of Idaho, Moscow, ID, 357p.
- Tasumi M., Trezza R., Allen R.G. and Wright, J.L. 2005. *Operational aspects of satellite-based energy balance models for irrigated crops in the semi-arid U.S.* J. Irrig. Drain. Syst., 19(3): 355-376
- DOI: 10.1007/s10795-005-8138-9.
- Tasumi M., Allen R.G. and Trezza R. 2008. *At-Surface Reflectance and Albedo from Satellite for Operational Calculation of Land Surface Energy Balance*. J. Hydrol. Eng., 13: 51-63.
- Tasumi M. 2019. *Estimating evapotranspiration using METRIC model and Landsat data for better understandings of regional hydrology in the western Urmia Lake Basin*. Agric. Water Manage., 226: 105805. <https://doi.org/10.1016/j.agwat.2019.105805>.
- Taylor J.R. 1982. *An introduction to error analysis – The study of uncertainties in physical measurements*. University Science Books, Oxford University Press, pp.270.
- Teixeira A.H.C., Bastiaanssen W.G.M., Ahmad M.D. and Bos M.G. 2009. *Reviewing SEBAL input parameters for assessing evapotranspiration and water productivity for the Low-Middle São Francisco River basin, Brazil Part A: Calibration and validation*. Agric. For. Meteorol., 149: 462-476.
- Trout T.J., Johnson L.F. and Gartung J. 2008. *Remote sensing of canopy cover in horticultural crops*. Hort. Sci., 43(2): 333-337.
- UNESCO-IHE. 2018. pySEBAL.
- Van Dijk A.I.J.M. and Bruijnzeel L.A. 2001. *Modelling rainfall interception by vegetation of variable density using an adapted analytical model. Part 1. Model description*. J. Hydrol., 247: 230-238.
- Vermote E.F., Tanré D., Deuze J.L., Herman M., Morcette J.J. 1997. *Second simulation of the satellite signal in the solar spectrum, 6S: An overview*. IEEE Trans. Geosci. Remote sensing, 35: 675-686.
- Vinukollu R.K., Wood E.F., Ferguson C.R., Joshua B. and Fisher J.B. 2011. *Global estimates of evapotranspiration for climate studies using multi-sensor remote sensing data: Evaluation of three process-based approaches*. Remote sensing environ., 115: 801-823; doi:10.1016/j.rse.2010.11.006.
- Wan Z.M. and Li Z.L. 1997. *A physics-based algorithm for retrieving land-surface emissivity and temperature from EOS/MODIS data*. IEEE Trans. Geosci. Remote sensing, 35(4): 980-996.
- Wang J., Ma Y., Menenti M., Bastiaanssen W.G.M., Mitsuta Y. 1995. *The scaling-up of processes in the heterogeneous landscape of HEIFE with the aid of satellite remote sensing*. J. Met. Soc. Japan, 73 (6): 1235-1244.
- Wang N., Jia L., Zheng C. and Menenti M. 2017. *Estimation of subpixel snow sublimation from multispectral satellite observations*. J. Applied remote sensing, 046017, 11(4); doi: 10.1117/1.JRS.11.046017.
- Wang T., Melton F.S., Poças I., Johnson L.F., Thao T., Post K. and Cassel-Sharma F. 2021. *Evaluation of crop coefficient and evapotranspiration data for sugar beets from landsat surface reflectances using micrometeorological measurements and weighing lysimetry*. Agric. Water Manage., 244, 106533; <https://doi.org/10.1016/j.agwat.2020.106533>.
- Webb E.K. 1970. *Profile relationships: the log-linear range, and extension to strong stability*. Quart. J. Roy. Meteorol. Soc., 96: 67-90.
- Willmott C.J. 1981. *On the validation of models*. Physical Geography, 2: 184-194.
- Wright J.L. 1982. *New evapotranspiration crop coefficients*. J. Irrig. Drain. Division (ASCE), 108: 57-74.

- Wu B.F., Xiong J. and Yan N.N. 2008. *ETWatch for monitor regional evapotranspiration with remote sensing*. *Advances Water Sci.*, 19(5): 671–678.
- Wu B.F., Xiong J. and Yan N.N. 2011. *ETWatch: models and methods*. *J. Remote sensing*, 15(2): 224–239.
- Wu B., Yan N., Xiong J., Bastiaanssen W.G.M., Zhu W. and Stein A. 2012. *Validation of ETWatch using field measurements at diverse landscapes: A case study in Hai Basin of China*. *J. Hydrol.*, 436–437: 67–80. <https://doi.org/10.1016/j.jhydrol.2012.02.043>.
- Wu B., Liu S., Zhu W., Yan N., Xing Q. and Tan S. 2017. *An improved approach for estimating daily net radiation over the Heihe River Basin*. *Sensors*, 17(1): 86 - doi:10.3390/s17010086.
- Wu B., Zhu W., Yan N., Xing Q., Xu J., Ma Z. and Wang L. 2020. *Regional actual evapotranspiration estimation with land and meteorological variables derived from multi-source satellite data*. *Remote sensing*, 12, 332; doi:10.3390/rs12020332.
- Wu F., Wu B., Zhu W., Yan N., Ma Z., Wang L., Lu Y. and Jiaming Xu J. 2021. *ETWatch Cloud: APIs for regional actual evapotranspiration data generation*. *Environmental Modelling & Software*, 145: 105174. <https://doi.org/10.1016/j.envsoft.2021.105174>.
- Wu J., Feng Y., Liang L., He X. and Zeng Z. 2022. *Assessing evapotranspiration observed from ECOSTRESS using flux measurements in agroecosystems*. *Agric. Water Manage.*, 269: 107706. <https://doi.org/10.1016/j.agwat.2022.107706>.
- Xu J., Wu B., Yan N. and Tan S. 2018. *Regional daily ET estimates based on the gap-filling method of surface conductance*. *Remote sensing*, 10, 554; doi:10.3390/rs10040554.
- Xu J.M., Wu B.F., et al. 2020. *Quantifying the contribution of biophysical and environmental factors in uncertainty of canopy conductance*. *J. Hydrol.*, 592: 125612.
- Xu J., Wu B., Ryu D., Yan N., Zhu W. and Ma Z. 2021. *A canopy conductance model with temporal physiological and environmental factors*. *Sci. Total Environ.*, 791, 148283. <https://doi.org/10.1016/j.scitotenv.2021.148283>.
- Xue J., Anderson M.C., Gao F., Hain C., Knipper K.R., Yang Y., Kustas W.P., Bambach N.E., McElrone A.J., Castro S.J., Alfieri J.G., Prueger J.H., McKee L.G., Hipps L.E., and Alsina M. 2022. *Improving the spatiotemporal resolution of remotely sensed ET information for water management through Landsat, Sentinel-2, ECOSTRESS and VIIRS data fusion*. *Irrig. Sci.*, 40: 609-634.
- Yang Y., Guan H., Long D., Liu B., Qin G., Qin J. and Batelaan O. 2015. *Estimation of surface soil moisture from thermal infrared remote sensing using an improved trapezoid method*. *Remote sensing*, 7: 8250-8270.
- Yao Y., Liang S., Li X., Zhang Y., Chen J., Jia K., Zhang X., Fisher J.B., Wang X., Zhang L., Xu J., Shao C., Posse G., Li Y., Magliulo V., Varlagin A., Moors E.J., Boike J., Macfarlane C., Kato T., Buchmann N., Billesbach D.P., Beringer J., Wolf S., Papuga S.A., Wohlfahrt G., Montagnani L., Ardo J., Paul-Limoges E., Emmel C., Hortnagl L., Sachs T., Gruening C., Gioli B., Lopez-Ballesteros A., Steinbrecher R. and Gielen B. 2017. *Estimation of high-resolution terrestrial evapotranspiration from Landsat data using a simple Taylor skill fusion method*. *J. Hydrol.*, 553: 508–526.
- Young N.E., Anderson R.S., Chignell S.M., Vorster A.G., Lawrence R. and Evangelista P.H. 2017. *A survival guide to Landsat preprocessing*. *Ecology*, 98(4): 920-932.
- Zhang H., Wu B., Yan N., Hu W. and Feng X. 2014. *An improved satellite-based approach for estimating vapor pressure deficit from MODIS data*. *J. Geophys. Res. Atmos.*, 119(21): 12,256–12,271 - doi:10.1002/2014JD022118.
- Zhang K., Kimball J.S., and Running S.W. 2016. *A review of remote sensing based actual evapotranspiration estimation*. *Wiley Interdisciplinary Reviews: Water*.
- Zheng C., Jia L., Hu G., Lu J., Wang K. and Li Z. 2016. *Global evapotranspiration derived by ETMonitor model based on earth observations*. *IEEE International Symposium on Geoscience and Remote Sensing (IGARSS)*, pp. 222-225. doi: 10.1109/IGARSS.2016.7729049.

Zheng C., Jia L., Hu G., Menenti M., Lu J., Zhou J., Wang K. and Li Z. 2017. *Assessment of water use in Pan-Eurasian and African Continents by ETMonitor with multi-source satellite data*. IOP Conf. Ser.: Earth Environ. Sci., 57 012050; doi:10.1088/1755-1315/57/1/012050.

Zheng C., Jia L., Hu G. and Lu J. 2019a. *Earth observations-based evapotranspiration in Northeastern Thailand*. Remote sensing, 11: 138; <http://doi:10.3390/rs11020138>.

Zheng C., Jia L., Hu G. and Lu J. 2019b. *Evapotranspiration Estimation in Tropical Monsoon regions Using Improved ETMonitor Algorithm*. 2019 IEEE International Geoscience and Remote Sensing Symposium (IGARSS), pp. 6891-6894, doi:10.1109/IGARSS.2019.8899883.

Zheng C. and Jia L. 2020. *Global canopy rainfall interception loss derived from satellite earth observations*. <https://doi.org/10.1002/eco.2186>.

Zheng C., Jia L. and Hu G. 2022. *Global land surface evapotranspiration monitoring by ETMonitor model driven by multi-source satellite earth observations*. J. Hydrol., 128444; <https://doi.org/10.1016/j.jhydrol.2022.128444>.

Zhuang Q., Wu B., Yan N., Zhu W. and Xing Q. 2016. *A method for sensible heat flux model parameterization based on radiometric surface temperature and environmental factors without involving the parameter KB-1*. International J. Applied Earth Observation and Geoinformation, 47: 50–59. <http://dx.doi.org/10.1016/j.jag.2015.11.015>.

ANNEX I

List of speakers of the remote sensing determination of evapotranspiration webinar series

List of speakers



Richard G. Allen

University of Idaho

Kimberly, Idaho, United States of America



Martha C. Anderson

USDA Agricultural Research Service - Hydrology and Remote Sensing Laboratory

Beltsville, Maryland, United States of America



Wim Bastiaanssen

IrriWatch

Maurik, the Kingdom of the Netherlands



Chandrashekhar Biradar

ICARDA

Cairo, Egypt



Arnaud Caiserman

University of Central Asia

Khorog-Dushanbe, Tajikistan



Richard Crago

Bucknell University

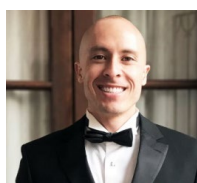
Lewisburg, Pennsylvania, United States of America



Mohamed Abdalla El-Sheikh

FAO-SD

Khartoum, Sudan



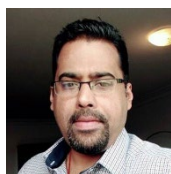
Joshua B. Fisher

Former **Science Lead at Jet Propulsion Laboratory (NASA)**

Pasadena, California, United States of America

Presently **Professor at Chapman University**

Orange County, California, United States of America



Ajit Govind

ICARDA

Cairo, Egypt



Radoslaw Guzinski

DHI GRAS

Hørsholm, Denmark



Christopher Hain

NASA's Marshall Space Flight Center

Huntsville, Alabama, United States of America



Jippe Hoogeveen

FAO-HQ

Rome, Italy



Li Jia

Chinese Academy of Science

Beijing, China



Ihab Jnad

ACSAD

Damascus, Syrian Arab Republic



Ayse Kilic

University of Nebraska-Lincoln

Lincoln, Nebraska, United States of America



Annemarie Klaasse

eLEAF

Wageningen, the Kingdom of the Netherlands



Benjamin Koetz

European Space Agency (ESA-ESRIN)

Frascati, Italy



Michel Massart

**Earth Observation Unit Directorate General for
Defence Industry and Space**

European Commission Brussels, Belgium



Forrest Melton

NASA Ames Research Center

& California State University, Monterey Bay

Moffett Field, CA, United States of America



Marloes Mul

IHE-Delft

Delft, the Kingdom of the Netherlands



Christopher Neale

**Robert B. Daugherty Water for Food Global
Institute at the University of Nebraska**

Lincoln, Nebraska, United States of America



Hector Nieto

University of Copenhagen

Copenhagen, Denmark



Osama Owaneh

National Agricultural Research Center of Jordan

Amman, Jordan



Livia Peiser

FAO-HQ

Rome, Italy



Henk Pelgrum

eLEAF

Wageningen, the Kingdom of the Netherlands



Lisa-Maria Rebelo

IWMI

Colombo District, Western, Sri Lanka



Gabriel Senay

USGS Earth Resources Observation & Science Center

Colorado State University

Fort Collins, Colorado, United States of America



Nabil Sghaier

AOAD

Khartoum, Sudan



Pasquale Steduto

Former FAO-RNE

Cairo, Egypt



Ayman Suleiman

University of Jordan

Amman, Jordan



Masahiro Tasumi

University of Miyazaki Miyazaki, Japan



Bingfang Wu

Chinese Academy of Science

Beijing, China

ANNEX II

Example of semi-empirical decomposition of RS ET uncertainty with METRIC

The matrix in Table 7 summarizes estimated accuracy of spatial ET determinations produced by the RS model METRIC (used as an example) over a range of time and/or spatial scales and for two levels of METRIC expertise: 'handling' and 'review'. Accuracy estimates are also stated for the traditional crop coefficient – reference ET method, for comparative purposes. Uncertainty percentages are all plus/minus and represent 95 percent of outcomes and two standard deviations of error from the true value. A METRIC "expert" is considered to be a person who has course work or study background in evaporation and radiation physics and in the theoretical basis for ET calculation and who is knowledgeable and experienced in the behavior of irrigated agriculture and cropping systems and in the expected ranges of ET under given weather and climate conditions. The latter is useful during review of RS ET values, where one can expect maximum ET in an image to approach an upper limit that is governed by energy available from the environment (solar radiation and advected sensible heat energy). Judgment on whether the RS ET model is behaving properly requires a good knowledge of the mechanics and assumptions of the RS ET process.

The accuracy estimates in Table A2.1 are derived from the following equation that empirically parses the final estimate of accuracy into three components:

$$\text{Accuracy} = \left(1.0 + \frac{ET_r F_{\text{representation error}}}{n}\right) \left(1.0 + ET_r F_{\text{image_systematic error}} + \frac{ET_r F_{\text{image_random error}}}{\sqrt{n}}\right) - 1.0 \dots\dots(x1)$$

where the various terms have been described in Chapter 8.3.

Table A2.1: Estimated error in ET produced by METRIC (plus or minus, where the values represent two standard deviations of error from the true value). Parameters in Eq. x1 are listed in A2.2.

Category	Individual Field		Large Number of Fields	
	n ¹	Estimated error (95% CI)	n ¹	Estimated error (95% CI)
Daily ET (for a single image date)				
--irrigated agriculture	1	METRIC-expert: 10%	100	METRIC-expert: 5%
		METRIC-nonexpert: 20%		METRIC-nonexpert: 11%
		K _C ET _r : 15%		K _C ET _r : 20%
--natural systems (desert, forest)	1	METRIC-expert: 15%	100	METRIC-expert: 11%
		METRIC-nonexpert: 25%		METRIC-nonexpert: 16%
		K _C ET _r : 25%		K _C ET _r : 30%
Monthly ET				
--irrigated agriculture	2	METRIC-expert: 17%	100	METRIC-expert: 13%
		METRIC-nonexpert: 26%		METRIC-nonexpert: 19%
		K _C ET _r : 15%		K _C ET _r : 20%

--natural systems 2 (desert, forest)	METRIC-expert: 22% METRIC-nonexpert: 31% $K_C ET_r$: 25%	100	METRIC-expert: 19% METRIC-nonexpert: 25% $K_C ET_r$: 30%
Growing Season ET			
--irrigated agriculture 10	METRIC-expert: 12% METRIC-nonexpert: 19% $K_C ET_r$: 20%	100	METRIC-expert: 7% METRIC-nonexpert: 13% $K_C ET_r$: 10%
--natural systems 10 (desert, forest)	METRIC-expert: 17% METRIC-nonexpert: 24% $K_C ET_r$: 30%	100	METRIC-expert: 12% METRIC-nonexpert: 18% $K_C ET_r$: 20%

¹ n = number of clear images per month or season or number of fields processed and sampled.

Source: Author's own elaboration.

Table A2.2: Values for ET_r representation error¹, ET_r image_systematic_error and ET_r image_random_error used to produce ET_r error estimates in Table 1. Values for ET_r are dimensionless.

Category	ET_r representation error			ET_r image_systematic_error		ET_r image_random_error
	For the Image Date	Monthly	Growing Season	For the Image Date	For the Image Date	
Expert – Irrigated Ag.	0	0.15	0.5	0.05		0.05
NonExpert – Irrigated Ag.	0	0.15	0.5	0.1		0.1
Expert – Non Ag.	0	0.15	0.5	0.1		0.05
NonExpert – Non Ag.	0	0.15	0.5	0.15		0.1

Source: Author's own elaboration.

The value for ET_r image_systematic_error is estimated to be 0.05 for expert appliers of METRIC (plus or minus two standard deviations) and 0.10 for non-expert or less careful appliers or reviewers of the model in the case of applications to agricultural land uses (Irrigated Ag.). The values for expert and non-expert are estimated to be 0.1 and 0.15, respectively, for non-agricultural (Non Ag.) land uses due to more challenging and non-uniform characteristics of those land uses. The value for ET_r image_random_error is estimated to be 0.05 for expert appliers of METRIC and 0.10 for non-expert or less careful appliers (or reviewers) for agricultural and nonagricultural land uses. Systematic error is expected to increase for nonagricultural land uses because of lower vegetation uniformity, impacts of shadowing from tall vegetation, varying aerodynamic conditions that may vary more, in space, than the more uniform conditions represented by METRIC functions, and less certainty in values for soil heat flux estimates (Allen *et al.*, 2007a).

The basis for the accuracy estimates in Tables x1 and x2 is derived from: experience with METRIC applications; reviewing work by various levels and capabilities of METRIC appliers; comparing differences in METRIC results among multiple users (Allen *et al.* 2007 and Morton *et al.*, 2013) and comparing METRIC results with ET measured by precision weighing lysimeters at Kimberly (Tasumi, 2003; Trezza, 2002; Tasumi *et al.*, 2005a,b).

Accuracy estimates also consider the accuracy of the ASCE standardized Penman-Monteith method (ASCE 2005) that is used for internal calibration to METRIC and as the basis for time-integration for monthly and growing season ET. The accuracy estimates assume that weather data have been quality controlled and are collected from weather stations located in or near agricultural areas. When weather data come from non-agricultural systems or non-irrigated weather stations such as airports, then some adjustment for aridity (causing high temperature and low vapor pressure readings) may be necessary (Allen *et al.*, 2021).

As an example for estimation of expected error for a METRIC "expert", one would expect the accuracy for a specific location (field) in an irrigation project having 10 cloud free images during the growing season to be: $(1.0 + 0.5/10) \times (1.0 + 0.05 + 0.05/(100.5)) - 1.0 = 1.05 \times (1.05 + 0.016) - 1.0 = +/-12$ percent. If cloud cover reduced the number of clear satellite images over the growing season to 7 images, the expected accuracy would be $(1.0 + 0.5/7) \times (1.0 + 0.05 + 0.05/(70.5)) - 1.0 = +/-15$ percent. Equation x1 is useful to gain some appreciation for the importance of frequent revisit time of satellite images, the impact of cloudiness and the impact of user or reviewer expertise.

Crop Coefficient Uncertainty. The estimated error in the crop coefficient-reference ET approach in Table A2.1 is 15 percent for experts and 25 percent for non-experts for individual irrigated fields, based on estimated, common uncertainties and error in estimating crop coefficient values without the aid of ground measurements or satellite-based calibration for localized adjustments. The estimates include typical values for uncertainty in estimated reference ET by the FAO56 and ASCE Standardized Penman-Monteith equation (Allen *et al.*, 1998; ASCE 2005). Smaller error in $K_c ET_o$ -based estimates has been obtained, for example, by Allen *et al.*, (1996) and Allen (2000) for bean, corn, and sugar beets at Kimberly, Idaho, and by Allen (1999) and Allen *et al.* (2005) for the 200 000 ha Imperial Irrigation District in southern California, United States of America (the). Error estimates in $K_c ET_o$ have also been produced by Hunsaker *et al.*, (2002) for alfalfa in Arizona and by Liu and Luo (2010) for winter wheat in China. Error estimates for nonagricultural land uses are larger than for agriculture due to increased uncertainty in estimating crop coefficients for varying ranges of vegetation density and water availability using published values. Estimated error increases as numbers of fields increases with the $K_c ET_o$ method, due to the likelihood that some fields will vary from typical conditions for vegetation density, water availability and agronomic practices. This compares to the reduction of error expected for METRIC applications as field numbers increase due to repeated sampling and due to individualized estimates, by field, by METRIC using land surface temperature and short-wave reflectance from each field. Er-Raki *et al.* (2010) discussed the benefits of local calibration of crop coefficients for olive trees on improving accuracy of the $K_c ET_o$ approach.

Monitoring water consumption (or evapotranspiration – ET) of agricultural and other vegetated land in space and time is extremely relevant for sustainable water resources management from local to global levels.

Feasible and affordable methods for ET determination over large areas, such as irrigation schemes, watershed, sub-national, national and basin scales, are through satellite Remote Sensing (RS).

The progress and advances in the availability of moderate resolution earth observations over recent years, along with the development of quite elaborated algorithms, has in fact provided an ample and diversified offer of RS ET models and platforms for the determination and provision of the spatial and temporal assessment of ET.

However, users are concerned with operational issues such as: proper spatial and temporal resolution for given applications; accuracy of the ET determinations provided by the various models and databases; methods to conduct qualitative and quantitative error analyses of RS-ET determinations; modalities to test the RS ET with field ET measurements; and criteria to know which ET data sources best fit one's purpose.

In fact, being mindful of the magnitude of uncertainty of these RS ET determinations allows the user to properly identify and select the method most suitable for a given application, so that these uncertainties are likely within acceptable limits for sound quantitative analysis leading to appropriate decisions.

These concerns have been addressed through two major enterprises undertaken by the FAO Regional Initiative on Water Scarcity for the Near East and North Africa, specifically: (i) a plan of a webinars series (<https://dgroups.org/fao/wateraccounting/library/sqff8vmt?o=lc>); (ii) the present publication reporting on the major outcomes of the webinars series, adding further insights, and providing an enriched literature review.

The present publication is intended to be a useful reference for several water actors and professionals working for the sustainability of water resources management.

Monitoring water consumption (or evapotranspiration – ET) of agricultural and other vegetated land in space and time is extremely relevant for sustainable water resources management from local to global levels.

Feasible and affordable methods for ET determination over large areas, such as irrigation schemes, watershed, sub-national, national and basin scales, are through satellite Remote Sensing (RS).

The progress and advances in the availability of moderate resolution earth observations over recent years, along with the development of quite elaborated algorithms, has in fact provided an ample and diversified offer of RS ET models and platforms for the determination and provision of the spatial and temporal assessment of ET.

However, users are concerned with operational issues such as: proper spatial and temporal resolution for given applications; accuracy of the ET determinations provided by the various models and databases; methods to conduct qualitative and quantitative error analyses of RS-ET determinations; modalities to test the RS ET with field ET measurements; and criteria to know which ET data sources best fit one's purpose.

In fact, being mindful of the magnitude of uncertainty of these RS ET determinations allows the user to properly identify and select the method most suitable for a given application, so that these uncertainties are likely within acceptable limits for sound quantitative analysis leading to appropriate decisions.

These concerns have been addressed through two major enterprises undertaken by the FAO Water Scarcity Initiative (WSI) of the Near East and North Africa (NENA) Region, specifically: (i) a plan of a webinars series (<https://dgroups.org/fao/wateraccounting/library/sqff8vmt?o=lc>); (ii) the present publication reporting on the major outcomes of the webinars series, adding further insights, and providing an enriched literature review.

The present publication is intended to be a useful reference for several water actors and professionals working for the sustainability of water resources management



ISBN 978-92-5-138242-4



9 789251 382424

CC8150EN/18/04.24